NONLINEAR DYNAMICS OF COUPLED ELECTRON-VIBRATIONAL SYSTEMS

By

Kirill Moskovtsev

A DISSERTATION

Submitted to
Michigan State University
in partial fulfillment of the requirements
for the degree of

Physics – Doctor of Philosophy

2018

ABSTRACT

NONLINEAR DYNAMICS OF COUPLED ELECTRON-VIBRATIONAL SYSTEMS

By

Kirill Moskovtsev

We study coupled electron-vibrational condensed-matter systems. Of primary interest are many-electron effects in two types of systems: nano- and micromechanical semiconductor resonators and electrons on the surface of liquid helium. Both types of systems are well characterized and display rich and unusual behavior, which makes them particularly attractive for revealing manifestations of the electron-vibrational coupling. We show that, in nano- and micro-mechanical resonators, the coupling leads to strong nonlinearity of the modes and a specific temperature dependence of their frequencies. The mechanism is the lifting of the degeneracy of the multi-valley electron energy spectrum by the vibration-induced strain. The redistribution of the electrons between the valleys is controlled by a large ratio of the electron-phonon coupling constant to the electron chemical potential or temperature. We find unusually large quartic in the strain terms in the electron free energy, which result in an unusually strong amplitude dependence of the mode frequencies. This dependence is calculated for silicon micro-systems, which at present are most broadly used in applications. It is significantly different for different modes and crystal orientations, and can vary nonmonotonously with the electron density and temperature. The proposed mechanism leads also to a very strong temperature dependence of the mode frequencies. These results explain the experimental observations and suggest ways of improving the stability and sensitivity of modern micromechanical devices. The other system studied, the electrons floating above the helium surface and coupled to the vibrations in the liquid helium, is special at least in two respects. First, this system is free from defects, which makes it the best known conductor and a perfect system for studying electron-vibrational coupling unmasked by disorder. Second, the electron-electron interaction is strong, so that the electrons form a strongly correlated liquid or a solid. We have developed an algorithm that allowed us to carry out extensive molecular dynamics simulations of the system with the account taken of the microscopic mechanisms of the electron scattering by the excitations in helium. The emphasis was made on calculating the experimentally observable characteristic, the many-electron mobility. The mobility displays particularly interesting features when the electrons are placed in a periodic potential. These features are a direct consequence of the strongly correlated electron motion. As we found, they enable a direct characterization of the correlations in the electron liquid and a direct measurement of the correlation length through its effect on the activated transport. They also provide a means for studying commensurate-incommensurate transitions through mobility measurements. We show that the crystallization in the electron system can be identified from the disappearance of self-diffusion. The way the diffusion coefficient vanishes is qualitatively different in the cases of incommensurate and commensurate electron systems. The mobility transverse to the periodic potential displays an activation dependence on the potential strength, with the exponent that strongly depends on the extent of the incommensurability.

ACKNOWLEDGEMENTS

First of all, I would like to thank my advisor, Dr. Mark Dykman. It is a privilege to have Mark as my guide into the beautiful world of physics. In addition to the invaluable scientific knowledge, I also learned from him how to thoroughly study large and complicated problems. Mark taught me to be patient in understanding every possible detail of a problem at hand before claiming any results. Only with this in mind was I able to produce the results presented in this thesis. I am also thankful to him for encouraging me to do difficult calculations that I would hesitate to do otherwise. Mark has always been caring and supportive beyond academic matters as well for which I greatly appreciate.

I would also like to thank my Thesis Committee members, Dr. Norman Birge, Dr. Carlo Piermarocchi, Dr. Scott Pratt, and Dr. Carl Schmidt, for the valuable discussions of my research and their useful comments. I also learned a lot of condensed matter physics from Norman and Carlo during the seminar and journal club discussions. I would like to thank Carl who taught me Electrodynamics which is useful in all of my studies. Special thanks go to Scott who helped me on multiple occasions during my PhD. In fact, Scott was the first to recommend me to meet Mark.

I am very grateful to Dr. Thomas Kenny and his graduate students Yushi Yang and David Heinz for providing ideas for my research and sharing their experimental results.

I would also like to thank Dr. Steven Shaw for useful and enjoyable discussions and for sharing his perspective on microelectromechanical systems.

I am thankful to Dr. Johannes Pollanen and Dr. Kostyantyn Nasyedkin for stimulating discussions and sharing their fascinating research ideas about the electrons on helium.

Many thanks go to my colleagues and officemates at MSU, Yaxing Zhang, Juan Atalaya, Pavel Pulunin, Ori Shoshani, and Nathan Satchell, with whom I enjoyed discussing physics and everything else.

I would also like to thank the staff at the Physics and Astronomy Department, who made my stay at MSU smooth and pleasant.

Last but not least, I would like to thank my family for their support and encouragement during my long journey at MSU.

TABLE OF CONTENTS

LIST OF TABLES

LIST OF FIGURES

CHAPTER 1

INTRODUCTION

The dynamics of an electron system interacting with a quantized vibrational field is one of the central problems of physics. This problem has been studied in quantum electrodynamics, but the results there are limited to the very weak coupling and largely to the single-electron formulation. In condensed matter systems, it is well-known that the electron-phonon interaction leads to a rich variety of phenomena, from superconductivity to small and large polarons. New aspects of the problem have come forth with the recent progress in technology. Two important breakthroughs in this respects is the emergence of nanomechanics and the studies of the many-electron physics in a quanitzed layer of electrons localized on the surface of liquid helium. The major feature of these systems, which makes them particularly attractive, is that the effects of the electron-vibrational coupling are not masked by defects. In nanomechanical systems, the vibrational modes are well characterized and can be accessed directly, whereas the electron density can be often independently controlled. For the electrons on helium, on the other hand, the electrons are floating in free space, and their coupling with each other and with the vibrations of the helium surface are the only couplings that are of importance.

Another important common feature of nanomechanical systems and the electrons on the helium surface is the substantial nonlinearity of the dynamics. The best-understood nonlinear system is a nonlinear oscillator. Even in a simplest system like this, the nonlinearity leads to an overwhelmingly rich set of phenomena, especially when the system is coupled to a thermal bath or other degrees of freedom. Nanomechanical systems provide an opportunity to explore all aspects of this rich phenomenology. Electrons on helium, on the other hand, are known to display remarkable nonlinear transport behavior that is due to coupling of strongly correlated electrons to the helium surface vibrations. It is the goal of this thesis to theoretically study some effects of the electron-phonon coupling and the electron-electron correlations in relation to the nonlinear behavior of these two systems.

A recently developed new type of vibrational systems, mechanical nanoresonators (MNRs), also known as nano-electro-mechanical systems (NEMS), are mesoscopic by nature. Because they are small, they display many features of microscopic systems. At the same time, they are sufficiently large to make it possible to study the dynamics of an individual vibrational system. Because of their small size, these devices become nonlinear even at comparatively small vibration amplitudes. Another universal feature arising from the small size is the invariable presence of fluctuations. Moreover, the system often displays nonlinear behavior already for thermal fluctuations. It is the interplay of fluctuations, dissipation, and nonlinearity that makes these systems fascinating objects for fundamental research and potential applications.

Interaction of vibrational modes with other degrees of freedom brings even more complex phenomenology and new opportunities. It may be the interaction with other vibrational or optical modes, a qubit, or an electronic system. Interaction with other vibrational modes leads to a variety of nonlinear resonance effects [8, 9, 10], while coupling to optical modes and qubits may lead to a new way of manipulating quantum information [11, 12, 13]. Interaction with electrons leads to a variety of effects as well, Coulomb blockade being a simple example [14, 15, 16, 17, 18, 19, 20, 21, 22, 23].

In Chapter 2, we present a theory of a recently observed effect [24] that arises because of the coupling between electronic and vibrational degrees of freedom in nano- and micro-mechanical systems. We explain strong mechanical nonlinearity that appears in semiconductor-based nano- and micro-mechanical systems with high concentrations of free carriers. We show that the mechanism is the lifting of the valley degeneracy by strain. Redistribution of the electrons between the valleys is controlled by a large ratio of the electron-phonon coupling constant to the electron chemical potential or temperature. The described effect is unusually strong and is the main source of nonlinearity in resonators made of doped multi-valley semiconductors. The presented theory provides tools for understanding and controlling the vibration nonlinearity in these systems. The results are also very important for applications, they are relevant for the majority of silicon MEMS devices, which are broadly used in modern electronics.

Electrons on the surface of liquid helium provide another well-characterized system where strongly nonlinear aspects of the electron dynamics and the electron-vibrational coupling can be investigated. This is one of the most perfect electronic systems, with the highest measured mobility [25]. A characteristic feature of this system is a strong electron-electron interaction. This interaction affects, and sometimes completely modifies the electron scattering by surface waves (ripplons) and phonons in helium. In typical experiments, the electron system is non-degenerate yet strongly correlated. The electrons crystallize into a Wigner solid at low temperatures, while they form a non-degenerate strongly correlated liquid for higher temperatures. Correlation effects should acquire new features and lead to pronounced consequences when the 2D electronic system is brought in contact with a substrate. The substrate may create quenched disorder or periodic modulation depending on its nature. So far, in other systems, two groups of substrate effects have been studied. One area is the effects of the substrate on the structure of a two-dimensional crystal deposited onto it, including the phase transitions related to restructuring of the crystal [26, 27]. The second area is depinning in response to a strong drive and the emerging dynamical phases, see Ref. [28] and papers cited therein. The dynamical effects have been studied primarily for vortices and skyrmions in superconductors and for colloidal particles in a periodic optical potential. In all studies we are aware of the motion was overdamped, inertial effects played no role. This is qualitatively different from the system of electrons on helium, where the electron relaxation time is extremely long and inertia is a major factor.

In Chapter 3, we present the results of a numerical study of the strongly correlated electron system on helium in an external periodic 1D potential. We find the effects of the modulation on the freezing transition and the structure of the ground state of the electron system. However, of the central interest to us are transport properties of the *strongly correlated electron liquid*. Such properties are accessible to direct experimental measurements. This makes them particularly interesting. We note that the presence of a long range order in the electron system can be revealed through transport measurements [29, 30]. In contrast, it is not known how to directly reveal strong electron correlations in the liquid phase.

Traditionally, commensurability effects have been considered for ordered phases. We show, however, that effective commensurability plays a crucial role in the transport even when no long-range order is present in the electron system. In this regime, no classical pinning can occur since the system remains disordered with dynamically changing structure due to thermal motion. Nevertheless, as we demonstrate, a periodic potential can dramatically suppress conductivity across the modulation troughs when the commensurability ratio is close to integer values. We also find an exponential dependence of the mobility on the modulation amplitude in the "commensurate" liquid phase, indicating activated behavior. This behavior is highly sensitive to the correlation length in the liquid, which can provide a direct means for measuring this length, an issue of significant broad interest for an electron liquid. The commensurability effects we observe persist in a wide range of regimes: from highly underdamped to overdamped dynamics. However, highly underdamped dynamics, such as that of the electrons on helium, allows one to measure the effects of particle-particle correlations in the cleanest way, not modified by friction.

To study the effect of the electron coupling to the quantized filed of excitations in helium on the dynamics of a strongly correlated electron system, we extend the conventional molecular dynamics method to include electron scattering by ripplons and phonons. This scattering is described microscopically in terms of the momentum-dependent scattering rate for the actual coupling to the excitations in helium.

CHAPTER 2

STRONG VIBRATION NONLINEARITY IN SEMICONDUCTOR-BASED NANOMECHANICAL SYSTEMS

2.1 Introduction

Understanding vibrational motion has always been one of the major motifs in physics. Historically, such motion was first studied for macroscopic systems. The progress in optics in the 20th century made it possible to study microscopic vibrational systems, in particular molecular systems and vibrational modes in solids. However, these studies relied on ensemble measurements, where the signal came from a large number of individual systems, e.g., a large number of molecules. Recent progress in nanotechnology has made it possible to study a new type of vibrational systems, mechanical nanoresonators (MNRs). Such systems are mesoscopic by nature. Because they are small, they display many features of microscopic systems. At the same time, they are sufficiently large to make it possible to study the dynamics of an individual vibrational system.

The interest in the MNRs is threefold. On the one hand, the vibrational excitations result from the collective motion of a large number of atoms, which leads to rich dynamics that involves various many-body effects. On the other hand, MNRs are one of the best systems for studying, in a well-characterized environment, statistical physics far from thermal equilibrium and quantum physics at the macroscale. Last but not least, they are of significant interest for various applications, from ultrasensitive mass, charge, and force detection [31, 32, 33, 34, 35, 36, 37, 38, 39, 40, 41, 42, 43, 44, 45, 46, 47, 48, 49, 50, 51, 52] to magnetometers with a single-spin sensitivity [53, 54, 55, 56, 57, 58] to applications in electronics [59] to mention but a few.

The MNRs were developed in the $90'$s [60] and quickly attracted considerable interest. It was realized that these systems are extremely versatile. The vibration frequency can be tuned not only through the dimensions and the shape of a device, but also *in situ* by electrostatic and optical means. In addition, the lifetime of vibrations has now been increased to milliseconds and above thanks to the progresses in nanofabrication. These advances have opened new possibilities in controlling the interaction of nanomechanical vibrations with electrons, photons, and propagating phonons and studying the effects of this interaction.

A consequence of the small size of MNRs expected from the general arguments of statistical physics [61] is the occurrence of comparatively strong quantum and classical fluctuations. These fluctuations play a significant role in the vibration dynamics. A feature of MNRs is that, along with the invariably present thermal fluctuations, they are subject to nonequilibrium fluctuations. Characterizing and understanding the nature of these fluctuations, as well as revealing their consequences is a major challenge.

Another basic feature of the MNRs is the vibration nonlinearity. Because of the small system size, vibrations with even comparatively small amplitudes become nonlinear. The nonlinearity often comes into play already for thermal fluctuations. It leads to the broadening of the spectra of the response to an external field, which is not related to energy dissipation. As a result, the shape of the spectra is determined by the interplay of dissipation, fluctuations, and nonlinearity. A consequence of the vibration nonlinearity is resonant and nonresonant coupling of different vibrational modes. This specific feature of MNRs leads to nonlinear inter-mode energy exchange and also to cross-modulation of the vibration frequencies.

The interplay of fluctuations and nonlinearity in the vibrational spectra can be understood from the following argument. The energy spectrum of a harmonic oscillator is equidistant, with the level spacing $\hbar\omega_0$, where ω_0 is the oscillator eigenfrequency. The response of the oscillator to a periodic field displays a resonant peak at ω_0. Because transitions between different neighboring energy levels are resonant at the same time, the response is nontrivial and has been a subject of interest from the early days of quantum mechanics [62]. It is somewhat surprising, from this point of view, that the resulting peak in the oscillator absorption spectrum often has a simple Lorentzian shape with a halfwidth determined by the oscillator decay rate Γ. Phenomenologically, this decay rate corresponds to a friction force $-2\Gamma m\dot{q}$, where q is the oscillator coordinate and m is the effective mass. In MNRs, the ratio $Q = \omega_0/2\Gamma$, which is called the Q factor, can be extremely high, approaching $10^7 - 10^8$ [63].

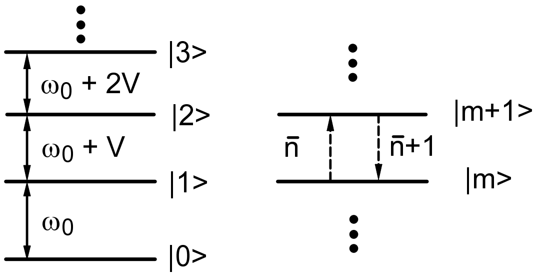

Figure 2.1 Left panel: energy levels of a nonlinear oscillator in the lowest order perturbation theory. Right panel: the simplest and most common type of relaxation processes of an oscillator. A transition between the neighboring oscillator states is accompanied by creation or annihilation of excitations in a thermal reservoir. The relative transition probabilities are determined by the oscillator Planck number $\bar{n} = [\exp(\hbar\omega_0/k_BT) - 1]^{-1}$. In the phenomenological description of the oscillator dynamics, the sketched processes are responsible for the friction force proportional to the oscillator velocity.

Even a comparatively small vibration nonlinearity can strongly change the shape of the spectrum. Indeed, for a nonlinear oscillator transitions between neighboring energy levels occur at different frequencies, see Fig. 2.1. The energy spectrum in this figure corresponds to the lowest order perturbation theory in the oscillator nonlinearity. If the frequency difference $|V|$ significantly exceeds the decay rate Γ, the response of the oscillator will display spectral peaks at frequencies $\omega_0 + nV$ with integer n. The overall spectral width then is $\sim |V|(2\bar{n}+1)$, where $\bar{n}$ is the typical number of excited states. In thermal equilibrium, the populations of the levels fluctuate, and therefore such spectral broadening is indeed fluctuational by nature.

The above mechanism is an example of non-dissipative spectral broadening due to fluctuations of the vibration eigenfrequency ω_0. There are different sources of such fluctuations. An example of another important source is attachment/detachment of molecules to an NMR. The resonator mass, and thus the frequency, depend on the number of attached molecules, which underlies the MNR-based mass spectroscopy [31, 32, 34, 38, 39, 46, 50]. However, frequency fluctuations associated with attachment, detachment, or diffusion of molecules along the resonator lead to spectral broadening [64]. It resembles [65, 66] the broadening due to the mode nonlinearity, with the different frequencies in Fig. 2.1 now corresponding to the different number or positions of attached molecules.

The interplay between fluctuations and nonlinearity remains an active topic of research. An example of such interplay is the recently observed nonlinear frequency transduction of nanomechanical Brownian motion [67, 68]. In that case, the Duffing nonlinearity transduces the fluctuational motion of the observed eigenmode and other nonlinearly coupled modes into frequency noise. Yet, even though there has been substantial progress in understanding of frequency fluctuations and nonlinearities, the fundamental limits of the frequency noise in nanomechanics are still not understood [69].

A profound consequence of the nonlinearity of MNRs is bi- (and multi-) stability of forced vibrations. It emerges already for comparatively weak driving force provided the force resonates with the mode frequency or its overtones. Periodically driven MNRs are among the best systems for studying the Floquet dynamics in the presence of dissipation and quantum and classical noise. The accessible phenomena range from the fluctuation squeezing to the statistical distribution and the rate of switching between coexisting metastable states far from thermal equilibrium, when a system has no detailed balance.

In addition to non-dissipative phenomena described above, MNRs often display dissipative nonlinear effects also known as nonlinear damping. One of the most important characteristics of nano-scale vibrational modes is their decay rate, which can be much smaller than the vibration frequency [70, 71, 72, 73, 53, 46, 49, 38, 44, 50]. The relaxation mechanisms include radiation into the bulk modes of the medium surrounding the nanosystem [74, 75, 76, 77, 78], nonlinear coupling between the modes localized inside the system [79, 80, 81, 82, 83, 84], and coupling with electronic excitations[18, 20, 21, 85] and two-level defects [86, 87]. Conventionally, decay of a vibrational mode is associated with an exponential fall-off of the vibration amplitude in time. This behavior is often observed in the experiment. In the phenomenological description of the mode dynamics, it comes from the friction force $-2\Gamma\dot{q}$, where q is the vibration coordinate and Γ is the friction coefficient. Such friction is called linear. Recent experiments have shown that, already for moderate vibration amplitudes, in various nano- and micromechanical systems the amplitude decay is nonexponential in time and/or the maximal amplitude of forced vibrations nonlinearly depends on the force amplitude [88, 89, 90, 91, 83]; respectively, the friction force is a nonlinear function of the mode coordinate and velocity. Nonlinear friction (nonlinear damping) has recently attracted considerable attention also in the context of quantum information processing with microwave cavity modes, where it was engineered to be strong [92, 93].

Nonlinear damping is well understood in quantum optics, where this is a major mechanism that limits the laser intensity [94]. In nanomechanical systems, the mechanism is scattering of thermally excited vibrational modes off the considered eigenmode [95]. The scattering is accompanied by energy transfer of $2\hbar\omega_0$ for nonlinear damping. Along with damping, scattering of phonons off the considered mode leads to its dephasing, i.e., loss of coherence, as was first discussed for high-frequency vibrations localized near defects in solids [96, 97]. In contrast to damping, the scattering that leads to dephasing is quasi-elastic, the energy of the mode is not changed. To the lowest order, the process comes from the quartic nonlinearity in the mode coupling, although the parameters are renormalized by the cubic nonlinearity, which is also the case for nonlinear friction.

Another important consequence of nonlinearity in vibrational systems is the appearance of nonlinear resonances [9]. Nonlinear resonance, where the energy-dependent vibrational frequencies are commensurate, has a long history in quantum and classical mechanics. It goes back at least to Laplace and Poincare on the classical side and to the Fermi resonance on the quantum side [98, 99], and occurs in a broad range of systems, from celestial bodies to ecological systems to molecules [100, 101, 102, 103]. Recently, nonlinear resonance has attracted particular interest in the context of nano- and micro-mechanical vibrational systems [8, 104, 10, 105, 106, 107, 108, 109, 110] and microwave cavities used in quantum information [92, 111]. These mesoscopic systems provide unprecedented access to studying, using, and controlling this complicated phenomenon.

In conservative classical systems, nonlinear resonance leads to energy oscillations between the resonating modes. This is reminiscent of the energy oscillations between two coupled harmonic oscillators with close frequencies. However, the actual picture in nonlinear resonance is more complicated, extending to dynamical chaos. On the quantum side, nonlinear resonance is in some sense simpler in the absence of dissipation, as its primary signature is the familiar level repulsion.

The quantum situation changes if the resonating modes are dissipative. If the modes have very different decay rates, one of them can serve as a thermal reservoir for another, cf. [112]. This effect has been used to drive a slowly decaying microwave cavity mode to a coherent quantum state [92]; it extends to driven modes [113], and such extension has attracted much attention in cavity optomechanics [72].

An important advantageous feature of mesoscopic oscillators is the possibility to tune them in and out of nonlinear resonance. This can be done by directly controlling their frequencies [8] or dynamically, using the dependence of the frequency on the vibration amplitude. Here, by driving a mode, one brings its overtone into resonance with an overtone of another mode, which is then also excited. The ensuing backaction significantly changes the dynamics of the driven mode and, in particular, its decay after the driving is switched off. Such decay is a major means of studying mesoscopic vibrational systems [69].

Electron-phonon coupling strongly affects vibrational modes of nano- and micro-electro-mechanical systems. Much interest have attracted the effects of this coupling related to the reduced dimensionality of the electron system, as they make it possible to reveal interesting consequences of the electron correlations at the nanoscale, the Coulomb blockade being a simple example, and their strong effect on the vibrational dynamics, cf. [14, 15, 16, 17, 18, 19, 20, 21, 22, 23] and references therein.

Much less attention has been paid to the consequences of the electron-phonon coupling, which are related to the discreteness of the vibrational spectrum of a nanosystem, but emerge in the absence of size quantization of the electron motion. One of such consequences, which we study in this paper, is the coupling-induced change of the vibration nonlinearity. Strong nonlinearity is a generic feature of vibrations in small systems [114, 115]. Its easily accessible manifestation is the dependence of the mode frequencies on the vibration amplitudes. This dependence corresponds to the “self-action" of the mode, and its familiar analog in bulk crystals are acoustic solitons [116, 117]; however, the nonlinearity required for observing such solitons usually is sufficiently strong only for high-frequency phonons. Also, the change of the eigenfrequency with the mode amplitude is of interest for modes with a discrete frequency spectrum, such as standing waves in mesoscopic systems, but not for propagating waves with a quasi-continuous spectrum.

Much attention have been recently attracting Si-based nano- and micromechanical systems, see [118, 69] and references therein. In such systems there was observed an unexpectedly large change of the amplitude dependence of the vibration frequency with the varying electron density [119, 24]. When the doping level was increased from 2.8×10^{18} cm^{-3} to 5.9×10^{19} cm^{-3}, the nonlinearity parameter increased by more than an order of magnitude. Moreover, the nonlinearity change was different for the vibrational modes with different spatial structure.

In this paper we develop a theory of the nonlinearity of vibrational modes in semiconductor nano- and micro-mechanical systems with high electron density. We show that the electron-phonon coupling can lead to a strong self-action of the vibrational modes, which in turn significantly modifies the amplitude dependence of the mode frequencies. We find the dependence of the effect on the electron density and temperature.

For bulk semiconductors, the effect of the electron-phonon coupling on the elastic properties, including the three-phonon coupling, was first analyzed by Keyes [120]. The analysis referred to *n*-Ge and was based on the deformation potential approximation. The idea was that deformation lifts the degeneracy of the equivalent electron valleys, which leads to a redistribution of the electrons over the valleys. In turn, such redistribution changes the speed of sound depending on the direction and polarization of the sound waves and also affects the sound speed in the presence of uniaxial stress. This theory was extended to silicon and the corresponding measurements were done by Hall [121]. However, Hall also observed the change of the speed of transverse sound waves and the effect of stress on sound propagation in the geometries, where these effects are due to shear deformation and do not arise in the deformation potential model. A theory of the change of the linear shear elastic constant in silicon due to the intervalley redistribution of the electrons was developed by Cerdeira and Cardona [122].

As we show, in mesoscopic systems the strain-induced redistribution of the electrons over the valleys of the conduction band leads to the previously unexplored strong fourth-order nonlinearity of the vibrational modes. This nonlinearity gives a major contribution to the amplitude dependence of the vibration frequency. The redistribution also leads to a temperature dependence of the frequencies. The magnitudes of the effects sensitively depends on the mode structure. We describe them for several types of modes, including those studied in the experiment [119, 24] and qualitatively compare the results with the observations. The theoretical results refer to both degenerate and nondegenerate electron systems. Specific calculations are done for silicon resonators.

In Sec. 2.2 we give, for completeness, the expressions for the mode normalization and the amplitude-dependent frequency shift of coupled nonlinear modes in a nano- or micro-system. In Sec. 2.3 and Appendix A.1 we provide expressions for the electron-phonon coupling induced change of the elasticity parameters, including the parameters of quartic nonlinearity. In Sec. 2.4 we discuss the asymptotic behavior of the parameters of quartic nonlinearity for low and high electron density and give their explicit form for silicon. In Sec. 2.5 we calculate the nonlinear frequency shift for several frequently used vibrational modes in single-crystal silicon systems and show the dependence of this shift on the electron density and temperature. The explicit analytical expressions are given in Appendices A.4 and A.5. Sec. 2.7 contains concluding remarks.

2.2 Nonlinear frequency shift of low-frequency eigenmodes

Of primary interest for nano- and micro-mechanical systems are comparatively low-frequency modes with wavelength on the order of the maximal size of the system. Examples are provided by long-wavelength flexural modes of nanotubes, nanobeams, and nano/micro-membranes, or acoustic-type modes in microplates or beams. These modes are easy to excite and detect. We will enumerate them by index ν. Their dynamics is described by the elasticity theory [123]. The spatial structure of the displacement field of a mode $\boldsymbol{u}^{(\nu)}(\boldsymbol{r})$ in the harmonic approximation is determined by the boundary conditions. We will choose $\boldsymbol{u}^{(\nu)}(\boldsymbol{r})$ dimensionless, so that in our finite-size system

$$\int d\boldsymbol{r}\,\boldsymbol{u}^{(\nu)}(\boldsymbol{r})\cdot\boldsymbol{u}^{(\nu')}(\boldsymbol{r}) = V\delta_{\nu\nu'}. \tag{2.1}$$

Here, V is the volume of the system. We assumed that the mode eigenfrequencies ω_ν are nondegenerate; including degenerate modes is straightforward. For simplicity, we also assumed that the system is spatially uniform; an extension to spatially nonuniform systems is straightforward as well.

We emphasize the distinction of the normalization (2.1) from the conventional normalization for bulk crystals, where ν corresponds to the wave vector and the branch number, and the normalization integral is independent of the volume. The normalization (2.1) is convenient for the analysis of low-frequency modes with the discrete spectrum characteristic of mesoscopic systems. Such modes are standing waves, and therefore vectors $\boldsymbol{u}^{(\nu)}$ can be chosen real.

The low-frequency part of the displacement can be written as

$$\boldsymbol{u}(\boldsymbol{r},t) = \sum_\nu Q_\nu(t)\boldsymbol{u}^{(\nu)}(\boldsymbol{r}). \tag{2.2}$$

Functions $Q_\nu(t)$ give the mode amplitudes. In the harmonic approximation the dynamics of the standing waves is described by the Hamiltonian

$$H_h = \frac{1}{2}\sum_\nu (M^{-1}P_\nu^2 + M\omega_\nu^2 Q_\nu^2), \tag{2.3}$$

where P_ν is the momentum of mode ν and M is the mass of the system.

The anharmonicity of the crystal leads to mode-mode coupling. Within the elasticity theory this coupling is described by the terms in the Hamiltonian, which are cubic and quartic in the strain tensor. We will not consider higher-order terms, which are small for the mode amplitudes of interest. From the expansion (2.2), we obtain the nonlinear part of the Hamiltonian in the form

$$\begin{aligned} H_{\mathrm{n}l} =& \frac{1}{3}\sum \beta_{\nu_1\nu_2\nu_3}Q_{\nu_1}Q_{\nu_2}Q_{\nu_3} \\ &+ \frac{1}{4}\sum \gamma_{\nu_1\nu_2\nu_3\nu_4}Q_{\nu_1}Q_{\nu_2}Q_{\nu_3}Q_{\nu_4}. \end{aligned} \tag{2.4}$$

Equation (2.4) is essentially an expansion in the ratio of the mode amplitudes to their characteristic wavelength, which is of the order of the appropriate linear dimension of the system. This is why mesoscopic systems are of particular interest, as here vibrations of low-frequency eigenmodes become nonlinear for already small vibration amplitudes.

A familiar consequence of nonlinearity in nano- and micromechanical systems is the dependence of the vibration frequency of a mode on its own amplitude and on the amplitudes of other modes, see Ref. [115] for a review. In particular, the change $\delta\omega_\nu$ of the mode frequency due to the vibrations of the mode itself, $Q_\nu(t) = A_\nu \cos\omega_\nu t$, is [124, 125]

$$\delta\omega_\nu \approx \left[\frac{3\gamma_\nu}{8M\omega_\nu} - \sum_{\nu'} \frac{\beta^2_{\nu\nu\nu'}(3\omega^2_{\nu'} - 8\omega^2_\nu)}{4M^2\omega^3_\nu(\omega^2_{\nu'} - 4\omega^2_\nu)}\right] A^2_\nu, \tag{2.5}$$

where $\gamma_\nu \equiv \gamma_{\nu\nu\nu\nu}$ and we kept the terms of the first order in γ and the second order in β.

The nonlinear mode coupling (2.4) leads also to the frequency shift due to thermal vibrations of the modes. The dominating contribution to this shift for low-frequency modes comes from their coupling to modes with frequencies $\sim k_B T/\hbar$, which have a much higher density of states. This shift is described by an expression that is similar to Eq. (2.5) with A^2_ν replaced by $A^2_{\nu'} \sim k_B T/M\omega^2_{\nu'}$ and placed under the sum over ν', in the classical limit.

2.3 The nonlinearity due to the electron-phonon coupling

We will consider the vibration nonlinearity due to the electron-phonon coupling in multi-valley semiconductors with cubic symmetry, silicon and germanium being the best known examples. In such semiconductors, the energy valleys of the conduction band are located at high-symmetry axes of the Brillouin zone. Strain lifts the symmetry and thus the degeneracy of the valleys.

The simplest mechanism of the electron-phonon coupling is the deformation potential. Here, the energy shift δE_α of valley α is determined by the deformation potential parameters Ξ_u and Ξ_d. Parameter Ξ_u gives the valley shift due to the strain along the symmetry axis of the valley. In contrast, parameter Ξ_d gives the shift related to dilatation; such shift is the same for all valleys. These parameters are well known for various semiconductors [126]. In terms of the strain tensor ε_{ij}, we have $\delta E_\alpha = \sum_{ij} \Xi^{(\alpha)}_{ij} \varepsilon_{ji}$, where $\hat{\Xi}^{(\alpha)} = \Xi_d \hat{I} + \Xi_u \boldsymbol{e}^{(\alpha)} \otimes \boldsymbol{e}^{(\alpha)}$, with $\boldsymbol{e}^{(\alpha)}$ being the unit vector along the symmetry axis of the valley. We use the hat symbol to indicate tensors and symbol “$\otimes$" to indicate tensor products ($\boldsymbol{e}^{(\alpha)} \otimes \boldsymbol{e}^{(\alpha)}$ singles out the strain along the axis of valley α). The analysis below is not limited to the deformation potential approximation. An important extension will be discussed using silicon as an example.

We assume that the strain varies in time and space slowly compared to the reciprocal rate of intervalley electron scattering and the intervalley scattering length, respectively. Then the electron system follows the strain adiabatically. The electron density $n^{(\alpha)}(\boldsymbol{r})$ in valley α is decreased or increased depending on whether the bottom of the valley goes up or down. In the single-electron approximation and for the deformation potential coupling, the electron free energy density for a given strain is $F_e = \sum_\alpha \{f_e[n^{(\alpha)}(\boldsymbol{r})] + n^{(\alpha)}(\boldsymbol{r})\Xi_{ij}^{(\alpha)}\varepsilon_{ji}(\boldsymbol{r})\}$ where $f_e[n(\boldsymbol{r})]$ is the free energy density for electrons with density $n(\boldsymbol{r})$ in a valley in the absence of coupling to phonons.

The electro-neutrality requires that the total electron density summed over the valleys be constant. The free energy density F_e has to be minimized over $n^{(\alpha)}(\boldsymbol{r})$ to meet this constraint. This gives the change of the electron chemical potential $\delta\mu$ due to strain $\hat{\varepsilon}$. The resulting increment of the electron free energy density has the form of a series expansion in the strain tensor,

$$\begin{aligned}\delta F_e =& \widehat{\Lambda}_1 \cdot \hat{\varepsilon} + \frac{1}{2}\widehat{\Lambda}_2 \cdot \hat{\varepsilon} \otimes \hat{\varepsilon} + \frac{1}{6}\widehat{\Lambda}_3 \cdot \hat{\varepsilon} \otimes \hat{\varepsilon} \otimes \hat{\varepsilon} \\ &+ \frac{1}{24}\widehat{\Lambda}_4 \cdot \hat{\varepsilon} \otimes \hat{\varepsilon} \otimes \hat{\varepsilon} \otimes \hat{\varepsilon} + \ldots \end{aligned} \tag{2.6}$$

Here $\widehat{\Lambda}_1, \widehat{\Lambda}_2, \widehat{\Lambda}_3$, and $\widehat{\Lambda}_4$ are tensors of ranks 2, 4, 6, and 8, respectively. They are contracted with the tensor products of the strain tensor $\hat{\varepsilon}$. Respectively, $\widehat{\Lambda}_k$ are the electronic contributions to the linear (for $k = 2$) and nonlinear (for $k > 2$) elasticity parameters of the crystal. These contributions are isothermal, but since the change of the mode frequencies from the electron-phonon coupling is small and the nonlinearity is also small, the difference with the adiabatic expressions can be disregarded.

To the third order in $\hat{\varepsilon}$ the expression for δF_e in terms of the shift of the valleys was found by Keyes [120] in the analysis of sound wave propagation. However, to find the parameters of the quartic nonlinearity of resonant modes in small systems, which is of primary interest to us, we also need to keep quartic terms in Eq. (2.6).

As seen from the explicit form of the parameters of the expansion (2.6) given in Appendix A.1, $\widehat{\Lambda}_k \propto \Xi_u[\Xi_u/\max(\mu_0, k_BT)]^{k-1}$ ($k = 1,2,...$), where μ_0 is the electron chemical potential in the absence of strain; it is determined by the total (summed over the valleys) electron density n. Of central importance for the analysis is that parameter $\Xi_u/\max(\mu_0, k_BT) \sim 10^3$ for electron densities $n \sim 10^{19}$ cm^{-3} and room temperatures, i.e.

$$\Xi_u/\max(\mu_0, k_BT) \gg 1. \tag{2.7}$$

As a consequence, the coefficients at the nonlinear in $\hat{\varepsilon}$ terms in Eq. (2.6) quickly increase with the increasing order of the nonlinearity [the overall series (2.6) is converging fast because of the smallness of the strain tensor].

The increase of $\widehat{\Lambda}_k$ with k allows us to keep in $\hat{\varepsilon}$ only the terms linear in the lattice displacement, i.e., to set $\varepsilon_{ij} = (1/2)(\partial u_i/\partial x_j + \partial u_j/\partial x_i)$, where u_i and x_i are the components of the displacement and the coordinates, respectively. Indeed, in this case a kth term of the series (2.6) is of order k in the displacement. If we included the quadratic in $\partial u_i/\partial x_j$ term into one of the $\hat{\varepsilon}$ tensors in the kth term, this term would become of order $k+1$ in the displacement. However, for linear $\hat{\varepsilon}$ the $(k+1)$th term in the series (2.6) is also of the $(k+1)$th order in the displacement, but is larger by factor $\Xi_u/\max(\mu_0, k_BT)$. We note that, for the modes that involve rotation, one should use the relative lattice displacement $\boldsymbol{u}(\boldsymbol{r})$ rather than the overall displacement [123].

For linear $\hat{\varepsilon}$, the total strain is a sum of partial contributions of strain from individual modes. For mode ν, such partial contribution is expressed in terms of the scaled displacement $\boldsymbol{u}^{(\nu)}(\boldsymbol{r})$ [see Eq. (2.2)] as $\hat{\varepsilon} = Q_\nu \hat{\varepsilon}^{(\nu)}$, where $\varepsilon_{ij}^{(\nu)}(\boldsymbol{r}) = \frac{1}{2}[\partial u_i^{(\nu)}(\boldsymbol{r})/\partial x_j + \partial u_j^{(\nu)}(\boldsymbol{r})/\partial x_i]$. We note that, in contrast to the dimensionless strain tensor $\hat{\varepsilon}$, tensor $\hat{\varepsilon}^{(\nu)}$ has dimension [length]$^{-1}$.

From Eq. (2.6) we find the electronic contributions to the nonlinearity parameters $\beta^{(e)}_{\nu_1\nu_2\nu_3}, \gamma^{(e)}_{\nu_1\nu_2\nu_3\nu_4}$ in Hamiltonian (2.4) ,

$$\begin{aligned}\beta^{(e)}_{\nu_1\nu_2\nu_3} =& \frac{1}{2}\int d\boldsymbol{r}\widehat{\Lambda}_3 \cdot \hat{\varepsilon}^{(\nu_1)} \otimes \hat{\varepsilon}^{(\nu_2)} \otimes \hat{\varepsilon}^{(\nu_3)},\\ \gamma^{(e)}_{\nu_1\nu_2\nu_3\nu_4} =& \frac{1}{6}\int d\boldsymbol{r}\widehat{\Lambda}_4 \cdot \hat{\varepsilon}^{(\nu_1)} \otimes \hat{\varepsilon}^{(\nu_2)} \otimes \hat{\varepsilon}^{(\nu_3)} \otimes \hat{\varepsilon}^{(\nu_4)},\end{aligned} \tag{2.8}$$

where $\hat{\varepsilon}^{(\nu)} \equiv \hat{\varepsilon}^{(\nu)}(\boldsymbol{r})$; tensors $\widehat{\Lambda}_k$ are independent of $\boldsymbol{r}$.

Similarly, the electronic contribution to the eigenfrequency is

$$\Delta\omega_\nu^{(e)} = \frac{1}{2M\omega_\nu} \int d\boldsymbol{r} \widehat{\Lambda}_2 \cdot \hat{\varepsilon}^{(\nu)} \otimes \hat{\varepsilon}^{(\nu)}. \tag{2.9}$$

Generally, the term $\propto \widehat{\Lambda}_2$ leads to mode mixing; however, if the mode frequencies are nondegenerate, this mixing is weak and can be disregarded, to the leading order in the electron-phonon coupling. One can see that the effect of the static stress $\propto \widehat{\Lambda}_1$ can be disregarded as well.

The frequency change (2.9) depends on temperature because of the temperature dependence of $\widehat{\Lambda}_2$. The nonlinearity (2.8) also leads to a temperature dependence of the mode eigenfrequency. Together they modify the temperature dependence of the mode eigenfrequencies compared to that of undoped crystals. This modification often weakens the temperature dependence of the eigenfrequencies, which proves very important for applications of micro-mechanical systems in devices that work in a broad temperature range [127].

Equations (2.6) - (2.9) are generic and apply beyond the deformation potential approximation. This is of particular importance for silicon. Here, the electron band valleys lie on the $\langle 100 \rangle$-axes close to the X-points on the zone boundaries where two electron energy bands cross. Lattice strain can lead to a band splitting at X-points and a shift of the valleys [128, 129]. Importantly, this shift results from a shear strain, which does not lead to a linear in the strain shift in the deformation potential approximation. The valley shift is quadratic in $\hat{\varepsilon}$ in this case, as explained in Appendix A.1, which corresponds to an effectively two-phonon coupling. The coupling parameter Ξ_{sh} is quadratic in the strain-induced band splitting, see Eq. (7). It is large, much larger than the constant Ξ_u. Therefore the arguments given below Eq. (2.7) apply in this case as well. For purely shear strain in silicon, terms of odd order in $\hat{\varepsilon}$ in δF_e, Eq. (2.6), vanish.

2.4 Explicit form of the tensors of nonlinear elasticity

Tensors $\widehat{\Lambda}_n$ can be obtained by minimizing the free energy density of the electron system for a given strain and expanding the result in a series in $\hat{\varepsilon}$. A general procedure that allows one to find

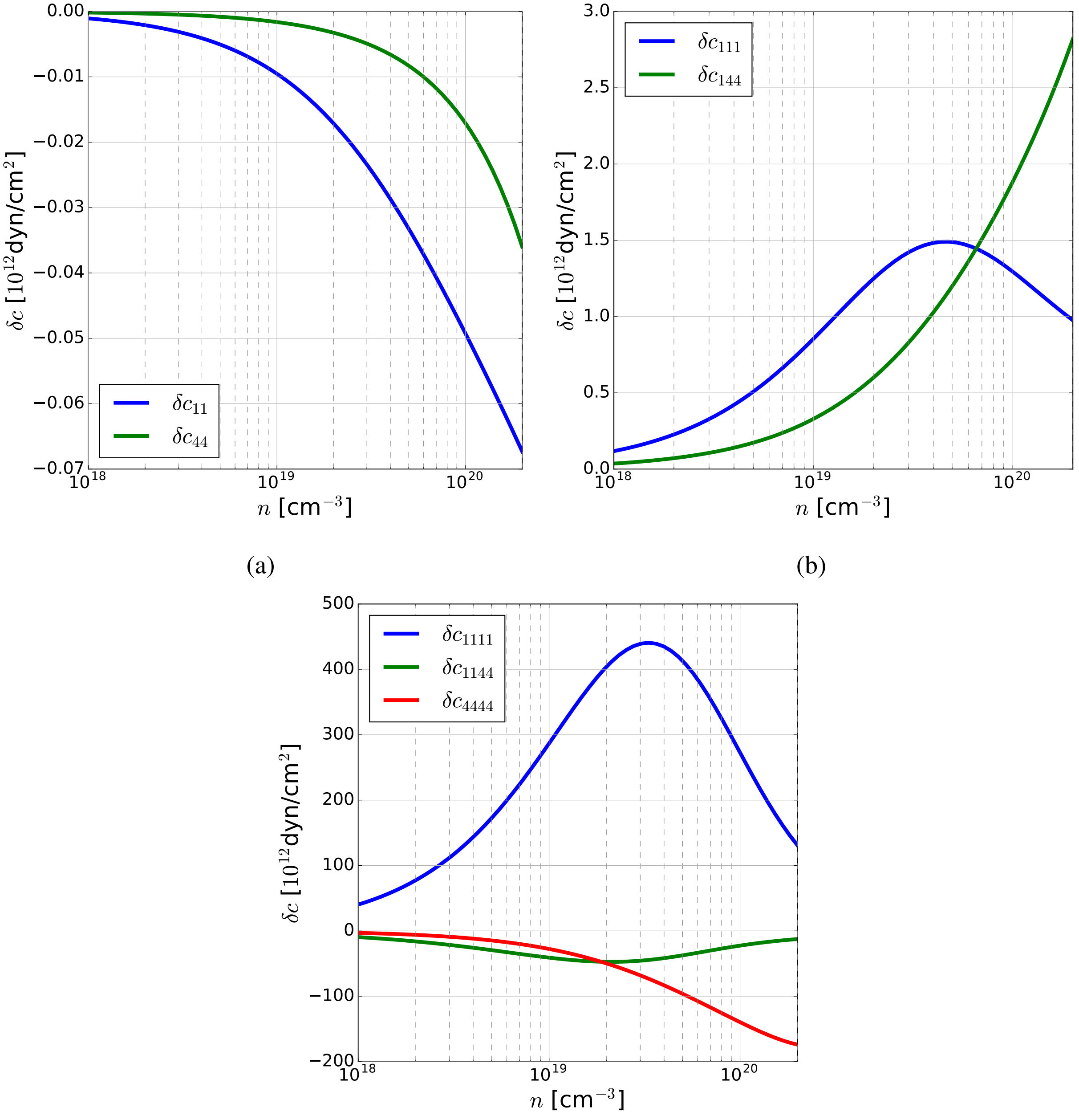

(a)

(b)

(c)

Figure 2.2 Corrections to some elastic constants as functions of *electron density*, at $T = 300$ K. (a) δc_{12} and δc_{44}; (b) δc_{111} and δc_{144}; (c) δc_{1111}, δc_{1144}, and δc_{4444}. Corrections to other constants are proportional to one of those depicted.

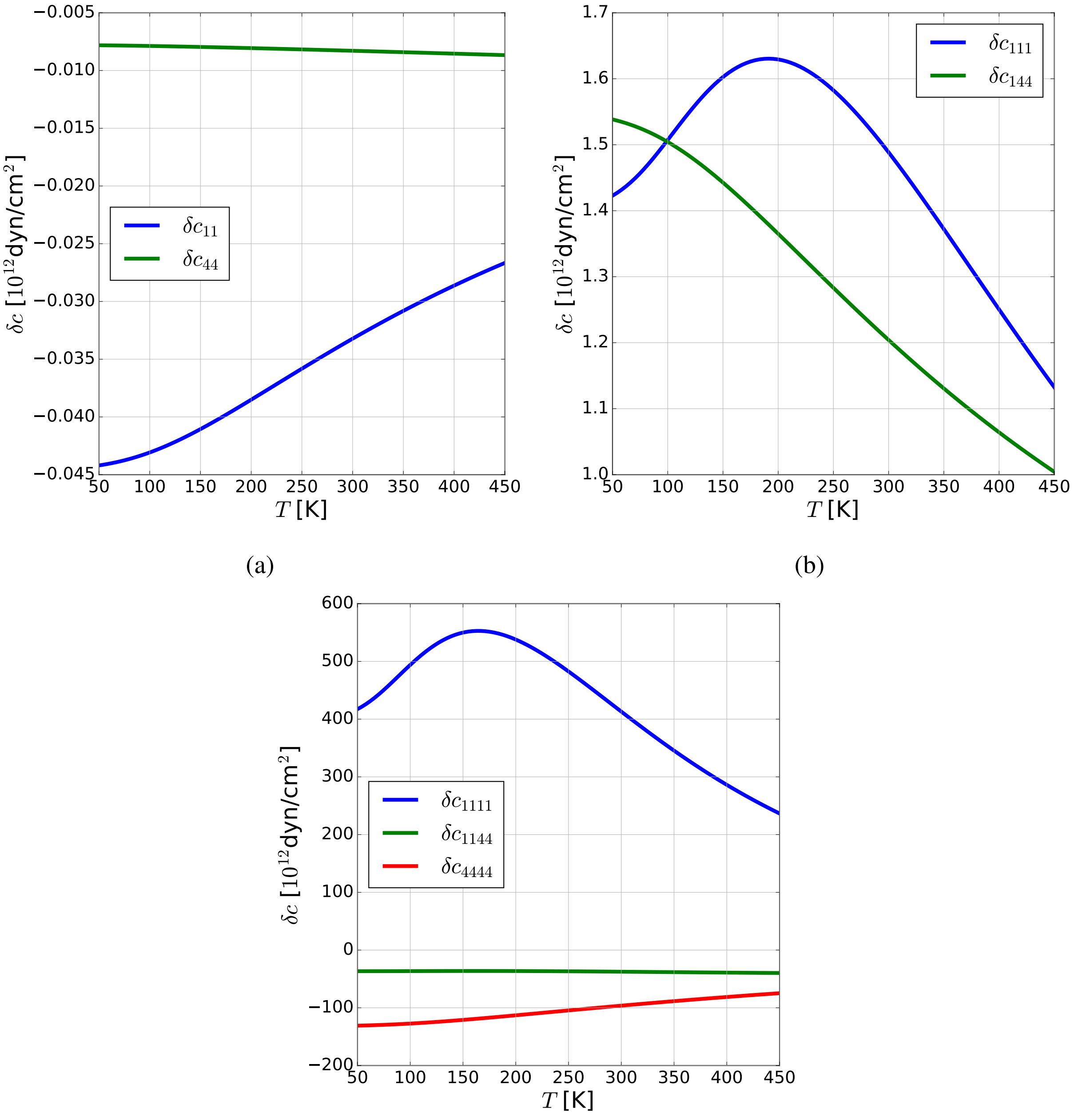

(a)

(b)

(c)

Figure 2.3 Corrections to some elastic constants as functions of *temperature*, at electron density $n = 5 \times 10^{19}$ cm^{-3}. (a) δc_{12} and δc_{44}; (b) δc_{111} and δc_{144}; (c) δc_{1111}, δc_{1144}, and δc_{4444}. Corrections to other constants are proportional to one of those depicted.

Table 2.1 The change of the components of the nonlinear elasticity tensors due to the strain-induced electron redistribution between equivalent energy valleys in doped silicon. The coordinate axes are chosen along the $\langle 100 \rangle$ axes. Parameter Ξ_{sh} characterizes the effectively two-phonon coupling to shear strain. This parameter as well as function $F_{1/2}(x)$ are defined in Appendix A.1; $x = \mu_0 / k_B T$ and n is the electron density.

$\delta c_{144} = -2\delta c_{155}$	$\frac{1}{9} n \Xi_u \Xi_{sh} C_1$	$C_1 = F'_{1/2} / F_{1/2} k_B T = d \ln n / d\mu_0$
$\delta c_{1111} = -2\delta c_{1112}$ $= 2\delta c_{1122}$	$\frac{2}{27} n \Xi_u^4 C_2$	$C_2 = (k_B T)^{-3} F'^2_{1/2} \left[d^2 (1/F'_{1/2}) / dx^2 \right] / F_{1/2}$ $= (dn/d\mu_0)^2 \left[d^2 (d\mu_0/dn) / d\mu_0^2 \right] / n$
$\delta c_{1144} = -2\delta c_{1155}$ $= -2\delta c_{1244} = \delta c_{1266}$	$-\frac{1}{27} n \Xi_u^2 \Xi_{sh} C_3$	$C_3 = F''_{1/2} / F_{1/2} (k_B T)^2 = n^{-1} d^2 n / d\mu_0^2$
$\delta c_{4444} = -6\delta c_{4455}$	$-\frac{1}{6} n \Xi_{sh}^2 C_4$	$C_4 = F'_{1/2} / F_{1/2} k_B T = d \ln n / d\mu_0$

the components $\widehat{\Lambda}_n$ for $n \leq 4$ is described in Appendix A.1. Using the symmetry arguments, the elasticity tensors are conveniently written in the contracted (Voigt) notation where the symmetric strain tensor is associated with a six-component vector. Then the nonlinear elasticity tensors $\widehat{\Lambda}_3$ and $\widehat{\Lambda}_4$ become tensors of rank three and four in the corresponding vector space. We use notation $\delta\hat{c}$ for tensors $\widehat{\Lambda}$ in these notations to emphasize that we are calculating corrections to the nonlinear elasticity tensors due to the electron-phonon coupling.

The explicit expressions for the nonlinear elasticity tensors $\delta\hat{c}$ are given in Table 2.1. They refer to silicon and include the contributions that come from both the deformation potential coupling and from the splitting of the electron bands due to shear strain. In the deformation potential approximation, the components of the third-rank tensor $\delta\hat{c}$, which determine the cubic in the strain terms in the free energy, were found earlier [121]. Therefore we give only the components that contain a contribution from shear strain. Numerically estimated concentration and temperature behavior of some elastic constants corrections are shown in Figs. 2.2 and 2.3.

The fourth-rank tensor $\delta\hat{c}$ determines the quartic in the strain terms in the free energy and has not been discussed before, to the best of our knowledge. We give all independent components of this tensor. It is expressed in terms of the derivative of the electron density n over the chemical potential in the absence of strain μ_0, which is a familiar thermodynamic characteristic. It is intuitively clear that the considered effect of the change of the electron density in different valleys in response to strain should be related to the derivative $dn/d\mu_0$. Interestingly, because we consider nonlinear response to strain, the expressions in Table 2.1 contain also higher-order derivatives of n over μ_0. As we will see, this leads to a nontrivial behavior of the nonlinear frequency shift with varying temperature and density. The considered mechanism of the strain-induced inter-valley electron redistribution does not contribute to the components c_{1123} and c_{1456}, therefore $\delta c_{1123} = \delta c_{1456} = 0$.

2.4.1 Nonlinear elasticity in the limiting cases

The expressions for $\delta\hat{c}$ simplify in the case of low doping (or high temperature), where the electron gas is strongly nondegenerate, and in the opposite case of a strongly degenerate electron gas. For a nondegenerate gas, where the chemical potential in the absence of strain is $\mu_0 < 0, |\mu_0| \gg k_BT$, we have in Table 2.1 $F_{1/2}(x) = \frac{1}{4}\pi^{1/2}e^x$ with $x = \mu_0/k_BT$. The μ_0-dependent factors $\exp(\mu_0/k_BT)$ in $F_{1/2}$ and its derivatives cancel each other in the expressions for $\delta\hat{c}$ and drop out from these expressions. The dependence of $\delta\hat{c}$ on density is then just linear, $\delta\hat{c} \propto n$. Parameters $C_{1,...,4}$ in Table 2.1 depend only on temperature, $C_1 \propto T^{-1}, C_2 \propto T^{-3}, C_3 \propto T^{-2}$ and $C_4 \propto T^{-1}$.

The decrease of the nonlinear elasticity parameters with increasing temperature in a nondegenerate electron gas is easy to understand. The effect we consider is determined by the competition between the energetically favorable unequal population of the electron energy valleys in a strained crystal and the entropically more favorable equal valley population. With increasing temperature the entropic factor becomes stronger, leading to a smaller population difference and thus smaller effect of the electron system on the vibrations.

For strong doping, where $\mu_0/k_BT \gg 1$, we have $\mu_0 \propto n^{2/3}$, and then $F_{1/2}(x) \approx \frac{2}{3}x^{3/2}$ with $x = \mu_0/k_BT$. Therefore parameters $C_{1,...,4}$ in Table 2.1 become temperature independent, with $nC_1 \propto n^{1/3}, nC_2 \propto n^{-1}, nC_3 \propto n^{-1/3}$, and $C_4 \propto n^{1/3}$.

The results on the asymptotic behavior of the corrections to nonlinear elasticity are not limited to silicon. Since parameters $C_{1,2,3,4}$ are given by the coefficients in the general expansion of the free energy in strain, (6), these results can be applied to the nonlinear elasticity induced by the electron-phonon coupling in other multi-valley semiconductors. To illustrate this point, in Appendix A.2 we give $\delta\hat{c}$ tensor in germanium.

The difference between the asymptotic behavior of the tensors $\delta\hat{c}$ in the limits of nondegenerate and strongly degenerate electron gas can lead to a peculiar density and temperature dependence of the nonlinear frequency shift of the vibrational modes. It comes from the coefficients $C_{1,\dots,4}$ containing higher-order derivatives of n with respect to μ_0. In the transition region $\mu_0 \sim k_BT$, thinking of the competition between the entropic and energetic factors does not provide a simple insight into the behavior of $\delta\hat{c}$, as both the energy and the entropy are complicated functions of density and temperature.

2.5 Doping-induced nonlinearity of simple vibrational modes

The nonlinear elasticity tensors in Table 2.1 give the doping-induced contributions to the nonlinearity parameters of the eigenmodes of micro- and nanomechanical systems. These contributions are described by Eq. (2.8). As mentioned before, an important characteristic of the mode nonlinearity is the dependence of the mode frequency on the vibration amplitude. To the leading order, it is given by Eq. (2.5). This dependence has a contribution from the nonlinearity of an undoped crystal, which is quadratic in the parameters of the cubic nonlinearity; for example, if the latter is described by the Grüneisen constant, the corresponding contribution is quadratic in this constant. It is typically small. There is also a contribution from the quartic nonlinearity; the parameters of such nonlinearity are not known in undoped crystals and are not expected to be large. Respectively, the amplitude dependence of the vibration frequency for low-frequency modes in weakly doped single-crystal micro-mechanical systems is relatively weak [24].

A feature of the doping-induced nonlinearity described by Table 2.1 is that the quartic in the strain term in the free energy has a large coefficient compared to the cubic term, cf. Eq. (2.7) and the discussion below this equation. Therefore, in Eq. (2.5) for the amplitude dependence of vibration frequency one can keep only the Duffing nonlinearity constant γ_ν. The contribution from the cubic nonlinearity terms $\propto \beta^2_{\nu\nu\nu'}$ can be disregarded. For a mode ν, the doping-induced

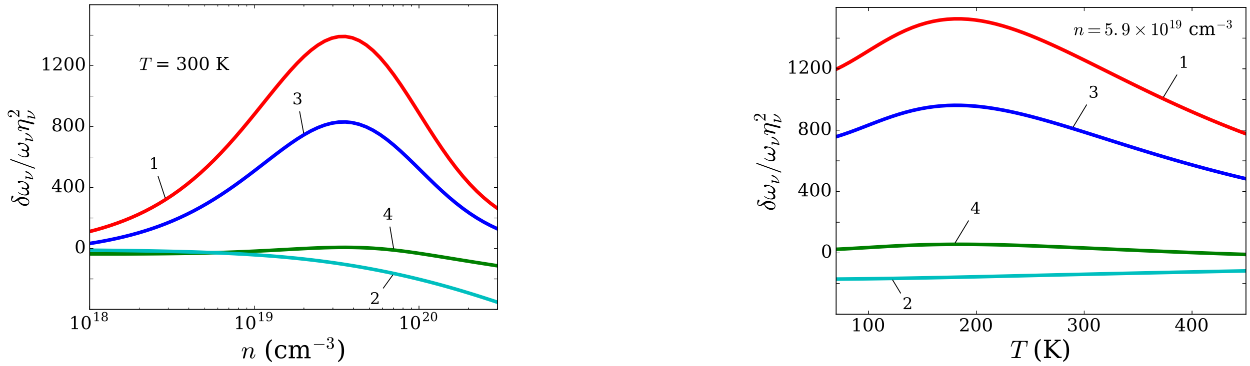

Figure 2.4 Relative change $\delta\omega_\nu/\omega_\nu$ of the vibration frequency of a mode with the vibration amplitude η_ν scaled by the relevant size of the system, cf. Eq. (2.10). The results refer to single crystal silicon resonators. Curves 1 and 2 refer to the first Lamé mode in square plates cut in $\langle 100\rangle$ and $\langle 110\rangle$ directions, respectively. In this case, the size of the resonator is the length of the side of the square. Curves 3 and 4 refer to the first extension mode in beams cut in $\langle 100\rangle$ and $\langle 110\rangle$ directions, respectively. In this case, the size of the resonator is the length of the beam.

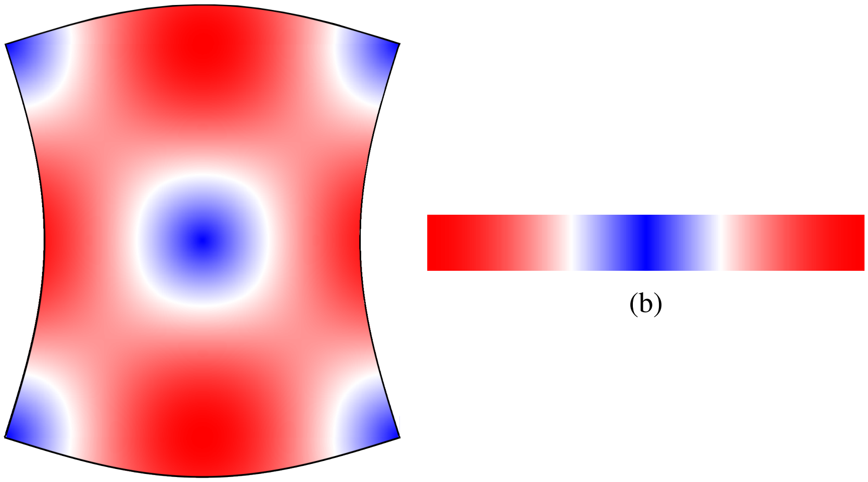

(a) (b)

Figure 2.5 Mode shapes, displacement shown by color from blue to red, dark blue denoting zero and red maximum displacement. (a) first Lamé mode, (b) length extension mode

contribution to γ_ν is equal to $\gamma^{(e)}_{\nu\nu\nu\nu}$ in Eq. (2.8).

To find the dependence of the mode frequency on the vibration amplitude we go through the following steps. First, we find the normal modes of interest for the given geometry of the system, with account taken of the boundary conditions, and normalize the displacements $\boldsymbol{u}^{(\nu)}(\boldsymbol{r})$ as indicated in Eq. (2.1). We use $\boldsymbol{u}^{(\nu)}(\boldsymbol{r})$ to find the strain tensor $\hat{\varepsilon}^{(\nu)}(\boldsymbol{r})$. The result is substituted into Eq. (2.8) and is convoluted with tensor $\widehat{\Lambda}_4$, giving the value of γ_ν, which is then used in Eq. (2.5) to find the frequency dependence on the vibration amplitude $\delta\omega_\nu$.

Of particular interest is the relative frequency shift $\delta\omega_\nu/\omega_\nu$. To find this shift to the leading order, one can disregard nonlinearity when calculating the eigenfrequency ω_ν. Then, from Eq. (2.5),

$$\frac{\delta\omega_\nu}{\omega_\nu} = \frac{3\gamma_\nu A_\nu^2}{8\int d\boldsymbol{r}\widehat{\Lambda}_2^{(f)}\cdot\hat{\varepsilon}^{(\nu)}\otimes\hat{\varepsilon}^{(\nu)}}, \tag{2.10}$$

where $\widehat{\Lambda}_2^{(f)}$ is the full tensor of linear elasticity, which includes the major term of the linear elasticity of the undoped crystal and the doping-induced correction $\widehat{\Lambda}_2$.

An important feature of the relative shift $\delta\omega_\nu/\omega_\nu$ is its scaling with the size of the system. The vibration amplitude A_ν in Eq. (2.10) can be scaled by the lateral dimension L, for example the length of a nanobeam or a nanowire for an extension mode, or the size of the square for a Lamé mode, or the diameter of a disk for a breathing mode in a disk. Respectively, we write $A_\nu = \eta_\nu L$. Then, if one takes into account the explicit form (2.8) of the parameter $\gamma_\nu = \gamma_{\nu\nu\nu\nu}^{(e)}$, one finds from Eq. (2.10) that the ratio $\delta\omega_\nu/(\eta_\nu^2\omega_\nu)$ is independent of the system size for the aforementioned modes. In this estimate we used that the tensors $\widehat{\Lambda}$ are material parameters and are independent of the geometry. We also used that the modes of interest have typical wavelength $\sim L$, and therefore $\hat{\varepsilon}^{(\nu)}$ scales as L^{-1}.

Most of the experiments in nano- and micromechanics are done with nanobeams, nanowires, membranes, or thin plates. In such systems the thickness is much smaller than the length or, in the case of membranes or plates, the lateral dimensions. Then, from the boundary condition of the absence of tangential stress on free surfaces [123], it follows that the strain tensor $\hat{\varepsilon}$ weakly depends on the coordinate normal to the surface. This simplifies the denominator in Eq. (2.10), making it proportional to the thickness. Similarly, from Eq. (2.8) γ_ν is also proportional to the thickness, and the thickness drops out of Eq. (2.10).

The explicit expressions for $M\omega_\nu^2$ and γ_ν that determine the denominator and the numerator in Eq. (2.10), respectively, are given in Appendices A.4 and A.5 for Lamé and extension modes. These expressions are cumbersome, and it is convenient to use symbolic programming to obtain

Table 2.2 Elastic constants of pure Si at room temperature in units of $10^{12}\,\mathrm{dyn/cm^2}$

c_{11}	c_{12}	c_{44}	c_{111}	c_{112}	c_{123}	c_{144}	c_{166}	c_{456}	Ref.
1.656	0.639	0.795	−7.95	−4.45	−0.75	0.15	−3.10	−0.86	[121]
1.658	0.639	0.796	−8.25	−4.51	−0.64	0.12	−3.10	−0.64	[130]

them. [1]

2.5.1 Temperature and electron density dependence of the scaled nonlinear frequency shift

The scaled ratio $\delta\omega_\nu/(\eta_\nu^2\omega_\nu)$ that characterizes the relative nonlinear frequency shift is shown in Fig. 2.4 for several modes that are often used in single-crystal silicon MEMS. This ratio depends on the type of the mode and the crystal orientation. Figure 2.4 refers to high-symmetry crystal orientations, in which case the modes have a comparatively simple spatial structure and the surfaces can be made smooth. We used the values $\Xi_u = 8.8$ eV [126], $\Xi_{sh} = 300$ eV, the effective mass for density of states $m_{eff} = 0.32m_e$ [129], and the temperature-dependent linear elasticity parameters given in Ref. [131]. We also used experimental values of third-order elastic constants of pure silicon measured in [121] (see Table 2.2).

Figure 2.4 shows that the electron-redistribution induced nonlinearity of vibrational modes is very strong. For the ratio of the vibration amplitude to the system size $\eta \sim 10^{-4}$ and the mode eigenfrequency $\omega_\nu/2\pi \sim 10$ MHz, the frequency change can be as a large as $\delta\omega_\nu/2\pi \sim$ 0.1 kHz. This explains, qualitatively, the observations [24]. A quantitative comparison with the experiment [24] is complicated, as the observations refer to different samples. Our preliminary results show an excellent quantitative agreement with the data obtained for the same sample at different temperatures and for different types of modes [132].

The nonlinear frequency shift displays several characteristic features, as seen from Fig. 2.4. One of them is the strong dependence of the shift on the type of the mode and the crystal orientation. For both the Lamé and the extension mode, the shift is much stronger for crystals cut out in

---

[1] The program that performs the analytical calculations and evaluates the numerical values of the parameters is available at `http://www.pa.msu.edu/people/dykman/nonlinear_elasticity`.

$\langle 100 \rangle$ direction than in $\langle 110 \rangle$ direction. This is a consequence of the electron energy valleys lying along the $\langle 100 \rangle$ axes, making the system more “responsive" to the lattice displacement along these axes. Interestingly, in the both configurations the shifts for the Lamé modes are larger than for the extension modes.

A somewhat unexpected feature is the nonmonotonic dependence of the nonlinear frequency shift on the electron density and temperature. The nonmonotoncity occurs in the range where the electron system is close to degeneracy, $\mu_0/k_BT \sim 1$, and it strongly depends on the crystal orientation. It is much stronger for crystals cut in $\langle 100 \rangle$ than $\langle 110 \rangle$ directions. For a crystal cut in $\langle 110 \rangle$ direction, both the density and temperature dependence of the shift are monotonic in the case of the Lamé mode, whereas for the extension mode the nonmonotonicity is weak.

The nonmonotonicity of the frequency shift stems from the behavior of the parameters $nC_{2,3,4}$ in the range $\mu_0 \sim k_BT$. As seen from Table 2.1, parameter nC_2 exponentially increases with the increasing μ_0/k_BT for negative μ_0/k_BT, but for large positive μ_0/k_BT it falls off as $(\mu_0/k_BT)^{-3/2}$. It has a pronounced maximum for $\mu_0/k_BT \approx 0.6$. Parameter nC_3 also displays a maximum, which occurs for $\mu_0/k_BT \approx 1.1$. In contrast, parameters $nC_{1,4}$ depend on μ_0/k_BT monotonically.

The results of Appendices A.4 and A.5 show that, for the Lamé and extension modes in crystals cut in $\langle 100 \rangle$ direction, the relative shift $\delta\omega_\nu/\omega_\nu$ is determined by coefficient nC_2, which explains the nonmonotonicity of the shift. For crystals cut in $\langle 110 \rangle$, the shift of the Lamé mode is fully determined by coefficient nC_4 and is monotonic, whereas for the extension mode the expression for the shift has contributions from nC_2, nC_3, and nC_4 that partly compensate each other, leading to a comparatively small shift all together and its weak nonmonotonicity.

2.6 Linear and nonlinear elasticity in polysilicon

In polycrystalline silicon, grains have random orientations. We will assume each grain to be a perfect single crystal, while on average the material is isotropic. In this section, we estimate effects of electron-phonon interaction on linear and nonlinear elasticity of polysilicon. We disregard effects of grain boundaries, which are not necessarily small, since there is no reliable way to account for them. Since so much depends on the actual material structure, the calculation that follows should be regarded as an order of magnitude estimate only. If the grains are small enough, one can assume that the chemical potential is the same in all grains under any spatially uniform strain. Then the calculation of corrections to tensors of elasticity proceeds in a way similar to that presented in Appendix A.1, but we must calculate the chemical potential and the free energy taking into account the polycrystalline nature of the material.

Each grain is characterized by its orientation. We will describe orientation of each grain with respect to some fixed orientation using Euler angles: rotation by ϕ around axis z, followed by a rotation by θ around x', and finally rotation by ψ around z''. The matrix of such rotation is

$$R = Z(\phi)X(\theta)Z(\psi)$$

where

$$X(\theta) = \begin{pmatrix} 1 & 0 & 0 \\ 0 & \cos(\theta) & -\sin(\theta) \\ 0 & \sin(\theta) & \cos(\theta) \end{pmatrix}$$

$$Z(\phi) = \begin{pmatrix} \cos(\phi) & \sin(\phi) & 0 \\ -\sin(\phi) & \cos(\phi) & 0 \\ 0 & 0 & 1 \end{pmatrix}$$

All possible orientations of a body are uniquely defined by $\phi \in [0, 2\pi)$, $\theta \in [0, pi)$, and $\psi \in [0, 2\pi)$. Valley bottom of valley x in a grain with orientation defined by R is shifted under strain by

$$\delta E_x = \Xi^{(x)}_{kl} \left(R^{-1}_{kp} R^{-1}_{lq} \varepsilon_{pq} \right) - \Xi_{sh} \left(R^{-1}_{yp} R^{-1}_{zq} \varepsilon_{pq} \right)^2 + \Xi_{s4} \left(R^{-1}_{yp} R^{-1}_{zq} \varepsilon_{pq} \right)^4, \tag{2.11}$$

where $\Xi^{(x)}$ is the deformation potential tensor in valley x, and $R^{-1} \equiv Z(-\phi)X(-\theta)Z(-\psi)$. Summation over repeated indices is assumed. Chemical potential in a single crystal is calculated through Eqs. (2) and (3). In a polycrystal, the calculation proceeds the same way, but we need to average terms of the form $\overline{\Delta^m_\varepsilon}$ over all possible orientations. If we denote this averaging by $\langle\rangle$, we obtain terms of the form $\langle \overline{\Delta^m_\varepsilon} \rangle$. We argue that $\langle \overline{\Delta^m_\varepsilon} \rangle = \langle (\delta E_x / k_B T)^m \rangle$ since all valleys become equivalent upon averaging over all grain orientations. The same averaging procedure should be applied to the free energy calculation, Eq. (6). Thus, the free energy calculation in a polycrystal should be done in the way described in Appendix A.1, but with $\overline{\Delta_\varepsilon^m}$ replaced with

$$\langle((\delta E_x/k_B T)^m\rangle = \frac{1}{(k_B T)^m}\left\langle \left(\Xi^{(x)}_{kl}\left(R^{-1}_{kp}R^{-1}_{lq}\varepsilon_{pq}\right) - \Xi_{sh}\left(R^{-1}_{yp}R^{-1}_{zq}\varepsilon_{pq}\right)^2 \right.\right. \\ \left.\left. + \Xi_{s4}\left(R^{-1}_{yp}R^{-1}_{zq}\varepsilon_{pq}\right)^4\right)^m\right\rangle \tag{2.12}$$

Then the corrections to tensors of elasticity are found by Eq. (8):

$$\begin{aligned}
\delta c^{(\mathrm{p})}_{11} &= -2\delta c^{(\mathrm{p})}_{12} = \frac{4}{3}\delta c^{(\mathrm{p})}_{44} = \frac{2n}{45}\left(3\Xi_{s2} - \frac{2\Xi_u^2 F'_{1/2}}{F_{1/2}T}\right)\\
\delta c^{(\mathrm{p})}_{111} &= -2\delta c^{(\mathrm{p})}_{112} = \delta c^{(\mathrm{p})}_{123} = -\frac{4}{3}\delta c^{(\mathrm{p})}_{144} = \frac{8}{3}\delta c^{(\mathrm{p})}_{155} = \frac{16}{9}\delta c^{(\mathrm{p})}_{456}\\
&= \frac{8n\Xi_u}{945F_{1/2}T}\left(9\Xi_{s2}F'_{1/2} + \frac{2F''_{1/2}}{T}\Xi_u^2\right)\\
\delta c^{(\mathrm{p})}_{1111} &= -2\delta c^{(\mathrm{p})}_{1112} = 2\delta c^{(\mathrm{p})}_{1122} = 4\delta c^{(\mathrm{p})}_{1144} = 4\delta c^{(\mathrm{p})}_{1155}\\
&= -8\delta c^{(\mathrm{p})}_{1244} = -8\delta c^{(\mathrm{p})}_{1266} = \frac{16}{9}\delta c^{(\mathrm{p})}_{4444} = \frac{16}{3}\delta c^{(\mathrm{p})}_{4455}\\
&= \frac{8n}{35}\Xi_{s4} - \frac{32n\Xi_{s2}^2F'_{1/2}}{525F_{1/2}T} - \frac{32n\Xi_u^2\Xi_{s2}F''_{1/2}}{1575F_{1/2}T^2} - \frac{16n\Xi_u^4F'''_{1/2}}{945F_{1/2}T^3} + \frac{16n\Xi_u^4{F''_{1/2}}^2}{675F_{1/2}T^3F'_{1/2}}\\
\delta c^{(\mathrm{p})}_{1123} &= 0\\
\delta c^{(\mathrm{p})}_{1456} &= 0
\end{aligned} \tag{2.13}$$

Numerical values of these corrections as functions of electron density and temperature are shown in Figs. 2.6 and 2.7 respectively. The predicted corrections in polysilicon are generally smaller than those in the single crystal, but still significant.

Above, we presented corrections to tensors of elasticity in polysilicon, but did not touch the calculation of intrinsic values of the tensors without electronic effects. The latter is done by averaging of single-crystal tensors for pure silicon over all possible orientations. Consider a single-crystal grain with orientation defined by R relative to the lab frame. In the lab frame, the stiffness tensor has a new value c'_{ijkl} that is related to its value in crystal coordinates c_{ijkl} through some tensor

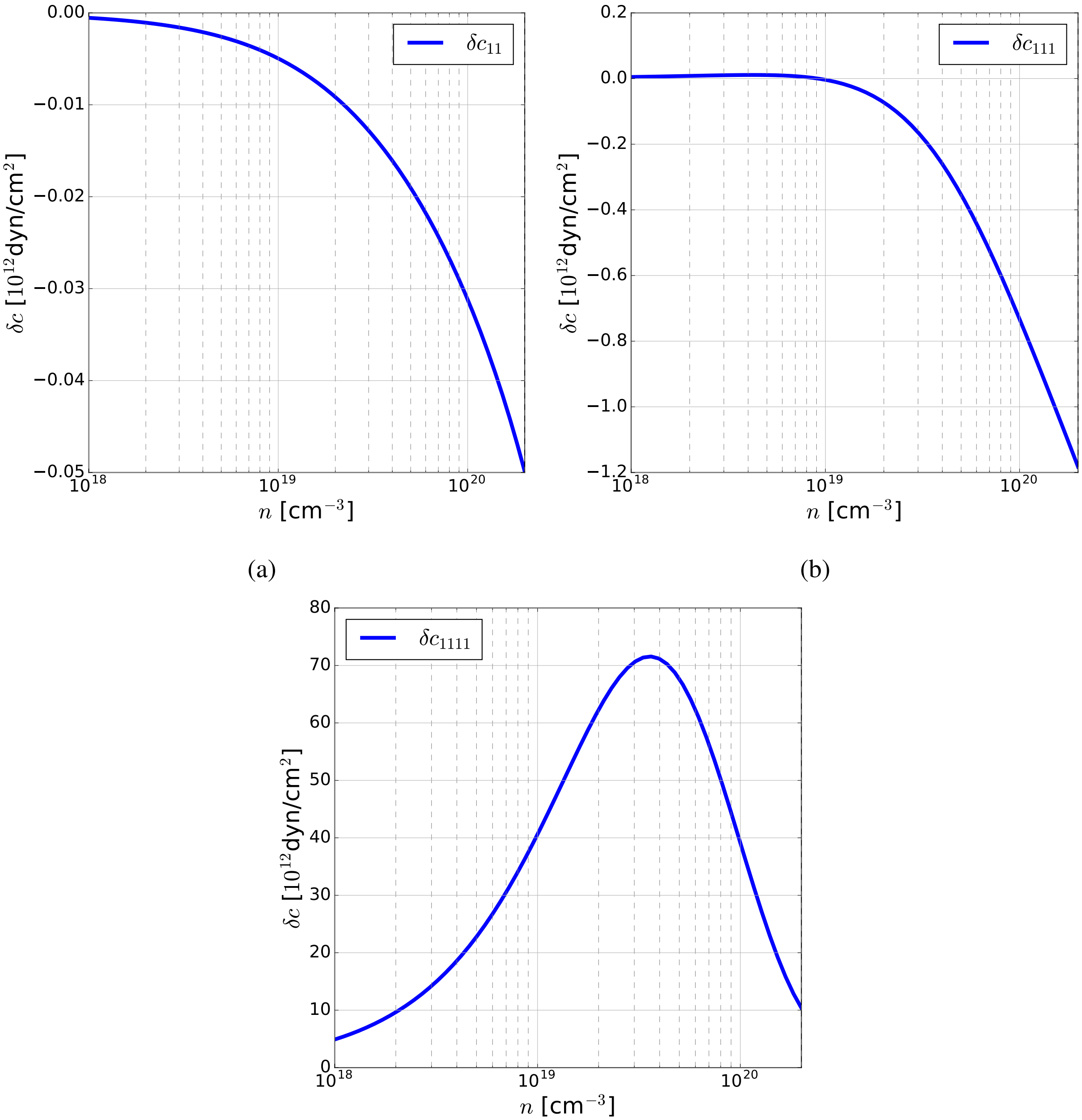

(a) (b)

(c)

Figure 2.6 Corrections to elastic constants of *polycrystalline* silicon as functions of *electron density*, at $T = 300$ K. (a) δc_{11}; (b) δc_{111}; (c) δc_{1111}. Corrections to other constants are proportional to one of those depicted.

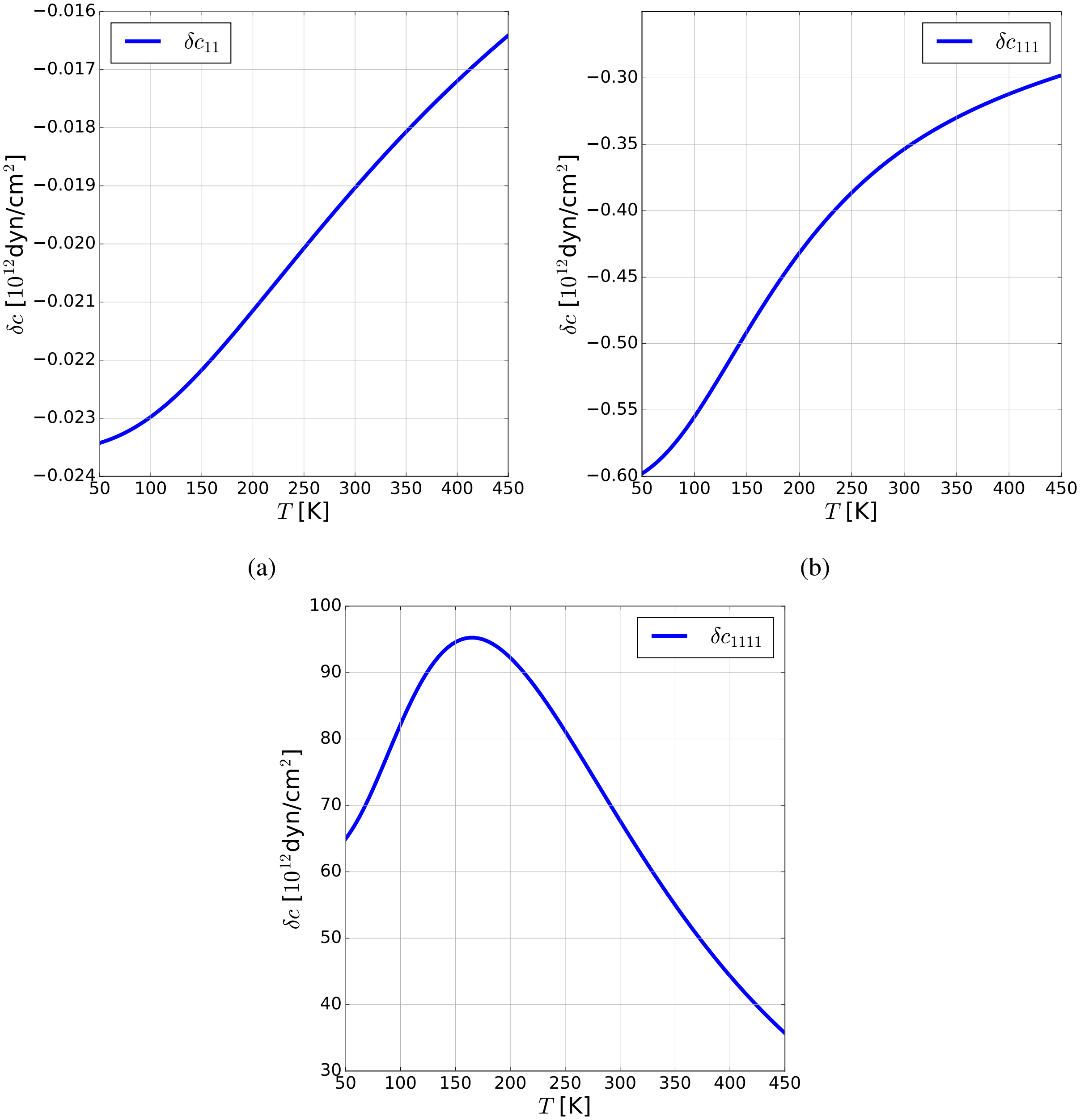

(a)

(b)

(c)

Figure 2.7 Corrections to elastic constants of *polycrystalline* silicon as functions of *temperature*, at electron density $n = 5 \times 10^{19}$ cm^{-3}. (a) δc_{11}; (b) δc_{111}; (c) δc_{1111}. Corrections to other constants are proportional to one of those depicted.

$A_{mnpqijkl}$:

$$c'_{ijkl} = A_{mnpqijkl} c_{mnpq}.$$

To find tensor A, we consider the elastic free energy that should be a scalar independent of the coordinate system choice:

$$\frac{1}{2} c'_{ijkl} \varepsilon_{ij} \varepsilon_{kl} = \frac{1}{2} A_{mnpqijkl} c_{mnpq} \varepsilon_{ij} \varepsilon_{kl} = \frac{1}{2} c_{mnpq} \hat{\varepsilon}_{mn} \hat{\varepsilon}_{pq}, \tag{2.14}$$

where the first and last expressions are written in the lab and crystal frames respectively. We know that in the crystal frame,

$$\hat{\varepsilon}_{pq} = R^{-1}_{pk} R^{-1}_{ql} \varepsilon_{kl}.$$

Therefore,

$$A_{mnpqijkl} c_{mnpq} \varepsilon_{ij} \varepsilon_{kl} = R^{-1}_{mi} R^{-1}_{nj} R^{-1}_{pk} R^{-1}_{ql} c_{mnpq} \varepsilon_{ij} \varepsilon_{kl},$$

that means $A_{mnpqijkl} \equiv R^{-1}_{mi} R^{-1}_{nj} R^{-1}_{pk} R^{-1}_{ql}$, which is of course the transformation for a fourth-order tensor. It means that the average tensor component in a polycrystal would be

$$c^{(poly)}_{ijkl} = \langle c'_{ijkl} \rangle = \int_0^{\pi} d\theta \int_0^{2\pi} d\phi \int_0^{2\pi} d\psi \sin\theta \rho(\boldsymbol{\alpha}) A_{mnpqijkl}(\phi, \theta, \psi) c_{mnpq} \tag{2.15}$$

where $\rho(\boldsymbol{\alpha}) = 1/8\pi^2$ for the uniform on $[0, 2\pi) \times [0, \pi) \times [0, 2\pi)$ distribution of angles. Third- and fourth- order elastic constants are found in a similar way, using appropriate transformation tensors.

The resulting values for second- and third- order elastic constants are given below:

$$
\begin{aligned}
c_{11}^{(\mathrm{p})} &= \frac{1}{5}(3c_{11}+2c_{12}+4c_{44}),\\
c_{12}^{(\mathrm{p})} &= \frac{1}{5}(c_{11}+4c_{12}-2c_{44}),\\
c_{44}^{(\mathrm{p})} &= \frac{1}{5}(c_{11}-c_{12}+3c_{44}),\\
c_{111}^{(\mathrm{p})} &= \frac{1}{35}\left(15c_{111}+18c_{112}+2c_{123}+12c_{144}+72c_{155}+16c_{456}\right),\\
c_{112}^{(\mathrm{p})} &= \frac{1}{35}\left(3c_{111}+26c_{112}+6c_{123}+8c_{144}-8c_{155}-8c_{456}\right),\\
c_{123}^{(\mathrm{p})} &= \frac{1}{35}\left(c_{111}+18c_{112}+16c_{123}-30c_{144}-12c_{155}+16c_{456}\right),\\
c_{144}^{(\mathrm{p})} &= \frac{1}{35}\left(c_{111}+4c_{112}-5c_{123}+19c_{144}+2c_{155}-12c_{456}\right),\\
c_{155}^{(\mathrm{p})} &= \frac{1}{35}\left(3c_{111}-2c_{112}-c_{123}+c_{144}+20c_{155}+6c_{456}\right),\\
c_{456}^{(\mathrm{p})} &= \frac{1}{35}\left(c_{111}-3c_{112}+2c_{123}-9c_{144}+9c_{155}+9c_{456}\right),
\end{aligned}
\tag{2.16}
$$

These values are not all linearly independent because of the isotropic symmetry, but we give them all here for completeness. Fourth-order elastic constants are not shown since the expressions are too lengthy and their values for pure silicon are unknown. One may notice that we can apply equations of the type (2.16) to electronic corrections δc_{IJKL} given in Table 2.1. That would give us $\delta c_{IJKL}^{(\mathrm{p})}$ calculated in the opposite limit of isolated grains, where chemical potential is independent in each grain. We note that numerical values obtained in this limit are remarkably close to those given in Eqs. (2.13), within 20%, and display similar dependence on temperature and electron density.

2.7 Conclusions

The results of this chapter show that the electron-phonon coupling strongly affects the nonlinearity of vibrational modes in semiconductor-based nano- and micromechanical systems. The mechanism of the effect is the strain-induced redistribution of the electrons between the valleys of the conduction band. The redistribution results from lifting the degeneracy of the electron energy spectrum by the strain from a vibrational mode. The analysis refers to the range of temperatures where the rate of intervalley scattering strongly exceeds the frequencies of the considered modes. In this case the valley populations follow the strain adiabatically.

The change of the valley populations is a strongly nonlinear function of the strain tensor. The respective expansion of the free energy in the strain is an expansion in the strain multiplied by the ratio of the electron-phonon coupling energy (in particular, the deformation potential) to the chemical potential of the electron system or the temperature. This ratio is large, $\gtrsim 10^3$. It is this parameter that makes the nonlinearity of the vibrational modes in doped semiconductor structures strong.

Of special interest in nano- and micromechanical systems is the amplitude dependence of the vibration frequency. To the leading order, it is determined by the quartic terms in the expansion of the free energy in strain. These terms are comparatively large in doped crystals.

We have calculated the nonlinear elasticity tensor that describes the electron contribution to the terms in the free energy, which are quartic in the strain. The explicit expressions for the tensor components refer to semiconductors with the valleys on $\langle 100\rangle$ axes, in particular, to silicon. We have also found this tensor for germanium. In silicon, along with the deformation potential coupling, an important role is played by the coupling to shear strain. Such strain lifts the band degeneracy at the zone boundary and is effectively described by a two-phonon coupling. We show that this coupling also leads to strong nonlinearity of vibrational modes.

The parameter of the electron coupling to shear strain in silicon is not easy to access in the experiment [129, 133]. Measurements of the nonlinear frequency shift provide a direct means for determining this parameter. In particular, the nonlinear frequency shift of the fundamental Lamé mode in a silicon plate cut along $\langle 110\rangle$ axes is determined by this parameter only, except for small corrections from the nonlinearity of the undoped crystal.

We found that the nonlinear frequency shift strongly depends on the type of a vibrational mode and the crystal orientation. We also found that the ratio of the frequency shift to the squared vibration amplitude can be profoundly nonmonotonic as a function of electron density and temperature. The results provide an insight into the experimentally observed strong mode nonlinearity in doped crystals [24]. In terms of applications, they enable choosing the appropriate range of doping and the temperature regime to optimize the operation of nano- and micromechanical resonators.

CHAPTER 3

ELECTRONS ON HELIUM IN A PERIODIC POTENTIAL

3.1 Introduction

Electrons on the surface of liquid helium have been studied extensively experimentally and theoretically [134]. They constitute one of the most perfect two-dimensional electron systems. The highest mobility among all known condensed matter systems has been measured in electrons on helium [25]. Such high mobility is a consequence of the absence of defects inherent to any solid state system. Therefore, electrons on helium surface are ideally suited for studying effects of the interaction of the electrons with each other as well as their interaction with the quantized fields of surface and bulk excitations in helium and with substrate-induced potentials.

A typical experimental geometry and the energy spectrum of electrons floating on the helium surface are shown schematically on Fig. 3.1. Liquid helium covers one plate of a parallel plate

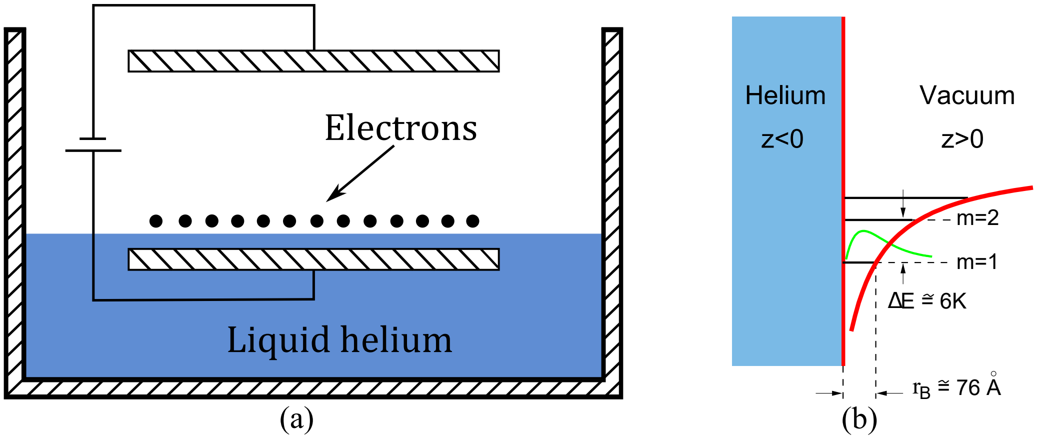

Figure 3.1 (a) The geometry of typical experiments on a spatially uniform electron system on the helium surface (schematically). Electrons reside in vacuum above the interface and are pressed to the surface by image potentials and the capacitor electric field. The capacitor electrode creates neutralizing background for electrons and determines the maximum electron density. (b) The hydrogenic energy levels of motion transverse to the helium surface in the image potential $V(z) = -\Lambda e^2/z$ for $z > 0$. Also sketched is the wave function of the ground state ($m = 1$) of motion normal to the surface.

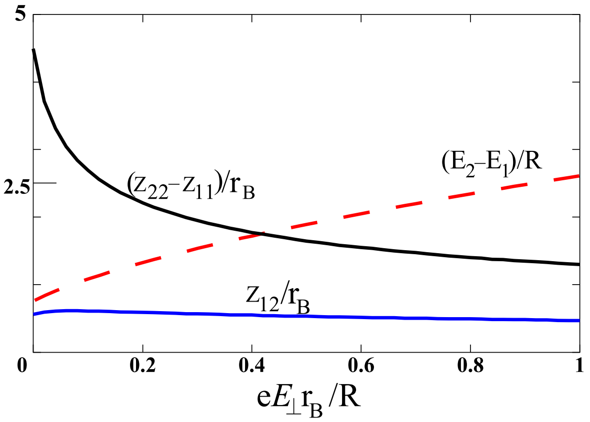

Figure 3.2 Matrix elements $\langle m|z|n\rangle$ of the electron coordinate z and the energy difference $E_2 - E_1$ between the first excited state $|2\rangle$ and the ground state $|1\rangle$ of the z motion vs the pressing field $E_\perp$. $eE_\perp r_B/R = 1$ for $E_\perp \approx 0.91$ kV/cm.

capacitor, which is connected to a voltage source. The thickness of the helium film is typically $d \geq 0.5$ μm. Electrons are supplied to the surface by briefly heating a filament (cathode) located near the top capacitor plate, while negative voltage is applied to the filament. The voltage applied across the capacitor determines the ultimate charge density on the surface and creates a uniform neutralizing background in the lower plate for the surface electrons. A variation of this geometry has been used recently where the electrons are confined in a narrow channel above the back gate [30], but the physics is essentially the same.

An electron is confined to the surface by a relatively weak image potential and by the voltage that can be applied to the capacitor. To a good approximation, the image potential is of the form $V(z) = -\Lambda e^2/z$ for $z > 0$ [134], where z is the direction normal to the surface and $\Lambda = (\varepsilon - 1)/4(\varepsilon + 1)$. Λ is quite small, $\Lambda \approx 0.01$, since the dielectric constant of liquid helium is $\varepsilon \approx 1.057$. There is a barrier of ~ 1 eV to penetrate into the helium, therefore the electron' motion normal to the surface (the z-direction) is quantized. The energy spectrum of the motion in z-direction has the form of the energy spectrum of a hydrogen atom, that is the m-th state has energy $E_m = -R/m^2$, with an effective Rydberg constant $R = \Lambda^2 e^4 m_e/2\hbar^2 \approx 8$ K. The effective Bohr radius is $r_B = \hbar^2/m_e e^2 \Lambda \approx 76$ Å. In the presence of an external pressing field $E_\perp$, the states and their energies are modified (see Fig. 3.2), although the qualitative picture remains the same.

The quantization described above was observed in the experiment by Grimes *et al.* in 1976 [135]. Grimes *et al.* observed a series of peaks corresponding to transitions between energy levels of motion transverse to the helium surface. The level spacing was controlled by an external electric field $E_\perp$ perpendicular to the helium surface, which shifts the energy levels through the Stark effect. The transitions were observed at frequencies from 130 to 220 GHz by measuring the derivative of the microwave absorption at a fixed frequency while tuning the splitting between the states by modulating the field $E_\perp$. The Stark shift of the levels is large, 0.3 GHz per V/cm for $m = 1$, and 1.1 GHz per V/cm for $m = 2$, and thus allows one to change the level spacing appreciably even with moderate fields.

While the electron's motion is quantized in the transverse direction, it is essentially free along the surface. For $T \gtrsim 0.7$, the interaction of an electron with the outside world is dominated by scattering by the He atoms in the gas phase, while for $T < 0.7$ K it becomes limited by the coupling to thermally excited capillary waves on the helium surface (ripplons), and to bulk phonons in helium. At low temperatures, electron-ripplon scattering is the fastest process and mostly determines transport properties. The dispersion relation for the ripplons has the form $\omega^2(k) = gk + (\sigma/\rho)k^3$ [134], where $\rho = 0.145$ g/cm^3 and $\sigma = 0.37$ erg/cm^2 are helium density and surface tension respectively, and g is the free fall acceleration. The height variation $\xi(\boldsymbol{r},t)$ of the surface caused by ripplons leads to the electron-ripplon coupling. To the first order in $\xi(\boldsymbol{r},t)$ the coupling Hamiltonian reads [136]:

$$H_i^{(1)} = \sum_{\boldsymbol{q}} \xi_{\boldsymbol{q}} e^{i\boldsymbol{q}\boldsymbol{r}} \hat{V}_{\boldsymbol{q}}, \tag{3.1}$$

with

$$\begin{aligned} \hat{V}_{\boldsymbol{q}} &= -\frac{i}{m}(\boldsymbol{q}\cdot\hat{\boldsymbol{p}})\hat{p}_z - \frac{i\hbar}{2m}q^2\hat{p}_z + eE_\perp + \Lambda q^2 v_{\mathrm{pol}}(qz), \\ v_{\mathrm{pol}}(x) &= x^{-2}\left[1 - xK_1(x)\right] \end{aligned} \tag{3.2}$$

Here, $\boldsymbol{r}$ is the in-plane electron coordinate, $\hat{\boldsymbol{p}} = -i\hbar\partial_{\boldsymbol{r}}$ is the 2D electron momentum, $\hat{p}_z = -i\hbar\partial_z$, and $\xi(\boldsymbol{r})$ is expanded in Fourier components $\xi(\boldsymbol{r}) = \sum_{\boldsymbol{q}} \xi_{\boldsymbol{q}} e^{i\boldsymbol{q}\boldsymbol{r}}$ with wave vectors $\boldsymbol{q}$. The first two terms in the operator $\hat{V}_{\boldsymbol{q}}$ describe a *kinematic* interaction, which arises because the electron wave function is set equal to zero on a non-flat surface. The third term is due to the external pressing electric field $E_\perp$. The last term $\Lambda q^2 v_{\text{pol}}(qz)$ describes the change of the polarization energy due to surface curvature [137, 138] ($K_1(x)$ is the modified Bessel function). The scattering rates due to electron-ripplon coupling have been carefully tested experimentally by measuring the in-plane electron mobility at low frequencies [139]. Good agreement has been found between the simple single-electron theory and experiment in a broad range of temperatures and electron densities with no magnetic field [134].

It has been pointed out that there are limitations on the wave numbers q of ripplons for which the electron-ripplon coupling has the form (3.2)–(3.2). According to Ref. [138], qr_B should be $\lesssim 1$, while another argument [140] is that q should certainly be small compared to the reciprocal width of the helium liquid-vapor interface and the reciprocal decay length of the electron wave function into helium. Both lengths are of order of a few angstroms, which means that the large-q cutoff $q_{\max}$ should be $\sim 10^7$ cm^{-1}.

While the quasielastic electron-ripplon scattering determines transport properties, it does not lead to energy relaxation. Energy relaxation in this system is governed by absorbing or emitting bulk phonons or pairs of short-wavelength ripplons [140, 141]. Experimentally the energy relaxation measurements are challenging. To our knowledge, there have only been measurements of total energy relaxation rate [142], which turned out to be of the order $\sim 10^6$ s^{-1} for $T = 0.57$ K. This is the average decay rate of states over several subbands, and it is impossible to resolve individual contributions of the two scattering processes mentioned above.

In typical experiments, the electron system is nondegenerate yet strongly correlated. The correlation strength in a classical low-density plasma is conventionally quantified by the ratio Γ of the average Coulomb energy to the average kinetic energy: $\Gamma = e^2(\pi n_s)^{1/2}/k_BT$ which usually exceeds 20 (n_s is the electron density, typically $n_s \sim 10^8$ cm^{-2}). One of the most striking effects of the electron-electron interaction is Wigner crystallization, in which electrons minimize the energy of mutual repulsion by forming a triangular crystal. The crystallization happens for $\Gamma > 130$ [1, 143, 144, 145, 146], the phase diagram is shown in Fig. 3.3. The phase diagram also contains a

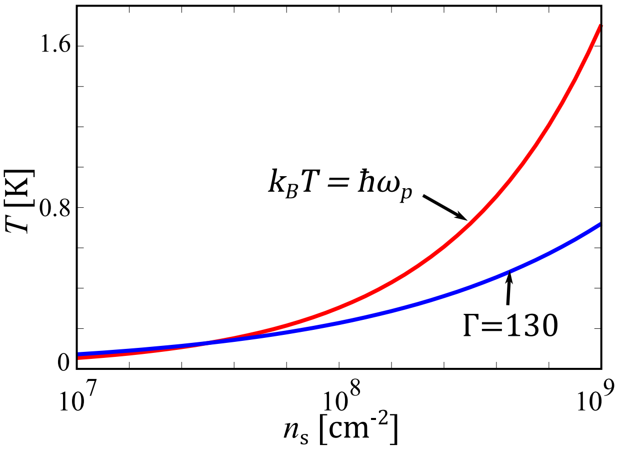

Figure 3.3 Phase diagram of a nondegenerate strongly correlated electron system. The system is a Wigner solid below the line $\Gamma \approx 130$. If the temperature exceeds the short-wavelength plasma frequency ω_p (in energy units), the electron dynamics is classical.

line corresponding to $k_BT = \hbar\omega_p$, where $\omega_p = (2\pi e^2 n_s^{3/2}/m_e)^{1/2}$ is the short-wavelength plasma frequency. Above this line all oscillations in the system are classical.

The crystallization was first experimentally observed in a beautiful experiment by Grimes and Adams [1]. In that experiment, the in-plane microwave conductivity as a function of frequency showed a complicated pattern of resonances below a certain temperature (see inset in Fig. 3.4, which refers to the electron density $n = 4.5 \times 10^8$ cm^{-2}; for this density the transition happens at $T = 0.457$ K). These resonances were explained by Fisher, Halperin and Platzman [147] and were attributed to the onset of long-range order in the electron system. Therefore, the resonance detection allowed Grimes and Adams to trace a portion of the phase boundary shown in Fig. 3.4. Recently Wigner crystallization was observed in quasi-one-dimensional channels on the surface of helium [30], and in a carbon nanotube [148]. There is also evidence that Wigner crystallization occurs in strong magnetic fields in 2D electron systems in semiconductor quantum wells [149, 150].

Wigner crystallization is known to make transport of electrons on helium remarkably nonlinear even at small driving fields [2, 30]. The velocity $\boldsymbol{v}$ of a Wigner crystal saturates when $\boldsymbol{v}\cdot\boldsymbol{G} = \omega(\boldsymbol{G})$, where $\boldsymbol{G}$ is a reciprocal lattice vector of the Wigner crystal. This effect is known as the Bragg-Cherenkov scattering [29]. Ripplons emitted by individual electrons that form a crystal moving

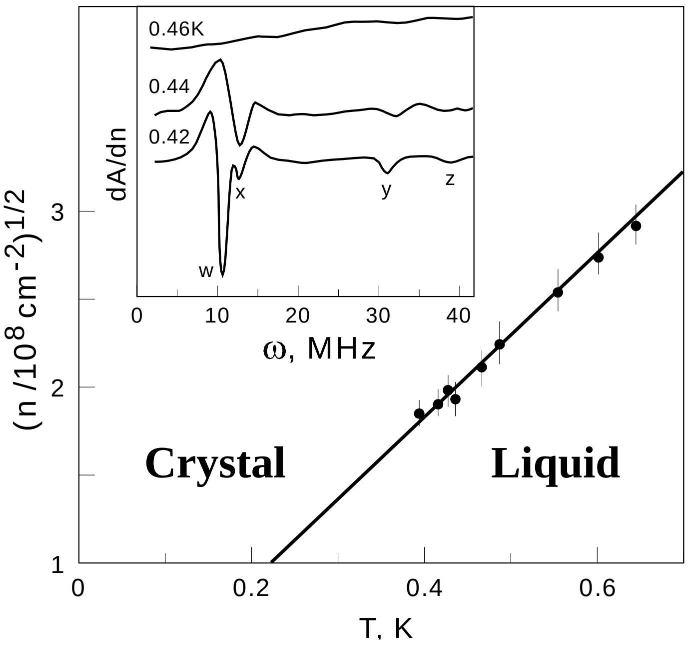

Figure 3.4 Portion of the liquid-solid phase boundary for a classical 2D electron system on the helium surface [1]. The data points denote the melting temperatures measured at different electron densities. The transition is detected from the sudden appearance of resonant electron absorption at radio-frequencies, an example of which is shown in the inset. The solid line corresponds to $\Gamma = 137$.

with this velocity constructively interfere, thereby increasing the momentum transferred to ripplons per unit time dramatically. Essentially, the reaction force becomes so strong, that the crystal can not accelerate above the Bragg-Cherenkov velocity unless the driving field is extremely strong [30].

Even for higher temperature, when electrons do not form a Wigner crystal, the electron-electron interaction is still strong, $\Gamma \gg 1$. The electron system is a strongly correlated non-degenerate electron fluid in this case. One might expect that the electron-electron interaction may substantially change the in-plane mobility. However, as has been shown [3], the mobility in a strongly correlated liquid remains close to that predicted by single-electron theory for a broad range of temperatures and electron densities, in a spatially uniform system without a magnetic field. This is explained by the short duration of electron-ripplon collisions, $\sim \hbar(k_B T)^{-1}$, during which the interaction with other electrons only slightly modifies the electron motion. The main difference comes from the fact that in a liquid electrons exchange momenta with each other much faster than with ripplons.

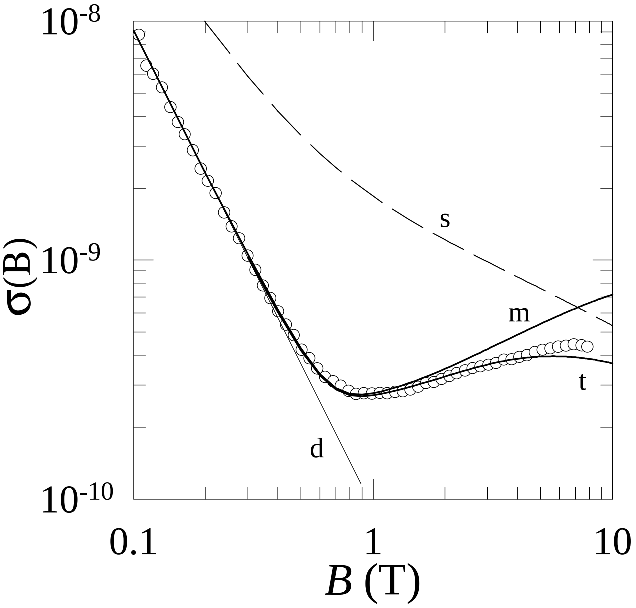

Figure 3.5 Measured magnetoconductivity σ for electron density $n = 0.55 \times 10^8 \text{cm}^{-2}$ at $T = 0.7$ K in the 2D electron fluid [2]. Theory lines show: **d**: Drude model, **s**: self-consistent Born approximation, **m**: many-electron theory [3] and **t**: phenomenological calculation that combines the results from the many-electron theory and the SCBA for strong magnetic fields.

This leads to a change of the expression for the mobility. However, numerically this change turns out to be comparatively small in the range studied in the early experiments.

The situation is very different in the presence of a magnetic field. In this case, the electron-electron interaction lifts the degeneracy of the single-electron energy spectrum and makes the spectrum continuous. It turns out that the magnetotransport can be described in terms of an easily calculated force on an electron from other electrons [3, 151]. This many-electron theory predicts a non-monotonic magnetoconductivity for moderate magnetic fields, which is in good agreement with the experimental data obtained by Lea, et al. [152, 2], see Fig. 3.5. The large difference between one-electron self-consistent Born approximation (SCBA) and the many-electron theory in Fig. 3.5 shows the importance of the electron-electron interaction in this system.

As mentioned before, a significant advantage of the electrons on helium over other two-dimensional strongly correlated systems is the absence of defects. One can study effects of the electron-electron interaction in this system unobstructed by disorder (which plays a very significant role for electrons in semiconductors or vortices in superconductors). Also, in contrast to macroscopic classical systems of colloidal particles, the coupling of electrons on helium to the substrate is weak, the electron motion is underdamped.

The role of correlations becomes particularly clear when the system is a crystal in the absence of the external potential. The role of a random potential in this case has been attracting much attention in various contexts, from superconductors to charge/spin density waves to Wigner crystals [153, 154, 155, 156, 157, 158]. It is well-known that a random potential in one- and two-dimensional systems causes pinning, with no threshold in the potential strength. An external field can lead to depinning and formation of dynamical phases, see [28] for a review.

Electrons on helium can be used to study the effect of quenched disorder by using thin helium films, in which case the electrons "feel" the random potential of the substrate. However, electrons on helium also provide a unique tool for investigating the role of correlations in the case where the external potential is periodic. Such potential can be created by creating a periodic potential on the substrate while keeping it further away from the electrons, at a distance $\gtrsim 1\mu$m. In fact, as we discuss below, the study of the electrons on helium in the presence of such a potential can provide a direct way to reveal and characterize the correlations in the electron system.

Various phenomena that emerge in correlated systems placed into a periodic external potential have been broadly discussed in the literature [159, 26, 160, 27]. In analyzing the ensuing dynamics one should consider separately atomic systems, in which the pair potential has a minimum and the structure of the crystal in the absence of the potential is defined by the form of the interparticle potential. The situation for a Wigner crystal or crystals formed by the dipolar interparticle repulsion is different. In this case the pair potential does not have a minimum. The structure of the crystal is determined just by the particle density and usually corresponds, in two-dimensional systems, to the closely packed triangualr.

The simplest example of an externally imposed periodic potential is the potential of a crystalline substrate on which a monolayer film of a different crystal is deposited [161, 162, 158]. Of primary interest here have been the effects of commensurability. Two periodic systems are considered to be commensurate (C) if one or more of their reciprocal lattice vectors coincide. They are said to be incommensurate (I) otherwise. Some parameter is usually introduced to describe the degree or commensurability, the choice of which depends on the system in question. Examples of commensurate-incommensurate (CI) transitions, besides those in monolayer films, include the transitions in magnetic materials [163], charge-density waves [164, 165], colloidal crystals in light-induced potentials [5, 166], vortex lattices in type-II superconductors [167, 168], metallic dot arrays [169]. Recently CI effects in stacked 2D materials, such as graphene on boron nitride [170], have also attracted substantial interest.

Colloidal crystals have proven to be especially useful in studying phase transitions and the effects of external potentials in strongly interacting systems, see [171] for a review. Typically, these systems consist of small dielectric particles, e.g. polystyrene spheres or silica spheres, in a liquid suspension. The particle size may vary from a few nanometers to a few microns. The interaction between the particles may have a variety of origins. Colloidal particles often become charged in the suspension through accumulation of ions on their surface [172], which makes the particles interact through the screened Coulomb potential. The charge of the particles is fluctuating, but often can be made reasonably uiniform, with a variation of a few percent. The concentration of ions in the solution determines the screening length. The inter-particle interaction can also arise due to polarization of the dielectric particles in an external electric field [173, 174], magnetic moments of the particles [175], etc. In most cases, the inter-particle potential does not have a minimum, in contrast to monolayer solid-state films. An advantageous feature of the colloidal systems is that the interaction is often tunable. The system can be made effectively two-dimensional by confining the particles to a thin layer by flat walls, or by pressing them to the bottom of the experimental cell by gravity. An external periodic potential is typically created by the interference pattern of laser beams [176]. Another important advantageous feature of colloidal systems is the possibility to resolve the structure of the system in real time directly by optical imaging.

It is clear from qualitative arguments that a 2D solid placed on a maximally commensurate substrate becomes pinned to the substrate. Another consequence of the fully commensurate substrate is the so-called modulation-induced freezing (also known as light induced freezing for potentials

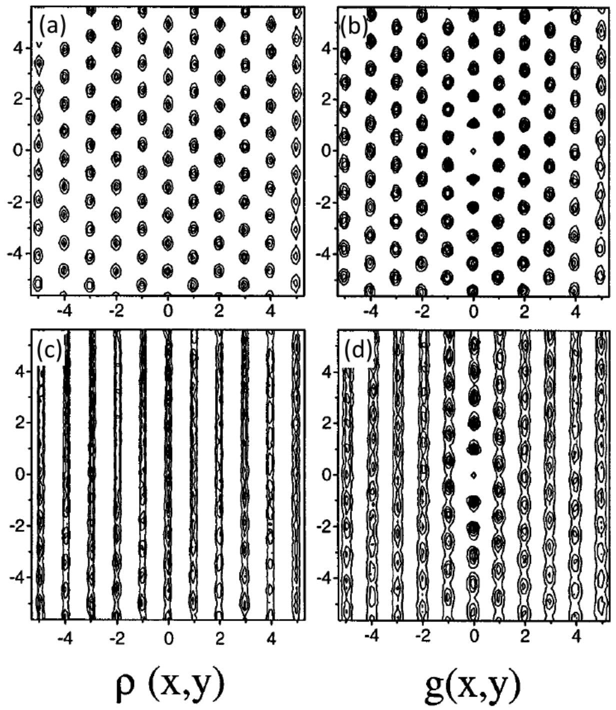

Figure 3.6 Contour plots of the averaged density distribution $\rho(x,y)$ and pair correlation function $g(x,y)$ obtained in the experiment [4] for two values of the potential strength: $2.1k_BT$**(a,b)** for which the crystal forms due to modulation-induced freezing, and $6.3k_BT$ **(c,d)** above the reentrant-melting threshold, for which the system is a modulated liquid. In both cases the temperature is above the melting temperature in the absence of modulation.

created by laser radiation) [172, 4, 27], where the melting temperature increases because of the commensurate potential. A less obvious effect may occur in colloidal systems of charged particles when the potential strength is increased even further beyond the modulation-induced freezing point. In a certain range of parameters above the freezing temperature in the absence of the modulation, the further increase of the potential amplitude leads to a reentrant modulation-induced melting transition, when the system becomes a modulated liquid again. Fig. 3.6 shows the experimental observation of this transition, the upper row corresponding to the crystal state induced by the modulation, and the lower row to the liquid state for the modulation strength above the modulation-induced melting threshold. Qualitatively, both effects are related to the suppression of thermal fluctuations of particles transverse to the imposed periodic potential [4, 166, 27].

Quantitatively, the effects of the commensurate potential can be understood using the free energy of the solid phase "locked" in the commensurate potential. For a one-dimensional periodic potential in the continuum approximation the elastic energy can be written as [27]:

$$H_{LFS} = \frac{1}{2} \int d^2 r \left\{ K_{\text{eff}} (\partial_y u_y)^2 + \mu_{\text{eff}} (\partial_x u_y)^2 \right\}, \tag{3.3}$$

where u_y is the y-component of the local displacement, and K_{eff} and μ_{eff} are the effective bulk and shear moduli respectively. The modulation troughs are oriented along the y axis. K_{eff} and μ_{eff} depend on both temperature and the external potential amplitude A. This model predicts the melting temperature for small A to be

$$T_m(A) \sim T_m(0) + [\ln(k_B T/A)]^{-1/\bar{\nu}}, \tag{3.4}$$

with $\bar{\nu} \approx 0.37$. The melting temperature is increasing with A, as expected for the modulation-induced freezing. For large A, on the other hand,

$$T_m(A) = T_m^{\infty} \left\{ 1 + \frac{5\left[(\kappa a)^2 - 31\right]}{64\pi^2} \left(1 + \frac{13}{3\kappa a} \frac{k_B T_m^{\infty}}{p^2 A} \right) \right\}, \tag{3.5}$$

where a is the lattice spacing, κ is the inverse of the Debye screening length, and $T_m^{\infty} = T_m(A \to \infty) > T_m(0)$ can be estimated in the model. This is a decreasing function of A for sufficiently large κ, corresponding to the modulation-induced melting described above.

For incommensurate 2D systems, the competition of periodicities leads to rich phenomenology. A typical feature of incommensurate solids is the instability against formation of defects that eliminate long-range order, or can themselves form ordered phases. Two types of topological defects are usually identified: solitons (or kinks) [160, 26] that enable formation of crystalline domains of uniform density, and a system of dislocations. Proliferation of dislocations can lead to a hexatic phase [177, 178, 159, 179]. It is the relative stability of the two types of defects that essentially determines the phase diagram. Another prominent feature of incommensurate phases is that often they can "float" without pinning to the substrate.

In the continuous limit, the free energy of a weakly incommensurate phase can be written in a way similar to Eq. (3.3), but with an additional term accounting for the potential energy of the particles in the external potential due to incommensurability. Consider a crystal in a weak external potential $V(\boldsymbol{r}) = \sum_{\boldsymbol{q}} V_{\boldsymbol{q}} e^{i\boldsymbol{q}\boldsymbol{r}}$, where $\boldsymbol{q}$ are the reciprocal vectors of the external potential. The particles in the crystal without modulation are assumed to form a lattice with positions $\boldsymbol{R}$ and reciprocal lattice vectors $\boldsymbol{b}$. Let us assume that only one pair of vectors $\boldsymbol{q}$ and $\boldsymbol{b}$ are close, so that for a small vector $\boldsymbol{s}$ we can write $\boldsymbol{q} = \boldsymbol{b} + \boldsymbol{s}$ (weak incommensurability). Then, at zero temperature, one can write the total potential energy in this system as [26]:

$$U = \int d^2 r \left\{ \frac{K}{2} \left(\partial_x u_x + \partial_y u_y \right)^2 + \frac{\mu}{2} \left[\left(\partial_x u_x - \partial_y u_y \right)^2 + \left(\partial_y u_x + \partial_x u_y \right)^2 \right] + f(\phi) \right\}, \tag{3.6}$$

where K and μ are the bulk and shear moduli respectively, and

$$f(\phi) = \sum_{n=-\infty}^{\infty} b^2 V_{n(\boldsymbol{b}+\boldsymbol{s})} e^{in\phi}, \tag{3.7}$$

with $\phi = \boldsymbol{u} + \boldsymbol{s}\boldsymbol{R}$. The term $f(\phi)$ represents the interaction of the lattice with the external potential. This interaction tends to place particles at the minima of the periodic potential. The elastic terms, however, tend to place the particles in their regular lattice, with a periodicity different from that of the potential. For s smaller than some critical value s_c, which depends on the periodic potential strength, the system will minimize its energy by becoming commensurate with the external potential. For $s > s_c$, however, the commensurate phase is not favorable and the particles are predicted to assume some compromise arrangement that minimizes the energy. For sufficiently small s, the system is divided into domains of commensurate structure separated by narrow sections where the inter-particle distances are substantially different from the lattice spacing in the rest of the system. These structural features are the solitons (kinks) mentioned in the previous paragraph. Further increasing of s leads to a superstructure better described as a periodic density modulation in the crystal. The density modulation is directed at some angle with respect to the reciprocal lattice vector $\boldsymbol{b}$ in a general case. The period of the superstructure continuously depends on parameters s and $V_{\boldsymbol{q}}$. The described superstructure, in a somewhat more complicated case of the external potential with two reciprocal lattice vectors being close to two reciprocal lattice vectors of the lattice, was experimentally observed in the system of charged colloidal particles [5]. The solitons can be seen

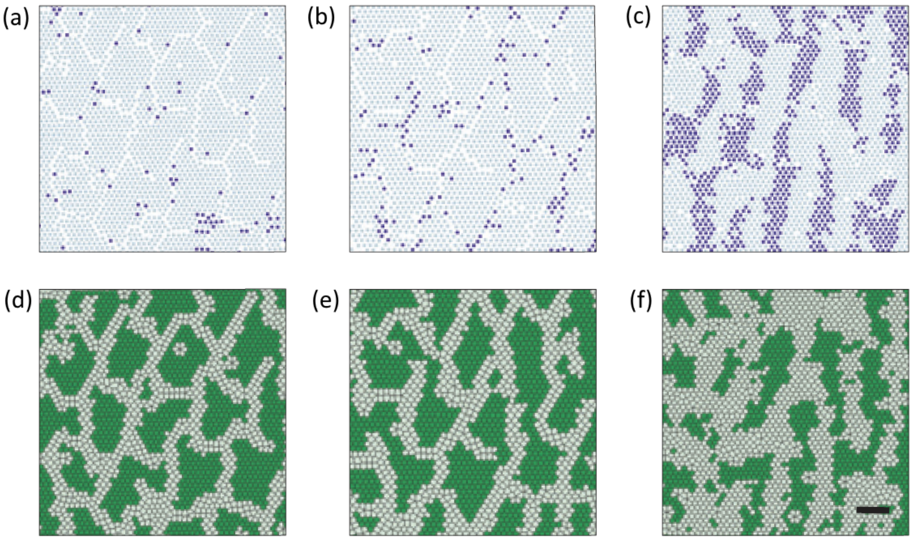

Figure 3.7 **a-c**, Snapshots of particle velocities in a colloidal monolayer in an incommensurate external potential with a triangular structure [5]. The colloidal lattice spacing is $a = 5.7$ μm, while the potential lattice spacing is $s = 5.2$ μm. Fast and slow particles are marked in dark and light blue depending on whether their velocities are above or below 70 % of the maximum particle velocity. **(d-f)**, Voronoi tessellation with color-coded areas of the Voronoi cells: light (large) to dark (small) green. The following driving forces were applied: 0 fN in **(a,d)**, 19 fN in **(b,e)**, and 82 fN in **(c,f)**.

in Fig. 3.7 (d,e) as narrow regions of small density. Because of the 2D nature of the potential in that experiment, the solitons form a complicated 2D structure instead of a series of 1D rows.

Although the continuum elasticity theories are powerful, they are limited to weak incommensurability. Also, it is very hard to describe transport using these theories. That is why numerical simulations are often used to study structural [6, 180, 181, 182, 183] and dynamical properties [184, 7] of commensurate and incommensurate phases. Molecular dynamics simulations for overdamped dynamics have been extensively performed to study vortex lattices in superconductors and colloidal systems. In this framework, for example, simulated annealing has been used to study a rich variety of ground state structures of vortex lattices with square and triangular pinning arrays [6] (Fig. 3.8). By applying a driving force to the particles, one can study depinning and dynamical phases as a function of commensurability. Fig. 3.9 shows the rich dynamic phase diagram obtained in the numerical experiment [7] with a vortex lattice driven across a 1D periodic potential. Monte Carlo simulations [181, 182, 183] have also been used to study structural and thermodynamic

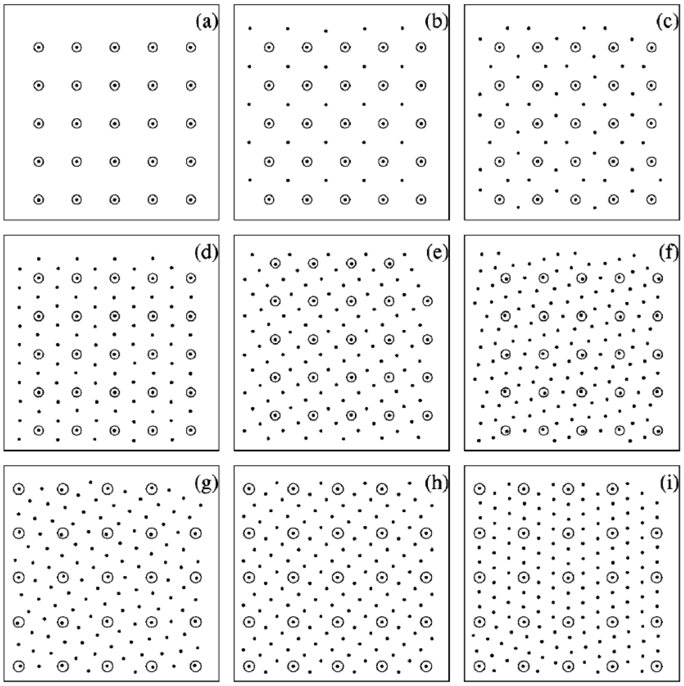

Figure 3.8 Vortex lattice structures observed in the simulation [6] in a superconductor in the presence of a square lattice of pinning sites. The vortices are represented by black dots, while the pinning sites are shown as empty circles. **(a-i)** represent different magnetic field magnitudes, corresponding to the number of vortices per pinning site from 1 to 9 in **(a)** through **(i)**.

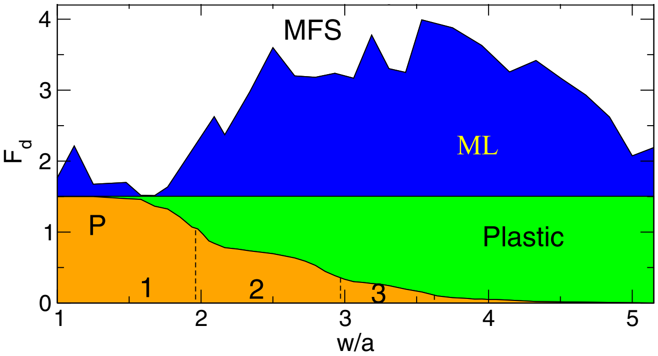

Figure 3.9 Dynamic phase diagram of a vortex lattice driven across a 1D external potential [7] as a function of the drive field F_d and the ratio w/a of the substrate lattice constant w to the vortex lattice constant a. P: pinned phase. Plastic: plastic flow regime. ML: moving modulated lattice state. MFS: moving flowing solid state

properties of atomic and molecular systems on periodic substrates, showing good agreement with experimental observations.

Simulations have also been used to study the effects of external (non-periodic) potentials in the electrons on helium. Reichhardt et al. [185] studied the depinning and subsequent dynamics for a Wigner solid in the quenched disorder, observing a transition from a plastic flow to a moving Wigner smectic. Damasceno et al. [186] considered a Wigner solid pinned to a single pinning site and its depinning with the subsequent plastic flow. Piacente and Peeters [187] simulated the transport of a quasi-1D electron system in a channel across a single constriction, observing elastic and quasielastic depinning. These studies use Langevin dynamics with the phenomenological friction and random noise to model the coupling to the helium surface. As it will be discussed later, a more rigorous treatment of scattering on the surface and bulk quantized excitations is required to adequately describe the dynamics in this system.

3.2 Motivation

We study the effects of periodic potentials in strongly correlated 2D systems using the electrons on helium. One cannot directly observe the spatial structure in this system. However, this system allows one to perform careful transport measurements. Such measurements are of particular interest for strongly correlated systems, as transport depends on the interplay of strong correlations, scattering by defects or a quantum field to which the system is coupled, and a periodic potential. We will concentrate on the liquid state. So far, for this state the effect of correlations on the electron transport have been identified only through the measurements of the magnetoconductivity. A periodic potential brings in a new tool which, we expect, should allow one to directly characterize the correlations in the electron liquid. The periodic potential can be created by an array electrodes in the substrate with a period on the order of one micron, see Fig. 3.10. The advantageous feature of electrons on helium over other 2D correlated systems is that all electrons are identical (for example, no difference in charge, in contrast to charged colloidal systems) and there are no defects, whereas scattering by the excitations in helium is extremely weak. Therefore the effects of the electron-electron interactions in a periodic potentials are not masked by disorder or by strong coupling to the helium excitations.

Our results are obtained by numerically simulating the electron system with the account taken of the long-range Coulomb forces, the microscopic mechanism of the electron scattering by the ex-

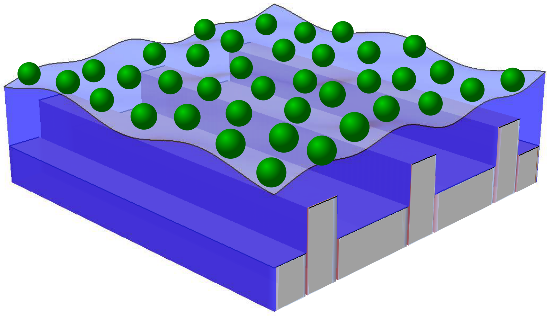

Figure 3.10 Electrons on the surface of liquid helium with a periodic substrate consisting of an array of electrodes (schematically).

citations in helium, and the periodic potential. We concentrate on the regime where the electrons form a classical liquid, but we also briefly study the behavior of the electron solid in a periodic potential as well as the dynamics in the regime where the electron-electron interaction is disregarded; the latter regime is studied primarily as a means to demonstrate the role of the correlations where the electron-electron interaction is present and is strong.

In a way, the system of electrons on helium is an ideal system for studying the effects of a periodic potential on transport of a strongly correlated system. The characteristic inter-electron distance is in the range of 1 μm. With modern technology, it is straightforward to create periodic structures with a comparable period. These structures can create an electrostatic potential, but they can also create a periodic magnetic field that will induce spin-orbit coupling in the electron system and will allow one to study the spin dynamics, a topic that so far has not been explored for electrons on helium at all. However, in this work we concentrate on the electrostatic potential.

The effects of a periodic potential on a solid and an ideal gas have been studied in much depth for other systems than the electrons on helium. In particular, the role of commensurability has been explored, as described above. In a classical ideal gas, the effect of the periodic potential becomes significant only when the potential is comparable to the temperature. For a strong potential, the mobility displays a simple activation behavior.

In contrast, very little is known about the effects of the periodic potential on the strongly correlated liquid phase, where the role of interactions is important but there is no long-range order. We expect that the periodic potential significantly affects all transport characteristics. We consider a one-dimensional periodic potential. It makes the system strongly anisotropic. The major transport characteristics we are interested in are many-electron diffusion and the current in response to an additional spatially uniform driving field.

We should emphasize that, in a correlated system, the very term "diffusion" has to be taken with care. There is diffusion associated with a smooth (on the scale of the correlation length) gradient of the particle density. This diffusion is described by Fick's law, with the current proportional to the density gradient. In noninteracting systems, as shown by Einstein, Fick's diffusion is simply related to fluctuations of particle positions, with the mean square displacement of a particle being proportional to time with the coefficient that enters Fick's law. This is because diffusion and mobility are determined by the same scattering processes. In systems of interacting particles, the relation between the Fick diffusion coefficient and the mean-square particle displacement generally does not hold. In a correlated liquid, particles are wondering around, but their mean square displacement is determined, in the first place, by their interaction with each other. Such an interaction does not change the total momentum of the system and therefore does not contribute to the mobility. Interestingly, we find that in the electron liquid the mean-square particle displacement is still linear in time. We use the term *diffusion coefficient* for the proportionality coefficient between the mean square displacement and the time over which it occurs. As we show, the diffusion coefficient defined this way displays a nontrivial behavior and provides an insight into the phase transition in the electron system.

Even in the absence of long-range order, an important characteristic of the system in a periodic potential is the commensurability. For a one-dimensional potential, we characterize it by the parameter p, which is equal to the ratio $p = K/G$ of the smallest reciprocal lattice vector K of the potential to the smallest reciprocal lattice vector G of the triangular lattice that would exist at the given density of the liquid. In the liquid phase, no conventional pinning can occur since the system remains disordered with dynamically changing structure. However, one may expect that, because of the strong electron correlations, the transport will change significantly if the electron system can perfectly “fit into” the potential.

Another property that can be expected is a strong effect of the periodic potential even where it is weak. One can think that the barriers imposed by the potential are “amplified" by the strong correlations, as the electrons cannot overcome them independently.

A topic of significant interest is thermalization in many-body systems. It has been studied for a long time, starting with the famous Fermi-Pasta-Ulam numerical experiment. That experiment was done on nonlinear vibrations in a chain which, in the case of the electron system, could be extended to vibrations in the electron solid. On the opposite side of the parameter range, where the electrons form a weakly nonideal plasma, thermalization has been well understood since the Landau work [188] on such a plasma. However, to the best of our knowledge, the question of thermalization in a strongly correlated liquid has not been addressed. The electron system on helium provides a natural platform for studying this effect.

To guide the experiment, it is necessary to include into the analysis the full microscopic coupling of the electrons to the quantum field of excitations in liquid helium. This coupling is known. Incorporating it requires a significant modification of the conventional means of numerical simulations of the dynamics of correlated systems. The conventional analysis proceeds by assuming that the motion of a particle is described by a Langevin equation with a phenomenologically added friction force and a random force that mimics the noise from the thermal reservoir. This has no relation to the system that we consider, it does not adequately describe the electron relaxation.

A distinct feature of our method is the direct simulation of both elastic and inelastic scattering processes. It is known that the electrons scatter elastically off the ripplons and inelastically off the phonons in helium; there is also inelastic two-ripplon scattering. We use realistic scattering parameters. It is known that the scattering rate is notoriously low. This refers to both elastic and inelastic scattering. In addition, the inelastic scattering rate is an order of magnitude smaller than the elastic one. This leads to exceptionally slow energy relaxation. In contrast to the Langevin approach, not only are the momentum and energy scattering rates very different, but they also depend on the electron energy, which should lead to a qualitatively different transport.

In Sec. 3.3, we present the methods that we use to study the electrons on the helium surface. The results of the simulations of a uniform system are described in Sec. 3.4. Sec. 3.5 is the central part of our study, focusing on the effects of a periodic potential on the strongly correlated electron system. The conclusions are presented in Sec. 3.6.

3.3 Method

3.3.1 Integration of the equations of motion

To study properties of the electrons on helium we integrate classical equations of motion numerically. We use HOOMD-Blue [189, 190] as the base code for our simulations, with the integrator, interaction potentials, and external forces developed specifically for our study[1]. The code is designed to be used on a graphics processing unit (GPU) which gives up to sixteen-fold acceleration compared with a single CPU core. For integration, we use the standard velocity Verlet algorithm, which is symplectic [191]. The algorithm is implemented numerically as follows:

$$\begin{aligned} \boldsymbol{v}_i\left(t+\Delta t/2\right) &= \boldsymbol{v}_i(t) + \frac{1}{2}\boldsymbol{a}_i(t)\Delta t, \\ \boldsymbol{r}_i\left(t+\Delta t\right) &= \boldsymbol{r}_i(t) + \boldsymbol{v}_i\left(t+\Delta t/2\right)\Delta t, \\ \boldsymbol{v}_i(t+\Delta t) &= \boldsymbol{v}_i\left(t+\Delta t/2\right) + \frac{1}{2}\boldsymbol{a}_i(t+\Delta t)\Delta t, \end{aligned} \tag{3.8}$$

where $\boldsymbol{v}_i$ is the i-th particle's velocity, and the acceleration $\boldsymbol{a}_i(t)$ is evaluated based on forces derived from the positions $\boldsymbol{r}_j(t)$ of all particles at time t. Δt is the time-discretization step. We modify this algorithm to accommodate for discrete scattering events that are described by abrupt changes of velocity $\boldsymbol{v} \to \boldsymbol{v}'$ according to some probability distributions. To conserve potential energy in such scattering to the second order in Δt, the scattering event must happen at integer time points. To see that, consider the energy of a single particle in an external potential $U(\boldsymbol{r})$. Assume that the particle scatters elastically at time t, i.e. its velocity at time t changes by $\Delta\boldsymbol{v}$ such that $|\boldsymbol{v}(t)+\Delta\boldsymbol{v}| = |\boldsymbol{v}(t)|$.

---

[1] Our fork of the HOOMD-Blue code can be found at `https://github.com/kmoskovtsev/HOOMD-Blue-fork`. Scripts used in simulations are available at `https://github.com/kmoskovtsev/Electrons-on-Helium-Scripts`

Then the velocity and position at time $t+\Delta t$ is

$$\begin{aligned} \boldsymbol{v}(t+\Delta t) &= \boldsymbol{v}(t)+\Delta\boldsymbol{v}+\frac{1}{2}(\boldsymbol{a}(t)+\boldsymbol{a}(t+\Delta t))\Delta t, \\ \boldsymbol{r}(t+\Delta t) &= \boldsymbol{r}(t)+\Delta t\left[\boldsymbol{v}(t)+\Delta\boldsymbol{v}+\frac{1}{2}\boldsymbol{a}(t)\Delta t\right]. \end{aligned} \tag{3.9}$$

Then it is easily shown that the energy difference over one step vanishes in the first order in Δt:

$$E(t+\Delta t)-E(t)=\frac{m}{2}\left(\boldsymbol{v}^2(t+\Delta t)-\boldsymbol{v}^2(t)\right)+U\left(\boldsymbol{r}(t+\Delta t)\right)-U\left(\boldsymbol{r}(t)\right)=O(\Delta t^2). \tag{3.10}$$

Since scattering events in our simulations are rare, about one scattering event per 10^5 time steps per particle, this accuracy is enough for our purpose.

We choose $\Delta t \approx 2.57\times 10^{-12}$ s for most simulations, which corresponds to $\Delta t \approx (2\pi/\omega_p)/50$, where ω_p is the short-wavelength plasma frequency. Reducing Δt proved to have no visible effect in the studied phenomena.

3.3.2 Ewald summation

Electrons on the surface of liquid helium interact through the Coulomb repulsion. In a real system, the interaction may be screened by the electrode placed under the helium surface. We will neglect any screening effects in this study for simplicity. These effects will be investigated in future studies. Since we are considering a system with periodic boundary conditions and long-range interactions, we use the Ewald summation to properly calculate the interaction forces and energies [144]. We consider a 2D unit cell that is periodically replicated in two dimensions by the lattice vectors $\boldsymbol{L}_n$, with a charges q_i placed at the coordinate ρ_i in the unit cell. The results in this section are valid for an arbitrary unit cell, however, only rectangular unit cells are used in our study. The system is neutralized by a uniform charge background with the charge density $-q_i/\Omega$, where Ω is the unit cell surface area. Then the potential created by all replicas of the charge q_i at an arbitrary point $\boldsymbol{r}$ in the unit cell, is

$$\phi_i(\boldsymbol{r})=\phi_i^L(\boldsymbol{r})+\phi_i^S(\boldsymbol{r}), \tag{3.11}$$

where

$$\phi_i^L(\boldsymbol{r}) = \frac{2\pi q_i}{\Omega} \sum_{\boldsymbol{k}_n}{}' \frac{1}{k_n} \mathrm{erfc}(k_n \eta) e^{i\boldsymbol{k}_n(\boldsymbol{r}-\boldsymbol{\rho}_i)}, \tag{3.12}$$

and

$$\phi_i^S(\boldsymbol{r}) = \sum_{\boldsymbol{L}_n} \frac{q_i}{|\boldsymbol{r}-\boldsymbol{\rho}_i-\boldsymbol{L}_n|} \mathrm{erfc}\left(\frac{|\boldsymbol{r}-\boldsymbol{\rho}_i-\boldsymbol{L}_n|}{2\eta}\right) - \frac{4\sqrt{\pi}\eta q_i}{\Omega}. \tag{3.13}$$

Here $\mathrm{erfc}(x)$ is the complementary error function. The summation in $\phi_i^L(\boldsymbol{r})$ is carried over all reciprocal lattice vectors of the lattice $\boldsymbol{L}_n$, excluding $k_n = 0$. The parameter η has the dimensionality of distance, and can be chosen arbitrarily. Typically, such η is chosen that it makes both $\phi_i^L(\boldsymbol{r})$ and $\phi_i^S(\boldsymbol{r})$ converge relatively quickly.

For the molecular dynamics simulations, we need forces as well as potentials. Therefore, we calculate the electric field created by all replicas of q_i by differentiating Eq. (3.11) over $\boldsymbol{r}$:

$$\begin{aligned}\boldsymbol{E}_i(\boldsymbol{r}) = {} & q_i \sum_{\boldsymbol{L}_n} \frac{\boldsymbol{r}-\boldsymbol{\rho}_i-\boldsymbol{L}_n}{|\boldsymbol{r}-\boldsymbol{\rho}_i-\boldsymbol{L}_n|^3} \mathrm{erfc}\left(\frac{|\boldsymbol{r}-\boldsymbol{\rho}_i-\boldsymbol{L}_n|}{2\eta}\right) \\ & + \frac{q_i}{\sqrt{\pi}\eta} \sum_{\boldsymbol{L}_n} \frac{\boldsymbol{r}-\boldsymbol{\rho}_i-\boldsymbol{L}_n}{|\boldsymbol{r}-\boldsymbol{\rho}_i-\boldsymbol{L}_n|^2} \exp\left(-\frac{|\boldsymbol{r}-\boldsymbol{\rho}_i-\boldsymbol{L}_n|^2}{4\eta^2}\right) \\ & - \frac{2\pi q_i}{\Omega} \sum_{\boldsymbol{k}_n}{}' \frac{i\boldsymbol{k}_n}{k_n} \mathrm{erfc}(k_n \eta) e^{i\boldsymbol{k}_n(\boldsymbol{r}-\boldsymbol{\rho}_i)}\end{aligned} \tag{3.14}$$

Both $e\phi_i(\boldsymbol{r})$ and $e\boldsymbol{E}_i(\boldsymbol{r})$ are tabulated on a mesh covering a quarter of the rectangular unit cell. The values in the rest of the unit cell are recovered by symmetry. The bilinear interpolation is used to obtain the values of these fields at an arbitrary point in the unit cell. Consider some field $f(\boldsymbol{r})$, tabulated as $f_{m,n}$ on the mesh (x_m, y_n) with indices m and n. The mesh steps are h_x and h_y along the x and y axes respectively. The value of $f(\boldsymbol{r})$ at a point (x, y) within the rectangle with corners (x_m, y_n) and (x_{m+1}, y_{n+1}) is interpolated as

$$f(x,y) \approx f_{\alpha,n} + \frac{\delta y}{h_y}(f_{\alpha,n+1} - f_{\alpha,n}), \tag{3.15}$$

where

$$f_{\alpha,n} = f_{m,n} + \frac{\delta x}{h_x}(f_{m+1,n} - f_{m,n}), \tag{3.16}$$

and $\delta x = x - x_m$, $\delta y = y - y_n$. The interpolation scheme is implemented in the new `table2D` pair interaction for HOOMD-Blue. The tables are prepared using the `ewald_module.py` module in our code base, that uses Eqs. (3.11)–(3.14). Grids of the size 2000 × 2000 are used in most of our simulations. The GPU version of the code provides the acceleration of up to sixteen times compared with a single CPU core. The electron-electron interaction is the bottle neck of our computations. The computation time scales as the number of particles squared. For 1600 particles, on NVIDIA® Tesla® K80 GPU, the computation speed is about 150 time steps per second.

3.3.3 Scattering of electrons by ripplons and energy relaxation

As it was discussed above, the electron-rippoon coupling is described by Eqs. (3.1)–(3.2). For simplicity we consider coupling in the case with no pressing field $E_\perp$. Then only the last term in Eq. (3.2) is relevant for the in-plane scattering. The scattering rate from the wave-vector $\boldsymbol{k}$ into $\boldsymbol{k}'$ is then determined by the square of the matrix element [3]

$$\overline{\left|H_{\boldsymbol{q}}^{(\mathrm{rpl})}\right|^2} = \frac{S^{-1} k_B T \hbar^4 q^2}{4\alpha m_e^2 r_B^4} \phi^2\left(\frac{q r_B}{2}\right), \tag{3.17}$$

where

$$\phi(x) = (x^2-1)^{-1} + (1-x^2)^{-3/2} \ln\left[\frac{1+(1-x^2)^{1/2}}{x}\right], \ x<1,$$
$$\phi(x) = (x^2-1)^{-1} - (x^2-1)^{-3/2} \tan^{-1}\left[(x^2-1)^{1/2}\right], \ x>1. \tag{3.18}$$

The total rate of scattering $w_k^{(\mathrm{rpl})}$ by ripplons from the wave-vector $\boldsymbol{k}$ to any other allowed state is determined by the Fermi golden rule with the matrix element (3.17). The scattering is elastic, therefore only scattering to states with $|\boldsymbol{k}'| = |\boldsymbol{k}|$ is allowed. Therefore, the total scattering rate is

$$w_k^{(\mathrm{rpl})} = \int_0^{2\pi} d\theta \, w_{k\theta}, \tag{3.19}$$

where

$$w_{k\theta}^{(\mathrm{rpl})} = \frac{k_B T \hbar q^2}{8\pi\alpha m_e r_B^2} \phi^2\left(\frac{q r_B}{2}\right)\Bigg|_{q=k\sqrt{2(1-\cos\theta)}} \tag{3.20}$$

is the distribution of scattering angles θ (normalized to the total scattering rate). The detailed derivation of this result is reproduced in Appendix A.7. To simulate this scattering process, we tabulate the total scattering rate $w_k^{(\mathrm{rpl})}$ on the grid of 200 k points from $k_{min} = 1\ \mu\mathrm{m}^{-1}$ to $k_{max} =$

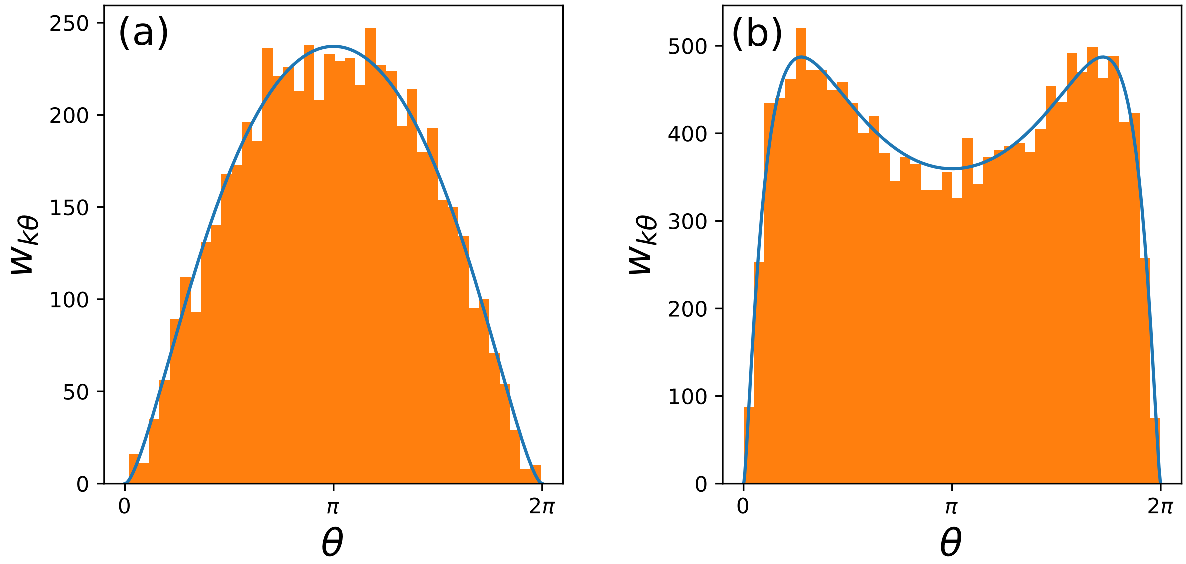

Figure 3.11 The histograms show the scattering angle distributions obtained in the simulation of 2×10^6 free non-interacting electrons over 100 time steps with all electrons having momentum corresponding to (**a**) $k = 2 \times 10^5$ cm^{-1}, (**b**) $k = 2 \times 10^6$ cm^{-1}. Elastic ripplon scattering is the only scattering in the simulation, and only particles that scattered during the simulation period contribute to the histograms. The y-axis shows the total count of scattering events in each of the 40 bins covering angles from 0 to 2π. Solid lines correspond to the values obtained directly from Eq. (3.20), normalized appropriately for comparison with the total count of scattering events.

150 μm^{-1}. The angle distribution is tabulated in the form of the inverse cumulative distribution function $W_{k\theta}^{-1}$ because we use the inverse transform sampling to generate random numbers with arbitrary distributions. $W_{k\theta}^{-1}$ is tabulated on a 150×1000 grid spanning the rectangle $[k_{min}, k_{max}] \times [0,1]$. The values are then linearly interpolated for $w_k^{(\mathrm{rpl})}$. Interpolation scheme (3.15)–(3.15) is used for $W_{k\theta}^{-1}$. One random number needs to be generated at every time step to determine whether scattering should take place at this step, and another random number is generated if scattering occurs to determine the scattering angle. The scattering rates and distributions measured in the simulations agree well with Eq. (3.20), see Fig. 3.11.

To have realistic energy relaxation in the system, we consider inelastic scattering. For the electrons on helium, two inelastic processes are important: emission and absorption of bulk phonons in helium and of pairs of short-wavelength ripplons [141]. Transport properties, on the other hand, are predominantly determined by quasielastic ripplon scattering. The energy relaxation rate is also much slower than the electron-ripplon scattering in this system. Therefore only the total energy relaxation rate is important for our study, and not the particular form of the scattering distributions. For simplicity, we only consider inelastic scattering by bulk phonons and artificially adjust the total scattering rate to be of the order of 10^6 s^{-1} at $T = 500$ mK [142] and of the order of 10^5 s^{-1} at $T = 58$ mK [192].

For the form of the inelastic scattering distribution functions, we choose that of the scattering of electrons by bulk phonons that is mediated by the polarization interaction hamiltonian (see Appendix A.9 for details):

$$H^{(\mathrm{ph})} = \Lambda \sum_{\boldsymbol{q}, Q_z > 0} Q q u_{Q_z,\boldsymbol{q}} e^{i\boldsymbol{q}\boldsymbol{r}} \Xi(\boldsymbol{Q}, z), \tag{3.21}$$

with

$$\Xi(\boldsymbol{Q}, z) \equiv \int_{-\infty}^{0} dz' \frac{\sin(Q_z z')}{2q|z-z'|} K_1\left(q(z-z')\right). \tag{3.22}$$

Here as before, $\boldsymbol{r}$ and z are the in-plane and perpendicular to the plane coordinates of the electron. $\boldsymbol{Q}$ is the total 3D phonon wavevector, $\boldsymbol{q}$ is the in-plane part of $\boldsymbol{Q}$, Q_z is the z-component of $\boldsymbol{Q}$, and $K_1(x)$ is the modified Bessel function. The $\boldsymbol{Q}$-component $u_{Q_z,\boldsymbol{q}}$ of the displacement field in the helium bulk has the form

$$u_{Q_z,\boldsymbol{q}} = \sqrt{\frac{\hbar}{\rho v_s V Q}} \left(b_{Q_z,\boldsymbol{q}} + b^{\dagger}_{Q_z,-\boldsymbol{q}}\right), \tag{3.23}$$

where ρ and V are the density and the volume of helium respectively, v_s is the speed of sound, and $b_{Q_z,\boldsymbol{q}}$, $b^{\dagger}_{Q_z,\boldsymbol{q}}$ are the annihilation and creation operators for a phonon mode with the wavevector $\boldsymbol{Q}$. Then by the Fermi golden rule, the rate of scattering from state $\boldsymbol{k}$ into the phase volume d^2k' through a phonon absorption is

$$dw^{(\mathrm{ph1})}_{\boldsymbol{k}'\boldsymbol{k}} = d^2k' \frac{\Lambda^2}{2\pi^2 \rho \hbar v_s^2} Q q^2 N_{Q_z,\boldsymbol{q}} \left|\langle O_z|\Xi|O_z\rangle\right|^2 \Bigg|_{\substack{\boldsymbol{q} = \boldsymbol{k}' - \boldsymbol{k} \\ Q_z = \frac{1}{\hbar v_s}(\varepsilon_{k'} - \varepsilon_k)}}, \tag{3.24}$$

where

$$\langle O_z|\Xi(\boldsymbol{Q}, z)|O_z\rangle = \int_0^{\infty} dz \frac{4z^2}{r_B^3} e^{-2z/r_B} \Xi(\boldsymbol{Q}, z), \tag{3.25}$$

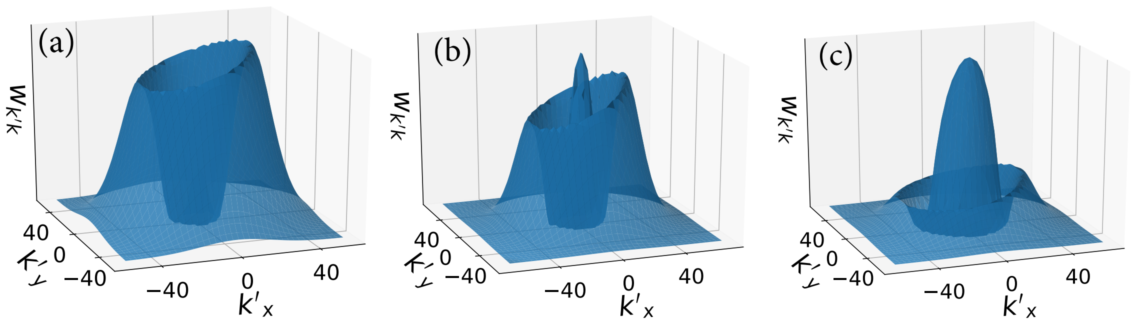

Figure 3.12 Scattering rate $w^{(\mathrm{ph})}_{\boldsymbol{k}'\boldsymbol{k}}$ as a function of $\boldsymbol{k}'$ for: **(a)** $\boldsymbol{k} = (10,0)\ \mu\mathrm{m}^{-1}$, **(b)** $\boldsymbol{k} = (15,0)\ \mu\mathrm{m}^{-1}$, **(c)** $\boldsymbol{k} = (25,0)\ \mu\mathrm{m}^{-1}$. Axes k_x and k_y have dimensions $\mu\mathrm{m}^{-1}$. The scattering rate vanishes at points where $|\boldsymbol{k}'| = |\boldsymbol{k}|$.

and $N_{Q_z,\boldsymbol{q}} = 1/\left(e^{\hbar\omega_Q/k_BT} - 1\right)$ is the average number of phonons with the wave-vector $\boldsymbol{Q}$ and energy $\hbar\omega_Q = \hbar v_s Q$ in thermal equilibrium. The electron kinetic energy is denoted as $\varepsilon_k = \hbar^2k^2/2m_e$. The second process, with a phonon emitted, has the rate

$$dw^{(\mathrm{ph2})}_{\boldsymbol{k}'\boldsymbol{k}} = d^2k' \frac{\Lambda^2}{2\pi^2\rho\hbar v_s^2} Q q^2 (N_{Q_z,\boldsymbol{q}} + 1) \left|\langle O_z|\Xi|O_z\rangle\right|^2 \Bigg|_{\substack{\boldsymbol{q} = \boldsymbol{k}' - \boldsymbol{k} \\ Q_z = \frac{1}{\hbar v_s}(\varepsilon_k - \varepsilon_{k'})}} . \qquad (3.26)$$

We can write the combined scattering rate for the two processes as

$$w^{(\mathrm{ph})}_{\boldsymbol{k}'\boldsymbol{k}} = \begin{cases} w^{(\mathrm{ph1})}_{\boldsymbol{k}'\boldsymbol{k}}, & k' > k, \\ w^{(\mathrm{ph2})}_{\boldsymbol{k}'\boldsymbol{k}}, & k' < k. \end{cases} \qquad (3.27)$$

The shape of $w^{(\mathrm{ph})}_{\boldsymbol{k}'\boldsymbol{k}}$ as a function of $\boldsymbol{k}'$ for three values of $\boldsymbol{k}$ is shown in Fig. 3.12. Due to the ratio $e^{\hbar\omega_Q/k_BT}$ of (3.26) to (3.24) for the same value of Q, this scattering mechanism supports the detailed balance condition for the Boltzmann distribution and leads to energy relaxation. As discussed above, we multiply the scattering rate (3.27) by a constant factor of 20 to have the total energy relaxation rate close to that obtained in the experiment [142, 192].

In the code, we simulate the inelastic scattering events by changing the electron momentum instantaneously according to the scattering rates given by Eqs. (3.24) and (3.26). The difference with the elastic scattering is that the magnitude of the momentum changes as well as the direction. At every time step, the total scattering rate $w^{(\mathrm{ph})}_{k}$ from momentum $\hbar\boldsymbol{k}$ into any other momentum is calculated. Then the probability for a given electron to scatter at the current time step is determined as $w_k^{(\mathrm{ph})}\Delta t$. A random number is generated to determine if scattering should occur at this step according to the probability to scatter. If the electron is scattered at this time step, the scattering momentum $\boldsymbol{k}'$ is determined in two steps. First, the absolute value of $\boldsymbol{k}'$ is drawn from the distribution $f_{k'k}$ of k' for the given k, where $f_{k'k}$ is an integral of $w_{\boldsymbol{k}'\boldsymbol{k}}^{(\mathrm{ph})}$ over the scattering angle θ. Second, θ is generated according to the angle cumulative distribution $Y_{k'k}$. This radial scheme is appropriate here because the scattering rate varies quickly with the absolute value of k' and rather smoothly with the angle.

All probability distributions are computed beforehand and tabulated in three tables. We use inverse transform sampling to draw random numbers from the distributions, therefore all distributions except $w_k^{(\mathrm{ph})}$ are stored as inverse cumulative distribution functions. The table for $w_k^{(\mathrm{ph})}$ is one-dimensional, on the k-grid used in the ripplon scattering. The table for $F_{k'k}^{-1}$ is two-dimensional, on the grid spanning $[k_{min}, k_{max}] \times [0,1]$. Finally, the table for $Y_{k'k}^{-1}$ is three-dimensional, on the grid spanning $[k_{min}, k_{max}] \times [k_{min}, k_{max}] \times [0,1]$.

Similar to the ripplon scattering, $w_k^{(\mathrm{ph})}$ is linearly interpolated, and $F_{k'k}^{-1}$ is interpolated with Eqs. (3.15)–(3.15). For the 3D table $Y_{k'k}^{-1}$ a trilinear scheme, in analogy with Eqs. (3.15)–(3.15), is used.

Both scattering mechanisms are implemented in the new `custom_scatter2D` integrator in HOOMD-Blue. The tables for the ripplon and phonon scattering are prepared using `ripplon_scattering_module.py` and `phonon_scattering_module.py` modules in the code base.

3.3.4 The simulation unit cell

In all of our simulations, we use a rectangular 2D unit cell with the aspect ratio of $\sqrt{3}/2$ to 1. The size of the cell along x, denoted by L_x, depends on the number of electrons. We keep the electron density $n_s = 2/\sqrt{3} \times 10^8 \approx 1.15 \times 10^8$ cm^{-2} constant in all simulations. This means that the lattice constant of a triangular lattice with this density is $a = 1$ μm. The system consists of $N = 1024$ electrons in all mobility calculations and $N = 1600$ electrons in all diffusion calculations, unless stated otherwise.

We impose periodic boundary conditions in both dimensions. Therefore, an electron is returned into the unit cell on the opposite side if it crosses the boundary. The periodic boundary conditions also dictate how we deal with the long-range Coulomb forces, see below.

3.3.5 Temperature definition

Strictly speaking, the temperature is defined only for a system in equilibrium. In this case it can be computed as

$$T(t) = \frac{m_e}{2k_B} \sum_{i=1}^{N} v_i^2(t). \tag{3.28}$$

However, we also want to have an analog of temperature for a system in the presence of an external drive field, which establishes the stationary drift velocity $\boldsymbol{v}_d$. In this case, we define the temperature in the frame moving with the velocity $\boldsymbol{v}_d$:

$$T(t) = \frac{m_e}{2k_B} \sum_{i=1}^{N} (\boldsymbol{v}_i(t) - \boldsymbol{v}_d)^2, \tag{3.29}$$

where the drift velocity is found as

$$\boldsymbol{v}_d = \frac{1}{NN_t} \sum_{i=1}^{N} \sum_{s=1}^{N_t} \boldsymbol{v}_i(s\Delta t). \tag{3.30}$$

Here s is the index enumerating time steps and N_t is the total number of time steps in the simulation. This definition makes sense since we use small driving fields, and in the strongly correlated system with a fast inter-electron energy exchange the velocity distribution remains close to the Maxwell-Boltzmann distribution but centered around $\boldsymbol{v} = \boldsymbol{v}_d$ instead of $\boldsymbol{v} = 0$. In the finite system with N particles, the temperature fluctuates with the characteristic fluctuation amplitude $\Delta T \propto T/\sqrt{N}$ (see below for more details). For this reason, we average the temperature over the simulation time:

$$T = \frac{1}{N_t} \sum_{s=1}^{N_t} T(s\Delta t). \tag{3.31}$$

The process $T(t)$ has a finite correlation time. Therefore, when we calculate the standard error of the mean, we must take the autocorrelation into account. The procedure for estimating the standard error of the mean for a random processes with a finite correlation time is described in Appendix A.10.

3.4 Dynamical properties of a spatially uniform electron system

3.4.1 Thermalization in a Wigner solid and a strongly correlated electron liquid

We study thermalization in the correlated electron system by following its time evolution from a state far from thermal equilibrium. A natural measure of the thermalization is the distribution over velocities: if the system is thermalized, this distribution should be of the Maxwell-Boltzmann form, in the considered classical formulation. The time it takes to approach this distribution is the characteristic thermalization time. The results of this section refer to the case where the electron scattering by excitations in helium is disregarded. Therefore the considered thermalization is the intrinsic property of the electron system itself.

First, we choose the initial state as a triangular lattice with all electrons but four having zero velocities. The four moving electrons have momenta, which are equal in the absolute value; they point in the opposite directions along two orthogonal axes, so that the total momentum is zero. The absolute values of the momenta are large. Therefore, if they are expanded in the normal modes of the finite-size crystal, the mode amplitudes are large and the dynamics of the crystal is substantially nonlinear. It is this nonlinearity that ultimately leads to the thermalization.

The evolution of the kinetic energy averaged over particles is shown in Fig. 3.13 (a). After a short transient, we found that the mean (over the electrons) kinetic energy reaches a steady value and fluctuates about it. The initial transition period is only a few oscillations with the characteristic frequency ω_p equal to the short-wavelength plasma frequency, Eq. (3.37). After the transition period the distribution of the electrons over the kinetic energy is close to the Boltzmann distribution (see Fig. 3.13 (b)). The kinetic energies of individual electrons are oscillating in time, in agreement with the picture that the electron motion is largely thermal fluctuations about quasiequilibrium positions in the correlated system.

The mean kinetic energy, or equivalently, the temperature are fluctuating in time. These fluctuations are seen in Fig. 3.13 (a). They result from the standing wave modes always present in the system. Fluctuations of the kinetic energy in a system of N electrons are easy to describe if the

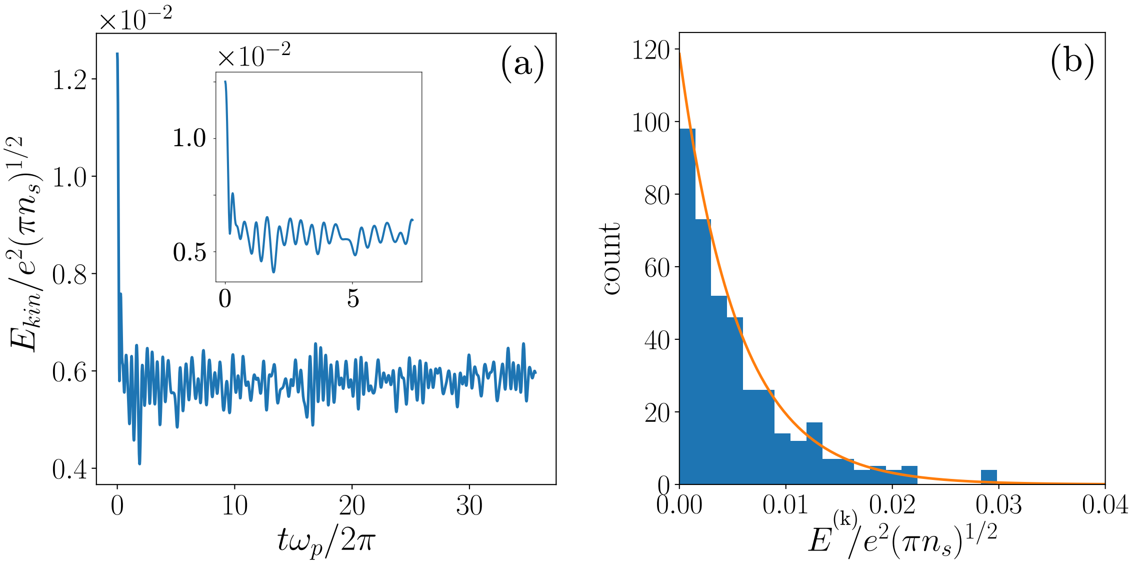

Figure 3.13 **(a)** Averaged over the particles kinetic energy $E_{kin} = (2N)^{-1}\sum_i m_e v_i^2$ of electrons as a function of time. At $t = 0$, the system of $N = 400$ electrons is prepared in a triangular lattice with zero velocities for all but four electrons. The velocities of the four moving electrons are set to a large magnitude of 3.4×10^6 cm/s and four different directions along the coordinate axes, so that the total momentum vanishes. The system then evolves with no scattering by the excitations in helium, remaining a crystal (with defects). The energy is measured in the units of the average Coulomb energy $e^2(\pi n_s)^{1/2}$. Time t is measured in units of $2\pi/\omega_p$. The inset shows the initial part of the evolution, with the same units on both axes. **(b)** The histogram of the distribution of the electrons over their kinetic energy $E^{(k)}$ after 800 time steps ($t\omega_p/2\pi \approx 15$). The instantaneous averaged over the particles kinetic energy at this point is $E_{kin}/k_B = 0.175$ K (for the mean inter-electron distance $a = 1\,\mu$m). The solid line depicts the Boltzmann distribution at this temperature (properly scaled to compare with the histogram).

electrons form a crystal and the electron motion can be represented as small-amplitude vibrations about the equilibrium positions. One can write the kinetic energy E_{kin} in terms of the creation and annihilation operators $b^\dagger_{\boldsymbol{k}\alpha}, b_{\boldsymbol{k}\alpha}$ of the normal modes (here, $\boldsymbol{k}$ is the wave vector and $\alpha = 1,2$ is the mode polarization)

$$E_{kin} = \frac{\hbar}{4N}\sum_{\boldsymbol{k}\alpha}\omega_{\boldsymbol{k}\alpha}(b^\dagger_{\boldsymbol{k}\alpha} - b_{-\boldsymbol{k}\alpha})(b^\dagger_{-\boldsymbol{k}\alpha} - b_{\boldsymbol{k}\alpha}). \tag{3.32}$$

From this expression, in the classical limit

$$\big\langle [E_{kin}(t) - \langle E_{kin}\rangle][E_{kin}(0) - \langle E_{kin}\rangle]\big\rangle = \frac{(k_BT)^2}{32\pi^2 N n_s}\sum_\alpha \int d\boldsymbol{k}\cos 2\omega_{\boldsymbol{k}\alpha}t, \tag{3.33}$$

where $\omega_{\boldsymbol{k}\alpha}$ are the mode frequencies. This expression shows that the limiting fluctuation frequency in the harmonic approximation is $\sim 2\omega_p$.

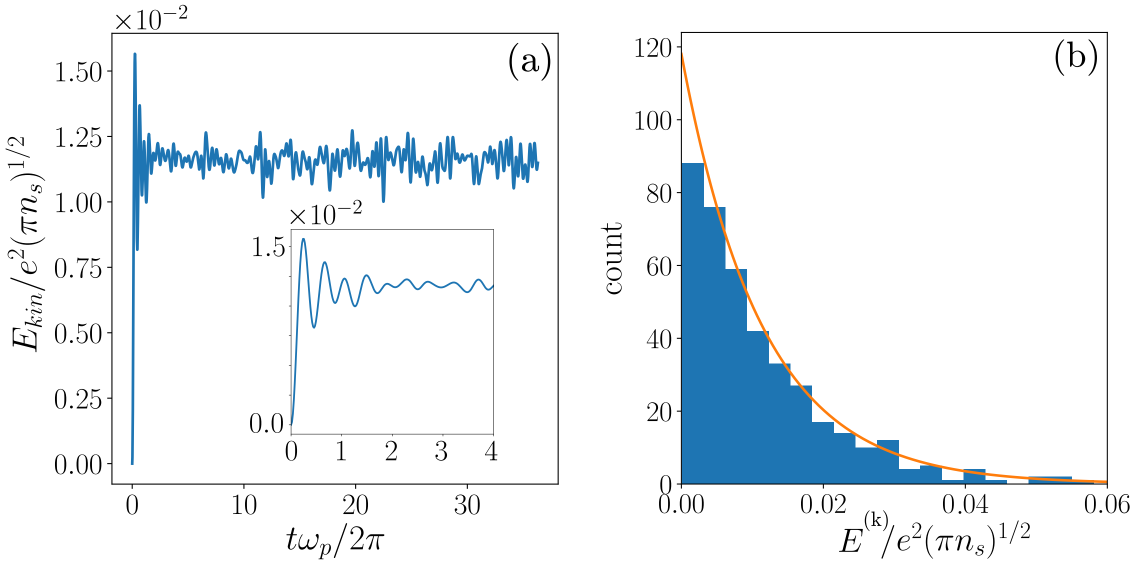

Figure 3.14 **(a)** Averaged over the particles kinetic energy $E_{kin} = (2N)^{-1}\sum_i m_e v_i^2$ of electrons as a function of time. At $t = 0$, the system of $N = 400$ electrons is prepared in a disordered liquid-like configuration with zero velocities. The system then evolves with no scattering by helium excitations and remains a liquid. The energy is measured in units of the average Coulomb energy $e^2(\pi n_s)^{1/2}$. Time t is measured in the units of $2\pi/\omega_p$. The inset shows the initial part of the plot, with the same units on both axes. **(b)** The histogram of the distribution of the electrons over their kinetic energy $E^{(k)}$ after 600 time steps ($t\omega_p/2\pi \approx 11$). The instantaneous averaged over the particles kinetic energy at this point is $E_{kin}/k_B = 0.362$ K (for the mean interelectron distance $a = 1\,\mu$m). The solid line depicts the Boltzmann distribution at this temperature (properly scaled to compare with the histogram).

The power spectrum of the fluctuations for the crystal is shown in Fig. 3.15 (a). The power spectrum is calculated as

$$Q_\omega = \frac{1}{t_s}\left|\int_0^{t_s} dt'\, Q(t') e^{-i\omega t'}\right|^2, \qquad (3.34)$$

where t_s is the simulation time, and $Q(t') = (2N)^{-1}\sum_i m v_i^2(t') - \langle E_{kin}\rangle$ is the averaged over the particles instantaneous value of the fluctuations of the kinetic energy at time t'. The actual maximum frequency is slightly different from $2\omega_p$ calculated using Eq. (3.37), because this value of the limiting frequency is an approximation. More importantly, the overall spectrum differs from the simple expression (3.33 in the low-frequency part. This is likely related to the presence of defects generated by the initial "kick"; such defects should lead to higher spectral density of low-frequency fluctuations. Overall, the results show a dramatic difference from the Fermi-Pasta-Ulam

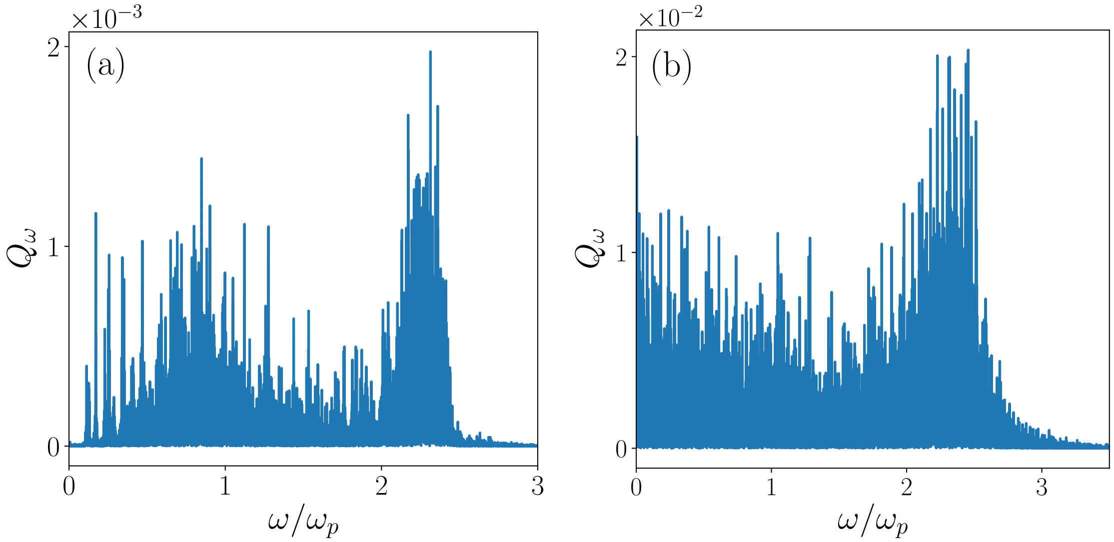

Figure 3.15 Power spectrum Q_ω of the fluctuations of the kinetic energy per particle E_{kin} (arbitrary units). **(a)** corresponds to the crystal, Fig. 3.13. **(b)** corresponds to the liquid, Fig. 3.14. Evolution of E_{kin} over a longer period of time was taken to produce the Fourier transforms. The constant component ($\omega = 0$) is removed in both plots.

observation for a weakly nonlinear chain of oscillators. In part, this is a consequence of the strong anahramonicity, but also of the long-range coupling and higher dimensionalty.

In another experiment, we study thermalization of a strongly correlated liquid. We prepare the system in a disordered state with zero velocities and then let it evolve. The total energy of the system is equal to the potential energy in the initial state. The energy is large enough for the system to remain in the liquid phase during the subsequent dynamics. The dynamics of the mean kinetic energy is shown in Fig. 3.14 (a). Fig. 3.14 (b) displays the established distribution of kinetic energies of individual electrons after the initial transition period. Qualitatively, the behavior is similar to that in the case of a crystal discussed above. The thermalization time and the characteristic frequencies of the fluctuations are approximately the same as in the case of a crystal. The Fourier spectrum of the kinetic energy fluctuations for the liquid is shown in Fig. 3.15 (b). The spectrum is close to the uniform spectrum from $\omega = 0$ to $\omega \approx 2\omega_p$, which is characteristic of chaotic systems and is a natural consequence of diffusion in the system.

These results demonstrate that the electron system does thermalize in both crystal and liquid phases. The electrons exchange momenta on the time scale of ω_p^{-1}, which determines the order of magnitude of the thermalization time.

3.4.2 Diffusion in a spatially uniform electron system

An important characteristic of a many-particle system is diffusion. It describes the mean squared particle displacement as a function of time. The diffusion constant D_x in one dimension is conventionally defined as:

$$2D_x t = \left\langle (x(t) - x(0))^2 \right\rangle, \tag{3.35}$$

where $x(t)$ is a particle's coordinate, and the average is the ensemble average over realizations of the particle's trajectories. In an ideal electron gas, the diffusion is determined by scattering of electrons off scattering centers, such as impurities, or quantized excitations of fields in the substrate, such as phonons or ripplons. When the system is a strongly correlated liquid, the electron-electron interaction limits the diffusion, and scattering by defects plays a less important role. In this case the diffusion is also referred to as self-diffusion. It quantifies the rate and magnitude of displacement of the particles with respect to each other. Therefore, vanishing of self-diffusion is a useful indicator of a freezing transition.

The correlation length in the liquid is increasing with decreasing temperature. When correlations become strong, one cannot adequately describe the dynamics of the system in terms of the motion of individual particles. In this regime, diffusion is better characterized by the motion of structural defects, in the first place, dislocations. We believe the activated character of this motion causes the diffusion constant to sharply depend on temperature. Even for a short correlation length, diffusion in liquids is thermally activated for low temperatures; it is usually associated with diffusion of individual particles and with creating a vacancy into which the particle can "jump" by overcoming a relevant barrier. However, in our case, where the correlation length is much larger than the interparticle distance, we believe the activation dependence is related primarily to diffusion of topological defects. The other factor that contributes to the temperature dependence of the diffusion coefficient is that the density of defects, in particular, of unbound dislocations, is strongly temperature dependent.

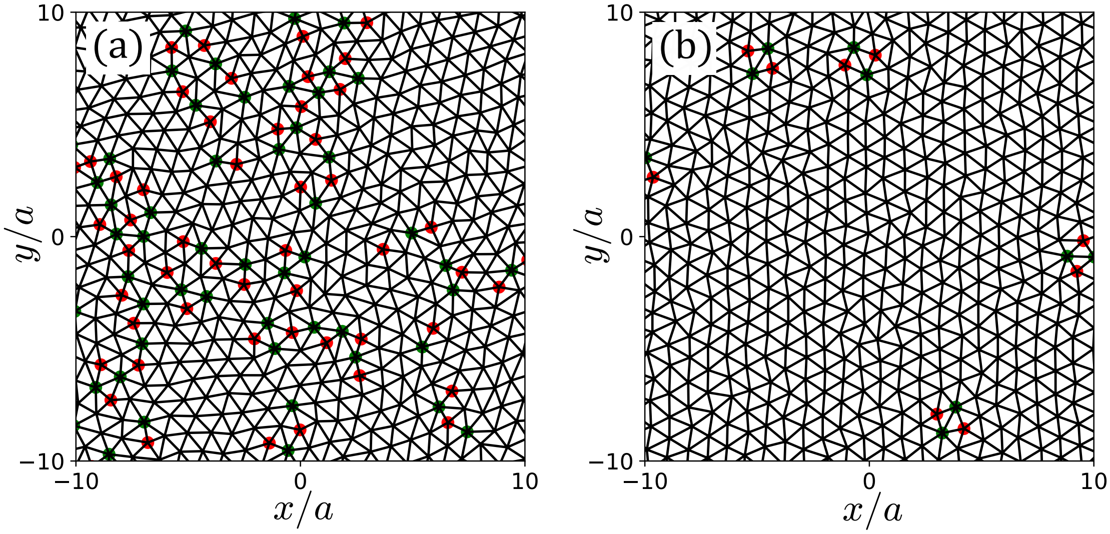

Figure 3.16 Delaunay triangulation of the electron positions for a portion of the system with $N = 1600$ electrons. Electrons are represented by the vertices. The red vertices are electrons with five nearest neighbors, while the green vertices are electrons with seven nearest neighbors. Pairs of red and green vertices represent dislocations. **(a)** Liquid phase with $\Gamma = 133$ close to the freezing transition, the diffusion constant $D_\perp = D_\| \approx 0.6$ cm^2/s. There are unbound dislocations, pairs of bound dislocations, and domain walls. **(b)** Solid phase with $\Gamma = 140$ and $D_\perp = D_\| = 0$. Only bound pairs of dislocations are present in the solid. The two snapshots refer to the two points from Fig. 3.17 (b) for the corresponding values of Γ.

According to the Berezinskii-Kosterlitz-Thouless picture, freezing of a liquid into a crystal results from dislocation binding into pairs. When this happens, the diffusion should sharply decrease, because diffusion would now require moving a pair of dislocations, which is virtually impossible. Therefore we expect that, by measuring the diffusion coefficient, one can find the crystallization transition as a point where the diffusion coefficient becomes equal to zero. As an illustration of this mechanism of the phase transition, we show two snapshots of of the electron system in Fig. 3.16. The two snapshots represent the liquid and the solid phases very close to the phase transition. The liquid phase contains ordered areas as well as unbound and bound dislocations. The solid phase is mostly ordered and only contains a few bound pairs of dislocations which do not contribute to diffusion. Bound dislocations in a crystal can spontaneously emerge, but then they annihilate; they do not unbind in the crystalline phase.

We measured the diffusion constants as a function of Γ in our simulations. The value of Γ was determined from the data using Eq. (3.28) above. For each value of Γ, which sets the temperature, the system was prepared in the triangular crystal lattice at a given temperature. Then the system is equilibrated for 10^6 time steps before collecting data. With scattering, the thermal bath created by phonons sets the temperature. Without scattering, we prepare the system with nonzero initial velocities and measure the resulting temperature after the equilibration. The diffusion coefficient was calculated in the following way. We simulate a trajectory by making N_t steps of duration Δt, so that the overall length of the trajectory is $2t = N_t\Delta t$. We then look at the sections of the trajectory of length t. These sections are shifted in time by $d_s\Delta t$, with sufficiently large d_s, so that the correlation between the motion in different sections of the trajectory separated by a multiple of $d_s\Delta t$ is small. We then sum up the squared displacement in different sections and also do the averaging over all particles. The resulting expression for one-dimensional diffusion along the x-axis is

$$D_x = \frac{1}{2tN}\frac{1}{(1+N_t/2d_s)}\sum_{s=0}^{N_t/2d_s}\sum_i [x_i(sd_s\Delta t + t) - x_i(sd_s\Delta t)]^2 \tag{3.36}$$

Here, s enumerates different sections of the trajectory: a section starts at $sd_s\Delta t$. In our simulations, d_s is typically 10^3 or 10^4. If a particle crosses the simulation cell boundary, its trajectory becomes discontinuous due to the periodic boundary condition. To correct for this non-physical behavior when calculating diffusion from the data, we reconstruct the continuous particle trajectories in such a way that a particle is allowed to continuously move into neighboring virtual cells. We found that the diffusion constant obtained this way is independent of time t, which indicates the applicability of our method; the method of calculating the diffusion constant described by Eq. (3.36) is conventionally applied in molecular dynamics simulations [193].

A natural scale for the diffusion constant in our system can be estimated by thinking that the electron displacement comes from fluctuations about quasi-equilibrium positions of the electron in the field of other electrons. The average squared displacement is $\sim 1/\Gamma n_s$. The characteristic time of vibrations in the classical system is the short-wavelength plasma frequency

$$\omega_p = (2\pi e^2 n_s^{3/2}/m_e)^{1/2}. \tag{3.37}$$

Therefore we expect that the scale of D far from the transition will be $\omega_p/\Gamma n_s$. This agrees with the simulations, to the order of magnitude. This is essentially the two-dimensional analog of the

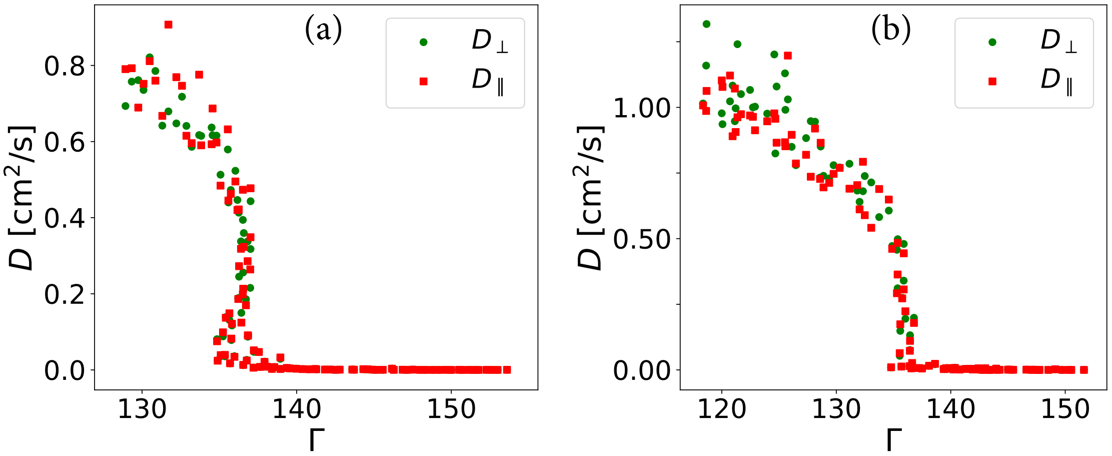

Figure 3.17 Diffusion constants as a function of Γ with: **(a)** no scattering, **(b)** elastic and inelastic scattering. For each point Γ, the system is prepared as a *triangular lattice* with the same density but with different random velocities. Then the system is equilibrated for 10^6 time steps before collecting data. The final temperature, and thus the value of Γ, are measured after the equilibration period. $N = 1600$ particles were used in both simulations. We plot both D_x and D_y to facilitate comparison with the results for the non-zero external periodic potential.

De Gennes scaling of the diffusion coefficient in atomic liquids [194] and of the Frenkel picture of atomic motion in liquids [195].

For convenience, we define $D_\perp \equiv D_x$ and $D_\parallel \equiv D_y$, which will serve as diffusion constants across and along the periodic potential troughs. We maintain this notation even when there is no periodic potential to enable direct comparison of all diffusion calculations. $D_\perp$ and $D_\parallel$ coincide in a uniform system, but they may be different in a periodic potential, when the system is anisotropic.

The results of the diffusion measurement in the absence of the scattering by ripplons or phonons are shown in Fig. 3.17 (a), whereas Fig. 3.17 (b) shows the results in the presence of the scattering. In both cases, we find a sharp change of D around $\Gamma = 135$–140. It indicates melting of the crystal. This value of Γ is in good agreement with the experiments [1, 143]. However, it is slightly higher than the value $\Gamma = 130$ found in most of the previous simulations [144, 145, 196, 146]. The difference may be related to the difference in the size of the simulated systems. The results in Ref. [144] and most of the results in Ref. [196] refer to the system of 100 electrons. The results in Ref. [146] were obtained for 256 electrons. We find (see Fig. 3.18) that, if we simulate a system with $N = 100$ and $N = 252$, the transition point is $\Gamma \approx 130$, in agreement with [144, 146]. Our

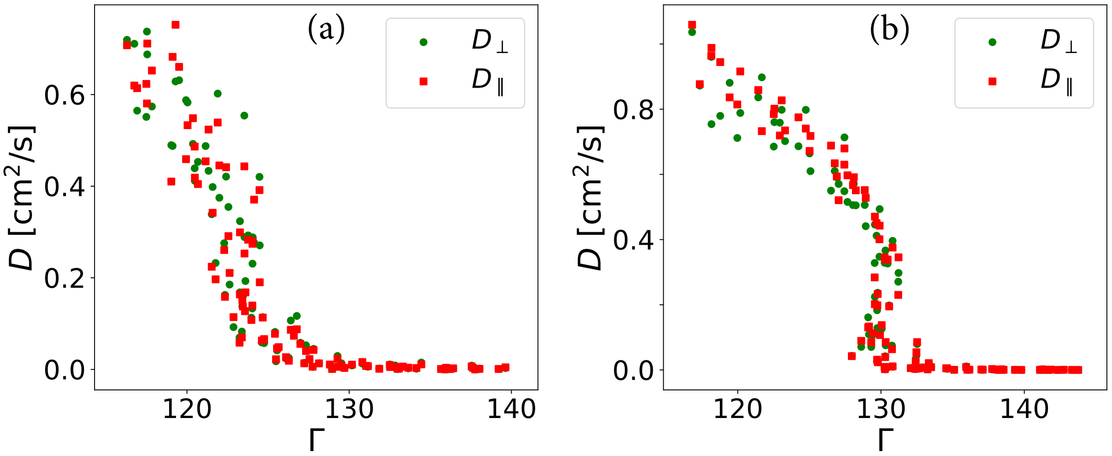

Figure 3.18 Diffusion constant as a function of Γ for the number of particles **(a)** $N = 100$, **(b)** $N = 252$. For each point Γ, the system is prepared as a *triangular lattice* at the temperature determined by Γ and then equilibrated for 10^6 time steps before collecting data. The final temperature is measured after the equilibration period. The transition point is slightly below $\Gamma = 130$ for $N = 100$ and at $\Gamma \approx 130$ for $N = 252$. The results are obtained without scattering.

result for $N = 1600$ is in agreement with a recent Monte Carlo simulation [197] with $N = 8100$ particles, where the melting transition was observed at $\Gamma = 138$–140.

Without scattering, as in Fig. 3.17 (a), the curve $D(\Gamma)$ has an unusual shape close to the freezing point. When it approaches zero, it passes through the point with the vertical slope, as if there were a bistability in a small range of temperatures close to freezing. We believe this to be a computational artefact due to the finite system size and the finite simulation time. We find that close to the freezing point, the temperature has large fluctuations on the time scale comparable with the simulation time. Note that the total energy is conserved in this simulation. Therefore, along with the temperature, the potential energy has similar fluctuations on the large time scales. It means that, close to the freezing transition, the structure of the system is changing on the time scale comparable with the simulation time. Therefore, the system spends a significant amount of time in non-equilibrium configurations due to the fluctuations. This is seen also from the power spectrum of the energy fluctuations in Fig. 3.19 (b), which displays a pronounced peak at zero temperature. Therefore, the measured temperature averaged over the simulation time may be lower than the temperature in the true equilibrium state for the same total energy by up to 1 %.

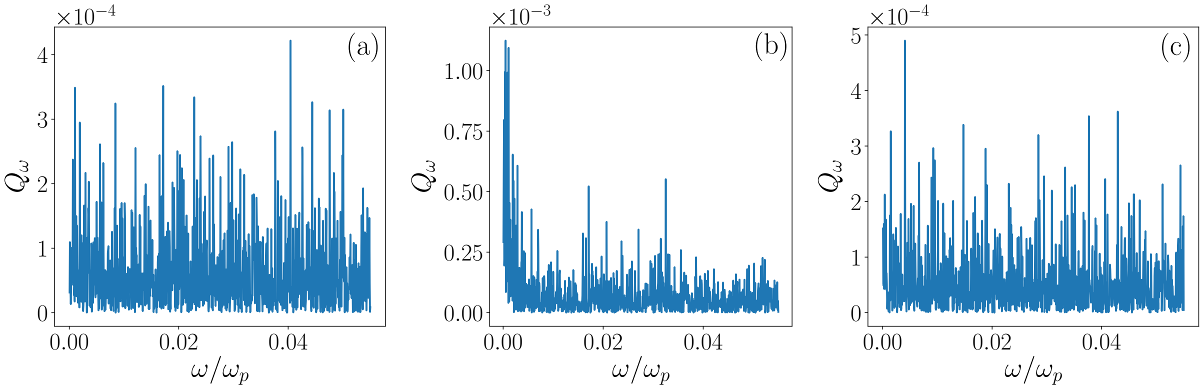

Figure 3.19 Low-frequency part of the power spectrum Q_ω of the temperature fluctuations close to the Wigner crystallization (arbitrary units). Q_ω is calculated using Eq. (3.34). The data correspond to three points in Fig. 3.17 (a). **(a)** Liquid at $\Gamma \approx 130$. **(b)** Liquid in the transition regime at $\Gamma \approx 137$. **(b)** Crystal at $\Gamma \approx 140$. The constant component ($\omega = 0$) is removed.

The long-lived fluctuations of temperature do not occur far from the freezing transition, as seen from the power spectrum in Figs. 3.19 (a), (c) for points above and below the crystallization transition. In a hot liquid, the dynamics is fast and the non-equilibrium states quickly decay. In a crystal, fluctuations of the kinetic and potential energies are not sufficient to bring the system to a long-lived non-equilibrium state, since it would require melting. The described slow fluctuations are more likely to occur in a small system, since temperature fluctuations scale with the system size as $\Delta T \propto T/N$. The boundary conditions can also prevent non-equilibrium configurations from decaying. As Fig. 3.17 (b) shows, electron scattering seems to eliminate this phenomenon. We believe that the scattering quickly destroys non-equilibrium states, as it imposes on the electron system the temperature of the thermal reservoir.

In the previous simulations, there was observed hysteresis in the temperature dependence of the total energy and the diffusion constant [145, 196, 146]. To relate our observations to these results, we carried out simulations where for each value of Γ we started with a liquid at $\Gamma_i = 45$ and then cooled it down to the desired value of Γ. The cooling is provided by the thermal bath of phonons when the inelastic scattering is present. To cool the system to the desired temperature, we simply set the thermal bath temperature to the desired value. The scattering rate is small, therefore the system is cooled down gradually over 7×10^5 time steps. Without scattering, we simulate the

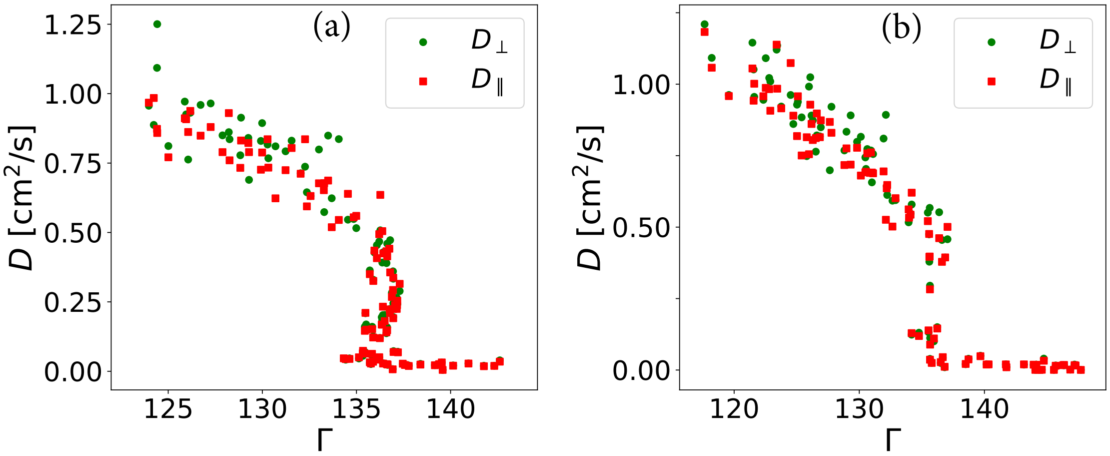

Figure 3.20 Diffusion constants as a function of Γ with: **(a)** no scattering, **(b)** elastic and inelastic scattering. For each point Γ, the system is prepared as a *liquid* at $\Gamma_i = 45$ and then cooled down to the temperature corresponding to Γ, as described in the text. $N = 1600$ particles were used in both simulations.

cooling in the following way: we run the system for consecutive intervals of time. At the end of each interval, for the given positions of the particles, we proportionately scale down their velocities. The duration of the intervals is gradually increased upon approaching the final temperature. On total we use 20 intervals and approximately 7×10^5 steps. Then we let the system evolve on its own for at least 10^6 time steps before we (i) measure the distribution over the velocities and thus determine the value of Γ and (ii) start accumulating data on diffusion. We repeatedly measure the effective Γ, which displays small fluctuations, see below.

By using this procedure, we obtain the Γ-dependence of the diffusion constant shown in Fig. 3.20. It turns out to be nearly the same as that obtained by starting with a crystal lattice for the same Γ. We do not observe hysteresis in the melting-freezing transition. The hysteresis observed in the previous simulations may be related to a shorter simulation time. This time is much longer in the present study. A long time is needed because, close to freezing, the dynamics is determined by diffusion of dislocations, which becomes very slow.

We also studied the effect of scattering by ripplons on the electron diffusion. Where the scattering is weak, as is the case for electrons on the helium surface, so that the scattering rate is small compared to ω_p, we do not expect a strong effect of the scattering on the diffusion. Primarily the diffusion is determined by the electron-electron interaction. This is indeed seen in the simulations, see Figs. 3.17 and 3.20. The result should be contrasted with the results obtained by assuming that the electron motion is overdamped, as it is often done in molecular dynamics simulations of interacting systems [28]. We carried out simulations of diffusion assuming a phenomenological friction force with the friction coefficient comparable to ω_p. In this case the change of the diffusion coefficient due to dissipation was very significant.

3.4.3 Mobility in a uniform system

As another benchmark for our setup, we study the mobility of the electron system without a periodic potential. This characteristic, which is of primary interested for the experiment, has not ever been studied in simulations for electrons on helium, as it requires taking into account the actual mechanism of the electron scattering rather than using a phenomenological overdamped dynamics. We use the conventional definition of the mobility μ

$$v_d = \mu E_d, \tag{3.38}$$

where v_d is the drift velocity induced by the constant uniform in-plane electric field E_d.

In a uniform system without a periodic potential, the mobility is mostly determined by the scattering by ripplons. We expect the mobility in the non-interacting system to follow the expression

$$\mu_{\text{se}} = \frac{e}{2m_e^3(k_BT)^2}\int_0^\infty dp\, p^3 \tau_{\text{se}}(p) e^{-p^2/2m_e k_B T}, \tag{3.39}$$

where

$$\frac{1}{\tau_{\text{se}}(p)} = \frac{\hbar k_B T}{8\pi\alpha m_e r_B^2}\int_0^{2\pi} d\theta\, q^2\phi^2\left(\frac{q r_B}{2}\right)(1-\cos\theta)\Big|_{\hbar q = p\sqrt{2(1-\cos\theta)}}. \tag{3.40}$$

This is a standard result obtain using the Boltzmann equation, see Appendix A.8 for details. In a strongly correlated uniform liquid, the momentum is transferred between electrons much faster than the time between scattering events. Therefore, the expression for the mobility is different from that in the non-interacting limit (see Ref. [3] and Appendix A.8.2):

$$\mu_{\text{me}} = \frac{e\tau_{\text{me}}}{m_e}, \tag{3.41}$$

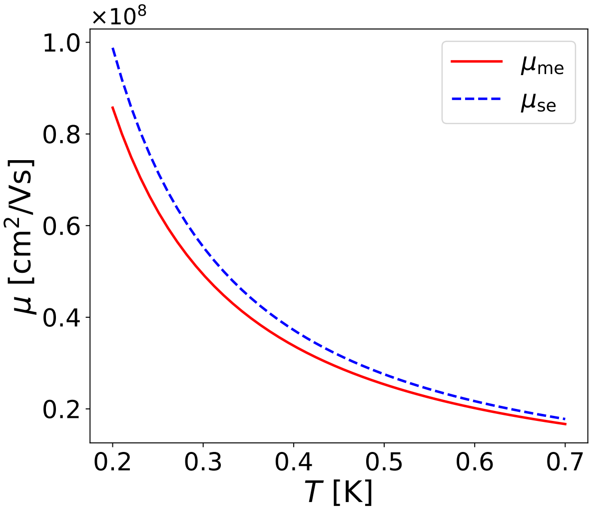

Figure 3.21 Theoretical calculation for the single-electron mobility $\mu_{\rm se}$ and the electron liquid mobility $\mu_{\rm se}$ vs temperature. The electron density $n_s = 2/\sqrt{3} \times 10^8$ cm^{-2} is assumed in the calculation for the strongly correlated system. The freezing transition is at $T \approx 0.23$ K. Above $T \approx 0.7$ K, the mobility is primarily limited by the scattering by the helium atoms in the vapor phase.

with

$$\tau_{\rm me}^{-1} = \frac{\hbar^4}{16 m_e^2 r_B^2 \alpha \sqrt{2\pi m_e k_B T}} \int_0^\infty dq\, q^4 \phi^2\left(\frac{q r_B}{2}\right) e^{-\frac{\hbar^2 q^2}{8 m_e k_B T}}. \tag{3.42}$$

The theoretical results for the mobility in the two cases are compared in Fig. 3.21. It turns out that the two expressions lead to very close numerical values. The difference is decreasing with the increasing temperature.

In the simulations, we determine the mobility in the following way. The procedure described below is also applied in the presence of an external periodic potential. In the first stage, the system is prepared in a liquid state with $\Gamma = 45$. Then the system is gradually cooled down for 2×10^4 steps without a driving field to bring it to the desired temperature T. If there is a periodic potential, the cooling is performed in the periodic potential. The cooling is mediated by the coupling to the thermal bath of phonons through the inelastic scattering. The phonon thermal bath has the temperature T. During the cooling time, the inelastic scattering rate is accelerated by a factor of 50 to reduce the computation time. The purpose of the cooling stage is to allow the system to adapt to its equilibrium structure in the presence of the external potential.

During the second stage, the inelastic scattering rate is returned to its regular value. The driving field $\boldsymbol{E}_d$ is turned on, and the system is allowed to establish the steady state over 10^6 time steps. In the steady state, the temperature may be different from T due to heating by the drive. We measure the temperature in the steady state using Eq. (3.29).

The third stage is the data collection in the steady state. For this stage, we run the simulation for 10^6 time steps, with data recorded every 10^3 or 10^4 time steps. It is indicated in the text where we use a different simulation time. The drift velocity is then computed as a simple average over all particles and all data snapshots:

$$\boldsymbol{v}_d = \frac{d_s}{NN_t} \sum_{i,s} \boldsymbol{v}_i(sd_s\Delta t), \tag{3.43}$$

where s enumerates the data snapshots, and d_s is the number of steps between the snapshots. The standard error of this estimate must take into account the nonzero autocorrelation of the velocity, $\langle(\boldsymbol{v}_i(t)-\boldsymbol{v}_d)(\boldsymbol{v}_i(t')-\boldsymbol{v}_d)\rangle \neq 0$, in a finite range of $t-t'$. The procedure for calculating the standard error is described in Appendix A.10, Eq. (129).

The obtained response, i.e., v_d vs. E_d for the non-interacting electron gas in the range of $\boldsymbol{E}_d$ from 0 to 0.7 mV/cm is shown in Fig. 3.22. The simulation result slightly deviates from the prediction of Eq. (3.39). There are two reasons for the deviation. First, the transport is not in the linear regime in the simulation, as can be seen from the small curvature of v_d vs E_d. The nonlinearity is caused by the substantial heating of the electrons from $T = 0.354$ K to $T = 0.4$ K. The difference of the simulations from Eq. (3.39) on the small-drive side is a consequence of the fact that Eq. (3.39) does not take into account the inelastic scattering that can potentially reduce the mobility by up to 15 %.

To test this hypothesis, we perform two additional simulations. First, we reduce the width of the range of E_d from 0.6 mV/cm to 0.06 mV/cm (we remind that the electron density is fixed in our simulation; therefore the field is measured in dimensional units). The result is shown in Fig. 3.23 (a). We can assume that the nonlinearity is negligible in this case. Nevertheless, the deviation from the theoretical line is not entirely eliminated. We continue by repeating the simulation with the 10 times smaller inelastic scattering rate. It makes the inelastic scattering rate two orders of magnitude smaller than the elastic scattering rate. The result is shown in Fig. 3.23 (b). Now

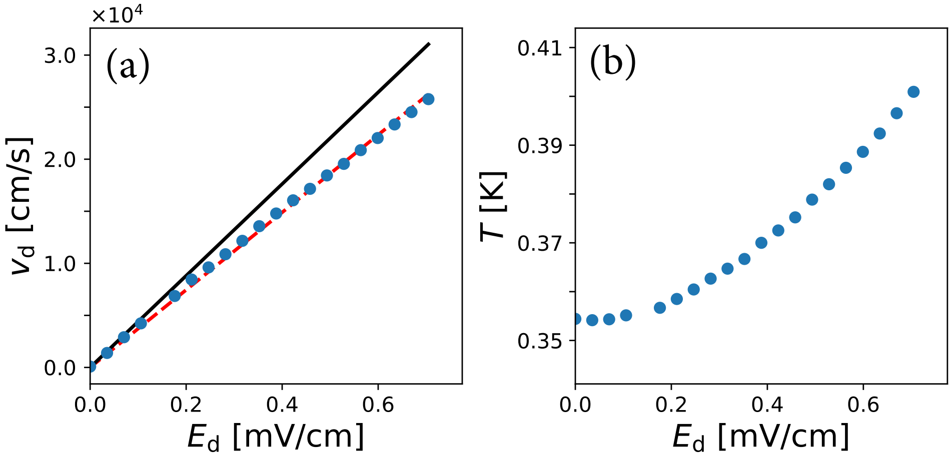

Figure 3.22 **(a)** Drift velocity v_d vs drive field E_d and **(b)** temperature vs drive field for a uniform system without electron-electron interaction. The filled circles are the simulation data, the dashed red line is the least-squares fit, and the solid black line is the prediction by Eqs. (3.39)–(3.40). The temperature T is computed using Eqs. (3.29)–(3.31). Error bars are not shown since they are smaller than the marker size.

the data points are very close to the theoretical line, as expected. This result confirms that our simulation correctly describes the response of the system to an external drive.

The nonlinearity observed already for $E_d \sim 0.7$ mV/cm suggests that we should operate at much smaller driving fields. However, this is computationally too expensive for simulations with the electron-electron interaction. Due to the low scattering rates, the drift velocity v_d fluctuates significantly on large time scales. Therefore, to obtain acceptable relative accuracy for v_d one needs either long simulation times or large E_d. To reduce the simulation time, we perform all transport simulations with $E_d \sim 0.7$ mV/cm and keep in mind that the transport in weakly nonlinear. The weak nonlinearity will not alter the phenomena described below in any significant way.

We also study the response of the uniform electron system to the drive with the electron-electron interaction taken into account. The result of the simulation of a strongly correlated liquid at $\Gamma = 90$ is shown in Fig. 3.24. The theoretical line in this case is calculated using Eqs. (3.41)–(3.42). As with the non-interacting system, the response curve deviates from the theoretical prediction. The reasons for the deviation are also the weak nonlinearity of the response and the inelastic scattering, which are not taken into account in Eqs. (3.41)–(3.42). Overall, this result confirms that

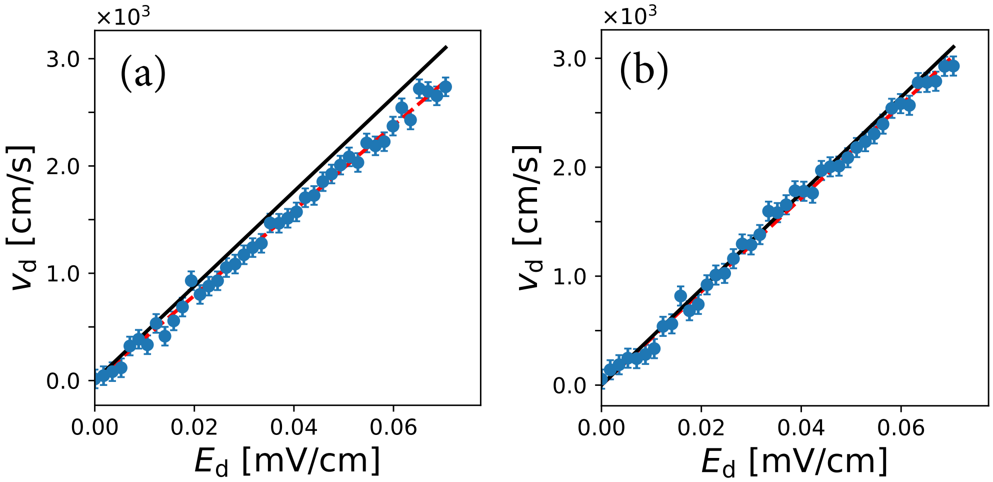

Figure 3.23 Drift velocity v_d vs drive field E_d for $E_d < 0.07$ mV/cm. **(a)** corresponds to the regular rate of inelastic scattering ($\sim 10^6\ \mathrm{s}^{-1}$). **(b)** corresponds to the rate of inelastic scattering reduced by a factor of 10 (to $\sim 10^5\ \mathrm{s}^{-1}$). The filled circles are the simulation data, the dashed red line is the least-squares fit by a straight line. The solid black line is the prediction by Eqs. (3.39)–(3.40). The error bars are one standard error. These simulations used 1.4×10^8 time steps and Δt was increased to $\Delta t = 2.57 \times 10^{-10}$ s.

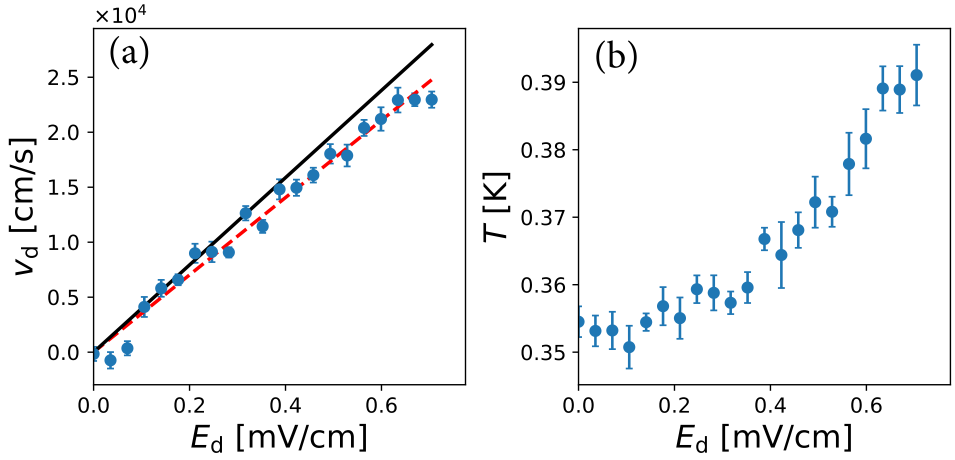

Figure 3.24 **(a)** The drift velocity v_d vs the drive field E_d and **(b)** the temperature T vs the drive field E_d for a uniform strongly correlated electron liquid initially at $\Gamma = 90$. The filled circles are the simulation data, the red dashed line is the least-squares fit, and the black solid line is the prediction by Eqs. (3.41)–(3.42). The effective temperature T is computed using Eqs. (3.29)–(3.31). The error bars correspond to one standard error.

our simulation procedure correctly describes mobility for non-interacting and interacting electrons on helium close to the linear regime. We note that our simulation is unable to capture the correct nonlinear transport behavior for a Wigner crystal, when the Bragg-Cherenkov scattering limits the mobility. However, the simulation should give a correct estimate for the linear mobility of a Wigner crystal corresponding to very small drive fields.

3.5 Strongly correlated electron system in a one-dimensional periodic potential

The central part of the study of the electron dynamics refers to the analysis of the effect of a periodic potential. We study this effect by calculating diffusion and mobility. We use diffusion as an important characteristic of the state of the system in the periodic potential, whereas the mobility is the parameter directly accessible to the experiment. We consider the simplest type of the periodicity, where the potential is one-dimensional, and we take it in the simple sinusoidal form

$$V_{\text{ext}}(\boldsymbol{r}) = -A\cos(Kx), \tag{3.44}$$

where A is the potential amplitude, K is the reciprocal lattice vector of the potential, and the origin is at the center of the cell. For convenience, and keeping in mind that our dimensional electron density is fixed, we measure A in kelvins, implying the value A/k_B. The minus sign is introduced for convenience, so that no potential minimum lies at the cell boundary. Because of the periodic boundary conditions, only $K = 2\pi n/L_x$ with integer n can be simulated this way.

In the periodic potential (3.44), the system becomes anisotropic. We calculate the diffusion coefficients and the mobility both across and along the periodic potential troughs. As discussed above, these quantities are not simply related in the correlated system. We will use the notations $D_\perp \equiv D_x$, $D_{||} \equiv D_y$ for the diffusion across and along the periodic potential troughs, and $\mu_\perp \equiv \mu_x$, $\mu_{||} \equiv \mu_y$ for the mobility across and along the periodic potential troughs.

Of particular interest are the effects of commensurability of the potential and the electron system. For a Wigner solid, we define the commensurability parameter p as the ratio $p = K/G$ of the smallest reciprocal lattice vector K of the potential to the smallest reciprocal lattice vector

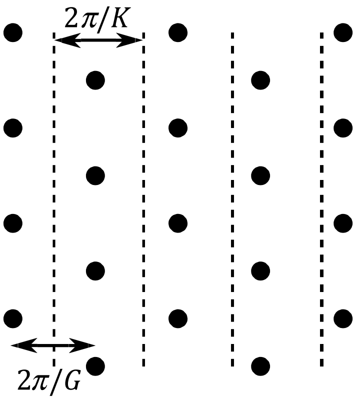

Figure 3.25 Triangular lattice with the distance between the vertical rows $\sqrt{3}a/2 = 2\pi/G$. The dashed lines display the maxima of the periodic potential, with the period $2\pi/K$. The commensurability parameter is defined as $p = K/G$.

$G = 4\pi/\sqrt{3}a$ of the triangular lattice (see Fig. 3.25). Here $a = (2/\sqrt{3}n_s)^{1/2}$ is the crystal lattice constant. We say that the system is commensurate if p is integer and is incommensurate otherwise; for $p = 1$ the period of the potential is equal to the minimal distance between the electron rows in the lattice. We note that, for a one-dimensional potential, there is another option of commensurability, where the lattice is rotated by $\pi/2$, so that in the fully commensurate configuration the period of the potential is $a/2$.

To a large extent, we focus on the properties of a strongly correlated liquid. For a liquid, we define p in the same way as for a crystal but using the reciprocal lattice vector G of the crystal that *would* exist at a given electron density n_s. In this case, the lattice constant a is also calculated as $a = (2/\sqrt{3}n_s)^{1/2}$.

The effect of the modulation on the mobility $\mu_{||}$ along the modulation troughs is most pronounced if the modulation changes the state of the electron system between the liquid and the ordered phase. We will briefly describe the ordering in the periodic potential, but this is not of primary interest to us. We will concentrate on the results for the transverse mobility $\mu_\perp$, where the effect of the periodic potential is often strong even where it is not accompanied by a phase transition.

3.5.1 Single-electron approximation

Before we present the results for a strongly correlated system in a periodic potential, let us briefly discuss the effects of the potential on a non-interacting electron gas. Let us assume that elastic scattering is the main scattering mechanism that determines diffusion. Only electrons with total energy above $2A$ can participate in transport across the modulation troughs. The fraction of such electrons, according to the Boltzmann distribution, is:

$$\frac{1}{C}\int d^2r d^2p e^{-\left(V_{\mathrm{ext}}(\boldsymbol{r})+\frac{p^2}{2m_e}\right)/k_BT}\theta\left[V_{\mathrm{ext}}(\boldsymbol{r})+\frac{p^2}{2m_e}-2A\right], \tag{3.45}$$

where

$$C=\int d^2r d^2p e^{-\left(V_{\mathrm{ext}}(\boldsymbol{r})+\frac{p^2}{2m_e}\right)/k_BT}, \tag{3.46}$$

and

$$\theta(x)=\begin{cases} 0, \; x\leq 0, \\ 1, \; x>0. \end{cases} \tag{3.47}$$

Both diffusion $D_\perp$ and mobility $\mu_\perp$ across the modulation troughs are roughly proportional to the expression (3.45). It is significantly different from unity when $2A$ is comparable to k_BT. Therefore, the effect of the modulation on transport is going to be appreciable only for $2A \gtrsim k_BT$.

3.5.2 Case $p \ll 1$

We will divide our analysis of the modulation effects into several parameter ranges. First, we consider the case $p \ll 1$, where the system is far from commensurability. In this range, the potential has very little effect on the strongly interacting electron system. Then we consider the case of maximal commensurability $p = 1$ where the effect of the potential is very strong. In the intermediate regime, where $p < 1$ but close to 1, the system is undergoing the commensurate-incommensurate (C-I) transition, and both structural and transport properties are significantly affected by the periodic potential. Finally, we show the results for the case $p > 1$.

We begin our analysis with $p \ll 1$. In Fig. 3.26, we show the results of the diffusion simulation for the electron system in an external potential with $A = 0.5$ K and $p = 0.3$. Interestingly, the

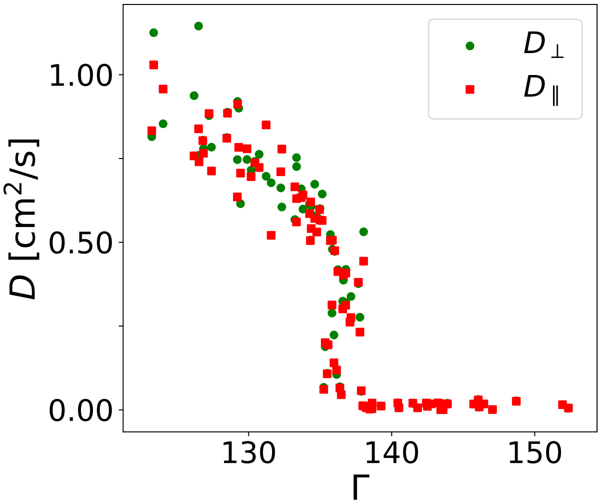

Figure 3.26 Diffusion constants $D_\perp$ and $D_\parallel$ vs Γ in the periodic potential with $A = 0.5$ K and $p = 0.3$. The simulation includes both elastic and inelastic scattering. For every point Γ, the system is prepared in a liquid state with $\Gamma = 45$ and then cooled down, as described in Sec. 3.4.2. electrons. The potential has a negligible effect on the diffusion and on the freezing transition for $p = 0.3$.

diffusion constants and the phase transition point are virtually unaffected by the external potential (cf. Fig. 3.17). For the non-interacting electron gas, the expression (3.45) predicts a significant reduction of $D_\perp$ since $2A > k_BT$. However, the electron-electron interaction in the strongly interacting system effectively averages out the potential for small p. The average Coulomb energy per particle is $e^2(\pi n_s)^{1/2} \approx 31.827$ K, it is much larger than $A = 0.5$ K. Far from the commensurability, the electron-electron interaction is a dominating factor that essentially fully determines system's properties.

To further illustrate the difference between the non-interacting and interacting systems, we plot the transverse mobility for both systems as a function of A for $p = 10/32 = 0.3125$ in Fig. 3.27. For both systems, the temperature is $T = 0.354$ K, which is smaller than the upper limit $A_{\max} = 0.5$ K of the potential amplitude. As predicted by Eq. (3.45), the mobility $\mu_\perp$ in the non-interacting gas is dramatically decreased by the potential when $2A \gtrsim k_BT$. In contrast, the mobility of the liquid is only slightly reduced for the same potential strength.

The system displays the effective averaging of the periodic potential in a broad range of the

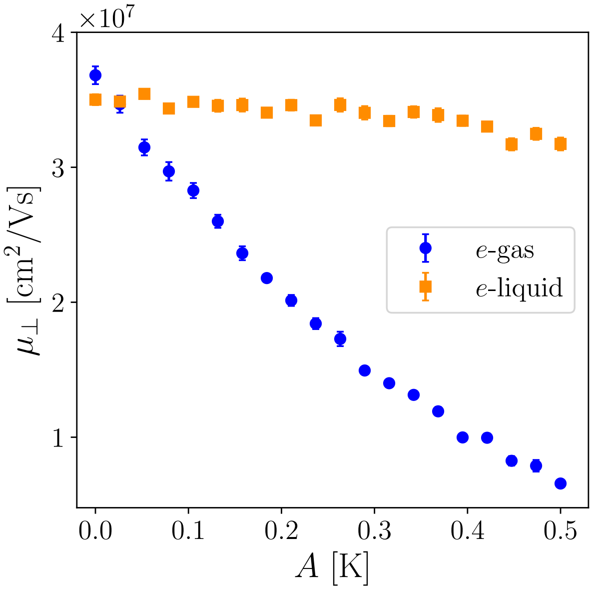

Figure 3.27 The mobility $\mu_\perp$ transverse to the modulation troughs as a function of the periodic potential amplitude A in a non-interacting electron gas and in a strongly correlated electron liquid for $p = 10/32 = 0.3125$. In both cases, $T = 0.354$ K which corresponds to $\Gamma = 90$ for the liquid. Error bars are not shown for clarity since most of them are smaller than the marker size. The potential with $p = 0.3125$ significantly changes the mobility in the gas, but only slightly in the liquid.

ratio of the periods where $p \ll 1$. This range depends on the relation between the modulation strength and the melting temperature. For $A = 0.5$ K, it is $p \lesssim 0.3$.

3.5.3 The case of the maximal commensurability, $p = 1$

The system is most sensitive to the periodic potential when p is integer. It turns out that in this case the transverse mobility and the both diffusion constants $D_\perp$ and $D_{||}$ are significantly affected even by a weak potential with $A \ll k_B T$. The crystallization transition is also very sensitive to the periodic potential amplitude.

We begin by studying diffusion in a relatively strong potential with $A = 0.5$ K and $p = 1$. Here, $2A$ is larger than the typical temperature in the simulation, but much smaller than the average Coulomb energy of the electron-electron interaction $e^2(\pi n_s)^{1/2}$. The diffusion constants calculated as a function of Γ for this case are shown in Fig. 3.28 (a). The first striking feature of the

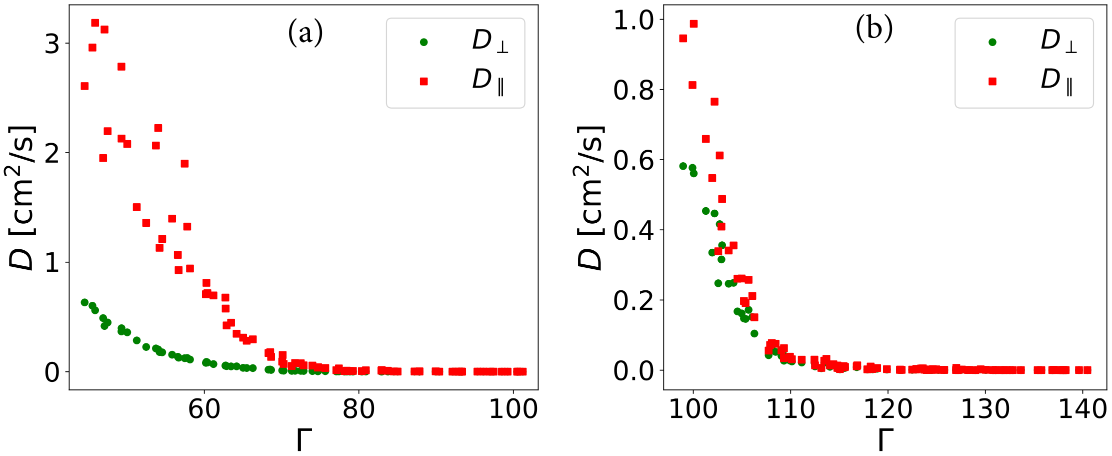

Figure 3.28 Diffusion constants $D_\perp$ and $D_\parallel$ vs Γ in the periodic potential with $p = 1$ and **(a)** $A = 0.5$ K, **(b)** $A = 0.05$ K. The simulations use $N = 1600$ electrons and include both elastic and inelastic scattering. For every point Γ, the system is prepared in a liquid state with $\Gamma_i = 45$ and then cooled down in the periodic potential, as described in Sec. 3.4.2.

data is the increased melting temperature. This effect is similar to the modulation-induced freezing observed in colloidal systems [172, 4, 27]. Close to the freezing point, the order in the system is governed by the competition of the potential energy and the entropy. In the commensurate potential, the system can gain more potential energy by ordering in a triangular lattice. Therefore, the transition happens at a higher temperature than in a uniform system.

Another notable difference from the case of a uniform system (cf. Fig. 3.17) is that the transition, as seen in the diffusion, becomes smooth. This can be understood in the case of a strong potential, if one thinks of the modulated liquid as a series of electron channels in the modulation troughs. Freezing occurs when the channels become strongly coupled with each other and eventually ordered. The nature of this transition is different from the Berezinskii-Kosterlitz-Thouless mechanism. Therefore, the transition in the presence of the commensurate potential is expected to have a different form.

The diffusion is also strongly anisotropic since the potential breaks the rotation symmetry. In the picture of weakly coupled electron channels, the electrons in different channels can move relative to each other, producing a high value of $D_\parallel$. Since longitudinal diffusion is mediated by an intra-channel motion, the results of simulating it in a finite-size system should display strong fluctuations. This is because the electrons within a channel are strongly correlated, and therefore essentially move all together, in a small system. The averaging over particles becomes less efficient and the values of $D_{\|}$ can be broadly spread. Such spreading of $D_{\|}$ is seen in Fig. 3.28 (a).

On the other hand, to diffuse in the transverse direction an electron needs to overcome a barrier of height $2A$ in addition to the barrier created by other electrons. These "other" electrons also have to move in a concerted way to create a vacancy for the hopping electron. Given that they are confined to a channel, this is less likely to happen than in an isotropic case. Therefore the activation energy of such process is larger than $2A$ and than the activation energy in the absence of the modulation, so that $D_{\perp}$ is significantly reduced.

The effect of the commensurate potential remains strong even for a much weaker potential, $2A \ll k_B T$. Fig. 3.28 (b) shows the diffusion constants as a function of Γ in the commensurate potential with $A = 0.05$ K. The potential amplitude is much smaller than the temperature for all points in the simulation. As in the case of $A = 0.5$ K, the diffusion smoothly approaches zero at $\Gamma \approx 110$. However, in this case there is no strong anisotropy of the diffusion coefficient and no strong spreading of the data for $D_{\|}$, because the binding into channels and the ordering of electrons in different channels occur simultaneously.

To confirm that the system is undergoing a freezing transition at this point, we plot the second-order correlation function $g^{(2)}(x,y)$ for three values of Γ approaching the freezing transition in Fig. 3.29. We calculate $g^{(2)}(x,y)$ as the average density of electrons (divided by n_s) at the coordinates (x,y) counted off from a given electron,

$$g^{(2)}(\boldsymbol{r}) = \frac{1}{n_s N(N-1)} \left\langle \sum_i \sum_{j \neq i} \delta(\boldsymbol{r} - \boldsymbol{r}_{ij}) \right\rangle . \tag{3.48}$$

As seen in Fig. 3.29, the system is gradually changing from a modulated liquid at $\Gamma = 100$ to an ordered crystal with sharp peaks of the triangular lattice at $\Gamma = 110$. The transition is accompanied by ordering within and between the channels simultaneously. The system remains a crystal with a pronounced long-range order for $\Gamma \gtrsim 110$.

Clearly, a crystal in a commensurate potential must be pinned to the potential. A liquid, on the other hand, should not be pinned and must exhibit nonzero transverse mobility. The nature of

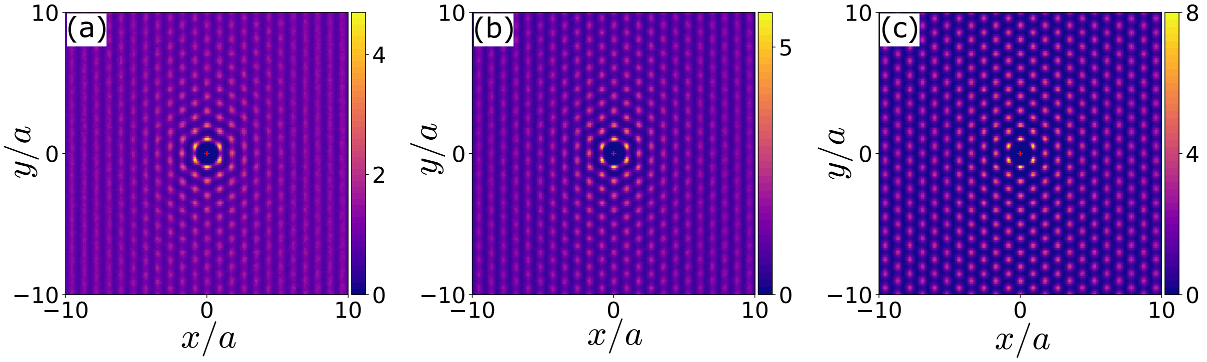

Figure 3.29 Pair correlation function $g^{(2)}(x,y)$ of the electron system in the external potential with $A = 0.05$ K and $p = 1$. **(a)** $\Gamma = 100$, **(b)** $\Gamma = 105$, and **(c)** $\Gamma = 110$. The correlation function is dimensionless. The red cross indicates the location of the origin.

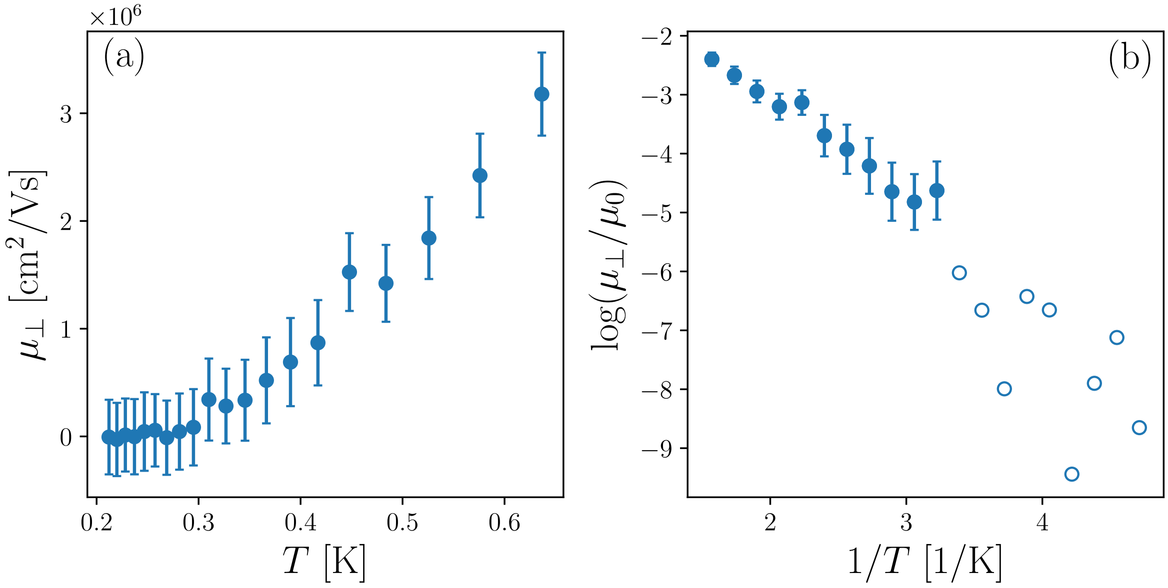

Figure 3.30 **(a)** The transverse mobility $\mu_\perp$ in the electron liquid as a function of temperature. **(b)** The logarithm of the transverse mobility $\mu_\perp/\mu_0$ as a function of the inverse temperature. Both panels are for the electron liquid in the periodic potential with $A = 0.05$ for $p = 1$. The hollow circles show $\log(\mu_\perp/\mu_0)$ for points with $T < 0.3$ K. These points correspond to the crystallized system ($\Gamma \gtrsim 110$), which is pinned. The nonzero values of $\mu_\perp$ here give the measurement error. The number of electrons in this and other mobility calculations is $N = 1024$.

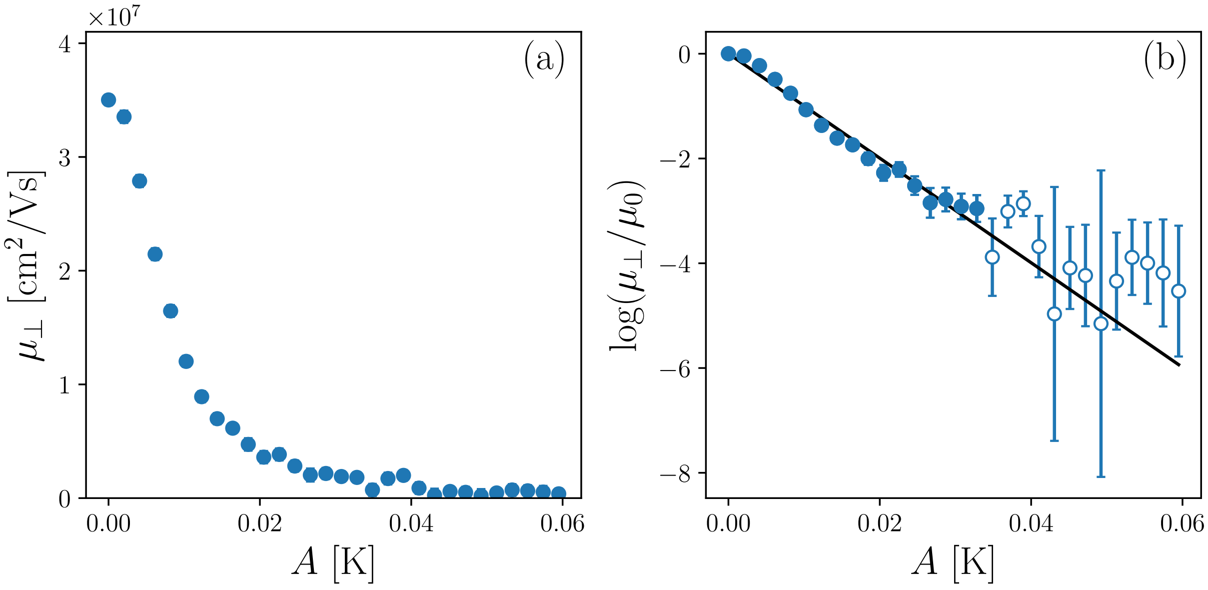

Figure 3.31 **(a)** The transverse mobility $\mu_\perp$ in the electron liquid as a function of the periodic potential amplitude A for $p = 1$. **(b)** The logarithm of the transverse mobility $\mu_\perp$ as a function of the periodic potential amplitude A for $p = 1$. The hollow circles represent the points where the calculation error is comparable to the value of $\mu_\perp$. The solid line is the least-squares fit, its slope is 100 ± 4 K^{-1}. The hollow points were excluded from the fitting procedure. $\Gamma = 90$ in both plots.

the transition between these two distinct states is of considerable interest. We study this transition by calculating the transverse mobility $\mu_\perp$ as a function of temperature. The result of the simulation for $A = 0.05$ K is displayed in Fig. 3.30 (a). As discussed above, the system is pinned for temperatures $T < 0.3$ K, which corresponds to the freezing point $\Gamma \approx 110$ for this system. For higher temperatures, the mobility is smoothly increasing the temperature. The shape of the curve suggests that the current is activated. Indeed, if we plot $\log(\mu_\perp/\mu_0)$ vs $1/T$ (see Fig. 3.30 (b)), it is close to a straight line for temperatures above freezing. Here $\mu_0 = 3.5 \times 10^7$ cm^2/Vs is a constant introduced for normalization; it corresponds to the mobility of the electron liquid at $T = 0.354$ K in a uniform system. Such revealing form of $\mu_\perp(T)$ is also reproduced for other values of A.

To confirm that the current is activated, we perform a series of simulations that compute $\mu_\perp$ as a function of the periodic potential amplitude. The result of the simulation for $\Gamma = 90$ ($T = 0.354$ K) is shown in Fig. 3.31. The mobility is reduced almost to zero for A as small as 0.05 K. The plot of $\log \mu_\perp$ vs A is nearly a straight line (Fig. 3.31 (b)) with some slope $-s$, indicating that $\mu_\perp$ decays

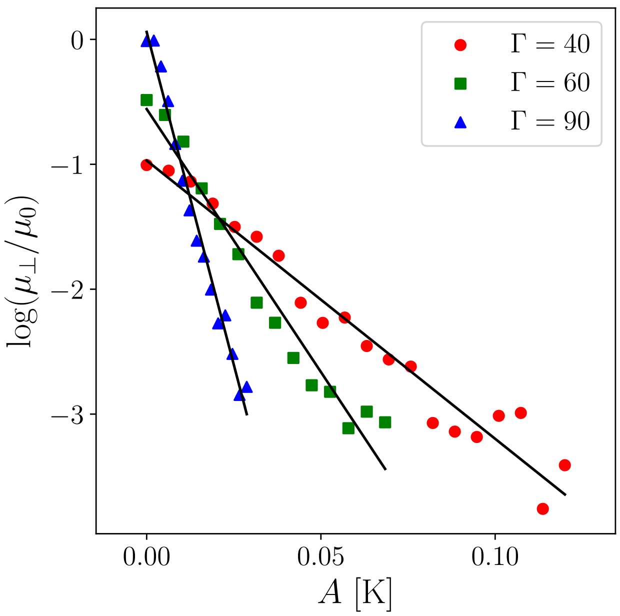

Figure 3.32 Logarithm of the transverse mobility $\mu_\perp$ as a function of the periodic potential amplitude A with $p = 1$. Three sets of points correspond to the electron liquid with $\Gamma = 40$ (red circles), $\Gamma = 60$ (green squares), and $\Gamma = 90$ (blue triangles). Error bars are not shown for clarity. The system consists of $N = 1024$ electrons. The solid lines are the least-squares fit. For each Γ, we excluded points with $\mu_\perp$ smaller than 5 % of the maximum value of $\mu_\perp$, since the calculation error for them is comparable with their value.

exponentially with A:

$$\mu_\perp \sim e^{-sA}. \tag{3.49}$$

The curve deviates from the exponential for very small A, where the scattering limits the mobility. However, already for A as small as 0.005 K the interplay between the periodic potential and the electron-electron interactions becomes the major factor that determines the mobility. The rate s of the exponential decay depends on temperature. This is clearly demonstrated by the plots of $\log \mu_\perp$ vs A for three values of Γ in Fig. 3.32.

The exponential decay of $\mu_\perp$ as a function of A or $1/T$ is an indication of the activated nature of the current. Simple activation of a single electron over the modulation barrier of height $2A$ would give the slope $s = 2/k_B T$, which would be $s = 5.66$ K^{-1} for the temperature $T = 0.354$ K used in Fig. 3.31. Instead, $s \approx 110$ K^{-1} in the correlated electron liquid at $T = 0.354$ K. An electron in the liquid cannot overcome a modulation barrier as a single particle since it moves in the field of other electrons. Instead, a collective motion of electrons should be considered. We expect the current to be mediated by locally ordered groups of particles overcoming the modulation barrier simultaneously.

To find the natural length scale over which the electrons are ordered, we consider the radial distribution function $g(r)$ in the absence of a periodic potential. It is defined as (divided by n_s) the average density of electrons at a distance r from a given electron,

$$g(r) = \frac{1}{2\pi r n_s N(N-1)} \left\langle \sum_i \sum_{j \neq i} \delta(r - r_{ij}) \right\rangle . \tag{3.50}$$

The function $g(r)$ for several values of Γ is shown in Fig. 3.33 (a). The envelope of $g(r)$ decays exponentially in a liquid, approaching unity at infinity. If we denote positions of the peaks of $g(r)$ as r_p, and the values at the peaks as g_p, then they are approximately related as $g_p \approx 1 + \gamma \exp(-r_p/\xi_c)$, with some constants γ and ξ_c. We will call ξ_c a correlation length. We find γ and ξ_c by fitting the peaks of $g(r)$ with the exponential form above.

Strictly speaking, the correlation length describes $g(r)$ at large r/a. In our case the parameter ξ_c/a is $\lesssim 1$. The typical distance over which the electron positions are correlated is $a + \xi_c$. It means that, for a weak periodic potential, the average number of electrons that have to collectively overcome the barrier in the activation process is $\sim \pi n_s(\xi_c + a)^2$. In accordance with this hypothesis, the slope s in Eq. (3.49) should be of the order

$$s \sim 2\pi n_s(\xi_c + a)^2/k_B T \tag{3.51}$$

To test the relation (3.51), we compute the correlation length ξ_c for several values of Γ and compare the obtained values of s with Eq. (3.51). We find the correlation length by fitting the peaks of $g(r)$ located at points r_p with a function of the form $\gamma e^{-r_p/\xi_c} + 1$. The fitting parameters are γ and ξ_c. The fitting curves are shown as the the dashed lines in Fig. 3.33.

We plot s vs $2\pi(\xi_c + a)^2/a^2 T$ in Fig. 3.33 (b). The points follow a linear trend with the slope 1.06 ± 0.02. If the relation Eq. (3.51) is valid, we should expect the slope to be of the order of $a^2 n_s \approx 1.15$, which is indeed the case up to a small factor. It is a strong evidence that the current

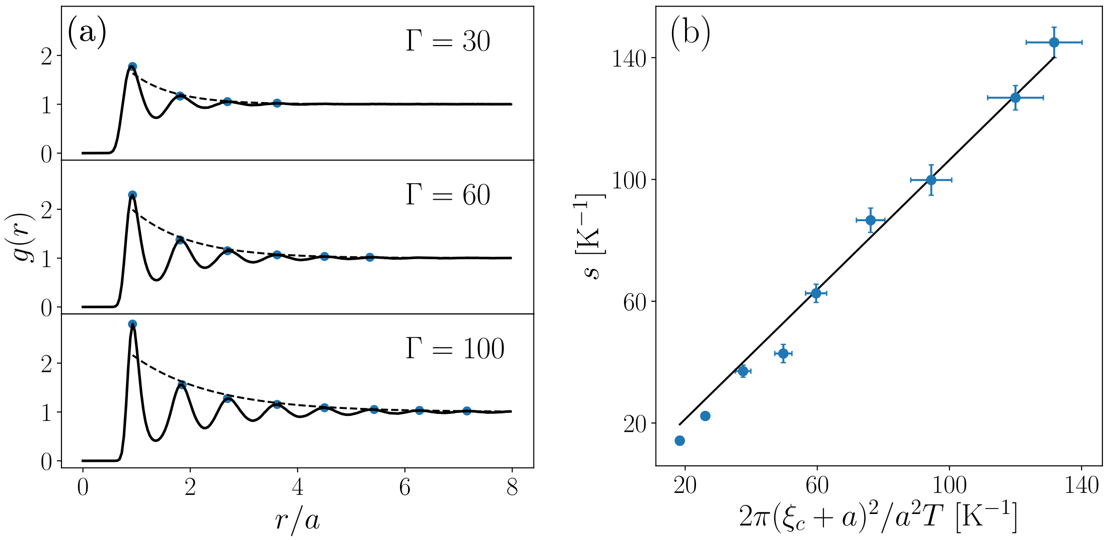

Figure 3.33 **(a)** The radial distribution function $g(r)$ (solid lines) of the electron system without modulation for $\Gamma = 30$ (top), $\Gamma = 60$ (middle), and $\Gamma = 100$ (bottom). The number of electrons is $N = 1024$. The dashed lines show the least-squares fit of the peaks g_p with a function of the form $\gamma e^{-r_p/\xi_c} + 1$, see the text for details. The found values of ξ_c are: $\xi_c = (0.76 \pm 0.05)a$ for $\Gamma = 30$, $\xi_c = (1.05 \pm 0.05)a$ for $\Gamma = 60$, and $\xi_c = (1.47 \pm 0.09)$ for $\Gamma = 100$. **(b)** The exponential decay rate s plotted vs $2\pi(\xi_c + a)^2/a^2T$. The values of s are found from the plots such as that in Fig. 3.32. Different points represent systems with Γ from 30 to 110. The correlation length is computed without the external potential or drive, as in panel (a). The solid line is the least-squares fit by a straight line passing through the origin. It has the slope 1.06 ± 0.02.

in the commensurate system is mediated by the activated collective motion of electrons within the radius of $\sim (a + \xi_c)$.

The relation (3.51) can potentially provide an opportunity of a direct experimental measurement of the correlation length in strongly correlated electron liquids.

The diffusion constants also depend on A in the system with $p = 1$, as shown in Fig. 3.34. However, the diffusion is not as sensitive to the modulation as the mobility. The diffusion constant $D_\perp$ is only reduced by a factor of $\sim 1/2$ by the potential with $A = 0.05$ K, while the same potential reduces the mobility by a factor of 50. This is a manifestation of the fact that diffusion and mobility in a strongly correlated liquid are not directly related. Without modulation, the liquid can easily slide along the helium surface as a whole even when the diffusion constant is small. The sliding velocity is limited by the scattering of electrons by ripplons. The weak commensurate potential

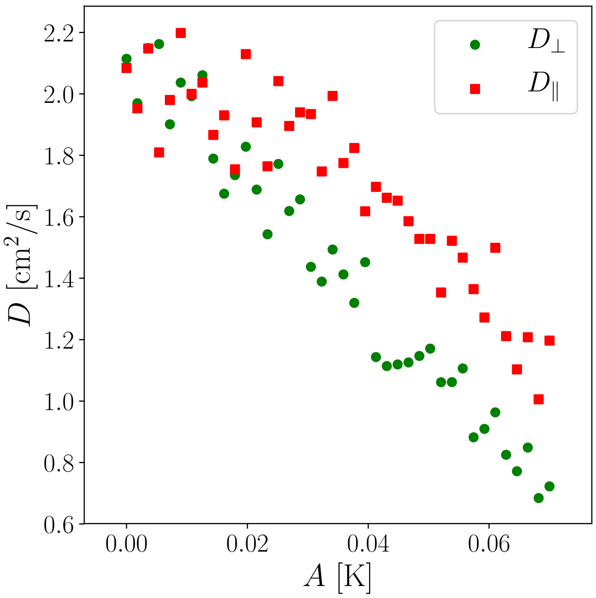

Figure 3.34 Diffusion constants $D_\perp$ and $D_\parallel$ as a function of the periodic potential amplitude A, with $p = 1$. The system consists of $N = 1024$ electrons and $\Gamma = 90$.

prevents the system from freely sliding across the modulation troughs, thus dramatically reducing the mobility. The diffusion constants, on the other hand, quantify the motion of electrons relative to each other, and are mostly limited by the inter-electron interaction. This motion is not as strongly affected by the potential as the ability to slide along the surface.

3.5.4 Structure and crystallization for $p < 1$ close to $p = 1$

In the intermediate range of p, where $p < 1$ but close to $p = 1$, the periodicities of the electron system and of the external periodic potential compete. In this range, multiple phenomena can occur. First, if we consider a Wigner crystal, it is expected to make a transition from an incommensurate crystal to a commensurate crystal. This transition should be accompanied by a structural change. According to the theory of Pokrovsky and Talapov [26], close to the C-I transition, the crystal is expected to develop one-dimensional solitons of density variation. As a consequence, at some point when p becomes close to $p = 1$, the system is expected to adjust to the potential and become commensurate. We also expect to find some intermediate structures in the transition region.

The liquid phase is also expected to change its structure in a similar way. Far from commen-

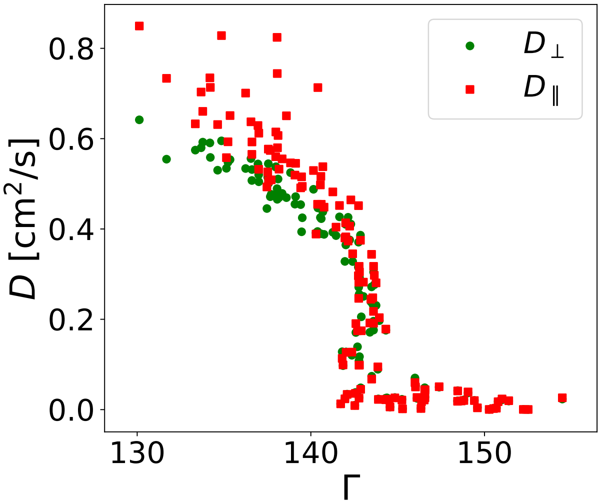

Figure 3.35 Diffusion constants $D_\perp$ and $D_\parallel$ vs Γ in the periodic potential with $A = 0.5$ K and $p = 30/40 = 0.75$, $N = 1600$. The simulation includes both elastic and inelastic scattering. For every point Γ, the system is prepared as a liquid at $\Gamma_i = 45$ in the periodic potential and then cooled down to the temperature corresponding to Γ, as described in Sec. 3.4.2. After cooling, the system is equilibrated for 10^6 more steps. The freezing transition occurs at $\Gamma \approx 145$.

surability, the liquid has a structure similar to that of a uniform system but with some density modulation. When p is approaching $p = 1$, for a sufficiently strong potential we expect the liquid to become a series of semi-ordered decoupled channels residing in the periodic potential minima. Since the potential in this range of p is expected to significantly affect the system's structure, it is also expected to change the freezing transition temperature.

In this section, we will study the structure of both liquid and solid phases of the electron system in the external potential with $A = 0.5$ K as we increase p from $p = 0.75$ to $p \approx 1$. For $A = 0.5$ K, the properties of the system become significantly different from the case $p \ll 1$ for $p \approx 0.75$. The diffusion coefficients as functions of Γ for $p = 30/40 = 0.75$ and $A = 0.5$ K are shown in Fig. 3.35. As seen in the figure, the freezing transition occurs at the point $\Gamma \approx 145$ instead of $\Gamma \approx 137$ that was observed in the uniform system and in the system with the periodic potential with $p \ll 1$. For Γ above the freezing point, the system assumes a structure of a triangular crystal with a superstructure formed by solitons of density. Two of such structures are shown in Fig. 3.36. In the figure, we show the Voronoi tessellation for the resulting structures. Each cell in the Voronoi tessellation contains

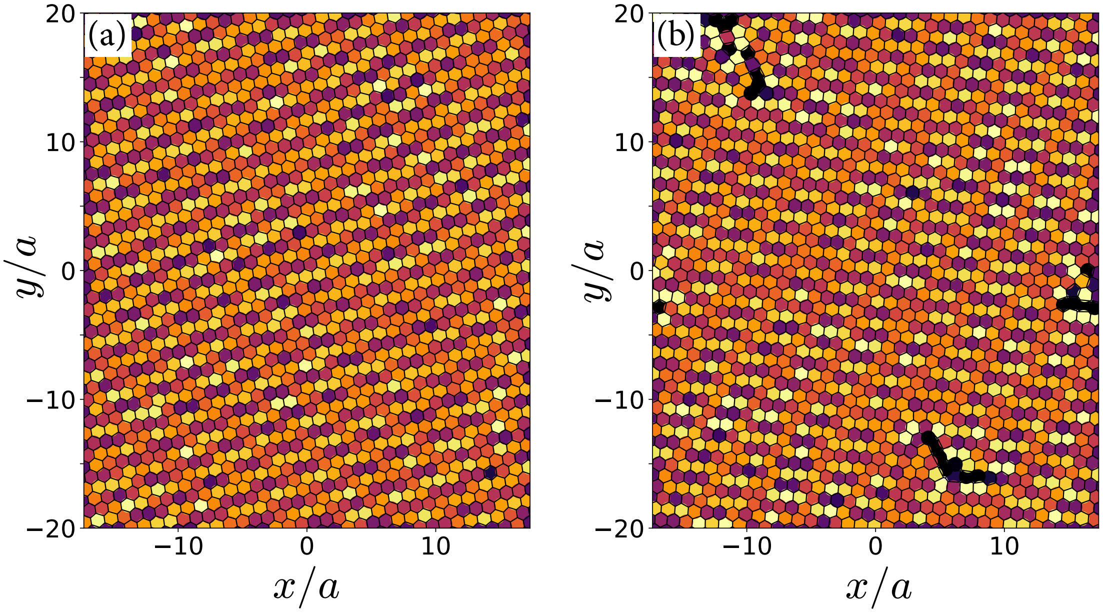

Figure 3.36 Voronoi tessellation of the Wigner crystal with the electron number $N = 1600$ in the incommensurate periodic potential with $A = 0.5$ K and $p = 30/40 = 0.75$. **(a)** $\Gamma \approx 156$, **(b)** and $\Gamma \approx 158$. Voronoi cells are colored depending on their surface area: from dark purple for smaller cells to light yellow for larger cells. The variation of the cell areas is from $0.84a^2$ to $0.88a^2$. The simulation procedure is the same as in Fig. 3.35. The electron positions are averaged over time to average over small-amplitude thermal fluctuations. Clear rows of increased density appear at a nonzero angle with the modulation direction, which correspond to the incommensuration solitons. The two different soliton structures correspond to slightly different orientation angles that the system crystallized into. Groups of black cells are a result of disorder and averaging over time.

points that are closer to a given electron than to any other electrons. Inspired by Ref. [5], we use color to show the surface area of each Voronoi cell. To reduce the disorder resulting from thermal motion, we average the electrons' positions over time. In both panels of Fig. 3.36, one can see superstructures of density modulation appearing due to the incommensurate periodic potential. We observe a variety of such superstructures. The structures are different for different orientation angles at which the crystal is formed. Only two of them are shown in Fig. 3.36.

To study the liquid phase at $p = 0.75$, we plot the pair correlation function $g^{(2)}(\boldsymbol{r})$ in Fig. 3.37 (a). The pair correlation function is defined in Eq. (3.48). The oscillations in the correlation function are rapidly decaying with the increasing distance from the origin, as one would expect for a liquid. The hexagonal shape of the rings means that there are ordered domains in the liquid, and in the relatively small data sample that was used to calculate $g^{(2)}(\boldsymbol{r})$, one orientation in the ordered domains prevailed. The correlation function also has a non-decaying periodic structure with the periodicity of the external potential, which reflects the average density modulation by the periodic potential.

We also plot the Delaunay triangulation for a snapshot of this system in Fig. 3.37 (b). The colored background displays the real part of the hexagonal bond order parameter ψ_6, which is defined in the following way:

$$\psi_6 = \frac{1}{M_{nn}} \sum_m e^{6i\theta_m}. \tag{3.52}$$

Here M_{nn} is the number of nearest neighbors of a given electron, m enumerates the neighbors, and θ_m is the angle between the bond to neighbor m and the x-axis. The real part of ψ_6 can be used as an indicator of the local orientation of the (quasi-)hexagonal structure in ordered parts of the liquid. To plot ψ_6, we interpolate it between the electron positions so that ψ_6 is constant within in each Voronoi cell. As seen in Fig. 3.37 (b), the liquid indeed has ordered domains with different orientations.

Increasing p to $p = 32/40 = 0.8$ leads to the shift of the freezing point up to $\Gamma \approx 160$. We plot the diffusion constants $D_\perp$ and $D_\|$ vs Γ for this case in Fig. 3.38. Below the freezing temperature, as in the previous case, the structures that appear have crystalline form with density modulated by solitonic superstructures. Two of the typical structures are shown in Fig. 3.39. The superstructure period is increased as compared with the case of $p = 0.75$. The structure of the liquid phase in the potential with $p = 0.8$ is qualitatively the same as in the case $p = 0.75$.

The appearance of solitons in the crystal structure is a general feature predicted by the theory of incommensurate crystals of Pokrovsky and Talapov [26]. The theory predicts that the orientation of the solitons is generally different from the orientation of the periodic potential troughs. Another prediction is that the period of the superstructure should increase when p is approaching the C-I transition threshold value p_c. We observe similar behavior in our simulations of the electron system. Even though the theory was developed for the atomic crystals with short-range inter-particle interactions, it appears to correctly describe the qualitative features of the behavior of the electron

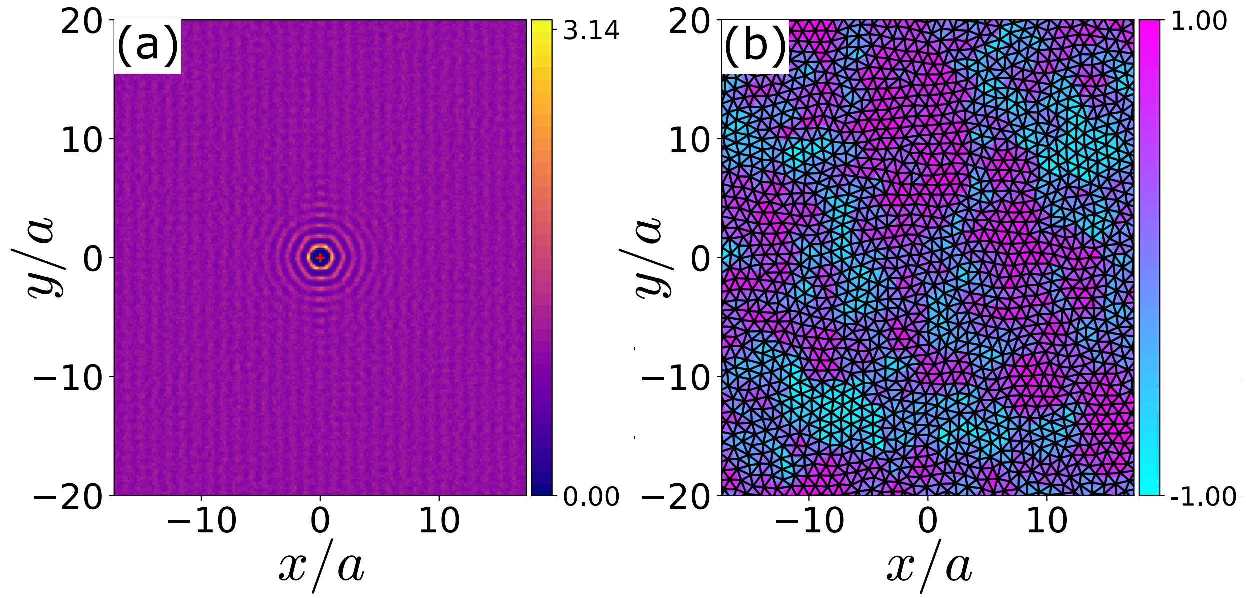

Figure 3.37 The system of $N = 1024$ electrons at $\Gamma \approx 131$ in the periodic potential with $A = 0.5$ K and $p = 30/40 = 0.75$. **(a)** Pair correlation function $g^{(2)}(\boldsymbol{r})$. **(b)** Delaunay triangulation of a snapshot of the system with electrons represented by vertices of the triangulation. The background color shows $\mathrm{Re}\left[\psi_6(\boldsymbol{r})\right]$ which essentially means the local orientation of the nearest-neighbor links in the ordered parts of the liquid.

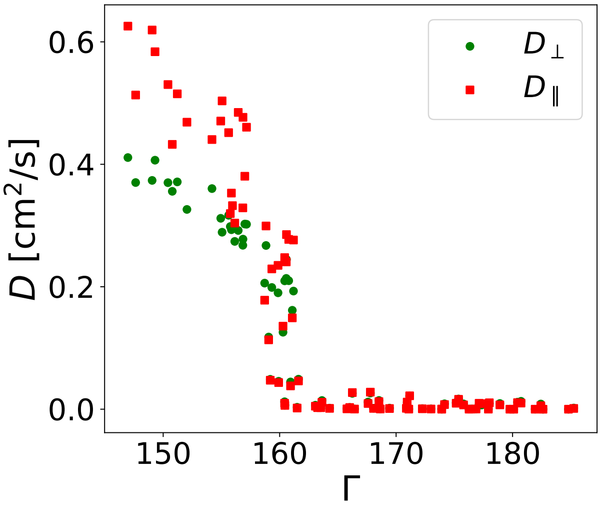

Figure 3.38 Diffusion constants $D_\perp$ and $D_\parallel$ vs Γ in the periodic potential with $A = 0.5$ K and $p = 32/40 = 0.8$ for $N = 1600$ electrons. The procedure is outlined in Fig. 3.35. The phase transition occurs at $\Gamma \approx 160$.

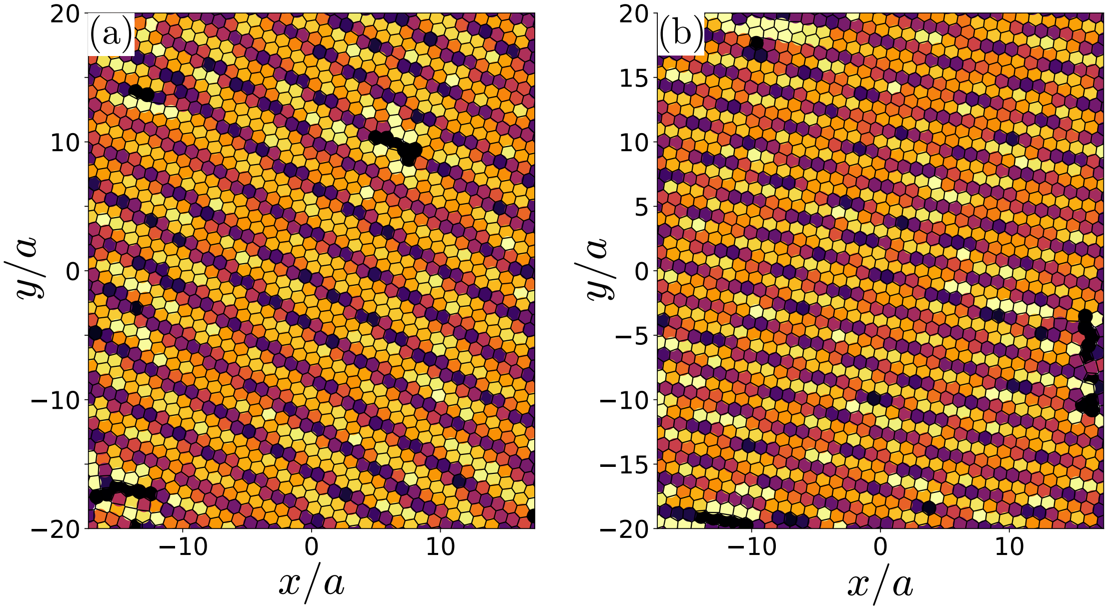

Figure 3.39 Soliton superstructures corresponding to different rotation angles of the crystal in the incommensurate periodic potential with $A = 0.5$ K and $p = 32/40 = 0.8$. Voronoi tessellation for the Wigner crystal with $N = 1600$ electrons is displayed for two very close values of Γ: **(a)** $\Gamma = 176.5$, **(b)** $\Gamma = 177.1$. Voronoi cells are colored depending on their surface area: from dark purple for smaller cells to light yellow for larger cells. The variation of the cell areas is from $0.84a^2$ to $0.88a^2$. The electron positions are averaged over time to average over small-amplitude thermal fluctuations. The simulation procedure is the same as in Fig. 3.35.

system with a long-range Coulomb interaction. Formally, the theory is not directly applicable to the coulombic system since the long-range interaction leads to non-acoustic longitudinal phonon modes.

If the periodic solitonic superstructure can be reproduced in the experiment with electrons on helium, it should be detectable with the standard experimental techniques. The additional periodicity in the crystal should lead to new plasmon-ripplon resonance peaks in the Grimes and Adams type of experiment. The superstructure may also be detectable by measuring the current along the modulation troughs. The solitonic superstructure should lead to the Bragg-Cherenkov scattering at a velocity much smaller than that in the case of a uniform crystal. By measuring the Bragg-Cherenkov saturation velocity, one can potentially measure the period of the superstructure. The proposed experimental methods would require fabrication of electrode arrays of high quality to create the periodic potential. Disorder introduced by imperfections of the electrodes may destroy

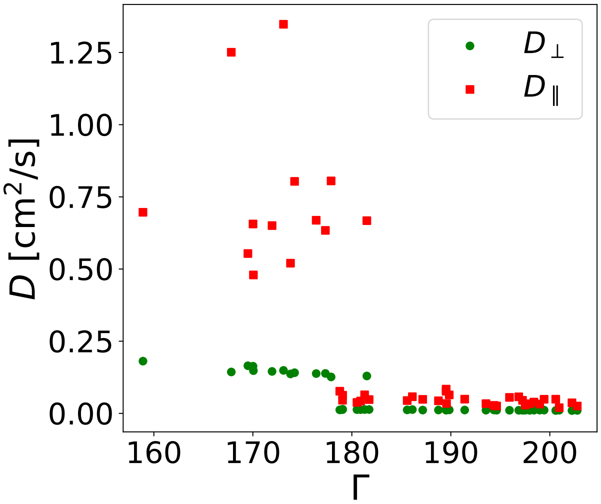

Figure 3.40 Diffusion constants $D_\perp$ and $D_\parallel$ in the periodic potential with $A = 0.5$ K and $p = 34/40 = 0.85$. The procedure is outlined in the caption to Fig. 3.35. The transverse diffusion ceases at $\Gamma \approx 180$.

the periodic structure and therefore eliminate the effects described above because they critically depend on periodicity.

The incommensurate structure with arrays of solitons exists for values of p up to some threshold value p_c. For $A = 0.5$ K, this threshold value turns out to be $p_c \approx 0.85$. For $p \gtrsim 0.85$, the structure of the system is qualitatively different. The diffusion vs Γ for $p = 34/40 = 0.85$ is shown in Fig. 3.40. The diffusion is behaving differently than for $p = 32/40 = 0.8$ in a number of ways. First, the transverse diffusion ceases for a significantly higher value of $\Gamma \approx 180$. Second, the computed $D_\parallel$ has large values for $\Gamma < 180$ (taking into account the small temperature) and a very large random error. The random error manifests itself as a wide spread of $D_\parallel$ points. Finally, $D_\parallel$ does not vanish completely even for $\Gamma > 180$. These changes suggest that the system is qualitatively different than the system with $p = 32/40 = 0.8$.

We plot the pair correlation function and the Delaunay triangulation for the system at $\Gamma \approx 200$ in Fig. 3.41. Instead of a triangular crystal with incommensuration solitons, this system has a structure consisting of semi-ordered electron channels along the minima of the periodic potential. The correlated motion of electrons within each channel leads to the large calculation error in our finite-size systems for $D_\parallel$. This issue is discussed in greater detail in Sec. 3.5.3 and below. The

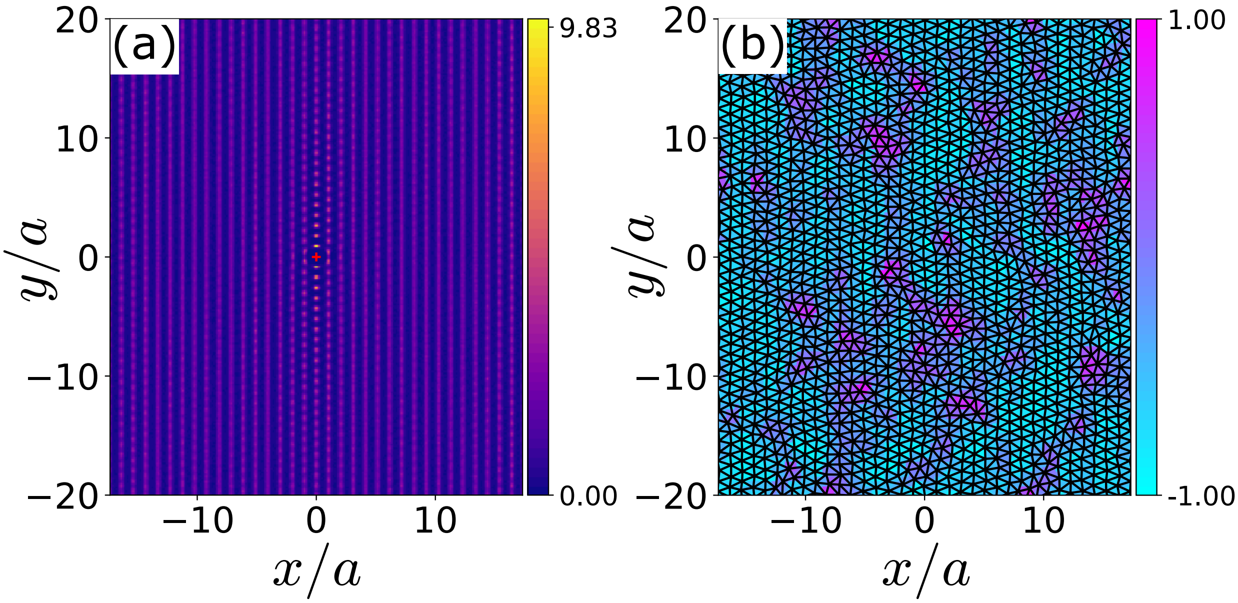

Figure 3.41 The system at $\Gamma \approx 200$ in the periodic potential with $A = 0.5$ K and $p = 34/40 = 0.85$. **(a)** Pair correlation function $g^{(2)}(\boldsymbol{r})$. **(b)** Delaunay triangulation of a snapshot of the system with electrons represented by vertices of the triangulation. The background color shows $\mathrm{Re}\left[\psi_6(\boldsymbol{r})\right]$.

electrons never form completely ordered channels. Some displacements of the channels relative to each other persists even for $\Gamma > 180$. That is why $D_{\|}$ never vanishes completely in Fig. 3.40. Qualitatively, there is no visible difference in the correlation function and the spatial structure of the system below and above the $\Gamma = 180$ threshold.

The structural change at $p \approx 0.85$ signifies approaching the C-I transition in the crystal phase. Due to the competing periodicities, the system assumes some intermediate structure with no long-range order even at very low temperatures. This structure is neither a triangular lattice nor a fully commensurate crystal. As p is approaching $p = 1$, the electron channels are expected to become more ordered at low temperatures and eventually form a commensurate crystal. At higher temperatures, the system is expected to remain a modulated liquid for all values of p.

This picture of the C-I transition is in agreement with the data for $p = 37/40 = 0.925$. The behavior of the diffusion constants vs Γ for this case is shown in Fig. 3.42. The diffusion is highly anisotropic with the wide spread of $D_{\|}$ values, which is a sign of the channel formation in the periodic potential troughs.

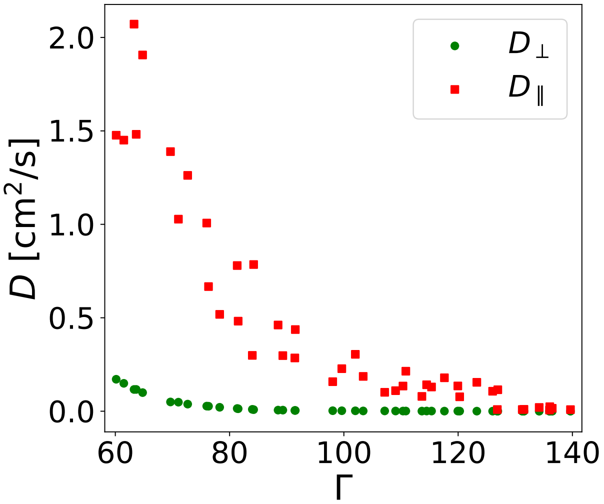

Figure 3.42 Diffusion constants $D_\perp$ and $D_\parallel$ in the periodic potential with $A = 0.5$ K and $p = 37/40 = 0.925$. The procedure of obtaining the data is outlined in the caption to Fig. 3.35. The freezing transition occurs at $\Gamma \approx 130$.

Below the freezing point, which is at $\Gamma \approx 128$ for $p = 37/40 = 0.925$, the electrons form a lattice with a small built-in disorder. The vertical rows of electrons reside in the periodic potential minima. Fig. 3.43 shows the pair correlation function and a snapshot of the system for $\Gamma \approx 130$. The lattice is similar to the triangular lattice in the uniform system, but the triangles are not equilateral since they have to accommodate the periodicity of the periodic potential. The disorder is also necessary to "adjust" the electrons to the incommensurate periodic potential. Therefore, there is no true long range order in this system.

At temperatures above the melting transition, the electron channels in the potential minima become more disordered and decouple from each other. At $\Gamma = 60$, the system's pair correlation function has clear vertical rows, which correspond to the partially-ordered channels in the troughs, see Fig. 3.44 (a). In the snapshot of the system in Fig. 3.44 (b), the disordered chains of electrons along the y-axis are visible.

To illustrate the fact that the longitudinal diffusion is governed by the displacements of entire electron channels, we show two snapshots of the system with $\Gamma \approx 115$ in Fig. 3.45. The snapshot in the left panel shows the electron positions in the first data frame. The snapshot on the right shows the electron positions 1.9×10^4 time steps later into the simulation. In the second snapshot,

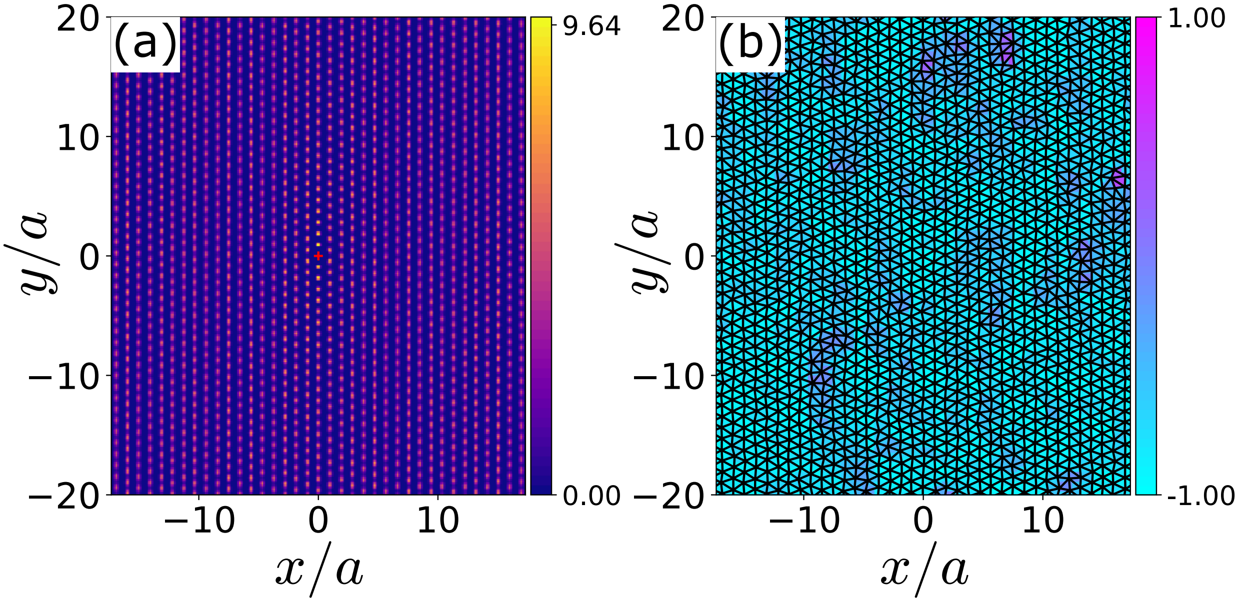

Figure 3.43 The system at $\Gamma \approx 130$ in the periodic potential with $A = 0.5$ K and $p = 37/40 = 0.925$. **(a)** Pair correlation function $g^{(2)}(\boldsymbol{r})$. **(b)** Delaunay triangulation of a snapshot of the system with electrons represented by vertices of the triangulation. The background color shows $\mathrm{Re}\left[\psi_6(\boldsymbol{r})\right]$.

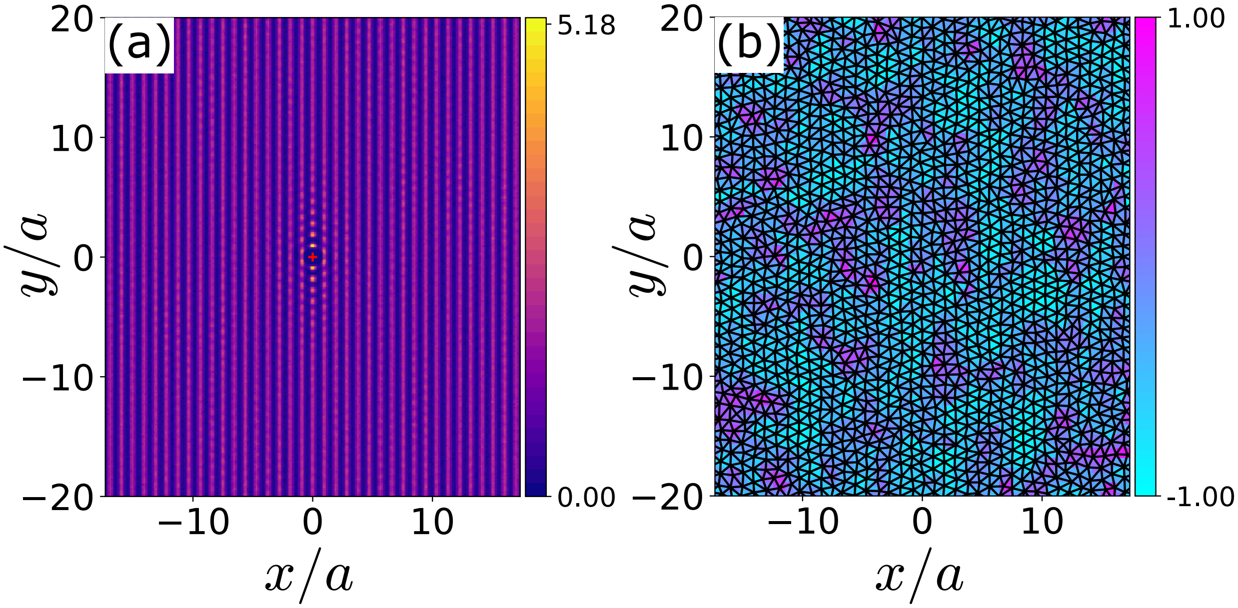

Figure 3.44 The system at $\Gamma \approx 60$ in the periodic potential with $A = 0.5$ K and $p = 37/40 = 0.925$. **(a)** Pair correlation function $g^{(2)}(\boldsymbol{r})$. **(b)** Delaunay triangulation of a snapshot of the system with electrons represented by vertices of the triangulation. The background color shows $\mathrm{Re}\left[\psi_6(\boldsymbol{r})\right]$.

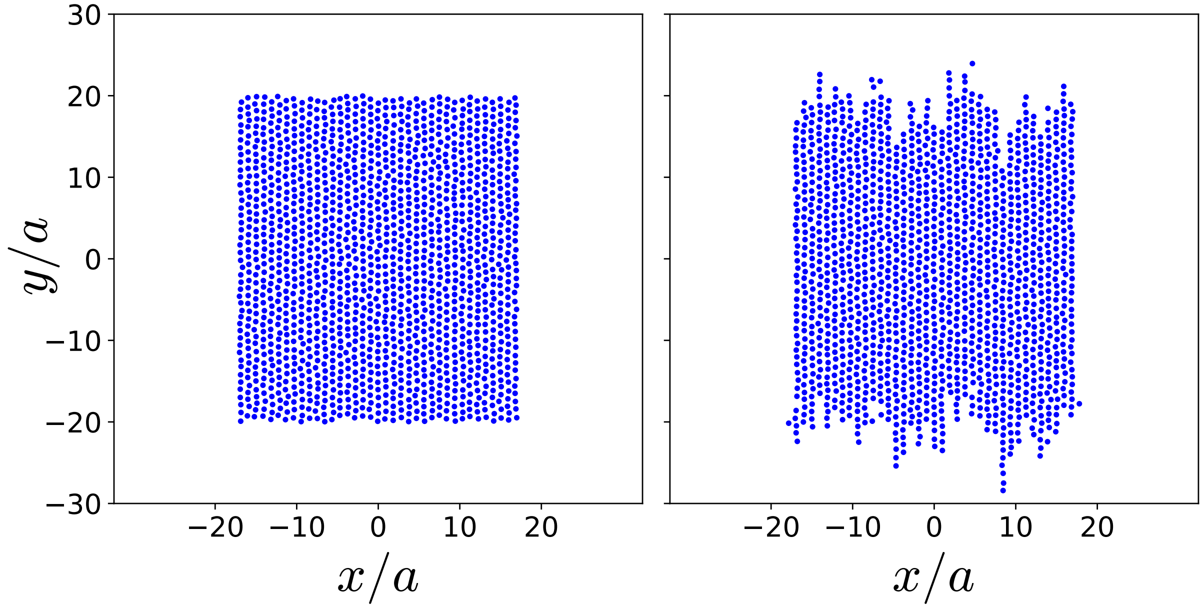

Figure 3.45 Snapshots of the system in the potential with $p = 37/40 = 0.925$ and $A = 0.5$ K taken at the beginning of the simulation (left) and 1.9×10^4 time steps later (right). Data for the point $\Gamma \approx 115$ from the simulation depicted in Fig. 3.42 is used. We reconstructed the electrons' trajectories to eliminate the effects of the periodic boundary conditions (details in the text). Comparing the two snapshots, one can see that the entire electron channels along the y axis (along potential troughs) are displaced. Only a few electrons were able to hop across the potential troughs, i.e.along x.

we reconstructed the positions in such a way that the electrons' trajectories remain continuous if an electron crosses the simulation cell boundary during the time from $t = 0$ to $t = 1.9 \times 10^4 \Delta t$. This allows us to track the electrons' positions relative to the initial configuration as if the periodic boundary conditions did not exist. One should look at the edges of the system in the right panel. The left and right edges remained clean and straight during the simulation, which indicates that very few electrons could hop transverse to the periodic potential barriers. In contrast, the top and bottom edges have a fence-like structure, which allows us to track which vertical channels shifted up or down relative to one another. This motion of entire channels makes $D_{\|}$ large compared to $D_{\perp}$. It also makes the averaging of the squared displacement over all electrons not efficient. Since electrons within a channel move coherently, one cannot assume that their trajectories are independent. Therefore, we observe large data spread in $D_{\|}$. The data collected in our finite system do to give accurate expectation values of the squared displacement.

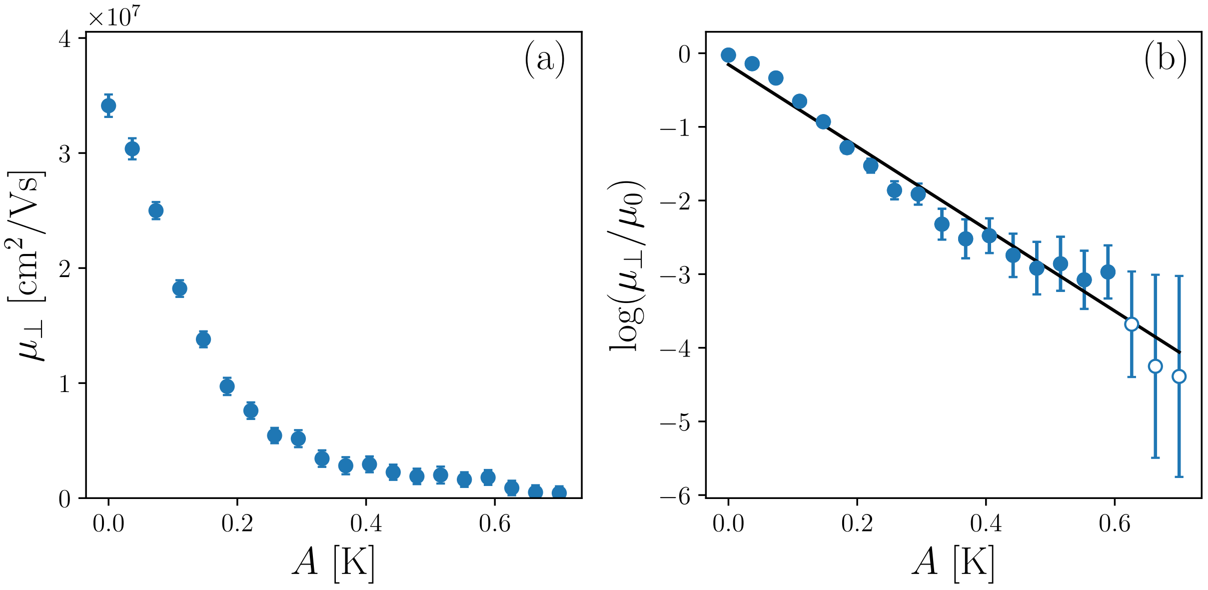

Figure 3.46 **(a)** The transverse mobility $\mu_\perp$ in the electron liquid as a function of the periodic potential amplitude A for $p = 23/32 \approx 0.72$. **(b)** The logarithm of the transverse mobility $\mu_\perp$ as a function of the periodic potential amplitude A for $p = 23/32 \approx 0.72$. The solid line is the least-squares fit, with the slope -5.6 ± 0.3 K^{-1}. $\Gamma = 90$ in the both plots.

3.5.5 Mobility in a liquid phase for $p < 1$ close to $p = 1$

The mobility of the electron liquid for $p \ll 1$ is remarkably insensitive to the periodic potential strength in a broad range of this strength (see Sec. 3.5.2). For $p = 1$, on the other hand, the transverse mobility is exponentially reduced even for $A \ll k_B T$ (see Sec. 3.5.3). In the intermediate range of p between $p \ll 1$ and $p = 1$, the system is expected to have a transition between the two opposite limits.

To probe the mobility in the intermediate range of p, we calculate the transverse mobility $\mu_\perp$ vs A for several values of p from $p = 23/32 \approx 0.72$ to $p = 15/16 \approx 0.94$. We keep $\Gamma = 90$ in all of these simulations. The results are displayed in Figs. 3.46–3.49. For all p in this range, the shape of the curve $\mu_\perp$ vs A is close to the exponential, but the decay rate s of the exponential is increasing as we increase p. To determine the decay rate, we plot $\log(\mu_\perp)$ vs A in Figs. 3.46–3.49. The decay rate s is increasing from $s \approx 5.6$ for $p \approx 0.72$ to $s \approx 78$ for $p \approx 0.94$.

As discussed in Sec. 3.5.3, the current in the commensurate system is governed by the acti-

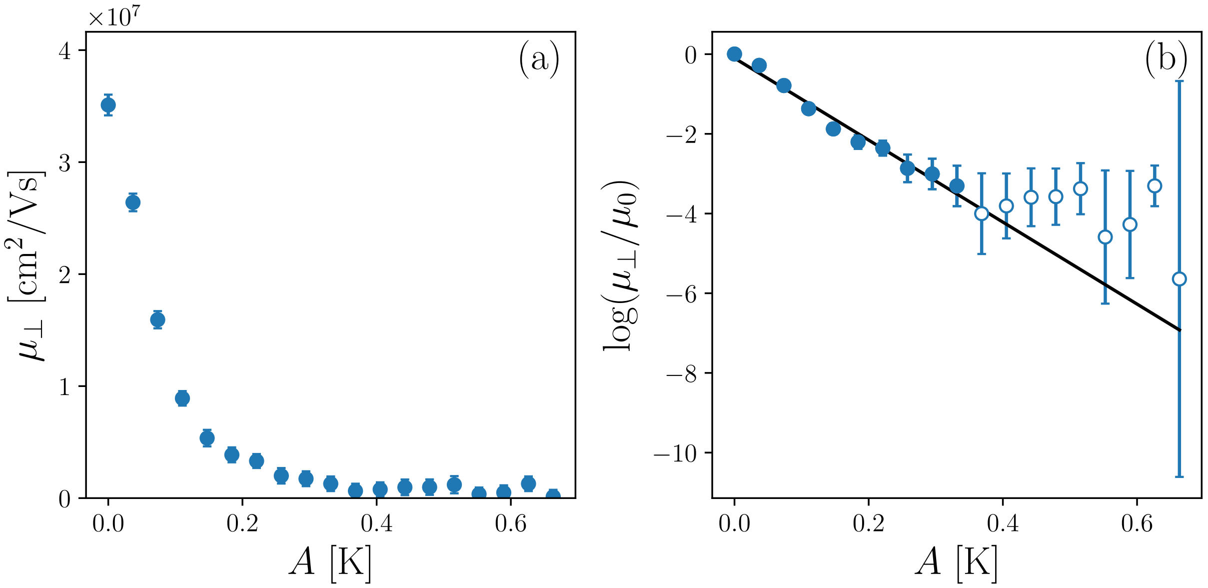

Figure 3.47 **(a)** The transverse mobility $\mu_\perp$ in the electron liquid as a function of the periodic potential amplitude A for $p = 25/32 \approx 0.78$. **(b)** The logarithm of the transverse mobility $\mu_\perp$ as a function of the periodic potential amplitude A for $p = 25/32 \approx 0.78$. The solid line is the least-squares fit, with the slope -10.3 ± 0.5 K^{-1}. The hollow circles were excluded from the fit, since the calculation error is comparable in size to the value $\mu_\perp$ for these points. $\Gamma = 90$ in the both plots.

vation of clusters of electrons with the activation energy $\sim 2\pi A n_s(\xi_c + a)^2$. As p deviates from 1, electrons in the liquid cannot on average occupy the potential trough minima, at least for small A. Therefore, the average activation energy becomes smaller than $2\pi A n_s(\xi_c + a)^2$ as $|p-1|$ is increasing. In the limit $p \ll 1$, approximately as many electrons reside in the periodic potential minima as near the maxima. Therefore, for $p \ll 1$ the activation energy for the collective motion is vanishing. This makes the system insensitive to the periodic potential, as discussed in Sec. 3.5.2. Thus, the activation energy of the collective motion is gradually increasing from zero for $p \ll 1$ to $2\pi A n_s(\xi_c + a)^2$ for $p = 1$.

3.5.6 Case $p > 1$

As p becomes larger than one but smaller than two, the electrons in the liquid cannot all reside in the potential minima on average, as for $p < 1$. Therefore, the activation energy for transport trans-

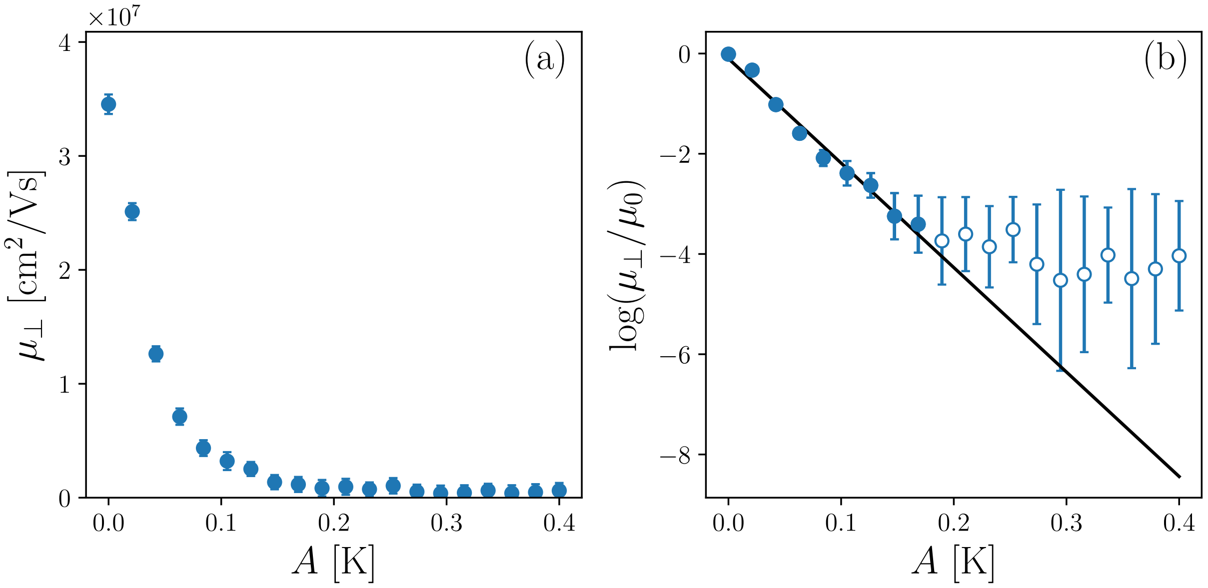

Figure 3.48 **(a)** The transverse mobility $\mu_\perp$ in the electron liquid as a function of the periodic potential amplitude A for $p = 27/32 \approx 0.84$. **(b)** The logarithm of the transverse mobility $\mu_\perp$ as a function of the periodic potential amplitude A for $p = 27/32 \approx 0.84$. The solid line is the least-squares fit, with the slope -21 ± 1 K^{-1}. The hollow circles were excluded from the fit, since the calculation error is comparable in size to the value $\mu_\perp$ for these points. $\Gamma = 90$ in the both plots.

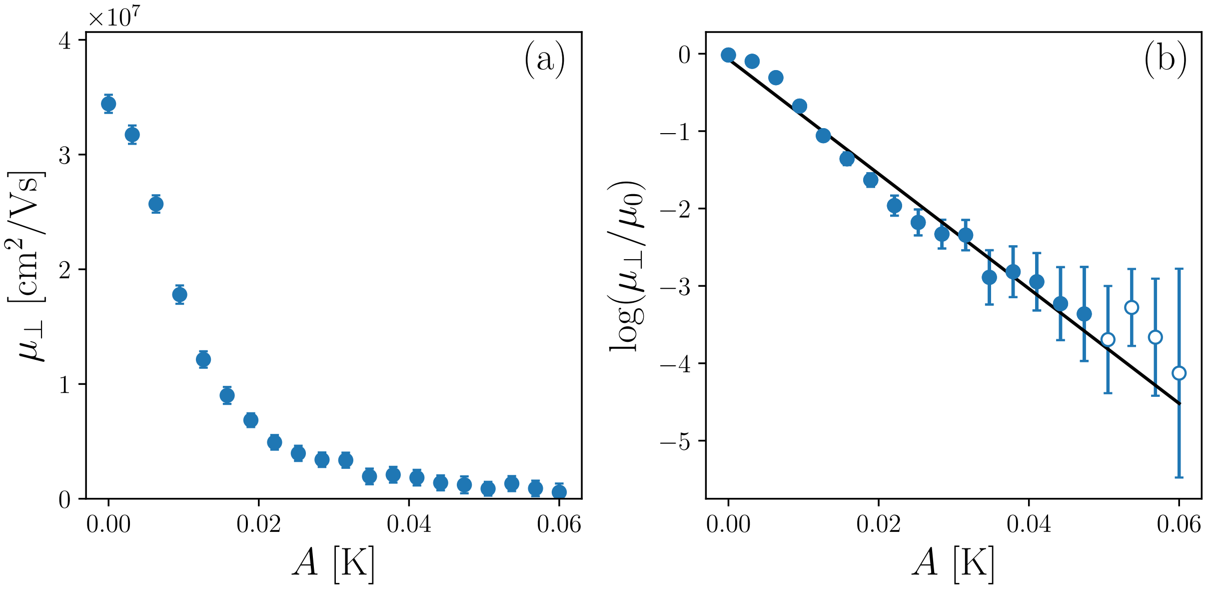

Figure 3.49 **(a)** The transverse mobility $\mu_\perp$ in the electron liquid as a function of the periodic potential amplitude A for $p = 30/32 \approx 0.94$. **(b)** The logarithm of the transverse mobility $\mu_\perp$ as a function of the periodic potential amplitude A for $p = 30/32 \approx 0.94$. The solid line is the least-squares fit, with the slope -74 ± 3 K^{-1}. The hollow circles were excluded from the fit, since the calculation error is comparable in size to the value $\mu_\perp$ for these points. $\Gamma = 90$ in the both plots.

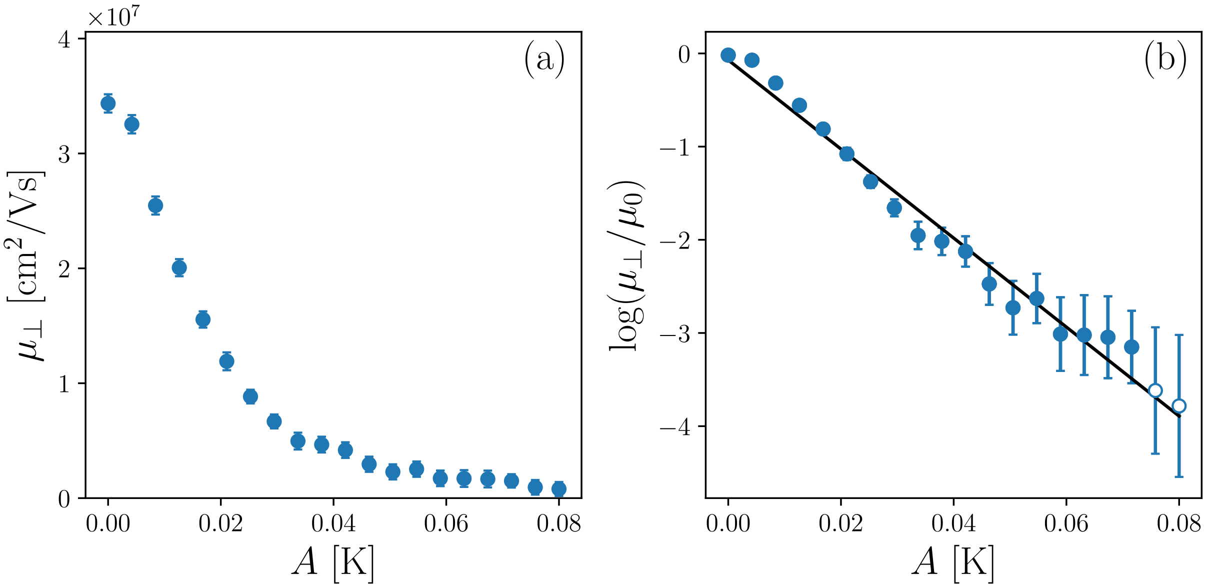

Figure 3.50 **(a)** The transverse mobility $\mu_\perp$ in the electron liquid as a function of the periodic potential amplitude A for $p = 35/32 \approx 1.09$. **(b)** The logarithm of the transverse mobility $\mu_\perp$ as a function of the periodic potential amplitude A for $p = 35/32 \approx 1.09$. The solid line is the least-squares fit, with the slope -48 ± 2 K^{-1}. The hollow circles were excluded from the fit, since the calculation error is comparable in size to the value $\mu_\perp$ for these points. $\Gamma = 90$ in the both panels.

verse to the potential troughs should decrease and the decay rate s of the exponential dependence of $\mu_\perp$ on A should decrease compared to the case $p = 1$.

We observe that s decreases to $s = 47$ K^{-1} in the system with $p = 35/32 \approx 1.09$, as shown in Fig. 3.50. As p is increased further to $p45/32 \approx 1.4$, s is reduced even more to $s = 29$ K^{-1}, see Fig. 3.51. At some point when p is approaching $p = 2$, s should start increasing again, since the system becomes commensurate again at $p = 2$. Indeed, for $p = 2$, the value of s increases again to $s = 51.4$ K^{-1}.

There may be another maximum of s at the point $p = \sqrt{3}$. At this point, the triangular lattice becomes commensurate with the potential since the lattice vector K of the potential coincides with a higher order reciprocal lattice vector of the lattice. This situation is shown in Fig. 3.54. However, we find that the mobility has a minimum at this special point only at low temperatures close to the freezing transition, see below.

The details of the structure of the liquid and solid phases for $p > 1$ remain a subject for future

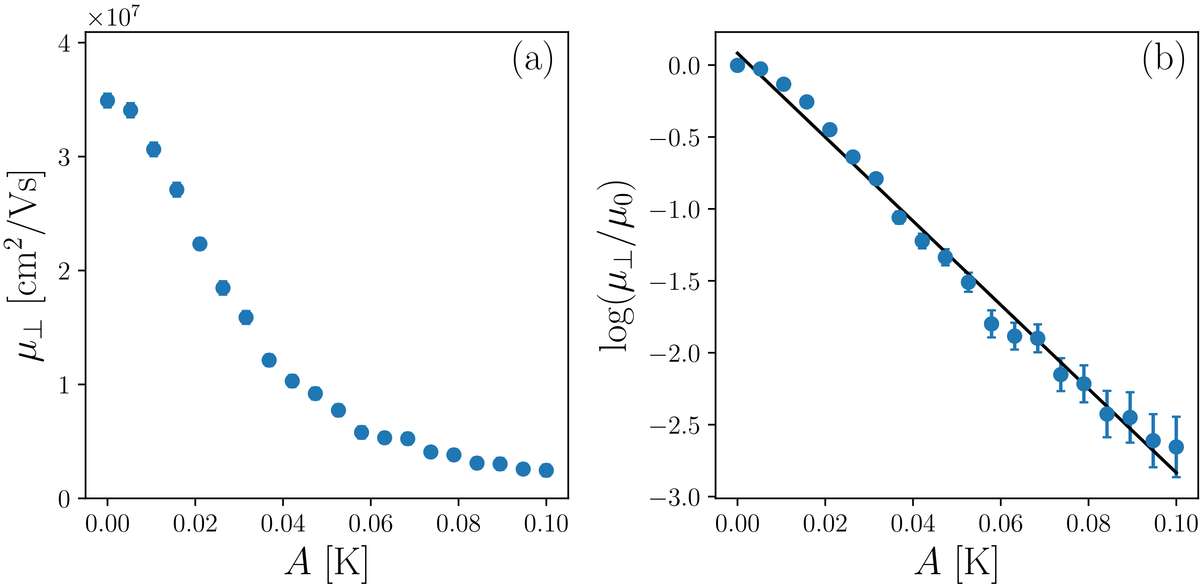

Figure 3.51 **(a)** The transverse mobility $\mu_\perp$ in the electron liquid as a function of the periodic potential amplitude A for $p = 45/32 \approx 1.4$. **(b)** The logarithm of the transverse mobility $\mu_\perp$ as a function of the periodic potential amplitude A for $p = 45/32 \approx 1.4$. The solid line is the least-squares fit, with the slope -29 ± 1 K^{-1}. $\Gamma = 90$ in the both plots.

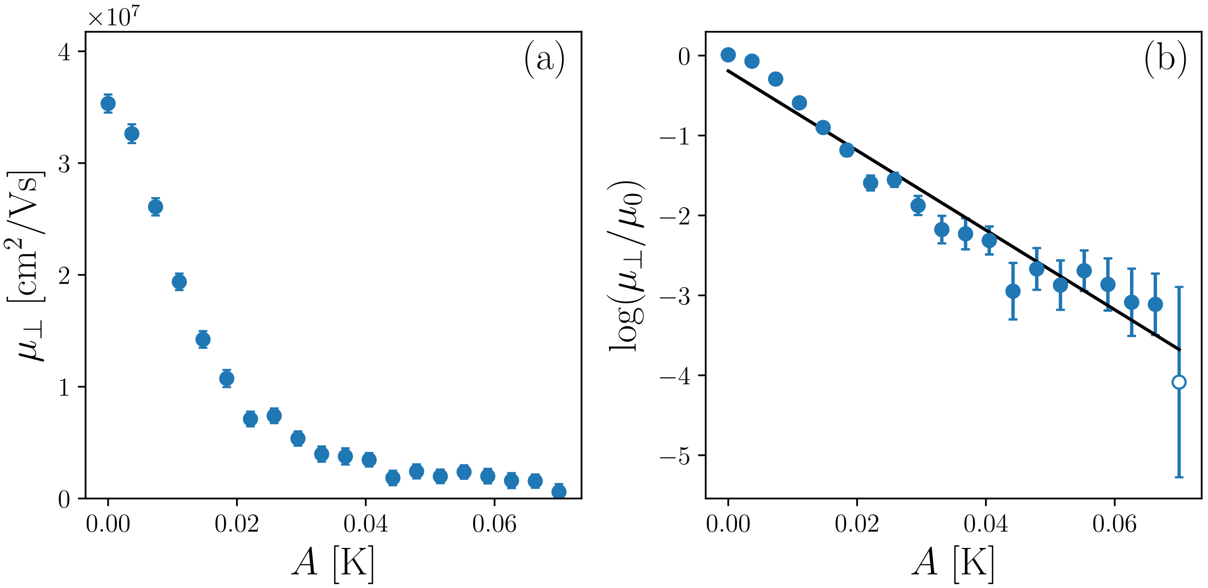

Figure 3.52 **(a)** The transverse mobility $\mu_\perp$ in the electron liquid as a function of the periodic potential amplitude A for $p = 2$. **(b)** The logarithm of the transverse mobility $\mu_\perp$ as a function of the periodic potential amplitude A for $p = 2$. The solid line is the least-squares fit, with the slope -50 ± 3 K^{-1}. $\Gamma = 90$ in the both plots.

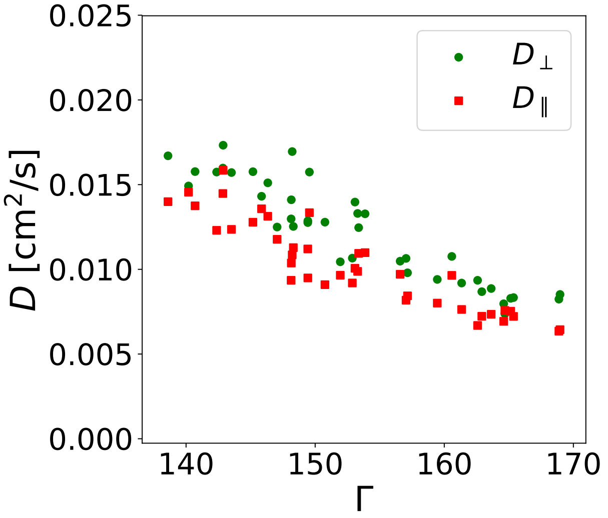

Figure 3.53 Diffusion constants $D_\perp$ and $D_\parallel$ vs Γ in the periodic potential with $A = 0.5$ K and $p = 56/40 \approx 1.4$. The procedure is outlined in the caption for Fig. 3.35. The diffusion constants are very small in the considered range of Γ, however the freezing transition does not occur for $\Gamma < 170$.

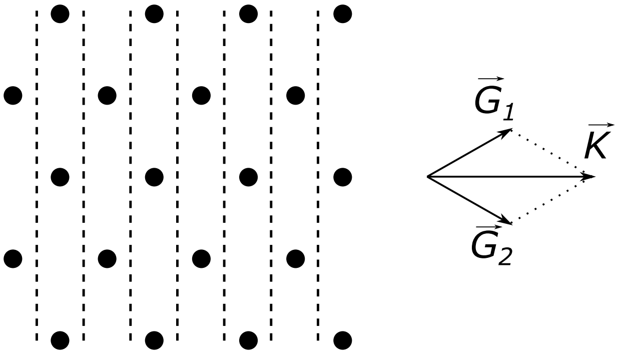

Figure 3.54 The higher order commensurate configuration, where $\boldsymbol{K} = \boldsymbol{G}_1 + \boldsymbol{G}_2$. Here $\boldsymbol{G}_1$ and $\boldsymbol{G}_2$ are two elementary reciprocal lattice vectors of the triangular lattice, $|G_1| = |G_2| = 4\pi/\sqrt{3}a$. The vertical dashed lines show the periodic potential maxima.

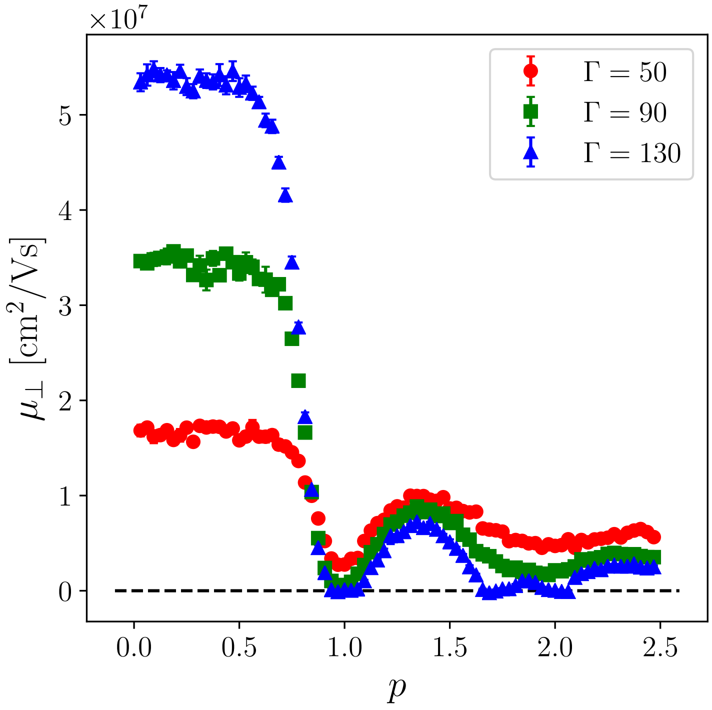

Figure 3.55 The Mobility $\mu_\perp$ of the strongly correlated electron system as a function of the commensurability ratio p for $\Gamma = 50$, 90, and 130. $A = 0.05$ K for all three curves.

studies.

3.5.7 Mobility $\mu_\perp$ as a function of p

To illustrate the behavior of the mobility as a function of commensurability, we calculated $\mu_\perp$ as a function of p for the fixed value of $A = 0.05$ K. Such curves for three values of Γ are shown in Fig. 3.55. The potential amplitude is small compared to the temperature for all three curves. For two curves, namely $\Gamma = 50$ and 90, the system remains a liquid in all points of the simulation. For $\Gamma = 130$, the system becomes frozen in small intervals around the points $p = 1$, $p = \sqrt{3}$, and $p = 2$. It remains in the liquid phase in all other points, where it is incommensurate with the potential.

All three curves share several general features already discussed in the previous sections. First, for small $p \ll 1$, $\mu_\perp$ has a plateau. At this plateau, the mobility is approximately equal to the mobility in a uniform system with the same temperature. Then all three curves have a sharp dip at the point $p = 1$. Here the system is most sensitive to the periodic potential. For $1 < p < 2$, the mobility is increasing up to the point $p \approx 1.4$, after which it begins to decrease until it reaches a minimum at $p \approx 2$. The curve $\Gamma = 130$ has an additional minimum at $p \approx \sqrt{3}$, where the system becomes frozen into the configuration shown in Fig. 3.54. We note that the curve $\Gamma = 130$ reaches zero at its minima, since the system is pinned when it is frozen into a commensurate crystal. The two other curves have small but nonzero values at their minima because they remain in the liquid phase for all p.

3.6 Conclusions

In this chapter, we studied the dynamical properties of a strongly correlated 2D electron system on the surface of liquid helium in an external 1D periodic potential. To study this system, we developed novel computational methods for microscopic simulation of the scattering of electrons by the quantized excitations in helium. We also developed a 2D Ewald summation algorithm that is parallelized for computations on a GPU. This increases the computation speed by a factor up to 16 compared to a single CPU. These are the necessary ingredients for studying transport properties of strongly correlated electrons on the helium surface.

With the developed tools, we studied structure, diffusion, and mobility in both a spatially uniform system and a system in a periodic potential. The diffusion coefficient was determined as the proportionality coefficient between the mean squared electron displacement and the time which, as we showed, was independent of time. In the spatially uniform system, we observed the Wigner crystallization transition. We simulated a large system with $N = 1600$ electrons, and observed the Wigner crystallization at $\Gamma \approx 137$, which is slightly larger than the values obtained in previous simulations. The previous studies were done with significantly smaller numbers of particles. The weak scattering by ripplons and phonons does not significantly change the diffusion or the phase transition in our study. We also calculated the mobility in the spatially uniform system with and without the inter-electron interaction. In both cases, the results are in good agreement with the theory in Ref. [3].

The central part of our study is devoted to the effects of a periodic potential on the system of strongly correlated electrons. In particular, we were interested in the effects of commensurability of the potential and the electron system. We found that the degree of commensurability plays an important role even when the electron system is in the liquid phase. In this case, the degree of commensurability is defined for the triangular lattice that would exist at a given electron density. We found that diffusion in the system is insensitive to the periodic potential when the period of the potential is much larger than the average inter-electron distance. In this case, the Wigner crystallization takes place at approximately the same point as it would in the uniform system. The transverse mobility is also very weakly affected by the potential, as opposed to the case of a non-interacting electron gas in the same potential. This remarkable insensitivity is a result of the effective averaging of the potential by the electrons. In this regime, approximately as many electrons reside in the periodic potential minima as near the maxima, due to the strong electron-electron interaction and a large mismatch between the period of the potential and the mean inter-electron spacing.

We found the situation to be dramatically different when the system is maximally commensurate with the potential. In this case, both the diffusion and the mobility are very sensitive to the periodic potential even for the potential amplitude much smaller than the temperature. For such a weak potential, there would be no effect in a non-interacting electron gas. However, the effect is strong in the interacting system because of the strong electron-electron correlations. The position and the way the diffusion goes to zero at the freezing transition are significantly altered by the commensurate potential. The freezing temperature is increased as compared to the uniform system, while the transition becomes smooth as seen in the diffusion behavior.

Some of the most interesting results were obtained for a strongly correlated liquid in the commensurate potential. We found that the transverse mobility is exponentially decreasing as a function of the periodic potential amplitude in the commensurate liquid. The strength of the effect is directly proportional to the correlation length squared in the liquid. One can understand that by considering the current as a series of collective displacements of many electrons. The activation energy of this process is proportional to the number of electrons within the radius determined by the correlation length. This relation can provide an opportunity to experimentally measure the correlation length in an electron liquid via transport measurements.

In an "incommensurate" liquid (i.e., for the periodic potential incommensurate with the electron crystal of the same density as the considered liquid) the mobility is also found to exponentially decay with the potential strength. However, the decay rate is significantly smaller than that in the commensurate case and quickly decreases with the increasing period of the potential. In an incommensurate liquid, the current also results from a strongly correlated electron motion. However, the electron distribution is less correlated with the potential, and as a result the average activation energy is reduced.

The commensurate-incommensurate transition in the Wigner solid was also studied. We find that, qualitatively, the C-I transition follows the scenario outlined by the theory of Pokrovsky and Talapov for a short-range inter-particle potential [26]. Close to the C-I transition, we observe density solitons in the Wigner crystal, as predicted by the theory. When the system is approaching maximal commensurability, the structure changes to a set of ordered electron channels residing in the periodic potential minima. We also observe some intermediate disordered structures in the transition region. The phase transition temperature and the temperature dependence of the diffusion coefficient are significantly modified in the C-I transition region. In the vicinity of the transition, the freezing temperature is significantly lowered compared to that in the uniform system. This is in contrast to the commensurate case, where the phase transition temperature is increased by the periodic potential.

We also studied thermalization in a Wigner crystal and in a strongly correlated electron liquid. We found that both systems thermalize in our simulations, with the thermalization time on the order of the short-wavelength plasma oscillation period. This behavior is substantially different from that observed in the well-known Fermi-Pasta-Ulam problem. The difference may be attributed to the difference in dimensionality and to the long-range nature of the Coulomb potential in our study.

The results of this work provide an insight into the behavior of the strongly correlated 2D electron system in a periodic potential. We show the importance of the electron-electron correlations in the liquid phase. The results also suggest that the periodic potential is a promising tool for an experimental investigation of various properties of strongly correlated electron systems.

CHAPTER 4

CONCLUSIONS

Electron-vibrational coupling, which is the topic of this thesis, plays a key role in condensed matter physics. This coupling has been studied in a variety of contexts, from transport phenomena to polaronic effects to transitions to a superconducting state. Recent progress in mesoscopic physics, that has led to a discovery of low-dimensional electron systems and to creation of nano- and microscopic mechanical resonators, has opened a new era in studying effects of the electron-vibrational coupling. Many aspects of these effects are novel and challenging, which makes investigating them interesting and important.

In this thesis we have shown that the electron-vibrational coupling can strongly modify the dynamics of nano- and micromechanical vibrational modes and that it enables revealing and characterizing strong electron correlations in a nondegenerate two-dimensional electron liquid. Even though these two groups of phenomena are very different, their analysis is based on the common ideas of the transport phenomena in condensed matter physics, and the results demonstrate the richness of the many-body phenomena in the nascent areas of condensed matter physics.

One of the most common types of nano- and micromechanical resonators are resonators made of semiconductors, which is an immediate consequence of the progress in semiconductor technology. By doping semiconductors with impurities, one can significantly change the density of electrons and holes. Our results show that such a change has a profound effect on the dynamics of vibrational modes in the resonators. We have studied the case of *n*-doping, where it is the electron density that is changed by doping. The specific calculations referred to the most broadly used semiconductors, silicon and germanium. These semiconductors have a multi-valley band structure. In the absence of strain, equivalent valleys are equally populated by the electrons. The strain associated with nanomechanical vibrations breaks the symmetry and makes the valleys non-equivalent. This leads to repopulations of the valleys. In the most cases of interest, the rate of electron redistribution over the valleys is much larger than the vibration frequency, so that the valley populations follow the vibrations adiabatically. In turn, the electron redistribution over the valleys affects the vibrations, so that overall we have a mechanism of a nonlinear electron-mediated self-action of the vibrations.

The change of the valley populations is a strongly nonlinear function of the strain tensor. It is controlled by a very large ratio of the electron-phonon coupling energy to the electron chemical potential or the temperature. It is this ratio that makes the nonlinearity of the vibrational modes in doped semiconductor structures strong. The most pronounced effect of the nonlinearity is the amplitude dependence of the vibration frequency. To the leading order, it is determined by the quartic terms in the expansion of the free energy in strain. For the reason described above, these terms are comparatively large.

We have calculated the quartic in the strain components of the nonlinear elasticity tensor in n-doped semiconductors. For silicon, the calculation required going beyond the standard deformation potential approximation and taking into account the band degeneracy in the absence of strain. As an application, we found the amplitude dependence of the vibration frequency for several modes used in silicon-based micromechanical resonators. This dependence has a characteristic form as a function of the electron density and temperature. We have also described the temperature dependence of the mode frequencies, which comes from the quadratic terms of the elasticity tensor induced by the electron-vibrational coupling.

Our results provide an insight into the experimentally observed strong mode nonlinearity in doped crystals. They also provide a means for measuring the parameters of the electron-phonon coupling which are not easy to directly access otherwise. In terms of applications, these results are important for developing thermally stable nanomechanical reosnators with a controllable amplitude dependence of the vibration frequency.

The electron-vibrational coupling in the other system that we studied, electrons on the helium surface, is of special interest, since the electron system is strongly correlated. It forms a nondegenerate liquid or a solid. If in the case of a solid one can at least characterize elementary excitations in the electron system, the very language of elementary excitations is not helpful in the case of a liquid. A natural path toward understanding a liquid is molecular dynamics simulations. We have performed these simulations for a record-large electron system, with the account taken of the microscopic mechanisms of the electron coupling to vibrational excitations in helium. Along with a spatially uniform system, we studied the electron system placed into a spatially periodic potential with the period comparable to the mean inter-electron distance.

Our results for a uniform system showed that self-diffusion in the system is a sensitive tool that allows one to identify the melting transition. The mobility, on the other hand, is basically unchanged at the transition and is totally controlled by the electron-vibrational coupling. The results obtained for a strongly correlated liquid are in agreement with the analytic theory based on the assumptions of a fast inter-electron momentum exchange and the independence of the scattering of an individual electron by helium excitations from the electron-electron interaction.

The results have also provided an insight into thermalization in strongly correlated electron liquids and solids driven away from equilibrium. We have found that the thermalization is fast and the Fermi-Pasta-Ulam absence of thermalization does not occur in a system with long-range interaction, irrespective of the presence of long-range order.

The major emphasis of the work was placed on the dynamics of the system in a periodic potential. We found that, even where the electrons form a liquid, the dynamics, and in particular the electron mobility transverse to the potential troughs, is highly sensitive to the effective commensurability, i.e., the relation between the mean inter-electron distance and the period of the potential. For a large potential period, the mobility is weakly affected by the potential even where the potential barriers are much higher than temperature, in contrast to a single-electron system. On the other hand, unexpectedly, in the fully commensurate case, the mobility displays an exponential dependence on the barrier height even where this height is small compared to the temperature. This dependence allows one to directly measure the correlation length in the electron liquid. This is one of our central results.

We have also found that a periodic potential can strongly affect the melting transition, leading to a different transition temperature and a qualitatively different dependence of the way the self-diffusion coefficient goes to zero at the transition. The shift of the transition temperature has opposite signs close and far from commensurability. In the commensurate solid phase, the mobility transverse to the potential troughs vanishes. It displays a characteristic dependence on the potential period close to full commensurability.

Overall, the results on the electrons on helium show that this system can be used to study commensurate-incommensurate transitions in the regime of an effectively weak electron-vibrational coupling. This regime has not been explored before. The transitions can be directly accessed by measuring the electron mobility, and moreover, the measurements can provide a direct means for determining the correlation length in the electron liquid.

4.1 Outlook

The theory developed in the thesis can be, and hopefully will be, extended in several directions. It is interesting and important for applications to understand the electron-vibrational coupling in semiconductor micromechanical resonators in the case of p-doping. A strong effect in this case comes, in the first place, from the strain-induced splitting of the valence band. Its anisotropy comes from the warping of the heavy hole band. Another open problem is the effect of the electron-vibrational coupling on decay of the mechanical modes and the possibility to control this decay in doped semiconductors using phononic crystals. Yet another problem emerges when the size of the resonator is reduced and the length associated with intervalley scattering becomes comparable to the resonator size.

For electrons on helium, one of the most challenging open problems is electron spin relaxation. The mechanism is not known and the attempts to measure the relaxation rate have not been successful so far. By putting the electrons into a spatially periodic magnetic field (with a nonzero mean), one “turns on" a spin-orbit coupling, which can modulate the electron density and lead to commensurate-incommensurate transitions. These transitions should be detectable through the mobility measurements, whereas an extension of the theory to this case is more or less straightforward. Yet another extension, which is important for a direct comparison with the experiment, is an incorporation of the screening of the electron-electron interaction by the image force in the substrate, which partly reduces the Coulombic tail of the interaction. This extension is also straightforward, given that it is the long-range part of the interaction that is most complicated to allow for.

APPENDIX

A.1 Expansion of the free energy in terms of the strain-induced shift of the energy valleys

The major effect of a strain on the electron free energy comes from the shift of the energy valleys. We will assume that valley α is shifted in energy by δE_α and the shift is small, $|\delta E_\alpha| \ll \max(k_BT, \mu_0)$, where μ_0 is the chemical potential in the absence of strain. We further assume that the vibrations are slow compared to the time it takes the electron system to come, locally, to thermal equilibrium for given values of δE_α, i.e., the temperature and the chemical potential are the same in all valleys. This is true for almost any realistic system, since inter- and intravalley relaxation times are smaller than 10^{-11} s [198, 199, 200]. Since for high electron densities the thermal conductivity is high, the change of the temperature compared to the ambient temperature can be disregarded; also, as mentioned in the main text, the electron density n summed over all valleys is constant.

The contribution $F^{(\alpha)}$ of the electrons in valley α to the free energy density can be written as $F^{(\alpha)} = \Omega^{(\alpha)} + \mu n^{(\alpha)}$ with

$$\Omega^{(\alpha)} = -k_BT \int_0^\infty dE\, \rho(E) \log\left[1 + e^{(\mu - E - \delta E_\alpha)/k_BT}\right],$$

where $\rho(E)$ is the electron density of states in a valley, which is the same for all valleys, μ is the chemical potential, and $n^{(\alpha)} = -\partial\Omega^{(\alpha)}/\partial\mu$ is the electron density in valley α. The total free energy can be rewritten in terms of Fermi-Dirac integrals:

$$F = \frac{nk_BT}{NF_{1/2}} \sum_{\alpha=1}^{N} \left[\frac{\mu}{k_BT} F_{1/2}\left(\frac{\mu - \delta E_\alpha}{k_BT}\right) - \frac{2}{3} F_{3/2}\left(\frac{\mu - \delta E_\alpha}{k_BT}\right)\right] \tag{1}$$

We use the standard notation $F_{1/2}(x) = \int_0^\infty dy\, y^{1/2}/[1 + \exp(y - x)]$; primes indicate differentiation over x, for example, $F'_{1/2} \equiv dF_{1/2}/dx$. Function $F_{1/2}$ and its derivatives are calculated for $x = \mu_0/k_BT$. The chemical potential in the strained crystal is changed by $k_BT\delta(\varepsilon)$, which is found from conservation of the total electron density:

$$n = \sum_{\alpha=1}^{N} n^{(\alpha)} = 2\pi^{-1/2} N_c \sum_{\alpha=1}^{N} F_{1/2}\left((\mu_0 + k_BT\delta(\varepsilon) - \delta E_\alpha)/k_BT\right), \tag{2}$$

that must be equal to its value in an unstrained crystal:

$$n = 2\pi^{-1/2} V N_c N F_{1/2}\left(\mu_0/k_B T\right), \tag{3}$$

where

$$N_c = \frac{2m_{\rm eff}^{3/2}}{\hbar^3}\left(\frac{T}{2\pi}\right)^{3/2}. \tag{4}$$

From (2), $\delta(\varepsilon)$ can be expressed in terms of δE_α, i.e., in terms of strain. Expanding Fermi integrals around the unstrained values and iteratively solving (2) for δ to the third order, we obtain:

$$\delta^{(3)}(\varepsilon) = \overline{\Delta_\varepsilon} + \frac{F''_{1/2}}{2F'_{1/2}}\left((\overline{\Delta_\varepsilon})^2 - \overline{\Delta^2_\varepsilon}\right) + \frac{F'''_{1/2}}{6F'_{1/2}}\left(\overline{\Delta^3_\varepsilon} - 3\overline{\Delta^2_\varepsilon}\,\overline{\Delta_\varepsilon} + 2\overline{\Delta_\varepsilon}^3\right) \tag{5}$$

Here, $\overline{\Delta^m_\varepsilon} = N^{-1}\sum_\alpha(\delta E_\alpha/k_B T)^m$. Third order terms in $\delta(\varepsilon)$ are enough to obtain fourth-order expansion of the free energy.

Using (5) to expand (1) to the 4th order in the strain-induced shifts δE_α, we find that, in an N-valley semiconductor, the change δF_e of the free energy density summed over the valleys is

$$\begin{aligned}\frac{\delta F_e}{n k_B T} =& \bar{\Delta}_\varepsilon + \frac{1}{2}\frac{F'_{1/2}}{F_{1/2}}\left[(\bar{\Delta}_\varepsilon)^2 - \overline{\Delta^2_\varepsilon}\right] + \frac{1}{6}\frac{F''_{1/2}}{F_{1/2}}\left[\overline{\Delta^3_\varepsilon} - 3\overline{\Delta^2_\varepsilon}\,\bar{\Delta}_\varepsilon + 2(\bar{\Delta}_\varepsilon)^3\right] \\ &+ \frac{1}{8}\frac{{F''_{1/2}}^2}{F_{1/2}F'_{1/2}}\left[(\overline{\Delta^2_\varepsilon})^2 - 2\overline{\Delta^2_\varepsilon}\,(\bar{\Delta}_\varepsilon)^2 + (\bar{\Delta}_\varepsilon)^4\right] \\ &+ \frac{1}{24}\frac{F'''_{1/2}}{F_{1/2}}\left[4\overline{\Delta^3_\varepsilon}\,\bar{\Delta}_\varepsilon - \overline{\Delta^4_\varepsilon} - 6\overline{\Delta^2_\varepsilon}\,(\bar{\Delta}_\varepsilon)^2 + 3(\bar{\Delta}_\varepsilon)^4\right].\end{aligned} \tag{6}$$

Equation (6) immediately gives the tensors $\widehat{\Lambda}_n$ of the expansion of the free energy increment (2.6) if one expresses the shift δE_α of the valleys in terms of the strain tensor. In the deformation potential approximation the relation between δE_α and $\hat{\varepsilon}$ is given in the main text, see also Eq. (7) below.

In the case of Si crystals, which are often used in micromechanical resonators, an important contribution to δE_α comes from the shear-strain induced splitting of the electron energy bands at the zone boundary. Shear strain does not lead to the valley shift in the deformation potential approximation. The overall shift of valley α, to the lowest order in the coupling that causes it (i.e., to the first order in the deformation potential where its contribution is nonzero and to the second order in the band splitting for shear strain) is [129]:

$$\delta E_\alpha = \sum_{ij} \Xi_{ij}^{(\alpha)} \varepsilon_{ij} - \Xi_{\mathrm{sh}} \varepsilon_\alpha^2, \quad \Xi_{\mathrm{sh}} = \frac{4\Xi_{\mathrm{u}'}^2}{\Delta E}. \tag{7}$$

The derivation of this equation using a symmetry argument is reproduced in Appendix A.6. Here we use that silicon has six valleys located at the $\langle 100 \rangle$ axes, and we chose the coordinate axes x, y, z along $\langle 100 \rangle$. Respectively, the valley index α takes on three values that correspond to the x, y, z axes (the valleys lying on the same axis, but in the opposite directions, are equivalent). The strain ε_α, which enters the second term in the right-hand side of Eq. (7), is a component of the strain tensor ε_{ij} with i, j such that $i, j \neq \alpha$ and $i \neq j$. The parameter $2\Xi_{u'}$ is the interband matrix element of the electron-phonon coupling calculated for the electron conduction bands Δ_1 and $\Delta_{2'}$ at the X point on the boundary of the Brillouin zone, where the bands cross; ΔE is the energy separation between the bands Δ_1 and $\Delta_{2'}$ at the value of the wave vector $\boldsymbol{k}$ that corresponds to the conduction band minimum. Parameter Ξ_{sh} is the effective deformation potential of two-phonon coupling to shear strain. The numerical value of Ξ_{sh} is not well known. The experimental data give $\Xi_{u'} \approx 7-8$ eV [129, 133] and the numerical data on the band splitting give $\Delta E \approx 0.7$ eV [201] so that Ξ_{sh} is in the range of $280-360$ eV; this is essentially an order of magnitude estimate.

In calculating δF_e in Eq. (6) we kept terms that are quartic in $\hat{\varepsilon}$. The components of the tensors $\widehat{\Lambda}_k$ in Eq. (2.6) are expressed in terms of δF_e as

$$(\Lambda_k)_{i_1 j_1 \ldots i_k j_k} = \frac{\partial^k \delta F_e}{\partial \varepsilon_{i_1 j_1} \ldots \partial \varepsilon_{i_k j_k}}. \tag{8}$$

Tensors $\widehat{\Lambda}$ are symmetric with respect to the interchange of indices $i_k \leftrightarrow j_k$ and the pairs $(i_k j_k) \leftrightarrow (i_{k'} j_{k'})$. For the considered long-wavelength strain, tensors $\widehat{\Lambda}_k$ are independent of coordinates. The corrections $\widehat{\Lambda}_2$ to the linear elasticity tensors were found previously [121, 122] and are not discussed in this paper.

A.2 Nonlinear elastic constants of germanium

In this section we provide the corrections to the nonlinear elastic constants of germanium, which are due to the redistribution of the electrons over the valleys. Germanium has four equivalent valleys in the conduction band, which are located on the boundary of the Brillouin zone along $\langle 111 \rangle$ axes. We use the Voigt notation and write the components of the corrections to the nonlinear elasticity tensor $\delta\hat{c}$ in the frame where the axes (x, y, z) are along the $\langle 100 \rangle$ directions of the crystal. Using the results of Appendix A.1, we obtain

$$\begin{aligned}
\delta c_{456} &= \frac{n\Xi_u^3 F''_{1/2}}{27 F_{1/2}(k_B T)^2}, \\
\delta c_{4444} &= \frac{n\Xi_u^4}{81(k_B T)^3}\left(\frac{3(F''_{1/2})^2}{F_{1/2}F'_{1/2}} - \frac{F'''_{1/2}}{F_{1/2}}\right), \\
\delta c_{4455} &= \frac{n\Xi_u^4}{81(k_B T)^3}\left(\frac{(F''_{1/2})^2}{F_{1/2}F'_{1/2}} - \frac{F'''_{1/2}}{F_{1/2}}\right).
\end{aligned} \tag{9}$$

The notations are the same as in Appendix A.1 and in Table 2.1. The electron-phonon coupling does not contribute to the other third- and fourth-order elastic constants.

Corrections δc_{44} and δc_{456} for germanium were found by Keyes [120]; however, his final expression for δc_{456} differs from Eq. (9) by a factor of 4 (our expressions for δc_{44} coincide with Ref. [120]). Parameters δc_{4444} and δc_{4455} have not been found before, to the best of our knowledge. In the limiting cases, corrections δc_{4444} and δc_{4455} have the same dependence on temperature and electron density as constant nC_2 discussed in Sec. 2.4.1.

A.3 Lamé and length extension modes in $\langle 100 \rangle$ and $\langle 110 \rangle$ orientations

In this appendix, we find the two modes we are interested in: length extension and Lamé. These results are well known [202], but it is convenient to have them derived here. First, we write general equations of motion of an elastic medium in linear approximation:

$$\rho \ddot{u}_i = c_{ijkl}\frac{\partial^2 u_k}{\partial x_j \partial x_l}. \tag{10}$$

Here ρ is the material density, u_i are components of the displacement tensor, and c_{ijkl} is the stiffness tensor in explicit coordinate subscript notation. Taking into account that in a cubic crystal the "off-diagonal" terms like c_{xxxy} or c_{xzxy} vanish, we obtain explicit equations of motion, with tensors written in Voigt notation:

$$\begin{aligned}
\rho\ddot{u}_x &= c_{11}\frac{\partial^2 u_x}{\partial x^2} + c_{12}\left(\frac{\partial^2 u_y}{\partial x\partial y} + \frac{\partial^2 u_z}{\partial x\partial z}\right) + c_{44}\left(\frac{\partial^2 u_x}{\partial y^2} + \frac{\partial^2 u_y}{\partial x\partial y} + \frac{\partial^2 u_x}{\partial z^2} + \frac{\partial^2 u_z}{\partial x\partial z}\right)\\
\rho\ddot{u}_y &= c_{11}\frac{\partial^2 u_y}{\partial y^2} + c_{12}\left(\frac{\partial^2 u_x}{\partial x\partial y} + \frac{\partial^2 u_z}{\partial y\partial z}\right) + c_{44}\left(\frac{\partial^2 u_y}{\partial x^2} + \frac{\partial^2 u_x}{\partial x\partial y} + \frac{\partial^2 u_y}{\partial z^2} + \frac{\partial^2 u_z}{\partial y\partial z}\right)\\
\rho\ddot{u}_z &= c_{11}\frac{\partial^2 u_z}{\partial z^2} + c_{12}\left(\frac{\partial^2 u_y}{\partial y\partial z} + \frac{\partial^2 u_x}{\partial x\partial z}\right) + c_{44}\left(\frac{\partial^2 u_z}{\partial y^2} + \frac{\partial^2 u_y}{\partial z\partial y} + \frac{\partial^2 u_z}{\partial x^2} + \frac{\partial^2 u_x}{\partial x\partial z}\right)
\end{aligned} \tag{11}$$

To obtain vibrational modes, we need to solve these equations for given boundary conditions. Before we do that, let us show how stiffness tensor is transformed under coordinate system rotations. This will help us to obtain modes in $\langle 110\rangle$ geometry. The symmetry of the stiffness tensor in coordinates rotated by an arbitrary angle around z-axis is modified. In general, the stiffness tensor becomes:

$$c' = \begin{pmatrix}
c'_{11} & c'_{12} & c'_{13} & 0 & 0 & c'_{16}\\
c'_{12} & c'_{11} & c'_{13} & 0 & 0 & -c'_{16}\\
c'_{13} & c'_{13} & c'_{33} & 0 & 0 & 0\\
0 & 0 & 0 & c'_{44} & 0 & 0\\
0 & 0 & 0 & 0 & c'_{44} & 0\\
c'_{16} & -c'_{16} & 0 & 0 & 0 & c'_{66}
\end{pmatrix} \tag{12}$$

In particular, if coordinates are rotated by $\pi/4$ around z-axis, we obtain:

$$c' = \begin{pmatrix}
\frac{c_{11}}{2}+\frac{c_{12}}{2}+c_{44} & \frac{c_{11}}{2}+\frac{c_{12}}{2}-c_{44} & c_{12} & 0 & 0 & 0\\
\frac{c_{11}}{2}+\frac{c_{12}}{2}-c_{44} & \frac{c_{11}}{2}+\frac{c_{12}}{2}+c_{44} & c_{12} & 0 & 0 & 0\\
c_{12} & c_{12} & c_{11} & 0 & 0 & 0\\
0 & 0 & 0 & c_{44} & 0 & 0\\
0 & 0 & 0 & 0 & c_{44} & 0\\
0 & 0 & 0 & 0 & 0 & \frac{c_{11}}{2}-\frac{c_{12}}{2}
\end{pmatrix} \tag{13}$$

In the rotated coordinates, the Eqs. (11) are modified as follows:

$$\begin{aligned}
\rho \ddot{u}_x &= c'_{11}\frac{\partial^2 u_x}{\partial x^2} + c'_{12}\frac{\partial^2 u_y}{\partial x \partial y} + c'_{13}\frac{\partial^2 u_z}{\partial x \partial z} + c'_{66}\left(\frac{\partial^2 u_x}{\partial y^2} + \frac{\partial^2 u_y}{\partial x \partial y}\right) + c'_{44}\left(\frac{\partial^2 u_x}{\partial z^2} + \frac{\partial^2 u_z}{\partial x \partial z}\right)\\
\rho \ddot{u}_y &= c'_{11}\frac{\partial^2 u_y}{\partial y^2} + c'_{12}\frac{\partial^2 u_x}{\partial x \partial y} + c'_{13}\frac{\partial^2 u_z}{\partial y \partial z} + c'_{66}\left(\frac{\partial^2 u_y}{\partial x^2} + \frac{\partial^2 u_x}{\partial x \partial y}\right) + c'_{44}\left(\frac{\partial^2 u_y}{\partial z^2} + \frac{\partial^2 u_z}{\partial y \partial z}\right)\\
\rho \ddot{u}_z &= c'_{33}\frac{\partial^2 u_z}{\partial z^2} + c'_{13}\left(\frac{\partial^2 u_y}{\partial y \partial z} + \frac{\partial^2 u_x}{\partial x \partial z}\right) + c'_{44}\left(\frac{\partial^2 u_z}{\partial y^2} + \frac{\partial^2 u_y}{\partial z \partial y} + \frac{\partial^2 u_z}{\partial x^2} + \frac{\partial^2 u_x}{\partial x \partial z}\right)
\end{aligned} \tag{14}$$

Young modulus and Poisson ratio are also modified in the rotated system. Poisson ratios for y and z directions are different now [203]. For <110> direction, the Poisson ratios and the Young modulus become:

$$\begin{aligned}
\sigma_2 &= \frac{{c'_{13}}^2 - c'_{33}c'_{12}}{c'_{11}c'_{33} - {c'_{13}}^2} = \frac{c_{11}\left(c_{11}+c_{12}-2c_{44}\right)-2c_{12}^2}{c_{11}\left(c_{11}+c_{12}+2c_{44}\right)-2c_{12}^2}\\
\sigma_3 &= \frac{c'_{13}\left(c'_{12}-c'_{11}\right)}{c'_{11}c'_{33} - {c'_{13}}^2} = \frac{4c_{12}c_{44}}{c_{11}\left(c_{11}+c_{12}+2c_{44}\right)-2c_{12}^2}\\
E &= \frac{c'_{33}\left({c'_{11}}^2 - {c'_{12}}^2\right) + 2{c'_{13}}^2\left(c'_{12}-c'_{11}\right)}{c'_{11}c_{33} - {c'_{13}}^2} = \frac{4c_{44}\left(c_{11}(c_{11}+c_{12})-2c_{12}^2\right)}{c_{11}(c_{11}+c_{12}+2c_{44})-2c_{12}^2}
\end{aligned} \tag{15}$$

In the case of <100> orientation, the expressions are greatly simplified by symmetry, and the result is well known:

$$\begin{aligned}
\sigma_2 = \sigma_3 \equiv \sigma &= -\frac{c_{12}}{c_{11}+c_{12}}\\
E &= \frac{c_{11}\left(c_{11}+c_{12}\right)-2c_{12}^2}{c_{11}+c_{12}}
\end{aligned} \tag{16}$$

Now we can find solutions to Eqs. (14) and (11) in a square plate with side L. One solution is

$$\begin{aligned}
u_x &= \frac{L}{\pi}\cos(\pi x/L)\sin(\pi y/L)e^{-i\omega t}\\
u_y &= -\frac{L}{\pi}\sin(\pi x/L)\cos(\pi y/L)e^{-i\omega t}\\
u_z &= 0
\end{aligned} \tag{17}$$

This solution has the name of first Lamé mode. This solution satisfies both Eqs. (14) and (11), with frequencies being

$$\omega^{(\text{Lame})}_{<100>} = \frac{\pi}{l}\sqrt{\frac{c_{11}-c_{12}}{\rho}},$$
$$\omega^{(\text{Lame})}_{<110>} = \frac{\pi}{l}\sqrt{\frac{2c_{44}}{\rho}}$$

for plate sides along <100> and <110> directions respectively. Strain field (without time factor) in <100> case is

$$\varepsilon_{xx} = \varepsilon_1 = -\sin(\pi x/L)\sin(\pi y/L),$$
$$\varepsilon_{yy} = \varepsilon_2 = \sin(\pi x/L)\sin(\pi y/L),$$

while in <110> case, the strain tensor has only a shear component:

$$\varepsilon_{xy} = \frac{1}{2}\varepsilon_6 = \sin(\pi x/L)\sin(\pi y/L).$$

Now let us turn to length extension modes. Since the plate extension mode is quite complicated, we consider a simplified model for a thin beam. In this approximation, the motion can be described by the Young modulus E only, and transverse strain can be found with the Poisson ratios. We assume that the resonator dimensions are $l_x \times l_y \times l_z$ and the center of it is fixed. The equation of motion is

$$\frac{\partial^2 u_x}{\partial x^2} - \frac{\rho}{E}\frac{\partial^2 u_x}{\partial t^2} = 0 \tag{18}$$

For free ends of the beam, the first solution is

$$u_x = -\frac{1}{k}\cos(kx)e^{-i\omega t}, \tag{19}$$

with $k = \pi/l_x$ and frequency $\omega = \frac{\pi}{l_x}\sqrt{\frac{E}{\rho}}$. Using Poisson ratios, one can obtain

$$u_y \approx \nu_y \varepsilon_{xx} y = \sigma_2 y \cos(kx)e^{-i\omega t}$$
$$u_z \approx \nu_z \varepsilon_{xx} z = \sigma_3 z \cos(kx)e^{-i\omega t}$$

Directions <100> and <110> are different only by the values of the Young modulus and Poisson ratios that one should use (Eqs. (15)–(16)). We will not calculate strain components for the length extension modes here for brevity.

A.4 Duffing nonlinearity parameter for a Lamé mode in a square single-crystal plate

We consider a square plate with side L and thickness h made out of a single crystal with cubic symmetry. If the crystal is cut out along $\langle 100\rangle$ or $\langle 110\rangle$ axes, one of the simplest modes is the first Lamé mode [202]. The normalized displacement field is

$$\begin{aligned} u_x^{(\nu)} &= \sqrt{2}\cos(\pi x/L)\sin(\pi y/L),\\ u_y^{(\nu)} &= -\sqrt{2}\sin(\pi x/L)\cos(\pi y/L). \end{aligned} \tag{20}$$

Here, x and y axes are in the lateral plane along the sides of the square, axis z is perpendicular to the plate and $u_z^{(\nu)} = 0$. Calculating the strain tensor for the displacement (20) and substituting the expressions into Eqs. (2.8) and the relation

$$M\omega_\nu^2 = \int d\boldsymbol{r}\widehat{\Lambda}_2^{(f)} \cdot \hat{\varepsilon}^{(\nu)} \otimes \hat{\varepsilon}^{(\nu)}, \tag{21}$$

for the plate cut out along $\langle 100\rangle$ axes we obtain, in Voigt notation for the elasticity tensors,

$$\begin{aligned} M\omega_\nu^2 &= \pi^2 h\left(c_{11} - c_{12}\right),\\ \gamma_\nu &= \frac{3\pi^4 h}{16L^2}\left(c_{1111} - 4c_{1112} + 3c_{1122}\right). \end{aligned} \tag{22}$$

If we consider silicon and take into account only the contribution $\delta\hat{c}$ to the nonlinear elasticity tensor $\hat{c}$, with the account taken of Table 2.1, the expression for γ_ν simplifies to

$$\gamma_\nu = (27\pi^4 h/32L^2)\delta c_{1111}. \tag{23}$$

For the Lamé mode cut along the $\langle 110\rangle$ axis, if the tensors are calculated in the axes $\langle 100\rangle$, we have

$$\begin{aligned} M\omega_\nu^2 &= 2\pi^2 h c_{44},\\ \gamma_\nu &= (3\pi^4 h/2L^2)\delta c_{4444}. \end{aligned} \tag{24}$$

Note that only coupling to shear strain contributes to the nonlinearity parameter γ_ν in this case.

A.5 Duffing nonlinearity parameter for an extension mode in a single-crystal narrow beam

We consider the fundamental extension mode in a thin beam of length L with a rectangular cross-section of area $S \ll L^2$. The beam is cut along a symmetry axis, and the sides are also along symmetry planes of a cubic crystal. From the free-surface boundary conditions, the normalized displacement field is [202]:

$$\begin{aligned}
u_x^{(v)} &\approx \sqrt{2}\cos(\pi x/L), \\
u_y^{(v)} &\approx \frac{\sqrt{2}\pi\sigma_2}{L} y\sin(\pi x/L), \\
u_y^{(v)} &\approx \frac{\sqrt{2}\pi\sigma_3}{L} z\sin(\pi x/L).
\end{aligned} \tag{25}$$

This expression takes into account transverse compression that accompanies beam extension and uses the smallness of the beam cross-section; corrections $\sim S/L^2$ are disregarded. The transverse compression in a cubic crystal cut in a symmetric direction is described by Poisson's ratios σ_2 and σ_3. Generally, they do not coincide. In Eq. (25) the transverse coordinates y and z are counted off from the center of the beam

For the longitudinal direction of the beam $\langle 100 \rangle$ and the sides parallel to (100) planes, the Poisson parameters are equal, $\sigma_2 = \sigma_3$ and $\sigma \equiv \sigma_2 = \sigma_3 = c_{12}/(c_{11}+c_{12})$. In this case Eqs. (2.8) and (21) give

$$\begin{aligned}
M\omega_v^2 &= \frac{\pi^2 S\left(c_{11}\left(c_{11}+c_{12}\right)-2c_{12}^2\right)}{L\left(c_{11}+c_{12}\right)}, \\
\gamma_v &= (\pi^4 S/4L^3)\,[c_{1111} - 8\sigma c_{1112} \\
&\quad + 12\sigma^2(c_{1122}+c_{1123}) - 8\sigma^3(c_{1112}+3c_{1123}) \\
&\quad + 2\sigma^4(c_{1111}+4c_{1112}+3c_{1122})\Big].
\end{aligned} \tag{26}$$

The expression for γ_v is simplified if in the nonlinear elasticity tensors we take into account only the contribution from the electron-phonon coupling as given in Table 2.1 and also allow for the interrelation between different components of the tensor $\delta\hat{c}$. Then for a silicon beam

$$\gamma_v = (\pi^4 S/4L^3)(1+\sigma)^4 \delta c_{1111}. \tag{27}$$

For extension along $\langle 110\rangle$ axis, with one side parallel to (100) plane and the other side parallel to $(1\bar{1}0)$ plane, the Poisson's ratios $\sigma_2 = \sigma(110,1\bar{1}0)$ and $\sigma_3 = \sigma(110,001)$ are given in Ref. [203]. Then Eqs. (2.8) and (21) give

$$\begin{aligned}
M\omega_v^2 &= \frac{4\pi^2 S}{L}\frac{c_{44}\left(c_{11}(c_{11}+c_{12})-2c_{12}^2\right)}{c_{11}(c_{11}+c_{12}+2c_{44})-2c_{12}^2},\\
\gamma_v &= \frac{\pi^4 S}{32L^3}\Big[c_{1111}\left(\sigma_2^4-4\sigma_2^3+6\sigma_2^2-4\sigma_2+8\sigma_3^4+1\right)\\
&\quad +4c_{1112}\left(\sigma_2-1\right)\left(\sigma_2^3+2\sigma_2^2\sigma_3-3\sigma_2^2-4\sigma_2\sigma_3+3\sigma_2+8\sigma_3^3+2\sigma_3-1\right)\\
&\quad +3c_{1122}\left(\sigma_2-1\right)^2\left(\sigma_2^2-2\sigma_2+8\sigma_3^2+1\right)+24c_{1123}\sigma_3\left(\sigma_2-1\right)^2\left(\sigma_2+\sigma_3-1\right)\\
&\quad +48c_{1144}\sigma_3^2\left(\sigma_2+1\right)^2+96c_{1244}\sigma_3\left(\sigma_2-1\right)\left(\sigma_2+1\right)^2+24c_{1155}\left(\sigma_2^2-1\right)^2\\
&\quad +24c_{1266}\left(\sigma_2^2-1\right)^2+8c_{4444}\left(\sigma_2+1\right)^4\Big].
\end{aligned} \tag{28}$$

If in the nonlinear elasticity tensor $\hat{c}$ we take into account only the contribution $\delta\hat{c}$ from the electron-phonon coupling, in the case of a silicon beam the expression for γ_v simplifies to

$$\gamma_v = \frac{\pi^4 S}{32L^3}\left(\left(\sigma_2-2\sigma_3-1\right)^4\delta c_{1111}+24\left(\sigma_2+1\right)^2\left(\sigma_2-2\sigma_3-1\right)^2\delta c_{1144}+16\left(\sigma_2+1\right)^4\delta c_{4444}\right). \tag{29}$$

Expressions (26) and (28) were generated using a computer code to calculate the sums and integrals in Eq. (2.8).

A.6 Strain effects on the conduction band in Si from a symmetry argument

In this appendix, we reproduce the derivation from [128] of electron-phonon coupling functional form in silicon using group theory arguments. It is the most convenient to use the theory of invariants. Silicon is an O_h crystal, with six minima in the conduction band, which are close to X points in the Brillouin zone. Point X has symmetry $D_{4h} = D_4 \times C_i$. It is known that the conduction band minimum corresponds to Δ_1 representation. Together with Δ_2', representation Δ_1

Table A.1 Characters of group elements for various representations of D_{4h} with basis functions up to third order for each representation. Here $[xy] \equiv \frac{1}{2}(xy+yx)$ and $\{xy\} \equiv \frac{1}{2}(xy-yx)$.

Representation	e	c_2	$2c_4$	$2u_2$	$2u'_2$	ie	ic_2	$2ic_4$	$2iu_2$	$2iu'_2$	Basis
A_1^+	1	1	1	1	1	1	1	1	1	1	$z^2; x^2+y^2$
A_1^-	1	1	1	1	1	-1	-1	-1	-1	-1	$\{xy\}z \sim J_z z$
A_2^+	1	1	1	-1	-1	1	1	1	-1	-1	J_z
A_2^-	1	1	1	-1	-1	-1	-1	-1	1	1	z; $(x^2+y^2)z$; z^3
B_1^+	1	1	-1	1	-1	1	1	-1	1	-1	x^2-y^2
B_1^-	1	1	-1	1	-1	-1	-1	1	-1	1	$[xy]z$
B_2^+	1	1	-1	-1	1	1	1	-1	-1	1	xy
B_2^-	1	1	-1	-1	1	-1	-1	1	1	-1	$(x^2-y^2)z$
E^+	2	-2	0	0	0	2	-2	0	0	0	J_x, J_y; xz, yz
E^-	2	-2	0	0	0	-2	2	0	0	0	x, y

turns into X_2 at point X (in notations of [128]). Therefore, one can find the Hamiltonian corresponding to X_2 representation of D_{4h} and assume it is valid up to the conduction band minimum point $k_0 \approx 0.85(2\pi/a)$ [204, 205]. More specifically, we need to find basis functions of $X_2 \times X_2^*$ representation of D_{4h}, according to Section 25 in [128].

A.6.1 Representations of D_{4h}

Representations of $D_{4h} = D_4 \times C_i$ are obtained from the representations of D_4 by splitting of each representation into two representations: '$-$' and '$+$'. The resulting representations and their characters are given in Table A.1. Fourth-order basis sets for these representations are given in a separate Table A.4. In the rest of this subsection we show how the basis functions in Table A.1 are obtained. Characters for D_4 representations are found in [128], Table 11.1. Characters of the elements ig, $g \in D_4$ are $\chi(ig) = \pm\chi(g)$, plus and minus corresponding to '$-$' and '$+$' representations. To obtain the basis functions, we first find representations for the basis sets x, y, z, and J_x, J_y, J_z. These representations are presented in Table A.2. Matrices of these representations for

Table A.2 Representations of D_{4h} with basis sets x, y, z, and J_x, J_y, J_z.

Representation	e	c_2	$2c_4$	$2u_2$	$2u_2'$	ie	ic_2	$2ic_4$	$2iu_2$	$2iu_2'$	Basis
D_1^-	3	−1	1	−1	−1	−3	1	−1	1	1	x, y, z
D_1^+	3	−1	1	−1	−1	3	−1	1	−1	−1	J_x, J_y, J_z

elements g without i are:

$$D(e) = \boldsymbol{I} = \begin{pmatrix} 1 & 0 & 0 \\ 0 & 1 & 0 \\ 0 & 0 & 1 \end{pmatrix}, D(c_2) = \begin{pmatrix} -1 & 0 & 0 \\ 0 & -1 & 0 \\ 0 & 0 & 1 \end{pmatrix},$$

$$D(c_4) = \begin{pmatrix} 0 & 1 & 0 \\ -1 & 0 & 0 \\ 0 & 0 & 1 \end{pmatrix}, D(u_2) = \begin{pmatrix} -1 & 0 & 0 \\ 0 & 1 & 0 \\ 0 & 0 & -1 \end{pmatrix},$$

$$D(u_2') = \begin{pmatrix} 0 & 1 & 0 \\ 1 & 0 & 0 \\ 0 & 0 & -1 \end{pmatrix}.$$

Matrices for elements g with i are

$$D(ie) = -\boldsymbol{I} = \begin{pmatrix} -1 & 0 & 0 \\ 0 & -1 & 0 \\ 0 & 0 & -1 \end{pmatrix}, D(ic_2) = \begin{pmatrix} 1 & 0 & 0 \\ 0 & 1 & 0 \\ 0 & 0 & -1 \end{pmatrix},$$

$$D(ic_4) = \begin{pmatrix} 0 & -1 & 0 \\ 1 & 0 & 0 \\ 0 & 0 & -1 \end{pmatrix}, D(iu_2) = \begin{pmatrix} 1 & 0 & 0 \\ 0 & -1 & 0 \\ 0 & 0 & 1 \end{pmatrix},$$

$$D(iu_2') = \begin{pmatrix} 0 & -1 & 0 \\ -1 & 0 & 0 \\ 0 & 0 & 1 \end{pmatrix};$$

Table A.3 Representation of D_{4h} with the basis set x^2, y^2, xy, yx.

Representation	e	c_2	$2c_4$	$2u_2$	$2u_2'$	ie	ic_2	$2ic_4$	$2iu_2$	$2iu_2'$	Basis
$E^- \times E^-$	4	4	0	0	0	4	4	0	0	0	x^2, y^2, xy, yx

Using equation (8.19) from [128], we find the irreducible representations entering D_1^+ and D_1^+:

$$N_\mu = \frac{1}{h} \sum_g \chi_\mu^* (g) \chi (g) . \tag{30}$$

The coefficient N_μ indicates the number of times the irreducible representation with characters $\chi_\mu (g)$ occurs in the given reducible representation D with characters $\chi(g)$. This number is called the multiplicity of the irreducible representation. We find that $D_1^- = A_2^- + E^-$ and $D_1^+ = A_2^+ + E^+$. Thus, we find that z is transformed according to A_2^-, and x, y are transformed according to E^-. Corresponding components of $\boldsymbol{J}$ are transformed by A_2^+ and E^+.

Now, we can find how the products such as xy are transformed. The functions x^2, y^2, xy, yx lead to a representation $E^- \times E^-$ with characters given in Table A.3. Therefore, we find irreducible representations contained in $E^- \times E^-$ by means of (30):

$$E^- \times E^- = A_1^+ + A_2^+ + B_1^+ + B_2^+ . \tag{31}$$

The basis functions for these irreducible representations are easily guessed. Products xz, yz are transformed according to $E^- \times A_2^- = E^+$. To find the basis functions, we use Eqs. (9.11) and (9.12) from [128]:

$$P^{E^+} xz = \frac{2}{16} \sum_g \chi_{E^+}^* (g) \mathscr{D}(g) xz = \frac{1}{8} (2xz + 2xz + 2xz + 2xz) = xz$$
$$P^{E^+} yz = \frac{2}{16} \sum_g \chi_{E^+}^* (g) \mathscr{D}(g) yz = \frac{1}{8} (2yz + 2yz + 2yz + 2yz) = yz$$

We thus find that xz and yz form the basis of E^+. Similarly, we can find the third order basis functions. Functions xxz, xyz, yxz, yyz are transformed as

$$E^- \times E^- \times A_2^- = A_1^- + A_2^- + B_1^- + B_2^- \tag{32}$$

Table A.4 Fourth-order basis sets for some reducible and irreducible representations of D_{4h}.

Reducible	Irreducible	Basis functions
$(E^-)^4$	$4A_1^+$	$xxxx + yyyy$; $xxyy + yyxx$; $xyxy + yxyx$; $xyyx + yxxy$
	$4A_2^+$	$xyxx - yxyy$; $xxxy - yyyx$; $yxxx - xyyy$; $xxyx - yyxy$
	$4B_1^+$	$xxxx - yyyy$; $xxyy - yyxx$; $xyyx - yxxy$; $xyxy - yxyx$
	$4B_2^+$	$xyxx + yxyy$; $xxxy + yyyx$; $yxxx + xyyy$; $xxyx + yyxy$
$(E^-)^3 \times A_2^-$	$4E^+$	$xxxz, yyyz$; $xxyz, yyxz$; $xyxz, yxyz$; $xyyz, yxxz$
$(E^-)^2 \times (A_2^-)^2$	A_1^+	$xxzz + yyzz$
	A_2^+	$xyzz - yxzz$
	B_1^+	$xxzz - yyzz$
	B_2^+	$xyzz + yxzz$
$(A_2^-)^4$	A_1^+	$zzzz$

Again, to find the basis functions, we act on the mentioned third-order functions by the operator P^μ. This way we find that $\{xy\}z$ is another basis set (with one function) of A_1^-. Similarly $(x^2+y^2)z$ is another basis function for A_2^-; $(xy+yx)z = [xy]z$ for B_1^-; and $(x^2-y^2)z$ for B_2^-.

Another third-order set of functions is $xxx, yxx, xyx, xxy, yyx, yxy, xyy, yyy$. They are transformed according to $E^- \times E^- \times E^- = 4E^-$. Their basis sets are easily found: xxx, yyy; xxy, yyx; xyx, yxy; xyy, yxx. However, do not really need their basis functions because E^- does not enter $D \times D^*$. In a similar manner we find basis sets of the fourth order, that are summarized in Table A.4.

A.6.2 Representations of D_{4h} entering $X_2 \times X_2^*$

To write the general form of Hamiltonian at point X that would be invariant under all symmetry operations at this point, we need to find all irreducible representations of D_{4h} entering $X_2 \times X_2^*$. First, we find representations X_2 and X_4, characters of which are summarized in Table A.5. Characters of $X_2 \times X_2$ and $X_4 \times X_4$ are the same, so they contain the same irreducible representations. Using Eq. (30), we find those representations in terms of $D_{4h} = D_4 \times C_i$:

$$X_2 \times X_2^* = A_1^+ + A_2^- + B_1^- + B_2^+ \tag{33}$$

Table A.5 Characters of X_2 and X_4 representations. The first column contains the elements of D_{4h} group, while the second contains the corresponding elements of the little group of the wave vector $k = k_X$. Other columns show characters of X_2, X_4, $X_2 \times X_2^*$, and $X_4 \times X_4^*$ representations.

D_{4h}	G_X	X_2	X_4	$X_2 \times X_2^*$	$X_4 \times X_4^*$
e	$(e\|0)$	2	2	4	4
c_2	$(c_{2z}\|0)$	2	2	4	4
c_4	$(c_{4z}\|\tau)$	0	0	0	0
c_4	$(c_{4z}^3\|\tau)$	0	0	0	0
u_2	$(c_{2x}\|0)$	0	0	0	0
u_2	$(c_{2y}\|0)$	0	0	0	0
u_2'	$(c_{2xy}\|\tau)$	0	0	0	0
u_2'	$(c_{2x\bar{y}}\|\tau)$	0	0	0	0
ie	$(ie\|\tau)$	0	0	0	0
$ic_2 = \sigma_z$	$(ic_{2z}\|\tau)$	0	0	0	0
ic_4	$(ic_{4z}\|0)$	0	0	0	0
ic_4	$(ic_{4z}^3\|0)$	0	0	0	0
$iu_2 = \sigma_x$	$(ic_{2x}\|\tau)$	0	0	0	0
$iu_2 = \sigma_y$	$(ic_{2y}\|\tau)$	0	0	0	0
$iu_2' = \sigma_{xy}$	(ic_{2xy})	2	-2	4	4
$iu_2' = \sigma_{x\bar{y}}$	$(ic_{2x\bar{y}})$	2	-2	4	4

We can also choose matrices $\boldsymbol{I}, \sigma_z, \sigma_y, \sigma_x$ that transform according to these representations. The resulting representations and and their basis functions of all required orders are summarized in Table A.6.

Table A.6 Irreducible representations contained in $X_2 \times X_2^*$ and basis functions of different orders, as well as matrices that transform according to the representations.

$X_2 \times X_2^*$:	Basis 1	Basis 2	Basis 3	Basis 4	Matrix
A_1^+		z^2, x^2+y^2		$xxxx+yyyy$; $xxyy+yyxx$; $xyxy+yxyx$; $xyyx+yxxy$; $xxzz+yyzz$; $zzzz$	$\boldsymbol{I}$
A_2^-	z		$(x^2+y^2)z$		σ_z
B_1^-			$[xy]z \sim J_z z$		σ_y
B_2^+		xy		$xyxx+yxyy$; $xxxy+yyyx$; $yxxx+xyyy$; $xxyx+yyxy$; $xyzz+yxzz$	σ_x

A.6.3 Effects of strain on the spectrum around the valley minimum

Using the basis functions of the irreducible representations of $X_2 \times X_2^*$, we write the Hamiltonian for the z-valley up to the second power in the most general form:

$$\begin{aligned} H^{(z)} =& \boldsymbol{I}\left[A_1 k_z^2 + A_2\left(k_x^2+k_y^2\right) + D_1\varepsilon_{zz} + D_2\left(\varepsilon_{xx}+\varepsilon_{yy}\right)\right] + \sigma_x\left[A_3 k_x k_y + D_3\varepsilon_{xy}\right] + A_4\sigma_z k_z \\ =& \begin{pmatrix} \lambda + A_4 k_z & A_3 k_x k_y + D_3\varepsilon_{xy} \\ A_3 k_x k_y + D_3\varepsilon_{xy} & \lambda - A_4 k_z \end{pmatrix}, \end{aligned} \tag{34}$$

Where A_1–A_4 and D_1–D_3 are some constants, we will identify their meaning later. Then, the spectrum around point X is determined by the equation $\det(H - \boldsymbol{I}E) = 0$:

$$\left(E^{(z)} - \lambda\right)^2 = A_4^2 k_z^2 + \left(A_3 k_x k_y + D_3\varepsilon_{xy}\right)^2. \tag{35}$$

From Eq. (35),

$$E^{(z)} = \lambda \pm \left[A_4^2 k_z^2 + \left(A_3 k_x k_y + D_3\varepsilon_{xy}\right)^2\right]^{1/2}. \tag{36}$$

We know that there is a minimum on the lower branch of this spectrum along k_z at point k_0. We expand the lower branch around the minimum to the fourth order in strain:

$$\begin{aligned}
E^{(z)} =& A_1\left(k_z-k_0\right)^2+2A_1k_0\left(k_z-k_0\right)+A_1k_0^2+A_2\left(k_x^2+k_y^2\right)+D_1\varepsilon_{zz}+D_2\left(\varepsilon_{xx}+\varepsilon_{yy}\right)\\
\approx& A_1\left(k_z-k_0\right)^2+2A_1k_0\left(k_z-k_0\right)+A_1k_0^2+A_2\left(k_x^2+k_y^2\right)+D_1\varepsilon_{zz}+D_2\left(\varepsilon_{xx}+\varepsilon_{yy}\right)\\
&-\frac{A_3D_3\varepsilon_{xy}k_x}{A_4k_0}k_y+\frac{A_3D_3^3\varepsilon_{xy}^3k_xk_y}{2A_4^3k_0^3}-A_4\left(k_z-k_0\right)-\frac{D_3^2\varepsilon_{xy}^2}{2A_4k_0}+\frac{D_3^2\varepsilon_{xy}^2\left(k_z-k_0\right)}{2A_4k_0^2}\\
&-\frac{D_3^2\varepsilon_{xy}^2\left(k_z-k_0\right)^2}{2A_4k_0^3}+\frac{D_3^4\varepsilon_{xy}^4}{8A_4^3k_0^3}-\frac{3D_3^4\varepsilon_{xy}^4\left(k_z-k_0\right)}{8A_4^3k_0^4}+\frac{3D_3^4\varepsilon_{xy}^4\left(k_z-k_0\right)^2}{4A_4^3k_0^5}.
\end{aligned}\tag{37}$$

Without strain, point k_0 should be a minimum, therefore we find $|A_4|=2A_1k_0$. Then, up to a constant,

$$\begin{aligned}
E^{(z)} =& A_1\left(k_z-k_0\right)^2+A_2\left(k_x^2+k_y^2\right)+D_1\varepsilon_{zz}+D_2\left(\varepsilon_{xx}+\varepsilon_{yy}\right)\\
&-\frac{D_3^2\varepsilon_{xy}^2}{\Delta E}+\frac{D_3^4\varepsilon_{xy}^4}{\Delta E^3}-\frac{2A_3D_3}{\Delta E}\varepsilon_{xy}k_xk_y+\frac{4A_3D_3^3}{\Delta E^3}\varepsilon_{xy}^3k_xk_y\\
&+\frac{D_3^2\varepsilon_{xy}^2\left(k_z-k_0\right)}{\Delta Ek_0}-\frac{3D_3^4\varepsilon_{xy}^4\left(k_z-k_0\right)}{\Delta E^3k_0}-\frac{D_3^2\varepsilon_{xy}^2\left(k_z-k_0\right)^2}{\Delta Ek_0^2}+\frac{6D_3^4\varepsilon_{xy}^4\left(k_z-k_0\right)^2}{\Delta E^3k_0^2}
\end{aligned}\tag{38}$$

We will use the following notation:

$$-\frac{D_3^2\varepsilon_{xy}^2}{2|A_4|k_0}=-\frac{D_3^2\varepsilon_{xy}^2}{4A_1k_0^2}=-\frac{D_3^2\varepsilon_{xy}^2}{E\left(\Delta_{2'}\right)-E\left(\Delta_1\right)}\equiv-\Xi_{sh}\varepsilon_{xy}^2 \tag{39}$$

$$\frac{D_3^4\varepsilon_{xy}^4}{8|A_4|^3k_0^3}=\frac{D_3^4\varepsilon_{xy}^4}{\left(4A_1k_0^2\right)^3}=\frac{D_3^4\varepsilon_{xy}^4}{\left[E\left(\Delta_{2'}\right)-E\left(\Delta_1\right)\right]^3}\equiv\Xi_{s4}\varepsilon_{xy}^4 \tag{40}$$

And D_3 is identified as $D_3\equiv 2\Xi_{u'}$ from [129]. We can also identify $D_1\equiv\Xi_u+\Xi_d$, $D_2\equiv\Xi_d$, $A_1\equiv\hbar^2/2m_{\parallel}$, $A_2\equiv\hbar^2/2m_{\perp}$, where Ξ_d and Ξ_u are the well-known deformation potential constants, and $m_{\parallel}$, $m_{\perp}$ are longitudinal and transverse masses in the valley. Constant A_3 is unknown to the best of our knowledge. We will not substitute all of theses values in the equations below for brevity.

There are three effects of strain that can be identified from Eq. (38): valley minimum is shifted in k-space, the effective mass is modified, and the valley minimum is shifted in energy. The shift of the minimum in k-space (to the second order in ε_{xy}) is obtained from:

$$0=\frac{d}{dk_z}\left[A_1\left(k_z-k_0\right)^2+-\Xi_{sh}\varepsilon_{xy}^2\left(\frac{\left(k_z-k_0\right)^2}{k_0^2}-\frac{\left(k_z-k_0\right)}{k_0}\right)\right],$$

and the result is

$$k_z^{min} \approx k_0 + \frac{-\Xi_{sh}\varepsilon_{xy}^2}{2k_0 A_1}.$$

The lowest order correction to A_1 is:

$$\delta A_1 = \frac{-\Xi_{sh}\varepsilon_{xy}^2}{k_0^2}.$$

From here, the longitudinal mass becomes

$$m_{\parallel} = m_{\parallel}^0 \left(1 + \frac{2m_{\parallel}^0 - \Xi_{sh}\varepsilon_{xy}^2}{\hbar^2 k_0^2}\right)^{-1}, \tag{41}$$

where $m_{\parallel}^0$ is the longitudinal mass without strain. We will not comment on the transverse mass effects since they are of no importance to our calculations. The most relevant result for us is the shift of the valley bottom in energy by

$$\delta E_z = (\Xi_u + \Xi_d)\varepsilon_{zz} + \Xi_d(\varepsilon_{xx} + \varepsilon_{yy}) - \Xi_{sh}\varepsilon_{xy}^2 + \Xi_{s4}\varepsilon_{xy}^4. \tag{42}$$

It includes the familiar deformation potential and two new terms. The term $-\Xi_{sh}\varepsilon_{xy}^2$ has been experimentally observed [129, 133]. The last term $\Xi_{s4}\varepsilon_{xy}^4$ has not been observed, and we drop it in the main calculation since it only leads to a very small correction of $\frac{1}{2}n\Xi_{s4}$ to δc_{4444}. However it may become important for very high electron concentrations, above 10^{20} cm^{-3}.

A.7 Electron-ripplon scattering

A.7.1 Capillary wave quantization

To quantize the capillary wave field, we first need to write the field Lagrangian, then find the conjugate variables, and construct the Hamiltonian. Afterwards we second-quantize the field, introducing the creation and annihilation operators. We will describe the system by the displacement $\xi(\boldsymbol{r},t)$ of the surface along the z axis, and the velocity potential $\Phi(\boldsymbol{r},z,t)$ in the bulk. The velocity is expressed through Φ as $\boldsymbol{v}(\boldsymbol{r},z,t) = -\nabla\Phi(\boldsymbol{r},z,t)$. It is convenient to solve the problem in the Fourier space. We are looking for the solutions $\Phi(\boldsymbol{r},z,t)$ that exponentially decay into the bulk, so we can write

$$\Phi(\boldsymbol{r},z,t) = \sum_{\boldsymbol{k}} \Phi_{\boldsymbol{k}}(t) e^{kz} e^{i\boldsymbol{kr}}$$

$$\xi(\boldsymbol{r},t) = \sum_{\boldsymbol{k}} \xi_{\boldsymbol{k}}(t) e^{i\boldsymbol{kr}} \tag{43}$$

Then the kinetic energy in the Fourier variables is

$$T = \int d^2r' \int_{-\infty}^{0} dz \frac{\rho}{2} (\nabla\Phi)^2 = \frac{\rho S}{2} \sum_{\boldsymbol{k}} k \Phi_{\boldsymbol{k}} \Phi_{-\boldsymbol{k}} = \frac{\rho S}{2} \sum_{\boldsymbol{k}} \frac{1}{k} \dot{\xi}_{\boldsymbol{k}} \dot{\xi}_{-\boldsymbol{k}}$$

In a similar way, find the gravitational potential energy:

$$V_g = \int d^2r' \int_0^{\xi(\boldsymbol{r},t)} dz \rho g z = \frac{\rho g}{2} \int d^2r' \left(\sum_{\boldsymbol{k}} \xi_{\boldsymbol{k}} e^{i\boldsymbol{kr}} \right)^2 = \frac{\rho g S}{2} \sum_{\boldsymbol{k}} \xi_{\boldsymbol{k}} \xi_{-\boldsymbol{k}} \tag{44}$$

To find the surface energy, we first calculate the change of the surface area due to the ripplon field:

$$S + \delta S = \int d^2r' \sqrt{1 + \left(\sum_{\boldsymbol{k}} i\boldsymbol{k} \xi_{\boldsymbol{k}} \sum_{\boldsymbol{k}'} i\boldsymbol{k}' \xi_{\boldsymbol{k}'} e^{i\boldsymbol{r}'(\boldsymbol{k}+\boldsymbol{k}')} \right)} \approx S + \tfrac{1}{2} S k^2 \sum_{\boldsymbol{k}} \xi_{\boldsymbol{k}} \xi_{-\boldsymbol{k}}. \tag{45}$$

Then the surface energy is expressed through δS and the surface tension α:

$$V_s = \alpha \delta S = \frac{\alpha S}{2} \sum_{\boldsymbol{k}} k^2 \xi_{\boldsymbol{k}} \xi_{-\boldsymbol{k}}. \tag{46}$$

The Lagrangian of the system is

$$L = T - V_g - V_s. \tag{47}$$

The conjugate variables are obtained are by differentiating the Lagrangian:

$$\pi_{\boldsymbol{k}} = \frac{\partial L}{\partial \dot{\xi}_{\boldsymbol{k}}} = \frac{\rho S}{k} \dot{\xi}_{-\boldsymbol{k}} \tag{48}$$

or

$$\dot{\xi}_{\boldsymbol{k}} = \frac{k}{\rho S} \pi_{-\boldsymbol{k}}. \tag{49}$$

With the conjugate variables, we can write the Hamiltonian

$$H = \sum_{\boldsymbol{k}} \left[\tfrac{1}{2m_k} \pi_{\boldsymbol{k}} \pi_{-\boldsymbol{k}} + \tfrac{m_k \omega_k^2}{2} \xi_{\boldsymbol{k}} \xi_{-\boldsymbol{k}} \right], \tag{50}$$

where we introduced the notations

$$m_k \equiv \frac{\rho S}{k},$$
$$m_k \omega_k^2 \equiv S(\rho g + \alpha k^2). \tag{51}$$

Now we quantize the field ξ by requiring that

$$[\xi_{\boldsymbol{k}}, \pi_{\boldsymbol{k}'}] = i\hbar \delta_{\boldsymbol{k}\boldsymbol{k}'}. \tag{52}$$

We introduce the second quantization operators $a_{\boldsymbol{k}}$ and $a_{\boldsymbol{k}}^\dagger$:

$$a_{\boldsymbol{k}} = \sqrt{\frac{m_k \omega_k}{2\hbar}} \left(\xi_{\boldsymbol{k}} + \tfrac{i}{m_k \omega_k} \pi_{-\boldsymbol{k}} \right),$$
$$a_{\boldsymbol{k}}^\dagger = \sqrt{\frac{m_k \omega_k}{2\hbar}} \left(\xi_{\boldsymbol{k}} - \tfrac{i}{m_k \omega_k} \pi_{-\boldsymbol{k}} \right). \tag{53}$$

Or equivalently,

$$\xi_{\boldsymbol{k}} = \sqrt{\frac{\hbar}{2 m_k \omega_k}} \left(a_{\boldsymbol{k}} + a_{-\boldsymbol{k}}^\dagger \right), \tag{54}$$

$$\pi_{\boldsymbol{k}} = i \sqrt{\frac{\hbar m_k \omega_k}{2}} \left(a_{\boldsymbol{k}} - a_{-\boldsymbol{k}}^\dagger \right). \tag{55}$$

One can check that $[a_{\boldsymbol{k}}, a_{\boldsymbol{k}'}^\dagger] = \delta_{\boldsymbol{k},\boldsymbol{k}'}$, and other familiar relations for bosonic operators are satisfied. The Hamiltonian in the second-quantized form is

$$H = \sum_{\boldsymbol{k}} \hbar \omega_k \left(a_{\boldsymbol{k}}^\dagger a_{\boldsymbol{k}} + \tfrac{1}{2} \right) \tag{56}$$

A.7.2 Polarization coupling to the surface displacement field

We consider a particle with coordinates $\boldsymbol{r}$ along the surface and z perpendicular to the surface. We are computing the energy of the coupling of the electron with the helium surface when the surface is perturbed by the vertical displacement field $\xi(\boldsymbol{r})$ created by ripplons. The energy of a polarized body in an electric field created by charge δq is written as [206]:

$$\delta F = -\int \boldsymbol{P} \cdot \delta \boldsymbol{C} dV \tag{57}$$

Here $\boldsymbol{P}$ is the polarization of the medium, and $\boldsymbol{C}$ is the electric field that would have been in the medium if the medium had permittivity of 1 (or there was no medium). Integration is done over the medium volume only. The polarization is found through the electric field as

$$\boldsymbol{P} = \frac{\varepsilon - 1}{4\pi}\boldsymbol{E} = \frac{\varepsilon - 1}{2\pi(\varepsilon + 1)}\boldsymbol{C}. \tag{58}$$

Then

$$\delta F = -\frac{\varepsilon - 1}{2\pi(\varepsilon + 1)} \int d\boldsymbol{r}' \int_{-\infty}^{\xi(\boldsymbol{r}')} \frac{q\delta q}{\left[(\boldsymbol{r}' - \boldsymbol{r})^2 + (z' - z)^2\right]^2} dz, \tag{59}$$

The full interaction energy of charge e with the surface is obtained by integrating over δq:

$$F(\boldsymbol{r}, z) = -\frac{\Lambda}{\pi} \int d\boldsymbol{r}' \int_{-\infty}^{\xi(\boldsymbol{r}')} \frac{dz'}{\left[(\boldsymbol{r}' - \boldsymbol{r})^2 + (z' - z)^2\right]^2} \tag{60}$$

where

$$\Lambda \equiv \frac{e^2(\varepsilon - 1)}{4(\varepsilon + 1)}. \tag{61}$$

Eq. (60) is the full energy of the electron-helium interaction, including the trivial attraction without the surface perturbation. For the electron-ripplon scattering, we are interested only in the part that is induced by the surface displacement, that we will denote as $\Delta F_{\boldsymbol{q}}$ for a single Fourier component of the surface displacement $\xi_{\boldsymbol{q}} e^{i\boldsymbol{q}\boldsymbol{r}}$. We will also make the coordinate transformation $\tilde{z} = z - \xi(\boldsymbol{r})$ for the reasons that will be explained in the next part. With this in mind,

$$\begin{aligned}
\Delta F_{\boldsymbol{q}}(\tilde{z}) &= -\frac{\Lambda}{\pi} \int d^2 r' \int_0^{\xi_{\boldsymbol{q}}(e^{i\boldsymbol{q}\boldsymbol{r}'} - e^{i\boldsymbol{q}\boldsymbol{r}})} \frac{dz'}{\left[(\boldsymbol{r}' - \boldsymbol{r})^2 + (z' - \tilde{z})^2\right]^2} \\
&\approx -\frac{\Lambda \xi_{\boldsymbol{q}} e^{i\boldsymbol{q}\boldsymbol{r}}}{\pi} \int \frac{d^2 r' (e^{i\boldsymbol{q}\boldsymbol{r}'} - 1)}{\left[r'^2 + \tilde{z}^2\right]^2} \\
&= \frac{\Lambda \xi_{\boldsymbol{q}} q^2 e^{i\boldsymbol{q}\boldsymbol{r}}}{\pi} \int \frac{dx\, d\theta\, x \left(1 - e^{ix\cos\theta}\right)}{\left[x^2 + (q\tilde{z})^2\right]^2}
\end{aligned} \tag{62}$$

Here we used the smallness of $\xi_{\boldsymbol{q}}$ compared to the typical electron coordinate z. The first part of this integral is

$$\int \frac{x\, dx\, d\theta}{\left[x^2 + (q\tilde{z})^2\right]^2} = \frac{\pi}{(q\tilde{z})^2}, \tag{63}$$

while the second is

$$\int \frac{dx\,d\theta\, x e^{ix\cos\theta}}{\left[x^2+(q\tilde{z})^2\right]^2} = \int \frac{dx\,d\theta\, x \sum_{n=-\infty}^{\infty} i^n J_n(x) e^{in\theta}}{\left[x^2+(q\tilde{z})^2\right]^2} = 2\pi \int \frac{dx\, x J_0(x)}{\left[x^2+(q\tilde{z})^2\right]^2} \tag{64}$$

Integration of terms with $n \neq 0$ over θ gives zero. The remaining integral is found using formula (11.4.44) in Ref. [207]:

$$2\pi \int_0^\infty \frac{dx\, x J_0(x)}{\left[x^2+(q\tilde{z})^2\right]^2} = \frac{\pi}{q\tilde{z}} K_1(q\tilde{z}) \tag{65}$$

Taking all terms in $\Delta F_{\boldsymbol{q}}$ together, and summing over $\boldsymbol{q}$, we obtain the coupling energy to the ripplon field ξ through polarization:

$$\Delta F(\boldsymbol{r},\tilde{z}) = \sum_{\boldsymbol{q}} \Delta F_{\boldsymbol{q}} = \Lambda \sum_{\boldsymbol{q}} \xi_{\boldsymbol{q}} e^{i\boldsymbol{q}\boldsymbol{r}} \frac{1}{\tilde{z}} \left[\frac{1}{\tilde{z}} - qK_1(q\tilde{z})\right] \tag{66}$$

A.7.3 Total coupling to the surface displacement field

In the presence of a pressing field $E_\perp$, the system is described by the Schrödinger equation

$$\frac{\hbar^2}{2m_e}\nabla^2\psi + \left[\lambda - eE_\perp z - F(r,z)\right]\psi = 0. \tag{67}$$

where λ is the eigenvalue of the Hamiltonian of the system. In addition to the polarization coupling outlined in Section A.7.2, the electron is coupled to the surface deformation through the modification of the boundary condition on the surface, which is not flat anymore. The wavefunction vanishes on the surface $z = \xi(\boldsymbol{r})$:

$$\psi(\boldsymbol{r},z)|_{z=\xi(\boldsymbol{r})} = 0. \tag{68}$$

In general, we do not know how to solve the problem with the curved boundary of arbitrary shape. In the case of small $\xi(\boldsymbol{r})$, however, we can facilitate solving the equation by a coordinate transformation:

$$\tilde{z} = z - \xi(\boldsymbol{r}), \tilde{r} = r. \tag{69}$$

In these coordinates, the problem has a flat boundary, and therefore can be solved with conventional approaches. However, we need to rewrite the equation in the new coordinates. The kinetic energy term in new coordinates is found by transforming $\nabla^2\psi$:

$$\hbar^2\nabla^2\psi = \hbar^2\tilde{\nabla}^2\psi + 2\left(\frac{\partial\xi}{\partial\tilde{x}}\tilde{p}_x + \frac{\partial\xi}{\partial\tilde{y}}\tilde{p}_y\right)\tilde{p}_z\psi - i\hbar\left(\frac{\partial^2\xi}{\partial\tilde{x}^2} + \frac{\partial^2\xi}{\partial\tilde{y}^2}\right)\tilde{p}_z. \tag{70}$$

Now if we expand ξ in the Fourier series $\xi = \sum_{\boldsymbol{q}} \xi_{\boldsymbol{q}} e^{i\boldsymbol{qr}}$ and drop tildes, we obtain

$$\frac{\hbar^2}{2m_e}\nabla^2\psi \to \frac{\hbar^2}{2m_e}\nabla^2\psi + \sum_{\boldsymbol{q}} \frac{i\xi_{\boldsymbol{q}}(\boldsymbol{q}\cdot\boldsymbol{p})}{m_e} e^{i\boldsymbol{qr}} p_z\psi + \sum_{\boldsymbol{q}} \frac{i\hbar}{2m_e} q^2 \xi_{\boldsymbol{q}} e^{i\boldsymbol{qr}} p_z\psi \tag{71}$$

We can write the additional terms arising from the transformation of ∇^2 as a perturbation term in energy

$$\begin{aligned} V_\nabla &= \sum_{\boldsymbol{q}} \xi_{\boldsymbol{q}} e^{i\boldsymbol{qr}} V_{\nabla q}, \\ V_{\nabla q} &= -\frac{i}{m_e}(\boldsymbol{qp})p_z - \frac{i\hbar}{2m_e} q^2 p_z \end{aligned} \tag{72}$$

This term can not lead to transitions between states with the same m quantum number of the motion transverse to the surface, and its magnitude is small. Since we are considering scattering only within the first subband, we can ignore this term in our calculation of scattering. The total potential energy is transformed to

$$V(\boldsymbol{r},z) = eE_\perp z + F_0(z) + eE_\perp\xi(\boldsymbol{r}) + \Delta F(\boldsymbol{r},z). \tag{73}$$

We dropped tildes here. The first two terms represent the coupling to helium with unperturbed surface. Therefore, the electron-ripplon coupling energy that contributes to the scattering within the first subband is

$$H^{(\mathrm{rpl})} = eE_\perp\xi(\boldsymbol{r}) + \Delta F(\boldsymbol{r},z), \tag{74}$$

and $\Delta F(\boldsymbol{r},z)$ is given by Eq. (66).

A.7.4 Scattering rate of electrons by ripplons

Now that we know the coupling energy of electrons with the ripplon field, we can calculate the rate of scattering and the distribution of scattering angles. Scattering rate from the state $\boldsymbol{k}$ into the volume d^2k', according to the Fermi golden rule, is

$$dw^{(\mathrm{rpl})}_{\boldsymbol{k}'\boldsymbol{k}} = \frac{2\pi}{\hbar}\left[\left|H^{(\mathrm{rpl})}_{1,\boldsymbol{k}'\boldsymbol{k}}\right|^2 + \left|H^{(\mathrm{rpl})}_{2,\boldsymbol{k}'\boldsymbol{k}}\right|^2\right]\delta(\varepsilon_{\boldsymbol{k}'} - \varepsilon_{\boldsymbol{k}})\frac{Sd^2k'}{(2\pi)^2} \tag{75}$$

where

$$\begin{aligned} H^{(\mathrm{rpl})}_{1,\boldsymbol{k}'\boldsymbol{k}} &= \langle \boldsymbol{k}', N_{\boldsymbol{q}} - 1, N_{-\boldsymbol{q}}|H^{(\mathrm{rpl})}|\boldsymbol{k}, N_{\boldsymbol{q}}, N_{-\boldsymbol{q}}\rangle, \\ H^{(\mathrm{rpl})}_{2,\boldsymbol{k}'\boldsymbol{k}} &= \langle \boldsymbol{k}', N_{\boldsymbol{q}}, N_{-\boldsymbol{q}} + 1|H^{(\mathrm{rpl})}|\boldsymbol{k}, N_{\boldsymbol{q}}, N_{-\boldsymbol{q}}\rangle, \end{aligned} \tag{76}$$

Here, the state vectors $|\boldsymbol{k}, N_{\boldsymbol{q}}, N_{-\boldsymbol{q}}\rangle$ are defined by the electron wavevector $\boldsymbol{k}$, the number of ripplons $N_{\boldsymbol{q}}$ in the $\boldsymbol{q}$ state, and the number of ripplons $N_{-\boldsymbol{q}}$ in the $-\boldsymbol{q}$ state. The average number of ripplons in thermal equilibrium is $N_{\boldsymbol{q}} = 1/(e^{\hbar\omega_q/k_BT} - 1)$. These two matrix elements represent two possible processes of scattering: with creation and absorption of a ripplon. The delta-function can be rewritten as:

$$\delta\left(\frac{\hbar^2k'^2}{2m_e} - \frac{\hbar^2k^2}{2m_e}\right) = \frac{m_e\delta(k'-k)}{\hbar^2k'} \tag{77}$$

Then, the scattering rate is

$$dw^{(\mathrm{rpl})}_{\boldsymbol{k}'\boldsymbol{k}} = \frac{mS}{2\pi\hbar^3}\left[\left|H^{(\mathrm{rpl})}_{1,\boldsymbol{k}'\boldsymbol{k}}\right|^2 + \left|H^{(\mathrm{rpl})}_{2,\boldsymbol{k}'\boldsymbol{k}}\right|^2\right]\delta(k'-k)dk'd\theta \tag{78}$$

We first find the matrix elements between states $|\boldsymbol{k}\rangle$ and $|\boldsymbol{k}'\rangle$, without the pressing field, which we will include later:

$$\langle \boldsymbol{k}'|H^{(\mathrm{rpl})}|\boldsymbol{k}\rangle = \sum_{\boldsymbol{q}}\int_0^\infty dz \int d^2r \frac{4z^2}{Sr_B^3}e^{-2z/r_B}e^{i\boldsymbol{r}(\boldsymbol{k}-\boldsymbol{k}'+\boldsymbol{q})}\xi_{\boldsymbol{q}}\frac{\Lambda}{z}\left[\frac{1}{z} - qK_1(qz)\right] \tag{79}$$

Integration over $\boldsymbol{r}$ gives $\delta_{\boldsymbol{k}'-\boldsymbol{k},\boldsymbol{q}}$, while integrals over z of the two terms give

$$\begin{aligned} \int_0^\infty dz e^{-2z/r_B} &= r_B/2, \\ \int_0^\infty dz z e^{-2z/r_B}K_1(qz) &= \frac{1}{q^2}\int_0^\infty dz z e^{-2z/qr_B}K_1(z) \equiv \frac{1}{q^2}\Omega_r(qr_B) \end{aligned} \tag{80}$$

The explicit form of Ω_r will be introduced later. Taking the above results into account, we obtain

$$\langle \boldsymbol{k}'|H^{(\mathrm{rpl})}|\boldsymbol{k}\rangle = \frac{4\Lambda}{r_B^3\pi^2}\xi_{\boldsymbol{q}}\left[\frac{r_B}{2} - \frac{1}{q}\Omega_r(qr_B)\right]\bigg|_{\boldsymbol{q}=\boldsymbol{k}'-\boldsymbol{k}} \tag{81}$$

In the full matrix elements, $(a_{\boldsymbol{q}}+a^{\dagger}_{-\boldsymbol{q}})$ will give $\sqrt{N_{\boldsymbol{q}}}$ and $\sqrt{N_{-\boldsymbol{q}}+1}$ in $H^{(\mathrm{rpl})}_{1,\boldsymbol{k}'\boldsymbol{k}}$ and $H^{(\mathrm{rpl})}_{1,\boldsymbol{k}'\boldsymbol{k}}$ respectively. Using the notation $\overline{\left|H^{(\mathrm{rpl})}_{\boldsymbol{q}}\right|^2}=\left|H^{(\mathrm{rpl})}_{1,\boldsymbol{k}'\boldsymbol{k}}\right|^2+\left|H^{(\mathrm{rpl})}_{2,\boldsymbol{k}'\boldsymbol{k}}\right|^2$ and the analytical result for the function $\Omega_r(x)$ [3], we obtain:

$$\overline{\left|H^{(\mathrm{rpl})}_{\boldsymbol{q}}\right|^2}=\frac{S^{-1}k_BT\hbar^4q^2}{4\alpha m_e^2r_B^2}\phi^2\left(\frac{qr_B}{2}\right), \tag{82}$$

where

$$\phi(x)=(x^2-1)^{-1}+(1-x^2)^{-3/2}\ln\left[\frac{1+(1-x^2)^{1/2}}{x}\right],\ x<1, \tag{83}$$

$$\phi(x)=(x^2-1)^{-1}-(x^2-1)^{-3/2}\tan^{-1}\left[(x^2-1)^{1/2}\right],\ x>1. \tag{84}$$

Function $\phi(x)$ is continuous at $x=1$ and is monotonically decreasing everywhere. Therefore, the scattering rate (78) will take the form

$$dw^{(\mathrm{rpl})}_{\boldsymbol{k}'\boldsymbol{k}}=\frac{\hbar k_BT}{8\pi\alpha m_er_B^2}\,q^2\phi^2\left(\frac{qr_B}{2}\right)\Big|_{q=k\sqrt{2(1-\cos\theta)}}\delta(k'-k)dk'\,d\theta. \tag{85}$$

Integrated over k', it gives the angle distribution (normalized to the total scattering rate):

$$w^{(\mathrm{rpl})}_{k\theta}=\frac{\hbar k_BT}{8\pi\alpha m_er_B^2}\,q^2\phi^2\left(\frac{qr_B}{2}\right)\Big|_{q=k\sqrt{2(1-\cos\theta)}} \tag{86}$$

The integral of this distribution over θ is the total scattering rate from the state $\boldsymbol{k}$ to all other allowed states:

$$w^{(\mathrm{rpl})}_{k}=\frac{\hbar k_BT}{8\pi\alpha m_er_B^2}\int_0^{2\pi}d\theta\ q^2\phi^2\left(\frac{qr_B}{2}\right)\Big|_{q=k\sqrt{2(1-\cos\theta)}}. \tag{87}$$

The expressions (87) and (86) are used in the simulations. For completeness, we also give the total scattering rate with the pressing field $E_\perp$, even though we do not use it in our study:

$$w^{(\mathrm{rpl})}_{k}\approx\frac{m_ek_BT}{2\pi\alpha\hbar^3}\int_0^{2\pi}d\theta\frac{1}{q^2}\left[\frac{4\Lambda}{r_B^3}\left(\frac{r_B}{2}-\frac{1}{q}\Omega_r(qr_B)\right)+\frac{eE_\perp}{2}\right]^2\Bigg|_{q=k\sqrt{2(1-\cos\theta)}} \tag{88}$$

In our simulations, we neglect the $eE_\perp$ term for two reasons. First, it is setup-dependent. Second, it causes the integral over θ to diverge at small angles. That, in principle, can be avoided by assuming a reasonable threshold on the long-wavelength ripplons that can participate in scattering. However, we choose not to complicate the problem further since the inclusion of this term is not expected change the qualitative behavior of the system that we study.

A.8 Mobility in a uniform electron system on the helium surface

A.8.1 Single-electron mobility

The mobility in the spatially uniform system of noninteracting electrons can be calculated from the Boltzmann equation. We assume that a uniform driving field $\boldsymbol{E}_d$ is applied to the electron gas. Then the Boltzmann equation in the relaxation time approximation can be written as

$$e\boldsymbol{E}_d \frac{\partial f}{\partial \boldsymbol{p}} \approx \frac{g(\boldsymbol{p})}{\tau_{\mathrm{se}}(p)}, \tag{89}$$

where $\boldsymbol{p}$ is the electron momentum, $f(\boldsymbol{p})$ is the equilibrium momentum distribution, and $g(\boldsymbol{p})$ is the additional term in the distribution that is induced by the driving field. The inverse relaxation time $1/\tau_{\mathrm{se}}(p)$ due to the ripplon scattering without a pressing field is calculated by an integral similar to Eq. (87). We only need to modify the integrand by a factor of $(1-\cos\theta)$:

$$\frac{1}{\tau_{\mathrm{se}}(p)} = \frac{\hbar k_B T}{8\pi\alpha m_e r_B^2} \int_0^{2\pi} d\theta\, q^2 \phi^2\left(\frac{q r_B}{2}\right)(1-\cos\theta)\bigg|_{q=k\sqrt{2(1-\cos\theta)}}. \tag{90}$$

Here $p=\hbar k$, and notations from Appendix A.7 are used. From Eq. (89),

$$g(\boldsymbol{p}) = \frac{e}{m_e}(\boldsymbol{E}_d \boldsymbol{p})\frac{\partial f}{\partial \varepsilon}\tau_{\mathrm{se}}(p). \tag{91}$$

To find the drift velocity v_x in the field $\boldsymbol{E}_d$ along the x axis, we integrate

$$v_x = \int d^2p\, \frac{p_x}{m_e} g(\boldsymbol{p}) = \frac{eE_d}{m_e^2}\int dp\, d\theta\, p^3 \cos^2(\theta)\frac{\partial f}{\partial \varepsilon}\tau_{\mathrm{se}}(p) \tag{92}$$

$$= \frac{\pi e E_d}{m_e^2}\int dp\, p^3 \frac{\partial f}{\partial \varepsilon}\tau_{\mathrm{se}}(p). \tag{93}$$

If we define the single electron mobility μ_{se} through

$$|v_x| = \mu_{\mathrm{se}} E_d, \tag{94}$$

then for μ_{se} we have

$$\mu_{\mathrm{se}} = -\frac{\pi e}{m_e^2}\int dp\, p^3 \frac{\partial f}{\partial \varepsilon}\tau_{\mathrm{se}}(p). \tag{95}$$

f must be normalized to give $\int d^2p\, f(\boldsymbol{p}) = 1$. For the Boltzmann distribution, this means

$$f(\boldsymbol{p}) = \frac{1}{2\pi m_e k_B T} e^{-\frac{p^2}{2m_e k_B T}}, \tag{96}$$

which gives the mobility

$$\mu_{\mathrm{se}} = \frac{e}{2m_e^3(k_BT)^2}\int_0^\infty dp\, p^3 \tau_{\mathrm{se}}(p) e^{-p^2/2m_e k_B T}. \tag{97}$$

A.8.2 Many-electron mobility

When the electron-electron interaction is strong, the electrons exchange momentum with each other much faster than with the ripplons. Therefore, the calculation of the mobility should be different from the non-interacting case. According to Eqs. (38) and (39) in Ref. [3], mobility in the strongly correlated nondegenerate electron fluid on the sufrace of helium without magnetic field is given by

$$\mu_{\mathrm{me}} = \frac{e\tau_{\mathrm{me}}}{m_e}, \tag{98}$$

where

$$\tau_{\mathrm{me}}^{-1} = \frac{1}{4m_e k_B T}\sum_{\boldsymbol{q}} q^2 \overline{|H_{\boldsymbol{q}}^{(rpl)}|^2}\zeta(\boldsymbol{q}) = \frac{S}{4m_e k_B T(2\pi)^2}\int_0^\infty dq\, 2\pi q^3 \overline{|H_{\boldsymbol{q}}^{(rpl)}|^2}\zeta(\boldsymbol{q}). \tag{99}$$

Here

$$\zeta(\boldsymbol{q}) = \int_{-\infty}^{\infty} dt \left\langle e^{i\boldsymbol{q}\boldsymbol{r}(t)} e^{-i\boldsymbol{q}\boldsymbol{r}(0)} \right\rangle \tag{100}$$

is the dynamical structure factor, and notations from Appendix A.7 are used. The statistical averaging is computed to the zeroth order in the coupling to the scatterers. To compute τ, we must calculate $\zeta(\boldsymbol{q})$ first. We expand $\boldsymbol{r}(t)$ to the first order and use the operator identity $e^{A+B} = e^B e^A e^{\frac{1}{2}[A,B]}$ for the case when $[A,B]$ commutes with both A and B:

$$\zeta(\boldsymbol{q}) \approx \int_{-\infty}^{\infty} dt \left\langle e^{i\boldsymbol{q}\boldsymbol{r}(0)+\frac{i\boldsymbol{q}\boldsymbol{p}(0)t}{m_e}} e^{-i\boldsymbol{q}\boldsymbol{r}(0)} \right\rangle = \int_{-\infty}^{\infty} dt \left\langle e^{i\boldsymbol{q}\boldsymbol{p}t/m_e} e^{-i\hbar q^2 t/2m_e} \right\rangle$$

It is convenient to compute the statistical average with the Boltzmann distribution first:

$$\begin{aligned}
\left\langle e^{-i\boldsymbol{q}\boldsymbol{p}t/m_e} \right\rangle &= \frac{1}{2\pi m_e k_B T}\int dp_x dp_y\, e^{-p_x^2/2k_B T m_e + iqtp_x/m_e} e^{-p_y^2/2m_e} \\
&= \frac{1}{\sqrt{2\pi m_e k_B T}}\int dp_x\, e^{-\frac{1}{2m_e}(p_x - iqtk_B T)^2} e^{-k_B T q^2 t^2/2m_e} \\
&= e^{-k_B T q^2 t^2/2m_e}.
\end{aligned}$$

Therefore,

$$\zeta(\boldsymbol{q}) = \int_{-\infty}^{\infty} dt\, e^{-k_B T q^2 t^2/2m_e} e^{-i\hbar q^2 t/2m_e} = \sqrt{\frac{2\pi m_e}{k_B T q^2}} e^{-\frac{\hbar^2 q^2}{8mk_B T}}. \tag{101}$$

Now we can calculate τ^{-1}:

$$\tau^{-1} = \frac{\hbar^4}{16 m_e^2 r_B^2 \alpha \sqrt{2\pi m_e k_B T}} \int_0^{\infty} dq\, q^4 \phi^2\left(\frac{q r_B}{2}\right) e^{-\frac{\hbar^2 q^2}{8m_e k_B T}}. \tag{102}$$

A.9 Electron-phonon scattering

A.9.1 Phonon quantization in half-space with free surface

In this appendix, we reproduce the derivation of the electron-phonon scattering rates following Ref. [141]. Only polarization effects are considered here, without the effects of the surface deformation by the phonons. Before we consider the scattering we must quantize the elastic waves (phonons) in the half-space occupied by the helium with a free surface boundary condition. The free surface condition implies zero stress at the surface. Since it is a liquid, the only stress that can exist is pressure. No pressure at the surface means

$$\left(\frac{\partial u_x}{\partial x} + \frac{\partial u_y}{\partial y} + \frac{\partial u_z}{\partial z}\right)\Bigg|_{z=0} = 0, \tag{103}$$

where u_i are the components of the displacement field. The displacement field in a liquid can be written as a superposition of longitudinal waves:

$$\boldsymbol{u} = \frac{1}{2}\sum_{\boldsymbol{Q}} u_{\boldsymbol{Q}} \frac{\boldsymbol{Q}}{Q} e^{i\boldsymbol{QR}}, \tag{104}$$

where $\boldsymbol{Q}$ are three-dimensional wavevectors. The free-surface condition (103) then reads as

$$\nabla \cdot \boldsymbol{u} = -\sum_{\boldsymbol{Q}} u_{\boldsymbol{Q}} Q u_{\boldsymbol{Q}} e^{i\boldsymbol{qr}} = 0 \tag{105}$$

where $\boldsymbol{r}$ and $\boldsymbol{q}$ are the coordinate and the wave vector in the plane parallel to the surface. The last equation must be true at any point $\boldsymbol{r}$, which means

$$u_{-Q_z,\boldsymbol{q}} = -u_{Q_z,\boldsymbol{q}}. \tag{106}$$

This leads to the following form of the expression (104), where we split the sum into two parts for convenience:

$$\boldsymbol{u} = \frac{1}{2}\sum_{\boldsymbol{q}}\left(\sum_{Q_z>0} u_{Q_z,\boldsymbol{q}}\frac{\boldsymbol{Q}}{Q}e^{iQ_zz}e^{i\boldsymbol{qr}} + \sum_{Q_z<0} u_{Q_z,\boldsymbol{q}}\frac{\boldsymbol{Q}}{Q}e^{iQ_zz}e^{i\boldsymbol{qr}}\right) \tag{107}$$

The term with $Q_z = 0$ vanishes due to the condition (106). Using (106) we can write the components of $\boldsymbol{u}$ as

$$\begin{aligned}
u_x &= i\sum_{\boldsymbol{q}}\sum_{Q_z>0} u_{Q_z,\boldsymbol{q}}\frac{q_x}{Q}\sin(Q_zz)e^{i\boldsymbol{qr}}, \\
u_y &= i\sum_{\boldsymbol{q}}\sum_{Q_z>0} u_{Q_z,\boldsymbol{q}}\frac{q_y}{Q}\sin(Q_zz)e^{i\boldsymbol{qr}}, \\
u_z &= \sum_{\boldsymbol{q}}\sum_{Q_z>0} u_{Q_z,\boldsymbol{q}}\frac{Q_z}{Q}\cos(Q_zz)e^{i\boldsymbol{qr}}.
\end{aligned} \tag{108}$$

To quantize the phonon field, we express the Lagrangian of the system in terms of the new Fourier variables $\boldsymbol{u}_{Q_z,\boldsymbol{q}}$, construct the Hamiltonian and then express the displacement and momentum in terms of ladder operators. The kinetic energy is

$$\begin{aligned}
T &= \frac{\rho}{2}\int d^3R\left(\dot{u}_x^2 + \dot{u}_y^2 + \dot{u}_z^2\right) \\
&\frac{\rho}{2}\left(i\sum_{\boldsymbol{q}}\sum_{Q_z>0}\dot{u}_{Q_z,\boldsymbol{q}}\frac{q_x}{Q}\sin(Q_zz)e^{i\boldsymbol{qr}}\right)\left(i\sum_{\boldsymbol{q}'}\sum_{Q'_z>0}\dot{u}_{Q'_z,\boldsymbol{q}'}\frac{q'_x}{Q}\sin(Q'_zz)e^{i\boldsymbol{q}'\boldsymbol{r}}\right) + \\
&\frac{\rho}{2}\left(i\sum_{\boldsymbol{q}}\sum_{Q_z>0}\dot{u}_{Q_z,\boldsymbol{q}}\frac{q_y}{Q}\sin(Q_zz)e^{i\boldsymbol{qr}}\right)\left(i\sum_{\boldsymbol{q}'}\sum_{Q'_z>0}\dot{u}_{Q'_z,\boldsymbol{q}'}\frac{q'_y}{Q}\sin(Q'_zz)e^{i\boldsymbol{q}'\boldsymbol{r}}\right) + \\
&\frac{\rho}{2}\left(\sum_{\boldsymbol{q}}\sum_{Q_z>0}\dot{u}_{Q_z,\boldsymbol{q}}\frac{Q_z}{Q}\cos(Q_zz)e^{i\boldsymbol{qr}}\right)\left(\sum_{\boldsymbol{q}'}\sum_{Q'_z>0}\dot{u}_{Q'_z,\boldsymbol{q}'}\frac{Q'_z}{Q}\cos(Q'_zz)e^{i\boldsymbol{q}'\boldsymbol{r}}\right).
\end{aligned} \tag{109}$$

Integral over $\boldsymbol{r}$ gives $S\delta_{\boldsymbol{q}',-\boldsymbol{q}}$, while the integral over z gives $\frac{1}{2}L_z\delta_{Q_z,Q'_z}$, where S is the surface area and L_z is the helium depth. Therefore,

$$T = \frac{\rho V}{4}\sum_{bq,Q_z>0}\dot{u}_{Q_z,\boldsymbol{q}}\dot{u}_{Q_z,-\boldsymbol{q}} \tag{110}$$

Similarly, the potential energy of the elastic excitations is expressed through the bulk modulus λ:

$$\begin{aligned} U &= \frac{1}{2}\lambda \int d^3R\,(\nabla\cdot\boldsymbol{u})^2 \\ &= \frac{1}{2}\lambda \int d^3R \left(\sum_{\boldsymbol{q},Q_z>0} Q u_{Q_z,\boldsymbol{q}} \sin(Q_z z) e^{i\boldsymbol{qr}}\right)^2 \\ &= \frac{1}{4}\lambda V \sum_{\boldsymbol{q},Q_z>0} Q^2 u_{Q_z,\boldsymbol{q}} u_{Q_z,-\boldsymbol{q}}. \end{aligned} \tag{111}$$

Integration in the last step is done in the same way it was done to obtain Eq. (110). Defining the Lagrangian as $L = T - U$, we obtain the momentum variables π_j through $\pi_j = \frac{\partial L}{\partial \dot{u}_j}$:

$$\begin{aligned} \pi_{Q_z,\boldsymbol{q}} &= \frac{\rho V}{2} \dot{u}_{Q_z,-\boldsymbol{q}}, \\ \dot{u}_{Q_z,\boldsymbol{q}} &= \frac{2}{\rho V} \pi_{Q_z,-\boldsymbol{q}}. \end{aligned} \tag{112}$$

This allows us to write the Hamiltonian:

$$H = \frac{1}{\rho V} \sum_{\boldsymbol{q},Q_z>0} \pi_{Q_z,\boldsymbol{q}} \pi_{Q_z,-\boldsymbol{q}} + \frac{1}{4}\lambda V \sum_{\boldsymbol{q},Q_z>0} Q^2 u_{Q_z,\boldsymbol{q}} u_{Q_z,-\boldsymbol{q}} \tag{113}$$

If we define $M \equiv \frac{1}{2}\rho V$ and $\omega_Q^2 = \frac{\lambda}{\rho} Q^2 \equiv v_s^2 Q^2$, then we can introduce the ladder operators $b_{Q_z,\boldsymbol{q}}$ and $b^\dagger_{Q_z,\boldsymbol{q}}$ in the standard way:

$$\begin{aligned} u_{Q_z,\boldsymbol{q}} &= \sqrt{\frac{\hbar}{2M\omega_Q}} \left(b_{Q_z,\boldsymbol{q}} + b^\dagger_{Q_z,-\boldsymbol{q}}\right), \\ \pi_{Q_z,\boldsymbol{q}} &= \sqrt{\frac{\hbar M \omega_Q}{2}} \left(a_{Q_z,\boldsymbol{q}} - a^\dagger_{Q_z,-\boldsymbol{q}}\right). \end{aligned} \tag{114}$$

Then

$$\begin{aligned} u_z &= \sum_{\boldsymbol{q},Q_z>0} \sqrt{\frac{\hbar}{2M\omega_Q}} \left(b_{Q_z,\boldsymbol{q}} + b^\dagger_{Q_z,-\boldsymbol{q}}\right) \frac{Q_z}{Q} \cos(Q_z z) e^{i\boldsymbol{qr}}, \\ u_x &= \sum_{\boldsymbol{q},Q_z>0} i\sqrt{\frac{\hbar}{2M\omega_Q}} \left(b_{Q_z,\boldsymbol{q}} + b^\dagger_{Q_z,-\boldsymbol{q}}\right) \frac{q_x}{Q} \sin(Q_z z) e^{i\boldsymbol{qr}}. \end{aligned} \tag{115}$$

A.9.2 Electron-phonon coupling

We consider only the polarization coupling to phonons for simplicity. We also consider the dielectric constant ε close to 1. In this model, the coupling Hamiltonian is

$$
\begin{aligned}
H^{(ph)} &\approx -\frac{1}{8\pi}\int d^3R'\,\delta\varepsilon(\boldsymbol{R})C(\boldsymbol{R}')^2 \approx \frac{\varepsilon-1}{8\pi}\int d^3R'\,\nabla\cdot\boldsymbol{u}\frac{e^2}{|\boldsymbol{R}'-\boldsymbol{R}|^4}\\
&\approx \frac{\Lambda}{\pi}\int d^3R'\frac{\nabla\cdot\boldsymbol{u}}{|\boldsymbol{R}'-\boldsymbol{R}|^4}.
\end{aligned}
\tag{116}
$$

Here $\delta\varepsilon(\boldsymbol{R}) \approx (1-\varepsilon)\nabla\cdot\boldsymbol{u}$ is the local change of the dielectric constant due to the phonon deformation field, $C(\boldsymbol{R}')$ is the electric field at point $\boldsymbol{R}'$ that would be created by an elementary charge located at position $\boldsymbol{R}$ above the surface without a dielectric. We use $\boldsymbol{R}$ for the 3D coordinate to distinguish it from the in-plane coordinate $\boldsymbol{r}$. Integration over $\boldsymbol{R}'$ is done in the $z<0$ half-space that is occupied by helium. We also used the approximation $\Lambda \equiv \frac{e^2(\varepsilon-1)}{4(\varepsilon+1)} \approx e^2(\varepsilon-1)/8$. We can find $\nabla\cdot\boldsymbol{u}$ using Eq. (108), therefore

$$
\begin{aligned}
H^{(ph)} &= \frac{\Lambda}{\pi}\sum_{\boldsymbol{q},Q_z>0} Qu_{Q_z,\boldsymbol{q}}\int_{-\infty}^{0} dz'\,\sin(Q_z z')\int d^2r'\,\frac{e^{i\boldsymbol{q}\boldsymbol{r}}}{\left[(z-z')^2+(\boldsymbol{r}-\boldsymbol{r}')^2\right]^2}\\
&= \frac{\Lambda}{\pi}\sum_{\boldsymbol{q},Q_z>0} Qu_{Q_z,\boldsymbol{q}}\int_{-\infty}^{0} dz'\,\sin(Q_z z')q^2\int_0^{\infty}\frac{dxx\int d\theta\sum_n e^{in\theta}J_n(x)i^n}{\left[q(z-z')^2+x^2\right]^2}\\
&= 2\Lambda\sum_{\boldsymbol{q},Q_z>0} Qu_{Q_z,\boldsymbol{q}}q^2\int_{-\infty}^{0} dz'\,\sin(Q_z z')\int_0^{\infty}\frac{dxxJ_0(x)}{\left[q(z-z')^2+x^2\right]^2}
\end{aligned}
\tag{117}
$$

It can be shown that

$$
\int_0^{\infty}\frac{dxxJ_0(x)}{\left[q(z-z')^2+x^2\right]^2} = \frac{1}{2q|z-z'|}K_1\left(q(z-z')\right),
\tag{118}
$$

Where $K_1(x)$ is a modified Bessel function. Then

$$
H^{(ph)} = \Lambda\sum_{\boldsymbol{q},Q_z>0} Qqu_{Q_z,\boldsymbol{q}}e^{i\boldsymbol{q}\boldsymbol{r}}\int_{-\infty}^{0} dz'\,\frac{\sin(Q_z z')}{2q|z-z'|}K_1\left(q(z-z')\right) \equiv \Lambda\sum_{\boldsymbol{q},Q_z>0} Qqu_{Q_z,\boldsymbol{q}}e^{i\boldsymbol{q}\boldsymbol{r}}\Xi(\boldsymbol{Q},z),
\tag{119}
$$

where we defined the integral by $\Xi(\boldsymbol{Q},z)$. The function $\Xi(\boldsymbol{Q},z)$ is calculated numerically.

A.9.3 Scattering of electrons by phonons

To calculate the rate of scattering of an electron from state $\boldsymbol{k}$ to state $\boldsymbol{k}'$, we need the corresponding matrix elements:

$$\langle \boldsymbol{k}'|H^{(ph)}|\boldsymbol{k}\rangle = \Lambda \sum_{Q_z,\boldsymbol{q}} Qqu_{Q_z,\boldsymbol{q}}\delta_{\boldsymbol{q},\boldsymbol{k}'-\boldsymbol{k}}\langle O_z|\Xi(\boldsymbol{Q},z)|O_z\rangle, \tag{120}$$

$$\langle O_z|\Xi(\boldsymbol{Q},z)|O_z\rangle = \int_0^\infty dz\frac{4z^2}{r_B^3}e^{-2z/r_B}\Xi(\boldsymbol{Q},z). \tag{121}$$

Here $r_B = \hbar^2/m_e\Lambda$ is the “Bohr radius” of the ground state of the electron motion along the z axis. There are two scattering processes, with creation and absorption of a phonon. The phonon-*absorption* process has the following matrix element:

$$\langle \boldsymbol{k}', N_{Q_z,\boldsymbol{q}}-1, N_{Q_z,-\boldsymbol{q}}|H^{(ph)}|\boldsymbol{k}, N_{Q_z,\boldsymbol{q}}, N_{Q_z,-\boldsymbol{q}}\rangle = \Lambda Qq\sqrt{\frac{\hbar N_{Q_z,\boldsymbol{q}}}{2M\omega_Q}}\,\langle O_z|\Xi|O_z\rangle|_{\boldsymbol{q}=\boldsymbol{k}'-\boldsymbol{k}}, \tag{122}$$

while the emission process matrix element is

$$\langle \boldsymbol{k}', N_{Q_z,\boldsymbol{q}}, N_{Q_z,-\boldsymbol{q}}+1|H^{(ph)}|\boldsymbol{k}, N_{Q_z,\boldsymbol{q}}, N_{Q_z,-\boldsymbol{q}}\rangle = \Lambda Qq\sqrt{\frac{\hbar (N_{Q_z,\boldsymbol{q}}+1)}{2M\omega_Q}}\,\langle O_z|\Xi|O_z\rangle|_{\boldsymbol{q}=\boldsymbol{k}'-\boldsymbol{k}}, \tag{123}$$

Here, the state vectors $|\boldsymbol{k}, N_{Q_z,\boldsymbol{q}}, N_{Q_z,-\boldsymbol{q}}\rangle$ are defined by the electron wavevector $\boldsymbol{k}$, the number of phonons $N_{Q_z,\boldsymbol{q}}$ in the $(\boldsymbol{q}, Q_z)$ state, and the number of phonons $N_{Q_z,-\boldsymbol{q}}$ in the $(-\boldsymbol{q}, Q_z)$ state. In thermal equilibrium, the average population of phonons is

$$N_{Q_z,\boldsymbol{q}} = \frac{1}{e^{\hbar\omega_Q/T}-1}. \tag{124}$$

Finally, the scattering rate corresponding to the first process is

$$\begin{aligned} dw^{(\mathrm{ph1})}_{\boldsymbol{k}'\boldsymbol{k}} &= \frac{2\pi}{\hbar}\sum_{Q_z>0}\Lambda^2Q^2q^2\frac{\hbar N_{Q_z,\boldsymbol{q}}}{2M\omega_Q}\,|\langle O_z|\Xi|O_z\rangle|^2\,\delta(\varepsilon_{k'}-\varepsilon_k-\hbar\omega_Q)\Bigg|_{\boldsymbol{q}=\boldsymbol{k}'-\boldsymbol{k}} \\ &= d^2k'\frac{\Lambda^2}{2\pi^2\rho\hbar v_s^2}Qq^2N_{Q_z,\boldsymbol{q}}\,|\langle O_z|\Xi|O_z\rangle|^2\Bigg|_{\substack{\boldsymbol{q}=\boldsymbol{k}'-\boldsymbol{k} \\ Q_z=\frac{1}{\hbar v_s}(\varepsilon_{k'}-\varepsilon_k)}}\quad . \end{aligned} \tag{125}$$

In direct analogy to this, the second process, with a phonon emitted, has the scattering rate

$$dw^{(\mathrm{ph2})}_{\boldsymbol{k}'\boldsymbol{k}} = d^2k'\frac{\Lambda^2}{2\pi^2\rho\hbar v_s^2}Qq^2(N_{Q_z,\boldsymbol{q}}+1)\,|\langle O_z|\Xi|O_z\rangle|^2\Bigg|_{\substack{\boldsymbol{q}=\boldsymbol{k}'-\boldsymbol{k} \\ Q_z=\frac{1}{\hbar v_s}(\varepsilon_k-\varepsilon_{k'})}} \tag{126}$$

A.10 Standard error estimation for a correlated process

In this appendix, we show the method used for calculating the standard error of the mean value estimate for a stochastic process with a finite correlation time. Let us assume that v_t is a stochastic process with the expectation value v and nonzero correlation time. In the simulation, we want to estimate v from the sample v_t of size N_t. The estimate is simply the average:

$$\bar{v} = \frac{1}{N_t}\sum_t v_t. \tag{127}$$

We want to estimate the standard error σ_s of this measurement. The definition of the standard error is

$$\sigma_s^2 = \langle(\bar{v}-v)^2\rangle.$$

Here $\bar{v}$ is treated as a random variable, and $\langle\rangle$ means the expectation value. σ_s is a measure of the width of the distribution of $\bar{v}$. Therefore, it is a good estimate of the statistical error of v calculated with Eq. (127) from a sample. It is convenient to introduce $\delta_t \equiv v_t - v$ with a zero expectation value. Then

$$\sigma_s^2 = \left\langle \left(\frac{1}{N_t}\sum_t v_t - v\right)^2 \right\rangle = \left\langle \left(\frac{1}{N_t}\sum_t \delta_t\right)^2 \right\rangle = \frac{1}{N_t^2}\sum_{tt'}\left\langle \delta_t \delta_{t'}\right\rangle. \tag{128}$$

With no correlation between δ_t and $\delta_{t'}$ at different time moments, the standard error would be simply $\sigma_s^2 = \langle\delta_t^2\rangle/N_t$. The more statistics we have the more precise estimate of v we can obtain.

For the time-correlated case, let us define the time-correlation function as $\rho(t-t') = \left\langle \delta_t \delta_{t'}\right\rangle$, which is symmetric around zero. Assuming that $\rho(t)$ decays after some short time t_ρ, we can approximately rewrite

$$\sigma_s^2 \approx \frac{1}{N_t}\sum_{t'=-t_\rho}^{t_\rho} \rho(t') \tag{129}$$

We summed over t since ρ depends only on the difference $t-t'$. One approximation here is that we truncate ρ at t_ρ. Another approximation is that we disregarded the edges $t=0$ and $t=N_t$ when summing over t. These approximations are good as long as $t_\rho \ll N_t$, which is usually satisfied in our simulations.

Finally, to estimate σ_s from the data, we need to estimate $\rho(t-t')$:

$$\overline{\rho}(t) = \frac{1}{(N_t - t)} \sum_{t'=1}^{N_t - t} \delta_{t'} \delta_{t'+t} \tag{130}$$

Together with Eq. (129), it gives the desired estimate of the standard error.

BIBLIOGRAPHY

BIBLIOGRAPHY

[1] C. C. Grimes and G. Adams. Evidence for a liquid-to-crystal phase-transition in a classical, 2-dimensional sheet of electrons. *Phys. Rev. Lett.*, 42(12):795–798, 1979.

[2] M. J. Lea and M. I. Dykman. Magnetotransport in the two-dimensional electron fluid and solid on liquid helium. *Physica B*, 251:628–635, June 1998.

[3] M. I. Dykman, C. FangYen, and M. J. Lea. Many-electron transport in strongly correlated nondegenerate two-dimensional electron systems. *Phys. Rev. B*, 55(24):16249–16271, June 1997.

[4] Q.-H. Wei, C. Bechinger, D. Rudhardt, and P. Leiderer. Experimental study of laser-induced melting in two-dimensional colloids. *Phys. Rev. Lett.*, 81:2606–2609, 1998.

[5] T. Bohlein, J. Mikhael, and C. Bechinger. Observation of kinks and antikinks in colloidal monolayers driven across ordered surfaces. *Nature Materials*, 11:126, December 2011.

[6] C. Reichhardt, C. J. Olson, and Franco Nori. Commensurate and incommensurate vortex states in superconductors with periodic pinning arrays. *Phys. Rev. B*, 57:7937–7943, Apr 1998.

[7] Q. Le Thien, D. McDermott, C. J. Olson Reichhardt, and C. Reichhardt. Orientational ordering, buckling, and dynamic transitions for vortices interacting with a periodic quasi-one-dimensional substrate. *Phys. Rev. B*, 93(1), JAN 7 2016.

[8] A. Eichler, M. del Ålamo Ruiz, J. A. Plaza, and A. Bachtold. Strong coupling between mechanical modes in a nanotube resonator. *Phys. Rev. Lett.*, 109(2):025503–, July 2012.

[9] O. Shoshani, S. W. Shaw, and M. I. Dykman. Anomalous decay of nanomechanical modes going through nonlinear resonance. *Scientific Reports*, 7:18091, 2017.

[10] M. H. Matheny, L. G. Villanueva, R. B. Karabalin, J. E. Sader, and M. L. Roukes. Nonlinear mode-coupling in nanomechanical systems. *Nano Lett.*, 13(4):1622–1626, April 2013.

[11] A. D. O'Connell, M. Hofheinz, M. Ansmann, R. C. Bialczak, M. Lenander, E. Lucero, M. Neeley, D. Sank, H. Wang, M. Weides, J. Wenner, J. M. Martinis, and A. N. Cleland. Quantum ground state and single-phonon control of a mechanical resonator. *Nature*, 464(7289):697–703, April 2010.

[12] Yiwen Chu, Prashanta Kharel, William H. Renninger, Luke D. Burkhart, Luigi Frunzio, Peter T. Rakich, and Robert J. Schoelkopf. Quantum acoustics with superconducting qubits. *Science*, 2017.

[13] K. Stannigel, P. Komar, S. J. M. Habraken, S. D. Bennett, M. D. Lukin, P. Zoller, and P. Rabl. Optomechanical quantum information processing with photons and phonons. *Phys. Rev. Lett.*, 109:013603, Jul 2012.

[14] D. Fedorets, L. Y. Gorelik, R. I. Shekhter, and M. Jonson. Quantum shuttle phenomena in a nanoelectromechanical single-electron transistor. *Phys. Rev. Lett.*, 92(16), 2004.

[15] N. M. Chtchelkatchev, W. Belzig, and C. Bruder. Charge transport through a single-electron transistor with a mechanically oscillating island. *Phys. Rev. B*, 70:193305, Nov 2004.

[16] J. Koch, M. E. Raikh, and F. von Oppen. Full counting statistics of strongly non-ohmic transport through single molecules. *Phys. Rev. Lett.*, 95(5):056801, July 2005.

[17] F. Pistolesi and S. Labarthe. Current blockade in classical single-electron nanomechanical resonator. *Physical Review B*, 76(16):165317, October 2007.

[18] O. Usmani, Ya. M. Blanter, and Yu. V. Nazarov. Strong feedback and current noise in nanoelectromechanical systems. *Phys. Rev. B*, 75:195312, May 2007.

[19] R. Leturcq, Ch. Stampfer, K. Inderbitzin, L. Durrer, Ch. Hierold, E. Mariani, M. G. Schultz, F. von Oppen, and K. Ensslin. Franck-condon blockade in suspended carbon nanotube quantum dots. *Nat. Phys*, 5(5):327–331, May 2009.

[20] G. A. Steele, A. K. Huttel, B. Witkamp, M. Poot, H. B. Meerwaldt, L. P. Kouwenhoven, and H. S. J. van der Zant. Strong coupling between single-electron tunneling and nanomechanical motion. *Science*, 325(5944):1103–1107, August 2009.

[21] B. Lassagne, Y. Tarakanov, J. Kinaret, D. Garcia-Sanchez, and A. Bachtold. Coupling mechanics to charge transport in carbon nanotube mechanical resonators. *Science*, 325(5944):1107–1110, August 2009.

[22] M. N. Kiselev, K. A. Kikoin, L. Y. Gorelik, and R. I. Shekhter. Kondo force in shuttling devices: Dynamical probe for a kondo cloud. *Physical Review Letters*, 110(6):066804, February 2013.

[23] G. Micchi, R. Avriller, and F. Pistolesi. Mechanical signatures of the current blockade instability in suspended carbon nanotubes. *Phys. Rev. Lett.*, 115:206802, Nov 2015.

[24] Y. Yang, E. J.. Ng, P. M. Polunin, Y. Chen, I. B. Flader, S. W. Shaw, M. I. Dykman, and T. W. Kenny. Nonlinearity of degenerately doped bulk-mode silicon mems resonators. *JMEMS*, 25(5):859, 2016.

[25] K. Shirahama, S. Ito, H. Suto, and K. Kono. Surface study of liquid-he-3 using surface-state electrons. *J. Low Temp. Phys.*, 101(3-4):439–444, November 1995.

[26] V. L. Pokrovsky and A. L. Talapov. The theory of two-dimensional incommensurate crystals. *Zh. Eksp. Teor. Fiz.*, 78:269, 1980.

[27] L Radzihovsky, E Frey, and DR Nelson. Novel phases and reentrant melting of two-dimensional colloidal crystals. *Phys. Rev. E*, 63(3, 1), MAR 2001.

[28] C. Reichhardt and C. J. Olson Reichhardt. Depinning and nonequilibrium dynamic phases of particle assemblies driven over random and ordered substrates: a review. *Rep. Prog. Phys*, 80(2), 2017.

[29] M. I. Dykman and Yuri G. Rubo. Bragg-cherenkov scattering and nonlinear conductivity of a two-dimensional wigner crystal. *Phys. Rev. Lett.*, 78:4813–4816, Jun 1997.

[30] D. G. Rees, N. R. Beysengulov, J.-J. Lin, and K. Kono. Stick-slip motion of the wigner solid on liquid helium. *Phys. Rev. Lett.*, 116:206801, 2016.

[31] V. Sazonova, Y. Yaish, H. Ustunel, D. Roundy, T. A. Arias, and P. L. McEuen. A tunable carbon nanotube electromechanical oscillator. *Nature*, 431(7006):284–287, September 2004.

[32] K. L. Ekinci and M. L. Roukes. Nanoelectromechanical systems. *Rev. Sci. Instrum.*, 76(6):061101, June 2005.

[33] J. S. Aldridge and A. N. Cleland. Noise-enabled precision measurements of a duffing nanomechanical resonator. *Phys. Rev. Lett.*, 94(15):156403, 2005.

[34] A. N. Cleland. Thermomechanical noise limits on parametric sensing with nanomechanical resonators. *New J. Phys.*, 7:235, November 2005.

[35] Y. T. Yang, C. Callegari, X. L. Feng, K. L. Ekinci, and M. L. Roukes. Zeptogram-scale nanomechanical mass sensing. *Nano Lett.*, 6(4):583–586, April 2006.

[36] E. Buks and B. Yurke. Mass detection with a nonlinear nanomechanical resonator. *Phys. Rev. E*, 74(4):046619, October 2006.

[37] J. Scott Bunch, Arend M. van der Zande, Scott S. Verbridge, Ian W. Frank, David M. Tanenbaum, Jeevak M. Parpia, Harold G. Craighead, and Paul L. McEuen. Electromechanical resonators from graphene sheets. *Science*, 315(5811):490–493, January 2007.

[38] K. Jensen, K. Kim, and A. Zettl. An atomic-resolution nanomechanical mass sensor. *Nature Nanotech.*, 3:533, 2008.

[39] B. E. DeMartini, J. F. Rhoads, M. A. Zielke, K. G. Owen, S. W. Shaw, and K. L. Turner. A single input-single output coupled microresonator array for the detection and identification of multiple analytes. *Appl. Phys. Lett.*, 93(5):054102, August 2008.

[40] J. D. Teufel, T. Donner, M. A. Castellanos-Beltran, J. W. Harlow, and K. W. Lehnert. Nanomechanical motion measured with an imprecision below that at the standard quantum limit. *Nature Nanotech.*, 4(12):820–823, December 2009.

[41] A. K. Naik, M. S. Hanay, W. K. Hiebert, X. L. Feng, and M. L. Roukes. Towards single-molecule nanomechanical mass spectrometry. *Nat. Nanotech.*, 4(7):445–450, JUL 2009.

[42] J. Lee, W. J. Shen, K. Payer, T. P. Burg, and S. R. Manalis. Toward attogram mass measurements in solution with suspended nanochannel resonators. *Nano Lett.*, 10(7):2537–2542, July 2010.

[43] K. Eom, H. S. Park, D. S. Yoon, and T. Kwon. Nanomechanical resonators and their applications in biological/chemical detection: Nanomechanics principles. *Phys. Rep.*, 503(4-5):115–163, June 2011.

[44] J. Chaste, A. Eichler, J. Moser, G. Ceballos, R. Rurali, and A. Bachtold. A nanomechanical mass sensor with yoctogram resolution. *Nat. Nano*, 7:301–304, 2012.

[45] V. Puller, B. Lounis, and F. Pistolesi. Single molecule detection of nanomechanical motion. *Phys. Rev. Lett.*, 110(12):125501, March 2013.

[46] J. Moser, J. Güttinger, A. Eichler, M. J. Esplandiu, D. E. Liu, M. I. Dykman, and A. Bachtold. Ultrasensitive force detection with a nanotube mechanical resonator. *Nat. Nanotech.*, 8:493, 2013.

[47] W. J. Venstra, H. J. R. Westra, and H. S. J. van der Zant. Stochastic switching of cantilever motion. *Nat. Commun.*, 4:2624, 2013.

[48] V. Singh, S. J. Bosman, B. H. Schneider, Y. M. Blanter, A. Castellanos-Gomez, and G. A. Steele. Optomechanical coupling between a multilayer graphene mechanical resonator and a superconducting microwave cavity. *Nat Nano*, 9(10):820–824, October 2014.

[49] Y. Tao, J. M. Boss, B. A. Moores, and C. L. Degen. Single-crystal diamond nanomechanical resonators with quality factors exceeding one million. *Nat Commun*, 5:3638, April 2014.

[50] M. Selim Hanay, Scott I. Kelber, Cathal D. O'Connell, Paul Mulvaney, John E. Sader, and Michael L. Roukes. Inertial imaging with nanomechanical systems. *Nat Nano*, 10(4):339–344, May 2015.

[51] K. Y. Fong, M. Poot, and H. X. Tang. Nano-optomechanical resonators in microfluidics. *Nano Lett.*, 15:6116, 2015.

[52] P. Weber, J. Guttinger, A. Noury, J. Vergara-Cruz, and A. Bachtold. Force sensitivity of multilayer graphene optomechanical devices. *Nature Communications*, 7:12496, August 2016.

[53] D. Rugar, R. Budakian, H. J. Mamin, and B. W. Chui. Single spin detection by magnetic resonance force microscopy. *Nature*, 430(6997):329–332, July 2004.

[54] H. J. Mamin, M. Poggio, C. L. Degen, and D. Rugar. Nuclear magnetic resonance imaging with 90-nm resolution. *Nature Nanotech.*, 2(5):301–306, May 2007.

[55] S. Kuehn, S. A. Hickman, and J. A. Marohn. Advances in mechanical detection of magnetic resonance. *J. Chem. Phys.*, 128(5):052208, feb 2008.

[56] E. W. Moore, S. Lee, S. A. Hickman, S. J. Wright, L. E. Harrell, P. P. Borbat, J. H. Freed, and J. A. Marohn. Scanned-probe detection of electron spin resonance from a nitroxide spin probe. *Proc. Natl. Acad. Sci. USA*, 106(52):22251–22256, December 2009.

[57] S. K. Hong, M. S. Grinolds, P. Maletinsky, R. L. Walsworth, M. D. Lukin, and A. Yacoby. Coherent, mechanical control of a single electronic spin. *Nano Letters*, 12(8):3920–3924, August 2012.

[58] Y. Tao, A. Eichler, T. Holzherr, and C. L. Degen. Ultrasensitive mechanical detection of magnetic moment using a commercial disk drive write head. *Nat. Comm.*, 7:12714, 2016.

[59] V. Gouttenoire, T. Barois, S. Perisanu, J. L. Leclercq, S. T. Purcell, P. Vincent, and A. Ayari. Digital and fm demodulation of a doubly clamped single-walled carbon-nanotube oscillator: Towards a nanotube cell phone. *Small*, 6(9):1060–1065, May 2010.

[60] A. N. Cleland and M. L. Roukes. Fabrication of high frequency nanometer scale mechanical resonators from bulk si crystals. *Appl. Phys. Lett.*, 69(18):2653–2655, October 1996.

[61] L.D. Landau and E. M. Lifshitz. *Statistical Physics. Part 1.* Pergamon Press, New York, 3rd, revised by e. m. lifshitz and l. p. pitaevskii edition, 1980.

[62] V. Weisskopf and E. Wigner. On the natural linewidth of radiation of the harmonic oscillator. *Z. Phys.*, 65:18–29, 1930.

[63] J. Moser, A. Eichler, J. Guettinger, M. I. Dykman, and A. Bachtold. Nanotube mechanical resonators with quality factors of up to 5 million. *Nature Nanotech.*, 9:1007, 2014.

[64] Y. T. Yang, C. Callegari, X. L. Feng, and M. L. Roukes. Surface adsorbates fluctuations and noise in nanoelectromechanical systems. *Nano Lett.*, 11:1753, 2011.

[65] M. I. Dykman, M. Khasin, J. Portman, and S. W. Shaw. Spectrum of an oscillator with jumping frequency and the interference of partial susceptibilities. *Phys. Rev. Lett.*, 105(23):230601, December 2010.

[66] J. Atalaya, A. Isacsson, and M. I. Dykman. Diffusion-induced dephasing in nanomechanical resonators. *Phys. Rev. B*, 83(4):045419, January 2011.

[67] O. Maillet, X. Zhou, R. Gazizulin, A. Maldonado Cid, M. Defoort, A. D. Fefferman, O. Bourgeois, and E. Collin. Non-linear frequency transduction of nano-mechanical brownian motion. *Phys. Rev. B*, 96:165434, 2017.

[68] Yaxing Zhang and M. I. Dykman. Spectral effects of dispersive mode coupling in driven mesoscopic systems. *Phys. Rev. B*, 92:165419, 2015.

[69] M. Sansa, E. Sage, E. C. Bullard, M. Gely, T. Alava, E. Colinet, A. K. Naik, G. L. Villanueva, L. Duraffourg, M. L. Roukes, G. Jourdan, and S. Hentz. Frequency fluctuations in silicon nanoresonators. *Nat. Nanotech.*, 11:552, June 2016.

[70] Menno Poot and Herre S.J. van der Zant. Mechanical systems in the quantum regime. *Physics Reports*, 511(5):273–335, February 2012.

[71] M. I. Dykman, editor. *Fluctuating Nonlinear Oscillators: from Nanomechanics to Quantum Superconducting Circuits*. OUP, Oxford, 2012.

[72] M. Aspelmeyer, T. J. Kippenberg, and F. Marquardt. Cavity optomechanics. *Rev. Mod. Phys.*, 86:1391, 2014.

[73] T. D. Stowe, K. Yasumura, T. W. Kenny, D Botkin, K . Wago, and D. Rugar. Attonewton force detection using ultrathin silicon cantilevers. *Applied Physics Letters*, 71:288–290, 1997.

[74] M. C. Cross and Ron Lifshitz. Elastic wave transmission at an abrupt junction in a thin plate with application to heat transport and vibrations in mesoscopic systems. *Phys. Rev. B*, 64:085324, Aug 2001.

[75] Y-H Park and K. C. Park. High-fidelity modeling of mems resonators. part i. anchor loss mechanisms through substrate. *JMEMS*, 13:238–247, 2004.

[76] John A. Judge, Douglas M. Photiadis, Joseph F. Vignola, Brian H. Houston, and Jacek Jarzynski. Attachment loss of micromechanical and nanomechanical resonators in the limits of thick and thin support structures. *J. Appl. Phys.*, 101(1), 2007.

[77] I. Wilson-Rae. Intrinsic dissipation in nanomechanical resonators due to phonon tunneling. *Phys. Rev. B*, 77:245418, Jun 2008.

[78] Alexander Croy, Daniel Midtvedt, Andreas Isacsson, and Jari M. Kinaret. Nonlinear damping in graphene resonators. *Phys. Rev. B*, 86:235435, 2012.

[79] Ron Lifshitz and M. L. Roukes. Thermoelastic damping in micro- and nanomechanical systems. *Phys. Rev. B*, 61:5600–5609, Feb 2000.

[80] Alessandro De Martino, Reinhold Egger, and Alexander O. Gogolin. Phonon-phonon interactions and phonon damping in carbon nanotubes. *Phys. Rev. B*, 79:205408, May 2009.

[81] K. Kunal and N. R. Aluru. Akhiezer damping in nanostructures. *Phys. Rev. B*, 84:245450, Dec 2011.

[82] S. Ghaffari and T. W. Kenny. *Resonant MEMS: Fundamentals, Implementation, and Application*, chapter Damping in Resonant MEMS, pages 55–71. Wiley VCH, Weinheim, 2015.

[83] I. Mahboob, N. Perrissin, K. Nishiguchi, D. Hatanaka, Y. Okazaki, A. Fujiwara, and H. Yamaguchi. Dispersive and dissipative coupling in a micromechanical resonator embedded with a nanomechanical resonator. *Nano Lett.*, 15(4):2312–2317, April 2015.

[84] Vibhor Singh, Olga Shevchuk, Ya. M. Blanter, and Gary A. Steele. Negative nonlinear damping of a multilayer graphene mechanical resonator. *Phys. Rev. B*, 93:245407, Jun 2016.

[85] K. J. Lulla, M. Defoort, C. Blanc, O. Bourgeois, and E. Collin. Evidence for the role of normal-state electrons in nanoelectromechanical damping mechanisms at very low temperatures. *Phys. Rev. Lett.*, 110:177206, 2013.

[86] F. Hoehne, Y. A. Pashkin, O. Astafiev, L. Faoro, L. B. Ioffe, Y. Nakamura, and J. S. Tsai. Damping in high-frequency metallic nanomechanical resonators. *Phys. Rev. B*, 81(18):184112, May 2010.

[87] Thomas Faust, Johannes Rieger, Maximilian J. Seitner, Jörg P. Kotthaus, and Eva M. Weig. Signatures of two-level defects in the temperature-dependent damping of nanomechanical silicon nitride resonators. *Phys. Rev. B*, 89:100102, Mar 2014.

[88] A. Eichler, J. Moser, J. Chaste, M. Zdrojek, I. Wilson-Rae, and A. Bachtold. Nonlinear damping in mechanical resonators made from carbon nanotubes and graphene. *Nature Nanotech.*, 6(6):339–342, June 2011.

[89] Stav Zaitsev, Oleg Shtempluck, Eyal Buks, and Oded Gottlieb. Nonlinear damping in a micromechanical oscillator. *Nonlinear Dynamics*, 67(1):859, 2012.

[90] Matthias Imboden, Oliver A. Williams, and Pritiraj Mohanty. Observation of nonlinear dissipation in piezoresistive diamond nanomechanical resonators by heterodyne down-mixing. *Nano Lett.*, 13(9):4014–4019, 2013.

[91] T. F. Miao, S. Yeom, P. Wang, B. Standley, and M. Bockrath. Graphene nanoelectromechanical systems as stochastic-frequency oscillators. *Nano Lett.*, 14(6):2982–2987, June 2014.

[92] Z. Leghtas, S. Touzard, I. M. Pop, A. Kou, B. Vlastakis, A. Petrenko, K. M. Sliwa, A. Narla, S. Shankar, M. J. Hatridge, M. Reagor, L. Frunzio, R. J. Schoelkopf, M. Mirrahimi, and M. H. Devoret. Confining the state of light to a quantum manifold by engineered two-photon loss. *Science*, 347(6224):853–857, February 2015.

[93] Ananda Roy, Zaki Leghtas, A. Douglas Stone, Michel Devoret, and Mazyar Mirrahimi. Continuous generation and stabilization of mesoscopic field superposition states in a quantum circuit. *Phys. Rev. A*, 91:013810, Jan 2015.

[94] L. Mandel and E. Wolf. *Optical Coherence and Quantum Optics*. Cambirdge University Press, Cambridge, 1995.

[95] Juan Atalaya, Thomas W. Kenny, M. L. Roukes, and M. I. Dykman. Nonlinear damping and dephasing in nanomechanical systems. *Phys. Rev. B*, 94:195440, Nov 2016.

[96] M. A. Ivanov, L. B. Kvashnina, and M. A. Krivoglaz. Spectral distribution of localized vibrations. *Sov. Phys. Solid State*, 7(7):1652–&, 1965.

[97] R. J. Elliott, W. Hayes, G. D. Jones, H. F. MacDonald, and C. T. Sennett. Localized vibrations of h- and d- ions in the alkaline earth fluorides. *Proc. Roy. Soc. London*, A289(1416):1–33, 1965.

[98] V. I. Arnold. *Mathematical Methods of Classical Mechanics*. Springer, New York, 1989.

[99] E. Fermi. The raman effect of carbon dioxide. *Zeitschrift Fur Physik*, 71(3-4):250–259, March 1931.

[100] All H Nayfeh, Dean T Mook, and Larry R Marshall. Nonlinear coupling of pitch and roll modes in ship motions. *Journal of Hydronautics*, 7(4):145–152, 1973.

[101] KT Alfriend. Stability and motion in two degree-of-freedom hamiltonian systems for two-to-one commensurability. *Celestial mechanics*, 3(2):247–265, 1971.

[102] Bernd Blasius, Amit Huppert, and Lewi Stone. Complex dynamics and phase synchronization in spatially extended ecological systems. *Nature*, 399(6734):354–359, 1999.

[103] K. Nakamoto. *Infrared and Raman Spectra of Inorganic and Coordination Compounds: Part A: Theory and Applications in Inorganic Chemistry*. Wiley, 2008.

[104] D. Antonio, D. H. Zanette, and D. Lopez. Frequency stabilization in nonlinear micromechanical oscillators. *Nature Communications*, 3:806, May 2012.

[105] I. Mahboob, K. Nishiguchi, A. Fujiwara, and H. Yamaguchi. Phonon lasing in an electromechanical resonator. *Phys. Rev. Lett.*, 110(12):127202, March 2013.

[106] KR Qalandar, BS Strachan, B Gibson, M Sharma, A Ma, SW Shaw, and KL Turner. Frequency division using a micromechanical resonance cascade. *Applied Physics Letters*, 105(24):244103, 2014.

[107] Sarah H Nitzan, Valentina Zega, Mo Li, Chae H Ahn, Alberto Corigliano, Thomas W Kenny, and David A Horsley. Self-induced parametric amplification arising from nonlinear elastic coupling in a micromechanical resonating disk gyroscope. *Scientific reports*, 5, 2015.

[108] F. Mangussi and D. H. Zanette. Internal resonance in a vibrating beam: A zoo of nonlinear resonance peaks. *PLOS One*, 11:e0162365, 2016.

[109] J. Güttinger, A. Noury, P. Weber, A. M. Eriksson, C. Lagoin, J. Moser, C. Eichler, A. Wallraff, A. Isacsson, and A. Bachtold. Energy-dependent path of dissipation in nanomechanical resonators. *Nat. Nano.*, 12:631, 2017.

[110] C. Chen, D. H. Zanette, D. A. Czaplewski, S. Shaw, and D. López. Direct observation of coherent energy transfer in nonlinear micromechanical oscillators. *Nat. Comm.*, 8:15523, 2017.

[111] Chen Wang, Yvonne Y. Gao, Philip Reinhold, R. W. Heeres, Nissim Ofek, Kevin Chou, Christopher Axline, Matthew Reagor, Jacob Blumoff, K. M. Sliwa, L. Frunzio, S. M. Girvin, Liang Jiang, M. Mirrahimi, M. H. Devoret, and R. J. Schoelkopf. A schrodinger cat living in two boxes. *Science*, 352(6289):1087–1091, May 2016.

[112] M. I. Dykman and M. A. Krivoglaz. Spectral distribution of nonlinear oscillators with nonlinear friction due to a medium. *Phys. Stat. Sol. (b)*, 68(1):111–123, 1975.

[113] M. I. Dykman. Heating and cooling of local and quasilocal vibrations by non-resonance field. *Sov. Phys. Solid State*, 20(8):1306–1311, 1978.

[114] A. N. Cleland. *Foundations of nanomechanics: from solid-state theory to device applications*. Springer, Berlin, 2003.

[115] R. Lifshitz and M. C. Cross. Nonlinear dynamics of nanomechanical and micromechanical resonators. In H. G. Schuster, editor, *Review of Nonlinear Dynamics and Complexity*, pages 1–52. Wiley, Weinheim, 2008.

[116] H.-Y. Hao and H. J. Maris. Experiments with acoustic solitons in crystalline solids. *Phys. Rev. B*, 64:064302, Jul 2001.

[117] A V Akimov, A V Scherbakov, P J S van Capel, J I Dijkhuis, T Berstermann, D R Yakovlev, and M Bayer. Acoustic solitons in semiconductor nanostructures. *J. Phys. Conference Series*, 92(1):012002–, 2007.

[118] S. Ghaffari, S. A. Chandorkar, S. S. Wang, E. J. Ng, C. H. Ahn, V. Hong, Y. S. Yang, and T. W. Kenny. Quantum limit of quality factor in silicon micro and nano mechanical resonators. *Scientific Reports*, 3:3244, November 2013.

[119] M Shahmohammadi, H Fatemi, and R Abdolvand. Nonlinearity reduction in silicon resonators by doping and re-orientation. In *IEEE 26th International Conference on Micro Electro Mechanical Systems*, pages 793–796, 2013.

[120] RW Keyes. The electronic contribution to the elastic properties of germanium. *IBM Journal of Research and Development*, 5(4):266–278, 1961.

[121] John J. Hall. Electronic effects in the elastic constants of *n*-type silicon. *Phys. Rev.*, 161:756–761, Sep 1967.

[122] Fernando Cerdeira and Manuel Cardona. Effect of carrier concentration on the raman frequencies of si and ge. *Physical Review B*, 5(4):1440, 1972.

[123] L.D. Landau and E.M. Lifshitz. *Theory of elasticity*. 1970.

[124] L. D. Landau and E. M. Lifshitz. *Mechanics*. Elsevier, Amsterdam, 3rd edition, 2004.

[125] M. I. Dykman and M. A. Krivoglaz. Quantum-theory of nonlinear oscillators interacting with a medium. *JETP*, 37(3):506, 1973.

[126] P. Y. Yu and M. Cardona. *Fundamentals of Semiconductors*. Springer, Berlin, 2001.

[127] E. J. Ng, Vu Hong, Yi Yang, Ch. H. Ahn, C. L. M. Evenhart, and T. W. Kenny. Temperature dependence of the elastic constants of doped silicon. *JMEMS*, 24:730–744, 2015.

[128] G. L. Bir and G. E. Pikus. *Symmetry and Strain-induced Effects in Semiconductors*. Wiley, N.-Y., 1974.

[129] J. C. Hensel, H. Hasegawa, and M. Nakayama. Cyclotron resonance in uniaxially stressed silicon. ii. nature of the covalent bond. *Physical Review*, 138(1A):A225, 1965.

[130] HJ McSkimin and P Andreatch Jr. Measurement of third-order moduli of silicon and germanium. *Journal of applied physics*, 35(11):3312–3319, 1964.

[131] Y. P. Varshni. Temperature dependence of the elastic constants. *Phys. Rev. B*, 2(10):3952, 1970.

[132] D. Heinz, K. Moskovtsev, and T. W. Kenny. Strong temperature-dependent nonlinearity of doped si resonators. *in preparation*, 2016.

[133] L. D. Laude, F. H. Pollak, and M. Cardona. Effects of uniaxial stress on the indirect exciton spectrum of silicon. *Physical Review B*, 3(8):2623, 1971.

[134] E. Andrei, editor. *Two-Dimensional Electron Systems on Helium and Other Cryogenic Surfaces*. Kluwer Academic, Dordrecht, 1997.

[135] C. C. Grimes, T. R. Brown, Michael L. Burns, and C. L. Zipfel. Spectroscopy of electrons in image-potential-induced surface states outside liquid helium. *Phys. Rev. B*, 13(1):140–, January 1976.

[136] V.B. Shikin and Yu.P. Monarkha. On the interaction of surface electrons in liquid helium with oscillations of the vapor-liquid interface. *J. Low Temp. Phys.*, 16(1-2):193–208, 1974.

[137] M. Saitoh. Warm electrons on the liquid 4he surface. *J. Phys. Soc. Jpn.*, 42(1):201–209, January 1977.

[138] Yu P Monarkha and VB Shikin. Low-dimensional electron systems at liquid helium surface. *Fiz. Nizk. Temp.*, 8(6):563–595, 1982.

[139] R. Mehrotra, B. M. Guenin, and A. J. Dahm. Ripplon-limited mobility of a two-dimensional crystal of electrons - experiment. *Physical Review Letters*, 48(9):641–644, 1982.

[140] M I Dykman, PM Platzman, and P Seddighrad. Qubits with electrons on liquid helium. *Phys. Rev. B*, 67(15):155402, 2003.

[141] D. I. Schuster, A. Fragner, M. I. Dykman, S. A. Lyon, and R. J. Schoelkopf. Proposal for manipulating and detecting spin and orbital states of trapped electrons on helium using cavity quantum electrodynamics. *Phys. Rev. Lett.*, 105(4):040503, July 2010.

[142] A. O. Badrutdinov, D. Konstantinov, M. Watanabe, and K. Kono. Experimental study of energy relaxation of hot electrons on liquid helium-4. *Epl*, 104(4):47007, November 2013.

[143] M. A. Stan and A. J. Dahm. Two-dimensional melting: Electrons on helium. *Phys. Rev. B*, 40:8995–9005, Nov 1989.

[144] R. C. Gann, Sudip Chakravarty, and G. V. Chester. Monte carlo simulation of the classical two-dimensional one-component plasma. *Phys. Rev. B*, 20:326–344, Jul 1979.

[145] R. H. Morf. Temperature dependence of the shear modulus and melting of the two-dimensional electron solid. *Phys. Rev. Lett.*, 43:931–935, Sep 1979.

[146] C. FangYen, M. I. Dykman, and M. J. Lea. Internal forces in nondegenerate two-dimensional electron systems. *Phys. Rev. B*, 55(24):16272–16279, June 1997.

[147] D. S. Fisher, B. I. Halperin, and P. M. Platzman. Phonon-ripplon coupling and the 2-dimensional electron solid on a liquid-helium surface. *Phys. Rev. Lett.*, 42(12):798–801, 1979.

[148] I. Shapir, A. Hamo, S. Pecker, C. Pascu Moca, Ö. Legeza, G. Zarand, and S. Ilani. Imaging the Wigner Crystal of Electrons in One Dimension. *ArXiv e-prints*, 2018.

[149] V. J. Goldman, M Santos, M Shayegan, and J. E. Cunningham. Evidence for two-dimentional quantum wigner crystal. *Phys. Rev. Lett.*, 65:2189–2192, Oct 1990.

[150] I. Jo, H. Deng, Y. Liu, L. N. Pfeiffer, K. W. West, K. W. Baldwin, and M. Shayegan. Cyclotron Orbits of Composite Fermions in the Fractional Quantum Hall Regime. *Phys. Rev. Lett.*, 120:016802, January 2018.

[151] M. I. Dykman and L. S. Khazan. Effect of the interaction between nondegenerate electrons localized in a thin surface layer on the cyclotron resonance and on the magnetoconductance. *JETP*, 50:747, 1979.

[152] M. J. Lea, P. Fozooni, A. Kristensen, P. J. Richardson, K. Djerfi, M. I. Dykman, C. Fang-Yen, and A. Blackburn. Magnetoconductivity of two-dimensional electrons on liquid helium:experiments in the fluid phase. *Phys. Rev. B*, 55:16280–16292, Jun 1997.

[153] AI Larkin. Effect of inhomogeneities on the structure of the mixed state of superconductors. *Sov. Phys. JETP*, 31:784, 1970.

[154] Yoseph Imry and Shang-keng Ma. Random-field instability of the ordered state of continuous symmetry. *Physical Review Letters*, 35(21):1399, 1975.

[155] MS Bello, EI Levin, BI Shklovskii, and AL Efros. Density of localized states in the surface impurity band of a metal–insulator–semiconductor structure. *Sov. Phys. JETP,*, 80(4):822–829, 1981.

[156] Hidetoshi Fukuyama and Patrick A Lee. Pinning and conductivity of two-dimensional charge-density waves in magnetic fields. *Physical Review B*, 18(11):6245, 1978.

[157] M. I. Dykman. Stability of crystals in a random field created by vibrations of the continuum. *Sov. Phys. JETP*, 54(4):1377–1388, 1981.

[158] S. N. Coppersmith, Daniel S. Fisher, B. I. Halperin, P. A. Lee, and W. F. Brinkman. Dislocations and the commensurate-incommensurate transition in two dimensions. *Phys. Rev. Lett.*, 46:549–552, 1981.

[159] David R. Nelson and B. I. Halperin. Dislocation-mediated melting in two dimensions. *Phys. Rev. B*, 19:2457–2484, Mar 1979.

[160] Per Bak. Commensurate phases, incommensurate phases and the devil's staircase. *Reports on Progress in Physics*, 45(6):587, 1982.

[161] J. K. Kjems, L. Passell, H. Taub, J. G. Dash, and A. D. Novaco. Neutron scattering study of nitrogen adsorbed on basal-plane-oriented graphite. *Phys. Rev. B*, 13:1446–1462, Feb 1976.

[162] M. D. Chinn and S. C. Fain. Structural phase transition in epitaxial solid krypton monolayers on graphite. *Phys. Rev. Lett.*, 39:146–149, Jul 1977.

[163] W. C. Koehler. *Magnetic Structures of Rare Earth Metals and Alloys ed. by R. J Elliot*, chapter 3. Springer US, 1972.

[164] J.A. Wilson, F.J. Di Salvo, and S. Mahajan. Charge-density waves and superlattices in the metallic layered transition metal dichalcogenides. *Advances in Physics*, 24(2):117–201, 1975.

[165] T. E. Felter, R. A. Barker, and P. J. Estrup. Phase transition on mo(100) and w(100) surfaces. *Phys. Rev. Lett.*, 38:1138–1141, May 1977.

[166] K Mangold, P Leiderer, and C Bechinger. Phase transitions of colloidal monolayers in periodic pinning arrays. *Phys. Rev. Lett.*, 90:158302, 2003.

[167] G. Blatter, M. V. Feigel'man, V. B. Geshkenbein, A. I. Larkin, and V. M. Vinokur. Vortices in high-temperature superconductors. *Rev. Mod. Phys.*, 66:1125–1388, Oct 1994.

[168] K Harada, O Kamimura, H Kasai, T Matsuda, A Tonomura, and VV Moshchalkov. Direct observation of vortex dynamics in superconducting films with regular arrays of defects. *Science*, 274(5290):1167–1170, 1996.

[169] A Alan Middleton and Ned S Wingreen. Collective transport in arrays of small metallic dots. *Physical review letters*, 71(19):3198, 1993.

[170] C. R. Woods, L. Britnell, A. Eckmann, R. S. Ma, J. C. Lu, H. M. Guo, X. Lin, G. L. Yu, Y. Cao, R. V. Gorbachev, A. V. Kretinin, J. Park, L. A. Ponomarenko, M. I. Katsnelson, Yu. N. Gornostyrev, K. Watanabe, T. Taniguchi, C. Casiraghi, H. . J. Gao, A. K. Geim, and K. S. Novoselov. Commensurate-incommensurate transition in graphene on hexagonal boron nitride. *Nature Physics*, 10(6):451–456, June 2014.

[171] B. Li, D. Zhou, and Y. Han. Assembly and phase transitions of colloidal crystals. *Nature Reviews Materials*, 1:15011, 2016.

[172] Aslam Chowdhury, Bruce J. Ackerson, and Noel A. Clark. Laser-induced freezing. *Phys. Rev. Lett.*, 55:833–836, Aug 1985.

[173] Simon O Lumsdon, Eric W Kaler, and Orlin D Velev. Two-dimensional crystallization of microspheres by a coplanar ac electric field. *Langmuir*, 20(6):2108–2116, 2004.

[174] Darrell Velegol, John L Anderson, and Stephen Garoff. Determining the forces between polystyrene latex spheres using differential electrophoresis. *Langmuir*, 12(17):4103–4110, 1996.

[175] Klaus Zahn, R Lenke, and Georg Maret. Two-stage melting of paramagnetic colloidal crystals in two dimensions. *Physical review letters*, 82(13):2721, 1999.

[176] P.W. Smith, A. Ashkin, and W.J. Tomlinson. Four-wave mixing in a artificial kerr medium. *Opt. Lett.*, 6:284–7, 1981.

[177] John Michael Kosterlitz and David James Thouless. Ordering, metastability and phase transitions in two-dimensional systems. *Journal of Physics C: Solid State Physics*, 6(7):1181, 1973.

[178] J M Kosterlitz. The critical properties of the two-dimensional xy model. *Journal of Physics C: Solid State Physics*, 7(6):1046, 1974.

[179] A. P. Young. Melting and the vector coulomb gas in two dimensions. *Phys. Rev. B*, 19:1855–1866, Feb 1979.

[180] C Reichhardt and CJ Olson. Novel colloidal crystalline states on two-dimensional periodic substrates. *Physical review letters*, 88(24):248301, 2002.

[181] Shaoyi Jiang, Keith E Gubbins, and John A Zollweg. Adsorption, isosteric heat and commensurate-incommensurate transition of methane on graphite. *Molecular Physics*, 80(1):103–116, 1993.

[182] Berend Smit and Theo LM Maesen. Commensurate âĂŸfreezingâĂŹof alkanes in the channels of a zeolite. *Nature*, 374(6517):42, 1995.

[183] R. Schuster, J. V. Barth, G. Ertl, and R. J. Behm. Phase transitions and domain-wall structures in the k/cu(110) system: Scanning-tunneling-microscopy observations and monte carlo simulations. *Phys. Rev. B*, 44:13689–13702, Dec 1991.

[184] Andrea Vanossi, Nicola Manini, and Erio Tosatti. Static and dynamic friction in sliding colloidal monolayers. *Proceedings of the National Academy of Sciences*, 109(41):16429–16433, 2012.

[185] C. Reichhardt, C. J. Olson, N. Grønbech-Jensen, and Franco Nori. Moving wigner glasses and smectics: Dynamics of disordered wigner crystals. *Phys. Rev. Lett.*, 86:4354–4357, May 2001.

[186] Pablo F Damasceno, Cláudio José DaSilva, José Pedro Rino, and Ladir Cândido. Temperature and pinning effects on driving a 2d electron system on a helium film: A numerical study. *Journal of Low Temperature Physics*, 160(1-2):58–67, 2010.

[187] G. Piacente and F. M. Peeters. Pinning and depinning of a classic quasi-one-dimensional wigner crystal in the presence of a constriction. *Phys. Rev. B*, 72:205208, Nov 2005.

[188] LD Landau. Die kinetische gleichung fuer den fall coulombscher wechselwirkung. *Phys. Z. Sowjet*, 10:154, 1936.

[189] Joshua A Anderson, Chris D Lorenz, and Alex Travesset. General purpose molecular dynamics simulations fully implemented on graphics processing units. *Journal of Computational Physics*, 227(10):5342–5359, 2008.

[190] Jens Glaser, Trung Dac Nguyen, Joshua A Anderson, Pak Lui, Filippo Spiga, Jaime A Millan, David C Morse, and Sharon C Glotzer. Strong scaling of general-purpose molecular dynamics simulations on gpus. *Computer Physics Communications*, 192:97–107, 2015.

[191] Ernst Hairer, Christian Lubich, and Gerhard Wanner. *Geometric numerical integration: structure-preserving algorithms for ordinary differential equations*, volume 31. Springer Science & Business Media, 2006.

[192] D. C. Glattli, E. Y. Andrei, and F. I. B. Williams. Thermodynamic measurement on the melting of a two-dimensional electron solid. *Phys. Rev. Lett.*, 60(5):420–423, 1988.

[193] James M Haile. *Molecular dynamics simulation: elementary methods*. John Wiley & Sons, Inc., 1992.

[194] P. G. De Gennes. Liquid dynamics and inelastic scattering of neutrons. *Physica*, 25(7-12):825–839, 1959.

[195] J. Frenkel. *Kinetic Theory of Liquids*. Dover Publications, Inc., 1955.

[196] R. K. Kalia, P. Vashishta, and S. W. de Leeuw. Melting of a two-dimensional electron lattice. *Phys. Rev. B*, 23:4794–4797, May 1981.

[197] Martial Mazars. The melting of the classical two-dimensional wigner crystal. *EPL (Europhysics Letters)*, 110(2):26003, 2015.

[198] I.P. Ipatova, A.V. Subashiev, and V.A. Voitenko. Electron light scattering from doped silicon. *Solid State Communications*, 37(11):893 – 895, 1981.

[199] M. Prunnila, P. Kivinen, A. Savin, P. Törmä, and J. Ahopelto. Intervalley-scattering-induced electron-phonon energy relaxation in many-valley semiconductors at low temperatures. *Phys. Rev. Lett.*, 95:206602, Nov 2005.

[200] Michel Dutoit. Microwave phonon attenuation measurements in n-type silicon. *Physical Review B*, 3(2):453, 1971.

[201] Brad D Malone and Marvin L Cohen. Quasiparticle semiconductor band structures including spin-orbit interactions. *J. Phys. C*, 25(10):105503, 2013.

[202] Karl F Graff. *Wave Motion in Elastic Solids*. Dover Publications, New York, 1991.

[203] Ray H. Baughman, Justin M. Shacklette, Anvar A. Zakhidov, and Sven Stafstrom. Negative poisson's ratios as a common feature of cubic metals. *Nature*, 392(6674):362–365, March 1998.

[204] G Feher. Electron spin resonance experiments on donors in silicon. i. electronic structure of donors by the electron nuclear double resonance technique. *Physical Review*, 114(5):1219, 1959.

[205] Donald Long. Energy bands in semiconductors. *Journal of Applied Physics*, 33(5):1682–1696, 1962.

[206] L. D. Landau and E. M. Lifshitz. *Electrodynamics of Continuous Media*. Elsevier Butterworth-Heinemann, Oxford, second edition, 2004.

[207] M. Abramowitz and I. A. Stegun, editors. *Handbook of Mathematical Functions with Formulas, Graphs, and Mathematical Table*. Dover Publications, Inc., 1972.